TU Delft

Delft University of Technology

Advanced Magnetocaloric Regenerators for Heat Pump Applications

Pineda Quijano, D.F.

DOI
10.4233/uuid:f5e1eb12-fb58-495d-a27f-8a19bccec5ba

Publication date
2025

Document Version
Final published version

Citation (APA)
Pineda Quijano, D. F. (2025). *Advanced Magnetocaloric Regenerators for Heat Pump Applications*. [Dissertation (TU Delft), Delft University of Technology]. https://doi.org/10.4233/uuid:f5e1eb12-fb58-495d-a27f-8a19bccec5ba

Important note
To cite this publication, please use the final published version (if applicable).
Please check the document version above.

Copyright
Other than for strictly personal use, it is not permitted to download, forward or distribute the text or part of it, without the consent of the author(s) and/or copyright holder(s), unless the work is under an open content license such as Creative Commons.

Takedown policy
Please contact us and provide details if you believe this document breaches copyrights.
We will remove access to the work immediately and investigate your claim.

This work is downloaded from Delft University of Technology.
For technical reasons the number of authors shown on this cover page is limited to a maximum of 10.

Advanced Magnetocaloric Regenerators for Heat Pump Applications

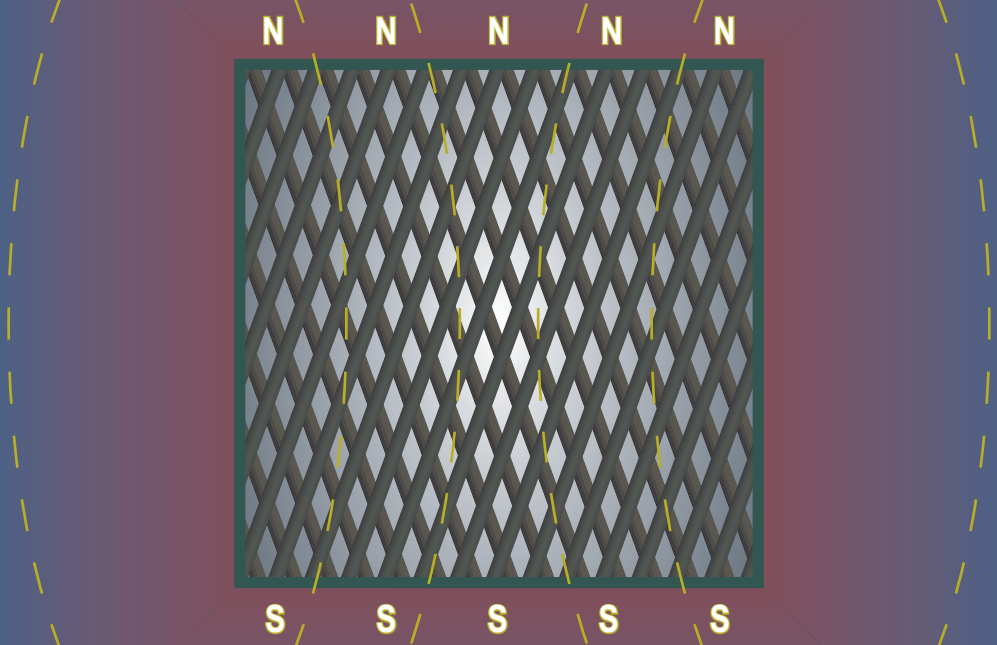

Diego Pineda Quijano

Advanced Magnetocaloric Regenerators for Heat Pump Applications

Advanced Magnetocaloric Regenerators for Heat Pump Applications

Dissertation

for the purpose of obtaining the degree of doctor
at Delft University of Technology by
the authority of the Rector Magnificus, Prof.dr.ir. T.H.J.J. van der Hagen,
chair of the Board for Doctorates,
to be defended publicly on
Wednesday 19 November 2025 at 10:00

by

Diego Fernando PINEDA QUIJANO

Master of Science in Mechanical Engineering,
Delft University of Technology, Delft, The Netherlands,
born in Bucaramanga, Colombia

This dissertation has been approved by the promotors.

Composition of the doctoral committee:

Rector Magnificus,	chairperson
Prof. Dr. E.H. Brück,	Delft University of Technology, *promotor*
Dr. ir. C.A. Infante Ferreira,	Delft University of Technology, *promotor*

Independent members:

Prof. Dr. K. Hooman	Delft University of Technology
Prof. Dr. ir. B.J. Boersma	Delft University of Technology
Prof. Dr. ir. M. Shahi	University of Twente
Prof. Dr. ir. D. Smeulders	Eindhoven University of Technology
Prof. Dr. A. Kitanovski	University of Ljubljana

This project has been implemented with support from the MMIP 3&4 scheme of the Ministry of Economic Affairs and Climate Change and the Ministry of the Interior and Kingdom Relations of the Netherlands.

Keywords: active magnetocaloric regenerator, layered AMR, numerical modeling, friction factor, heat transfer coefficient, additive manufacturing

Printed by: Proefschriftspecialist

Cover by: Diego Pineda

Copyright © 2025 by D.F. Pineda Quijano

ISBN 978-94-6518-147-9

An electronic copy of this dissertation is available at https://repository.tudelft.nl/.

Dedicated to my beloved wife Adriana Guzmán, and my children Daniel and Amelia. To my parents Jose Luis and Teresa, my brothers Fabián, Jose Luis, Oscar, Sebastián, and my sister Maria Paula.

Diego Fernando Pineda Quijano

CONTENTS

NOMENCLATURE

Variables

A	area (m^2)
a	constant (-)
B	magnetic field intensity (T)
b	constant (-)
C	constant (-)
c	specific heat capacity ($J\,kg^{-1}\,K^{-1}$)
COP	coefficient of performance (-)
D	diameter (m)
DF	degradation factor (-)
f	frequency (Hz)
ff	friction factor (-)
g	specific Gibbs energy ($J\,m^{-3}$)
$\dot{g}$	heat generation rate per unit volume ($W\,m^{-3}$)
H	height (m)
h	heat transfer coefficient ($W\,m^{-2}\,K^{-1}$)
$\bar{h}$	average heat transfer coefficient ($W\,m^{-2}\,K^{-1}$)
H_0	magnetic field ($A\,m^{-1}$)
I	electrical current (A)
k	thermal conductivity ($W\,m^{-1}\,K^{-1}$)
L	regenerator length (m)
M	magnetization ($A\,m^{-1}$)
m	mass (kg)
$\dot{m}$	mass flow rate ($kg\,s^{-1}$)
N	number (-)
Nu	Nusselt number (-)
P	pressure (Pa)
P_{cs}	perimeter of cross section (m)
Pe	Peclet number (-)

Pr	Prandtl number (-)
q	specific heat ($\mathrm{J\,m^{-3}}$)
$\dot{Q}$	heat transfer rate (W)
$\dot{q}$	heat transfer rate per unit area ($\mathrm{W\,m^{-2}}$)
$\dot{Q}_\mathrm{c}$	cooling capacity (W)
$\dot{Q}_\mathrm{h}$	heating capacity (W)
Re	Reynolds number (-)
S	inter-fiber pitch (m)
s	specific entropy ($\mathrm{J\,kg^{-1}\,K^{-1}}$)
s_p	inter-plate spacing (m)
T	temperature (K)
t	time (s)
$\bar{T}$	average temperature (K)
t_p	plate thickness (m)
U	overall heat transfer coefficient ($\mathrm{W\,m^{-2}\,K^{-1}}$)
u	specific internal energy ($\mathrm{J\,m^{-3}}$)
V	volume ($\mathrm{m^3}$)
v	velocity ($\mathrm{m\,s^{-1}}$)
$\dot{V}$	volumetric flow rate ($\mathrm{m^3\,s^{-1}}$)
$\mathcal{V}$	voltage (V)
W	width (m)
w	specific work ($\mathrm{J\,m^{-3}}$)
$\dot{W}$	power input (W)
x	axial coordinate (m)
y	coordinate perpendicular to flow direction (m)
Z	vertical coordinate during 3D printing process (m)

Greek symbols

β	specific surface area ($\mathrm{m^2\,m^{-3}}$)
Δ	difference (-)
δ	inexact differential (-)
η	efficiency (-)
μ	dynamic viscosity (Pa s)
μ_0	permeability of vacuum ($\mathrm{T\,m\,A^{-1}}$)
ρ	density ($\mathrm{kg\,m^{-3}}$)

τ	cycle period (s)
ε	porosity or void fraction (-)
φ	utilization (-)
ξ	intermediate auxiliary variable (m^{-2})

Subscripts

ad	adiabatic
air	in air
amb	ambient
AMR	active magnetocaloric regenerator
Arch	Archimedes
block,bottom	surface of block in contact with bottom copper plate
block,left	left surface of the block when facing downstream
block,right	right surface of the block when facing downstream
block,top	surface of block in contact with top copper plate
bottom	first printed layer of fibers
c	cold reservoir
Carnot	reversible cycle
chan	channel
cold	cold side
cs	cross section
Curie	Curie
D	Darcy
displ	displacement
eff	effective
end	end MCM layer
eth	in ethanol
ext	external dimension of 3D printed block
f	fluid
fiber	3D printed fiber of MCM
h	hot reservoir
H_0	constant magnetic field
HEX	heat exchanger
hom	homogeneous
hot	hot side
hp	heat pump

hyd	hydraulic
hys	hysteresis
inner	inner MCM layers
int	internal
l	lattice
layer	layer of printed fibers
m	magnetic
max	maximum
MCE	magnetocaloric effect
mod	modified
model	obtained from geometric model
nozzle	3D printing nozzle
out	outdoor
ovr	overlapping
p	particle
P	constant pressure
par	particular
post	after heat treatment
pump	by pump
RAF	region available for flow
room	indoor
s	solid
sp	spherical particle
span	span
sup	superficial
T	constant temperature
th	based on theoretical geometry
top	last printed layer of fibers
uc	unit cell
V	constant volume
water	water
wire	wire
XCT	x-ray computed tomography

Superscripts

e	electronic

f	final (high)
i	initial (low)
in	entering
l	lattice
m	magnetic
max	maximum
min	minimum
out	leaving

Abbreviations

AFM	antiferromagnetic
AMR	active magnetocaloric regenerator/regenerative
BAM	Bundesanstalt für Materialforschung und -prüfung
CAD	computer-aided design
CHEX	cold-side heat exchanger
COP	coefficient of performance
DC	direct current
DMM	digital multimeter
EG	ethylene glycol
EU	European Union
FAME	Fundamental Aspects of Materials and Energy
FDM	fused deposition modeling
FEPA	Federation of European Producers of Abrasives
FM	ferromagnetic
GHG	greenhouse gas
GPIB	general purpose interface bus
GSHEX	ground source heat exchanger
GWP	global warming potential
HFC	hydrofluorocarbon
HHEX	hot-side heat exchanger
HTF	heat transfer fluid
IEA	International Energy Agency
IEBB	Integrale Energie Transitie in Bestaande Bouw
Lpm	liter per minute
MCE	magnetocaloric effect
MCHP	magnetocaloric heat pump

MCM	magnetocaloric material
OD	outer diameter
PBCP	packed bed crushed particles
PBSP	packed bed spherical particles
PID	Proportional-Integral-Derivative controller
PM	paramagnetic
PP	parallel plate
PWM	pulse width modulation
RAF	region available for flow
ROI	region of interest
RTD	resistive temperature detector
RVO	Rijksdienst voor Ondernemend Nederland
SCOP	seasonal coefficient of performance
SEM	scanning electron microscopy
UFH	underfloor heating
XCT	x-ray computed tomography

1

INTRODUCTION

1.1. WHY MAGNETOCALORIC HEAT PUMPS?

Our planet is warming as a consequence of uncontrolled human actions. It has been demonstrated that the continued release of greenhouse gases (GHGs) into the atmosphere originated from human activities has caused a steady rise in global temperatures [1]. If this trend continues, we will face the devastating consequences of climate change. Fortunately, although somewhat delayed, world leaders have taken steps to reverse this trend. The Paris Agreement, signed in 2015 by 195 countries, demonstrates the global commitment to implement measures that reduce GHG emissions in order to keep global warming below 2 K relative to preindustrial levels.

In line with the Paris Agreement, in June 2019 the Netherlands signed a national climate agreement with the main goal of reducing GHG emissions by 49% in the year 2030 compared to 1990 levels. It also aims to reach near net-zero emissions by 2050. This national agreement sets specific goals and measures in the following sectors: the built environment, mobility, industry, agriculture and land use, and electricity [2]. For the built environment in particular, the main goal is to eliminate natural gas consumption in 1.5 million homes by 2030 and, ultimately, in 7 million homes and 1 million buildings by 2050. These goals were motivated not only by the need to address climate change but also by the urgency to discontinue natural gas production in Groningen and reduce the risks associated with reliance on foreign energy sources. This risk materialized in 2022 with the start of the war in Ukraine and the resulting energy crisis in the Netherlands.

To address this dependency and reduce the use of natural gas for indoor heating of homes and buildings, two main actions are identified in the Dutch climate agreement: improving insulation of homes and buildings and implementing district-oriented renewable heating strategies, including the use of district heating systems, the distribution

of sustainable gases (biogas, hydrogen) through the existing natural gas networks, and the replacement of boilers with heat pumps running on clean electricity. Heat pumps, in particular, will play a crucial role in reducing natural gas consumption in the Netherlands, as the installation of stand-alone gas boilers will no longer be allowed in new houses and residential buildings starting in 2026.

This policy shift places heat pump technology at the center of residential heating strategies in the Netherlands. However, commercial heat pumps rely on vapor compression technology that uses liquid refrigerants, some of which have global warming potentials (GWPs) exceeding by more than 1000 times that of CO_2. Since the continued use of such refrigerants would undermine efforts to reduce GHG emissions, many of them, especially hydrofluorocarbons (HFCs), are being phased out globally through environmental regulations such as the Kigali Amendment (2016) to the Montreal Protocol, the European F-Gas Regulation (2014), which applies in the Netherlands, the American Innovation and Manufacturing Act (2020), to name just the most prominent examples. This global effort to phase out HFCs aligns directly with the objectives of the Paris Agreement, reinforcing the broader commitment to reduce GHG emissions and limit global warming.

In light of these increasingly strict environmental regulations on high-GWP refrigerants, heat pump manufacturers have responded in two main ways. The first is by adopting natural refrigerants such as CO_2, ammonia, and propane. These substances pose specific safety challenges due to the high pressures of CO_2 systems, the toxicity of ammonia, and the flammability of propane. As a result, their safe handling requires trained and skilled technicians. The second approach involves exploring alternative heat pump technologies. Among the environmentally friendly alternatives, magnetocaloric heat pump (MCHP) technology is considered by many to be one of the most promising and advanced options [3, 4].

Building on this, MCHPs for room-temperature applications could, in theory, achieve better performance due to the reversible nature of the magnetocaloric effect (MCE), lower noise levels resulting from the absence of compressors, and reduced maintenance due to a reduced number of moving parts [5]. These systems exploit the MCE, which manifests as either an adiabatic temperature change or an isothermal entropy change in a magnetocaloric material (MCM) subjected to changes in magnetic field. Room-temperature MCHPs typically operate on the so-called active magnetic regenerative (AMR) cycle, which enables an increased temperature span and combines well with Erikson or Brayton magnetic thermodynamic cycles [6, 7]. Moreover, because water is typically used as the heat transfer fluid (HTF) and the MCMs are non-toxic, non-flammable, and have zero global warming and ozone depletion potential, the technology can also be

considered environmentally friendly and safe. Despite its potential, this technology still requires further development before it can reach commercial viability. Several research groups and private companies around the world are working to improve its cost-effectiveness and efficiency to make it competitive with conventional vapor compression systems.

The global relevance of heat pumps is reflected in estimates by the International Energy Agency, which reported that by 2021 only 5% of global households used heat pumps to meet their heating needs, and that this share must triple by 2030 to achieve the Sustainable Development Goals. This translates to the installation of 600 million heat pumps worldwide between 2022 and 2030 [8]. This is a truly challenging target that requires strong national policies supporting the adoption of this heating technology. Fortunately, as the Dutch government has done, governments around the world are increasingly recognizing the importance of heat pumps and have introduced policies to encourage their deployment not only in new buildings but also in renovations of existing ones. As a result, the global heat pump market is expected to expand significantly in the coming years. In this context, there is an urgent need for alternative technologies that combine high efficiency with low environmental impact. MCHPs, if successfully developed, have the potential to meet these demands and benefit from a rapidly growing market. Continued investment in research and development remains critical for unlocking this potential.

1.2. FOUNDATIONAL CONCEPTS AND FURTHER READING

Readers who are less familiar with the fundamental principles of the magnetocaloric technologies are encouraged to consult chapter 2. This chapter provides a detailed overview of the core physical and engineering concepts that form the basis for the analysis and methodologies applied throughout the thesis. It covers topics such as the definition and quantification of the MCE, the properties and behavior of MCMs, thermodynamic cycles, and the operational principles of magnetocaloric devices. Several of these concepts are essential for understanding specific discussions already presented in the current chapter. Therefore, readers seeking deeper clarity or foundational knowledge are advised to refer to chapter 2 before proceeding further.

1.3. MAGNETOCALORIC HEAT PUMPS FOR THE BUILT ENVIRONMENT

The integration of MCHPs into residential buildings has recently been a topic of investigation in Europe. Johra et al. [9] proposed a

configuration for a residential MCHP system based on a ground-source heat exchanger (GSHEX) and underfloor heating (UFH) as external heat exchangers, as illustrated in Figure 1.1. In parts of this thesis, this configuration is adopted to define the operating conditions of the heat pump.

The use of GSHEXs is particularly advantageous for MCHPs employing layered AMRs, as ground temperature fluctuates significantly less than ambient air temperature over the course of a heating season. Operating between relatively fixed reservoir temperatures is essential to ensure activation of all layers in a layered AMR, since each layer is designed to operate within a specific temperature range. Furthermore, all heat pumps, including MCHPs, achieve a higher coefficient of performance (*COP*) when operating across smaller temperature spans, a condition that this configuration helps to fulfill. Specifically, UFH systems require lower inlet temperatures than traditional radiators, and GSHEXs can provide higher return temperatures during the coldest periods of the heating season compared to air heat exchangers. As a result, this configuration offers favorable boundary conditions for maximizing the efficiency and effectiveness of MCHPs.

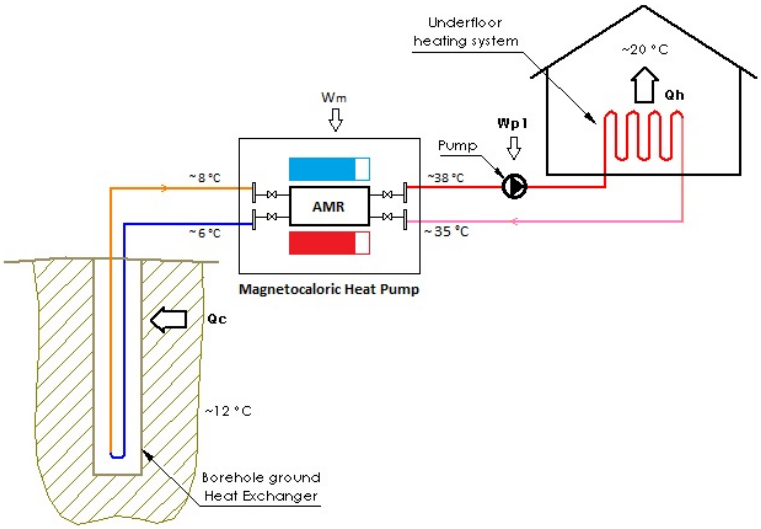

Figure 1.1.: Basic configuration of a residential MCHP system using a single hydraulic circuit [9]

As shown in Figure 1.1 and highlighted by Johra et al. [10], this heat pump configuration requires only one hydraulic circuit. This represents a major difference compared to vapor-compression heat pump systems, which require two separate circuits, one connected to the GSHEX and the other to the UFH system. MCHP systems could, however, also adopt

this dual-circuit configuration by using intermediate heat exchangers, as illustrated in Figure 1.2.

The single-circuit configuration offers two main advantages. First, only one circulation pump is needed, which helps reduce the overall system energy consumption. Although additional pumps could, in some cases, improve system control or performance, they also introduce motor-related inefficiencies that may outweigh those benefits. Second, losses associated with heat transfer processes in intermediate heat exchangers are eliminated. This simplicity, however, comes at the cost of reduced design and operational flexibility, as the GSHEX and UFH become coupled through the same mass flow rate circulating through all components.

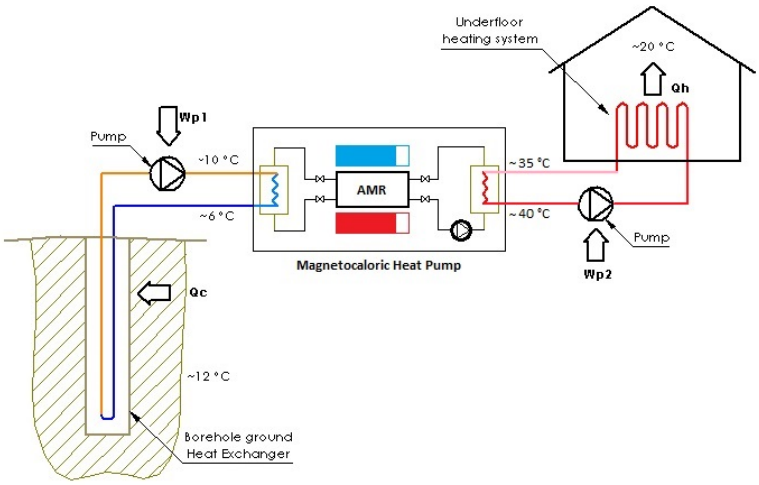

Figure 1.2.: Alternative configuration of a residential MCHP system using two external hydraulic circuits and intermediate heat exchangers.

In a single-circuit configuration, the limited adiabatic temperature change of the MCMs constrains the maximum allowable temperature change of the HTF in the external heat exchangers. As a result, a higher flow rate is required to deliver the necessary thermal power. Under these conditions, the design of the external heat exchangers must depart from standard practices commonly followed by manufactures, typically by increasing pipe diameter or adding parallel circuits, to keep fluid velocity within acceptable limits while ensuring that the available heat transfer area is not compromised. Notably, this limitation is avoided in the dual-circuit configuration, where each heat exchanger operates independently and their design is not directly constrained by the thermal limitations of the AMRs.

In terms of implementation, for renovations or replacements of existing heating systems, the dual-circuit configuration may be preferred to avoid the need to replace or retrofit the external heat exchangers. Furthermore, given the natural reluctance of manufacturers to change established practices, this alternative configuration could also be applied in new constructions, since the external heat exchangers can likely be designed similarly to those used in vapor-compression heat pump systems.

1.4. CHALLENGES OF THE MCHP TECHNOLOGY

The MCHP technology must still overcome several challenges before it can reach commercial viability. These challenges include limited efficiency, noise, reliability, system complexity, scalability issues, and material-related limitations. The following section explores these issues in detail.

Regarding efficiency, to the best of our knowledge, only one research group has reported second-law efficiencies exceeding 50% in a magnetocaloric refrigeration device [11]. This result was achieved using gadolinium as the MCM and a superconducting magnet providing a 5 T magnetic field, with the device delivering 600 W of cooling power across a temperature span of 10 K [11]. However, the vast majority of prototypes exhibit second-law efficiencies below 20 % [12–16], which is typical of small vapor compression systems [4]. A recent experimental comparison between a magnetocaloric refrigeration unit and a vapor-compression system, both operating the same wine cooler cabinet, demonstrated the inferior performance of the magnetocaloric system, despite the already low efficiency of the vapor-compression one [17].

The efficiency of MCHP systems is constrained not only by the high pumping power required to circulate the fluid through the porous AMR structure, which can be reduced using an optimized geometry, but also by the intrinsic irreversibilities within the AMRs. These include heat leaks to the ambient, axial heat conduction from the hot to the cold side, heat transfer over a finite temperature difference, and flow-related issues such as channeling [13]. In addition, the relatively modest magnitude of the MCE achievable with permanent magnets further limits the cooling and heating capacity and overall efficiency. Hence, the development of MCMs exhibiting a giant MCE, particularly a high adiabatic temperature change, is urgently needed to achieve efficient MCHP operation.

Beyond efficiency, noise performance has also been identified as a potential advantage of magnetocaloric systems [18], frequently attributed to the absence of compressors [19]. In practice, however, the pump and its motor, the magnet drive train, and especially the valve

system, which consists of solenoid valves in many prototypes, generate significant noise, often exceeding that of vapor compression devices with comparable capacity. This is partly because most prototypes have not been specifically optimized for noise reduction, as development efforts have primarily focused on improving AMR performance. For future commercial MCHP devices, solenoid valves should be avoided, not only because of their characteristic ticking noise, but also due to their energy consumption, which is largely dissipated as heat into the HTF, thereby reducing both the overall capacity and the *COP* of the heat pump.

In addition to noise, reliability is a key factor that will influence the long-term adoption of MCHP systems. While it is often stated that these systems require less maintenance [11], the opposite may be in fact true. This is primarily due to the reciprocating nature of the flow in AMRs, which requires complex valve systems with multiple connections and moving parts that are prone to leakage, friction, and wear, ultimately requiring maintenance or replacement. Furthermore, AMRs are porous structures with very small flow channels that are highly susceptible to fouling, demanding periodic cleaning or replacement. Although this issue could potentially be mitigated with a high-quality filtration stage, the filters themselves would then become the components requiring regular replacement. Additionally, the solid MCM in the AMRs may degrade over time due to erosion from prolonged cyclic flow, leading to a gradual decline in overall system performance.

In parallel with these reliability concerns, the inherent complexity of MCHP systems presents major barriers to their commercial adoption. On one hand, manufacturers do not yet fully understand the working principles, capabilities, and limitations of MCHPs. So, training, education, and knowledge transfer from academia to industry are essential to improve the positioning of MCHP technology within the manufacturing community. On the other hand, MCHP systems are inherently more complex than vapor-compression systems, particularly in small-scale applications, and manufacturers often prefer simpler solutions unless no viable alternative exists. Whereas a small vapor-compression system requires basically only a compressor and an expansion device, along with heat exchangers, a functional MCHP unit involves a (rotating) magnet, a fluid circulation pump, a valve system, and multiple carefully engineered AMRs. To better understand what makes MCHPs challenging to implement, it is useful to break down the key sources of mechanical and operational complexity:

- The magnetic field intensity in the air gap of magnet assemblies increases as the air gap is reduced. Since higher magnetic fields are generally preferred for improved performance, only a limited amount of MCM can typically be placed in a single AMR. As a result, an MCHP often requires multiple AMRs to achieve useful heating or

cooling capacities. This increases the complexity of the hydraulic system due to the multiple piping and valve connections required.

- The HTF moves in a reciprocating manner inside the AMRs, requiring complex valve systems. The timing of these valves must be precisely synchronized with the magnetization and demagnetization cycles of the AMRs, i.e. with the movement of the magnet. As mentioned earlier the valve system itself is a source of potential issues.

- Differences in flow resistance between the cold and hot blows in even a single AMR of a multi-bed device may lead to flow imbalance across the entire system [20]. To compensate, additional pressure drop is introduced, typically by using needle valves in the flow path with lower resistance [20–22]. Without proper flow balancing, the system cannot achieve its full potential in terms of temperature span, cooling or heating capacity, and *COP*. The flow balancing process itself is complex and requires expertise as well as extensive testing of each manufactured device. However, this issue has the potential to be partially improved by manufacturing AMRs using additive manufacturing techniques.

- The small magnitude of the adiabatic temperature change in the MCMs typically used in MCHPs, when operated with permanent magnets, limits the maximum allowable temperature change of the HTF in the external heat exchangers. As a result, higher flow rates are required to absorb or reject a given amount of heat at the source or sink, respectively. This limitation can be addressed by introducing intermediate heat exchangers, although doing so adds complexity and introduces irreversibilities to the system. Manufacturers may resist changing the design of such heat exchangers.

Among all system components, the AMR is particularly complex and presents unique engineering difficulties. While Gd AMRs are relatively simple and easy to manufacture in different shapes thanks to the favorable properties of gadolinium, this rare earth metal is still expensive and has a limited, although relatively broad, operating temperature window. For heat pump applications in particular, materials with higher Curie temperatures than that of Gd are necessary. Alternative giant-MCE MCMs with higher Curie temperatures are available, and their production has become scalable to some extent. However, these materials typically exhibit their MCE over a narrower temperature range, making layered configurations necessary to achieve useful temperature spans. Determining the optimal length of each layer in such AMRs is a complex task that requires detailed numerical modeling and precise knowledge of thermal and magnetic properties of each material

involved. An additional complication is the limited predictability of these properties from raw materials to finished components, requiring each layer to be individually tested, at least to determine its Curie temperature. While this is currently the case, ongoing improvements in material synthesis and process control may reduce or eliminate the need for such layer-by-layer verification in the future.

Furthermore, due to the limited reproducibility of the available MCMs, it is currently difficult to produce a series of layered AMRs with identical thermal and magnetic properties. As a result, while all AMRs in a multi-bed device should ideally be identical, in practice there will always be differences in the distribution of Curie temperatures, heat capacities, and MCE peaks across AMRs placed in the same device [23]. The impact of these differences has not yet been thoroughly studied, but they are expected to undermine the overall performance of the system [24]. The manufacturing process of this type of AMRs is therefore complex and characterized by low repeatability.

Another important consideration for commercial implementation is the physical footprint of MCHP systems. Magnetocaloric devices are typically heavy and bulky due to the need for large magnets to generate high magnetic fields. Slaughter et al. [22] suggested that small magnetocaloric systems up to 200 W working with Gd as MCM could have comparable power densities (W/kg) as those of vapor compression counterparts. However, when scaled up, the power density of magnetocaloric systems tends to be much lower than that of vapor compression systems of similar capacity. A reasonable approach to increase power density is to raise the operating frequency [25]. However, the reciprocating flow in AMRs imposes limits on the maximum achievable frequency. Furthermore, geometries that provide high heat transfer coefficients and feature small flow channels and thin walls are necessary to enable rapid heat transfer from the MCM.

In addition to system-level challenges, several material-specific issues continue to hinder development and scalability. These include:

- Limited MCE in currently available materials at low magnetic field intensities
- Trade-offs between magnetic field strength and the mass, volume, and cost of permanent magnets
- Brittleness of giant-MCE materials, which complicates their mechanical processing and shaping into fine or complex geometries. However, additive manufacturing has the potential to address this issue
- Poor long-term mechanical stability of scalable MCM families such as MnFePSi and LaFeSi, leading to degradation under thermal or

magnetic cycling and requiring mitigation strategies like protective coatings or alloy tuning

- Low reproducibility of MCM properties, at small-scale production

Taken together, these technical challenges directly affect the pace of industrial development and the ability to bring magnetocaloric technology to market. Despite the difficulties, a small number of companies, including two in Europe and one in the UK, are fully focused on developing this technology from a systems perspective. Additionally, two other European companies are working on the manufacturing of AMRs using scalable MCMs. Several large enterprises in the refrigeration, heat pump, and air conditioning sectors are also exploring the development of magnetocaloric devices. However, the commercial viability of magnetocaloric systems will only be realized when these devices offer a clear advantage in either upfront cost or efficiency compared to current available technologies, where improved efficiency also translates into long-term operational cost savings. As neither condition has yet been met despite ongoing research and development, the path to widespread adoption of MCHP technology remains long and uncertain. Continued interdisciplinary efforts across materials science, mechanical engineering, and systems integration will be crucial to unlock the full potential of this promising—but currently immature—technology.

1.5. TOWARDS ADVANCED AMRS

Although many of the challenges in the development of magnetocaloric systems are not directly related to the AMRs, significant improvements to the technology are possible by implementing regenerators produced using advanced manufacturing techniques.

Additive manufacturing offers new opportunities to address several of the challenges associated with the design and fabrication of magnetocaloric regenerators. Additive manufacturing techniques, particularly extrusion-based methods, provide the flexibility needed to implement complex regenerator geometries that simultaneously optimize heat exchange by reducing flow channel size and increasing heat transfer area, minimize pressure drop through reduced tortuosity, and ensure effective interaction with the applied magnetic field. With additive manufacturing, the MCM can also be shaped into geometries with thinner features, potentially enabling operation at higher frequencies and thus increasing the power density of the magnetocaloric system.

Furthermore, additive manufacturing supports the scalable production of layered AMRs using first-order MCMs such as MnFePSi- and LaFeSi-based compounds. It facilitates the integration of multiple materials

with different Curie temperatures into a layered regenerator, allowing improved control over MCM positioning. Sharper interfaces between layers can be achieved, and the materials remain fixed during operation, eliminating the need for adhesives often required in packed bed assemblies. Additionally, this manufacturing method could enable the production of series of geometrically similar AMRs, thereby reducing the flow balancing issues in multi-bed devices.

Such capabilities support the realization of advanced AMRs that can operate more effectively across wider temperature spans moving the technology one step closer to commercial viability.

1.6. THESIS OUTLINE

In line with the Dutch Climate Agreement, the Dutch government, through the Netherlands Enterprise Agency (RVO, from the Dutch *Rijksdienst voor Ondernemend Nederland*), provided financial support for research into various aspects of the energy transition in existing buildings. Within this framework, the Integral Energy Transition in Existing Buildings (IEBB, from the Dutch *Integrale Energie Transitie in Bestaande Bouw*) program generated knowledge across a broad spectrum, ranging from building renovations and behavioral aspects of energy use to heating technologies. Among these, MCHPs received particular attention for their potential application in the built environment.

This project provided an opportunity to explore key questions such as: Are MCHPs suitable for efficiently providing heat to well-insulated houses in the Netherlands? How can an AMR for a MCHP be optimally designed to cope with variations in heating demand and source/sink temperatures? And can 3D printing techniques and the resulting geometries contribute to improved AMR performance? This thesis addresses these and related questions.

To begin addressing them, we first examined the influence of material layering strategies on AMR performance. The distribution of Curie temperatures as well as the positioning and length of each material in layered AMRs have a significant impact on performance and are closely linked to the chosen manufacturing method. Ideally, the Curie temperature should vary continuously along the AMR to maximize the MCE at every position. While this is challenging to achieve in practice, materials scientists in the Fundamental Aspects of Materials and Energy (FAME) group hypothesize that it could be made feasible by combining additive manufacturing techniques with an appropriate heat treatment process. The concept involves printing the AMR using a few carefully selected compositions of the MnFePSi material, followed by the induction of a quasi-continuous Curie temperature gradient through diffusion of elements within the matrix during the sintering process. Assuming

this approach is viable, we numerically evaluated the performance of AMRs produced by arranging the initial compositions in three different ways: (1) a linear distribution of Curie temperatures, (2) a sigmoidal distribution, and (3) a linear distribution with extended first and last layers. The methodology and results of this study are presented in **chapter 3**.

Building upon this, we subsequently assessed the performance of a MCHP system under realistic seasonal conditions. Specifically, we conducted a numerical evaluation of a system designed to supply heat to a well-insulated house in the Netherlands. The analysis was based on an AMR comprising several layers of MnFePSi materials with a linear distribution of Curie temperatures spanning from 8 °C to 35 °C. To determine the operating temperatures of the heat pump, we adopted the system configuration described in section 1.3. For capacity control under part-load conditions, we proposed a strategy involving continuous modulation of both the flow rate and operating frequency. Additionally, we introduced a modularization approach in which the heat pump is divided into modules containing multiple AMRs, which can be selectively activated or deactivated depending on the heating demand of the house. The objectives, methodology, and findings of this study are detailed in **chapter 4**.

While these simulations offered valuable insights, their accuracy depends heavily on the reliability of the underlying numerical model and the correlations used. Although the model was initially validated using experimental data from a single-AMR device based on gadolinium, further validation was deemed necessary to ensure the robustness of our predictions, particularly for multi-layered and multi-bed configurations representative of pre-commercial MnFePSi-based heat pump systems. As a possible route for such validation, we considered testing multi-layer MnFePSi AMRs, fabricated through additive manufacturing, in the FAME cooler [26]. However, accurate AMR simulation requires reliable estimates of pressure drop and heat transfer, and existing correlations did not adequately represent the behavior of 3D-printed geometries. Therefore, as a first step, we prioritized the development of new, geometry-specific correlations through experimental investigation. To this end, we designed and built an experimental setup to characterize the flow resistance and heat transfer properties of MnFePSi blocks produced via additive manufacturing. The setup design, experimental procedures, results, and data analysis are presented in **chapter 5**. Due to time constraints and delays in the production of the 3D-printed blocks, AMR testing for further model validation could not be completed within the scope of this thesis.

2

THEORETICAL FRAMEWORK

2.1. INTRODUCTION

Building on the motivation for exploring sustainable heat pump solutions presented in the previous chapter, this chapter introduces the fundamental physical principles that govern the magnetocaloric heat pump (MCHP) technology. A comprehensive understanding of the magnetocaloric effect and the active magnetocaloric regenerative cycle is essential for the evaluation and design of high-performance MCHP systems. This theoretical background sets the stage for subsequent discussions on materials, system design, and performance evaluation.

2.2. THE MAGNETO CALORIC EFFECT

The discovery of the magnetocaloric effect (MCE) is attributed to Weiss and Piccard in 1917 [27]. It refers to the thermal response that magnetocaloric materials (MCMs) exhibit when subjected to a change in magnetic field. The nature of this response depends on how the magnetization process is carried out, whether under adiabatic or isothermal conditions.

When the magnetization process occurs under adiabatic conditions, the temperature of the material increases, and when it occurs under isothermal conditions, the magnetic entropy decreases and heat is released. Figure 2.1 illustrates the adiabatic (from point A to point B) and isothermal (from point A to point C) processes that an MCM exhibits when magnetized from a low field, H_0^{i}, to a high field, H_0^{f}. The arrows indicate the corresponding changes in temperature and entropy. The MCE is considered reversible in principle, as the MCM returns to its original state, when demagnetized under adiabatic or isothermal conditions.

To understand the physical origin of the MCE, it is essential to understand how the different sources of entropy contribute to the

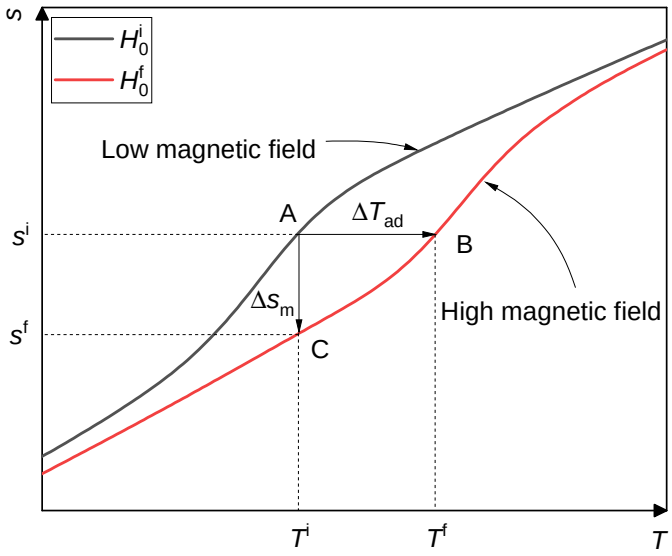

Figure 2.1.: The MCE expressed either as an adiabatic temperature change (ΔT_{ad}) or as an isothermal entropy change (Δs_m).

magnetocaloric response. The total specific entropy of an MCM, s, is a function of both temperature, T, and magnetic field, H_0, and comprises three components, as shown in Equation 2.1: magnetic entropy, associated with the degree of order of the magnetic moments in the material; lattice entropy, related to the vibrational motion of the crystal lattice; and electronic entropy, arising from the distribution of electronic states.

$$s(T, H_0) = s^m(T, H_0) + s^l(T) + s^e(T) \tag{2.1}$$

The lattice and electronic contributions are typically considered functions of temperature only and assumed to be independent of the magnetic field [28, 29]. Therefore, during an isothermal magnetization process, the entropy change involves only the magnetic component, as the temperature remains constant and the other contributions are invariant. For this reason, the designation *magnetic entropy change*, denoted by the symbol Δs_m, will also be used throughout this thesis to refer specifically to the isothermal entropy change. On the other hand, during an adiabatic magnetization process, the total entropy remains constant. The resulting temperature increase is due to a reduction in magnetic entropy (caused by increased alignment of magnetic moments), which is compensated by a corresponding increase in lattice entropy.

The adiabatic temperature change (ΔT_{ad}) and the isothermal entropy

change (Δs_m) depend on both the initial temperature of the material and the variation in the magnetic field. They typically reach their maximum values at the Curie temperature of the MCM, where the material undergoes a magnetic phase transition, most often from a ferromagnetic (FM) to a paramagnetic (PM) state. As illustrated in Figure 2.1, ΔT_{ad} and Δs_m can be calculated from total entropy curves, using Equation 2.2 and Equation 2.3, respectively [30]. These curves are typically derived from specific heat capacity measurements taken at zero field and under different applied fields, following methods described in literature [31–33].

$$\Delta T_{ad} = T(s^i, H_0^f) - T(s^i, H_0^i) \tag{2.2}$$

$$\Delta s_m = s(T^i, H_0^f) - s(T^i, H_0^i) \tag{2.3}$$

In practice, however, in-field heat capacity measurements are not readily available, as they often require custom-built setups or time-consuming methods such as thermal relaxation [34]. As an alternative, the magnitude of Δs_m is frequently derived from magnetization data at various fields and temperatures [33], using the thermodynamic relations introduced in section 2.3. Some researchers also estimate ΔT_{ad} using magnetization data in combination with zero-field heat capacity measurements, as also presented in section 2.3. However, this approach involves unphysical assumptions and should be avoided [31].

2.3. MCE FROM THERMODYNAMIC RELATIONS

The derivation of expressions to calculate the adiabatic temperature change and isothermal entropy change from specific heat capacity and magnetization data relies on several key thermodynamic relations. For a more detailed treatment of the underlying thermodynamics of magnetocaloric systems, the interested reader is referred to the works of Kitanovski and Egolf [35] and Smith et al. [29], which present comprehensive discussions on this topic.

Assuming constant pressure and volume, a first law analysis of a magnetic sample placed in a magnetic field leads to Equation 2.4, where for simplicity the one-dimensional form of magnetization and magnetic field has been adopted [35].

$$\mathrm{d}u = \delta q + \delta w = T\mathrm{d}s - \mu_0 H_0 \mathrm{d}M \tag{2.4}$$

In Equation 2.4, u denotes the specific internal energy, q is the specific heat, w represents the specific work, μ_0 is the permeability of free space, and M stands for the magnetization.

The specific Gibbs free energy, g, defined in Equation 2.5, is a useful property for describing the thermodynamic state of magnetic materials. Beyond the physical significance of this potential, it can be used to derive important thermodynamic relations. Taking the total differential of Equation 2.5 and simplifying the result using Equation 2.4 leads to Equation 2.6. From this result, it is evident that the specific Gibbs free energy is naturally expressed as a function of temperature T and magnetic field H_0, i.e., $g = g(T, H_0)$.

$$g = u - Ts + \mu_0 H_0 M \tag{2.5}$$

$$\mathrm{d}g = -s\mathrm{d}T + \mu_0 M \mathrm{d}H_0 \tag{2.6}$$

Comparing the total differential of the functional form $g = g(T, H_0)$, shown in Equation 2.7, with the differential expression derived from the definition of the Gibbs free energy in Equation 2.6, it becomes clear that the first derivatives of g with respect to temperature and magnetic field correspond to entropy and magnetization, respectively, as given in Equation 2.8 and Equation 2.9. This identification is particularly useful for the classification of MCMs as first- or second-order materials. Furthermore, applying the equality of mixed partial derivatives for exact differentials to these expressions yields the Maxwell relation shown in Equation 2.10. This is an important thermodynamic relation that links the thermal variation of magnetization to the field dependence of entropy in magnetic materials.

$$g = g(T, H_0) \therefore \mathrm{d}g = \left(\frac{\partial g}{\partial T}\right)_{H_0} \mathrm{d}T + \left(\frac{\partial g}{\partial H_0}\right)_T \mathrm{d}H_0 \tag{2.7}$$

$$\left(\frac{\partial g}{\partial T}\right)_{H_0} = -s \tag{2.8}$$

$$\left(\frac{\partial g}{\partial H_0}\right)_T = \mu_0 M \tag{2.9}$$

$$\left(\frac{\partial M}{\partial T}\right)_{H_0} = -\frac{1}{\mu_0}\left(\frac{\partial s}{\partial H_0}\right)_T \tag{2.10}$$

On the other hand, as introduced earlier, total entropy is a function of temperature and magnetic field. Thus, it can be expressed in the form $s = s(T, H_0)$, the exact differential of which is presented in Equation 2.11.

$$\mathrm{d}s = \left(\frac{\partial s}{\partial T}\right)_{H_0} \mathrm{d}T + \left(\frac{\partial s}{\partial H_0}\right)_T \mathrm{d}H_0 \tag{2.11}$$

When an MCM undergoes an isothermal magnetization or demagnetization process, the first term on the right-hand side of

Equation 2.11 vanishes, and the Δs_m can then be calculated by integration of the resulting equation, as presented in Equation 2.12. Introducing the Maxwell relation given in Equation 2.10, it is possible to indirectly calculate the isothermal entropy change from magnetization measurements by the numerical integration of Equation 2.12, as indicated by Pecharsky and Gschneidner [31].

$$\Delta s_\mathrm{m} = \int_{H_0^\mathrm{i}}^{H_0^\mathrm{f}} \left(\frac{\partial s}{\partial H_0}\right)_T \mathrm{d}H_0 = -\mu_0 \int_{H_0^\mathrm{i}}^{H_0^\mathrm{f}} \left(\frac{\partial M}{\partial T}\right)_{H_0} \mathrm{d}H_0 \tag{2.12}$$

The specific heat capacity of the material at constant magnetic field, c_{H_0}, can be determined from calorimetric measurements performed under an applied constant magnetic field, and is related to the total entropy of the material through Equation 2.13.

$$c_{H_0}(T, H_0) = T\left(\frac{\partial s}{\partial T}\right)_{H_0} \tag{2.13}$$

Multiplying Equation 2.11 by temperature yields Equation 2.14. In an adiabatic process, the left-hand side of Equation 2.14 vanishes, as $\mathrm{d}s = 0$. Solving for $\mathrm{d}T$, and substituting the definitions of specific heat capacity introduced in Equation 2.13 and the Maxwell relation introduced in Equation 2.10, results in an expression for the adiabatic temperature change based on indirect measurements of heat capacity at constant fields and magnetization, as shown in Equation 2.15.

$$T\mathrm{d}s = T\left(\frac{\partial s}{\partial T}\right)_{H_0} \mathrm{d}T + T\left(\frac{\partial s}{\partial H_0}\right)_T \mathrm{d}H_0 \tag{2.14}$$

$$\Delta T_\mathrm{ad} = \mu_0 \int_{H_0^\mathrm{i}}^{H_0^\mathrm{f}} \left(\frac{T}{c_{H_0}}\right)_{H_0} \left(\frac{\partial M}{\partial T}\right)_{H_0} \mathrm{d}H_0 \tag{2.15}$$

However, the use of Equation 2.15 is considered impractical, as noted by Pecharsky and Gschneidner [31], because specific heat measurements are generally not performed at the same magnetic field intervals as magnetization measurements, since the former are significantly more time-consuming. Furthermore, they argue that applying Equation 2.15 offers no added value when specific heat capacity data at various magnetic fields is available, in which case Equation 2.2 can be used directly. Equation 2.15 is frequently approximated by assuming that $\left(T/c_{H_0}\right)$ is magnetic-field independent to obtain an expression that can be evaluated using only magnetization and zero-field heat capacity data, as presented in Equation 2.16. However, due to the inaccuracy of the underlying assumptions, this expression should be avoided, particularly in applications such as modeling of active magnetic regenerators (AMRs).

$$\Delta T_{\mathrm{ad}} \approx \frac{T}{c_{H_0=0}} \Delta s_{\mathrm{m}} \tag{2.16}$$

2.4. MAGNETOCALORIC MATERIALS FOR ROOM TEMPERATURE APPLICATIONS

2.4.1. FIRST AND SECOND ORDER MCMS

Following the Ehrenfest classification of phase transitions, MCMs can be classified as first- or second-order materials depending on the order of the derivative of the Gibbs free energy that presents discontinuity at the phase transition [36]. Based on this, MCMs that show discontinuous entropy and/or magnetization curves at the transition temperature (discontinuous first derivatives of the Gibbs energy, as shown in Equation 2.8 and Equation 2.9) are classified as first-order MCMs. On the other hand, the second derivative of the Gibbs free energy with respect to temperature at constant magnetic field is equal to the specific heat capacity at constant magnetic field divided by temperature, as presented in Equation 2.17, which is obtained from Equation 2.8 and Equation 2.13. Therefore, second order MCMs are characterized by continuous magnetization and entropy curves and discontinuous heat capacity at the transition, i.e. discontinuous second derivative of Gibbs free energy.

$$\left(\frac{\partial^2 g}{\partial T^2}\right)_{H_0} = -\frac{C_{H_0}}{T} \tag{2.17}$$

First-order MCMs are generally characterized by a giant MCE, typically exhibiting a larger isothermal entropy change than second-order materials. However, this is not always accompanied by a correspondingly large adiabatic temperature change [11]. Latent heat accompanies the phase transition in first order MCMs as well as a coexistence of magnetic phases (such as FM and PM, or FM and antiferromagnetic (AFM)) during the transition. Hysteresis in temperature and/or magnetic field is also commonly observed at the transition [29].

In addition, some first-order materials also exhibit a sudden change in volume at the transition temperature, which can lead to mechanical stability problems or an early material degradation [18]. Others undergo magnetoelastic transitions with negligible volume changes but significant changes in lattice parameters, which can likewise compromise mechanical stability [37, 38].

Conversely, second-order MCMs exhibit neither latent heat nor hysteresis during the phase transition. Moreover, the maximum

isothermal entropy change in these materials increases with magnetic field, and experimental studies have shown that this dependence is well described by a power-law relationship of the form H_0^n, where n is generally close to 2/3 [29]. Figure 2.2 shows characteristic curves for both first- and second-order MCMs.

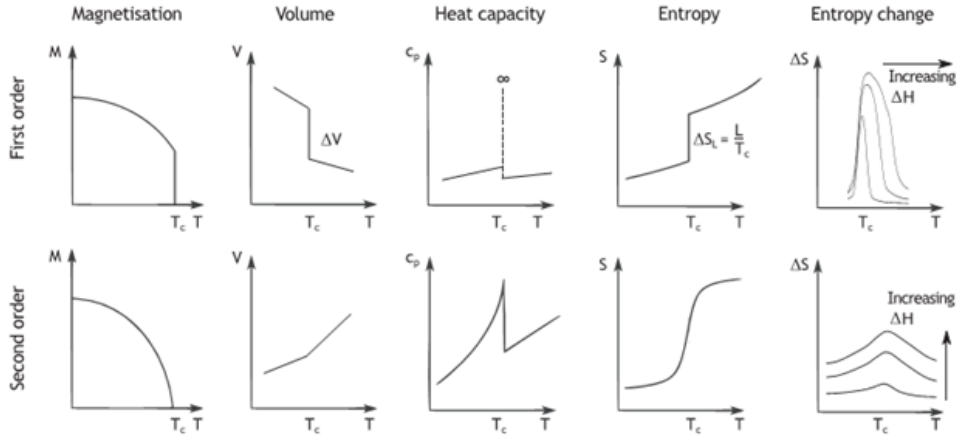

Figure 2.2.: Characteristic behavior of first order and second order MCMs. Adapted from [36].

2.4.2. IDEAL PROPERTIES OF MCMS

An ideal MCM for room temperature refrigeration or heat pump applications should exhibit the following properties [11, 18, 28]:

- Large entropy change, enabling high refrigeration capacity
- Large adiabatic temperature change at and around the transition temperature
- Low or negligible hysteresis
- High thermal conductivity to minimize internal temperature gradients and improve heat transfer
- Non-toxic composition for safe handling and operation
- Good mechanical properties (e.g., hardness, strength, ductility)
- Long-term mechanical and chemical stability
- Abundance of raw materials and low manufacturing costs
- High electrical resistivity to reduce eddy current losses

As indicated by Lyubina [36], the selection of MCMs depends on the application. From an engineering perspective, the ΔT_{ad} is an important characteristic to consider given that the temperature difference is the driving force for heat transfer. A low heat capacity is usually associated with high adiabatic temperature change, but in first-order MCMs, larger changes in transition temperature with magnetic field (dT_{Curie}/dH_0) is often linked with larger magnitudes of the ΔT_{ad} [36, 39].

Several comprehensive review articles about MCMs are available in literature [18, 36, 40–42]. A summary of some important families of MCMs for room temperature applications developed in the last decades is given in what follows. This summary will focus on materials with transition temperatures near room temperature and will provide information relevant from an engineering perspective.

2.4.3. GADOLINIUM AND ITS RARE-EARTH ALLOYS

The development of magnetic refrigeration at room temperature was made possible by the discovery of the magnetocaloric properties of gadolinium (Gd), the only pure element with a Curie point near room temperature. Gadolinium has been the default MCM in most room temperature magnetic refrigeration prototypes built to date [4, 43, 44], and it has also become the reference material for the comparison of performance of newly developed MCMs.

Gadolinium exhibits a second-order transition from a FM to a PM phase at approximately 293 K, its Curie temperature. This transition temperature can vary from 292 to 295 K depending on the purity [40]. The MCE of Gd at its Curie point is characterized by a Δs_m of approximately $-5\,J\,kg^{-1}\,K^{-1}$ and a ΔT_{ad} of approximately 5.6 K when subjected to a field change from 0 to 2 T [45].

Gadolinium can be alloyed with other rare earth elements such as Tb, Dy, Ho, and Er to produce solid solutions with tunable Curie temperatures [29, 36]. Pure lanthanide elements Tb, Dy, Ho, and Er exhibit complex phase transitions at temperatures below 240 K [40]. Alloying Gd with these lanthanides causes a reduction of the transition temperature of pure Gd and also a reduction of the maximum isothermal entropy change [40]. $Gd_{1-x}Tb_x$, $Gd_{1-x}Dy_x$, $Gd_{1-x}Er_x$ alloys have been tested in layered-bed regenerators of room temperature magnetic refrigeration demonstrators [11].

Being a metal, Gd also exhibits good mechanical properties, such as strength and ductility, which facilitate its fabrication in various shapes and geometries [46]. Furthermore, it demonstrates mechanical and chemical stability under repeated thermal and magnetic cycling. However, to ensure long-term durability, anticorrosion agents are required to protect the material during extended operation. The main drawback of Gd is its high price, which results from its relative scarcity,

as well as the high costs associated with raw material processing and purification. As a result, Gd is still not considered a viable candidate for widespread commercial deployment of magnetocaloric systems.

2.4.4. $Gd_5(Si, Ge)_4$ compounds

The compound $Gd_5(Si_2Ge_2)$ exhibits a first-order magneto-structural transition from FM to PM phase at 277 K. The MCE for a magnetic field change from 0 to 2 T is characterized by a Δs_m of $-14\,J\,kg^{-1}\,K^{-1}$ (almost 3 times that of Gd at its Curie temperature for the same magnetic field change) and a ΔT_{ad} of 7.2 K. When the magnetic field changes from 0 to 5 T, the Δs_m is $-18.5\,J\,kg^{-1}\,K^{-1}$ and the ΔT_{ad} is 15 K [45].

By reducing the amount of Si in the compounds $Gd_5(Si_x, Ge_{1-x})_4$, the transition temperature decreases from 277 K for $x = 0.5$ to 20 K for $x = 0$, while maintaining a first-order transformation. Conversely, when the amount of Si increases, i.e. for $x > 0.5$, the resulting compounds exhibit second order phase transitions (FM to PM), the corresponding MCE decreases, and the transition temperature increases up to 335 K at $x = 1$. It is also possible to rise the transition temperature to 285 K without losing too much of the giant MCE by replacing a minor amount of (Si + Ge) with Ga [11].

The giant MCE of this family of compounds is accompanied by a large thermal hysteresis of near 10 K, which makes them impractical for use in magnetocaloric systems, even without considering the high cost of Gd and Ge [36].

2.4.5. $LaFe_{13-x}Si_x$ compounds

The $LaFe_{13-x}Si_x$ series of compounds exhibit a first order transition characterized by a giant MCE and a low hysteresis for values of $x < 1.6$. The transition temperature of the compound $LaFe_{11.6}Si_{1.4}$ is in between 196 and 201 K, depending on the metal forming technique [36]. These compounds exhibit also a large volume change at the phase transition. For increasing concentrations of Si above $x > 1.6$, the compounds undergo second-order phase transitions at increasing transition temperatures up to 262 K [18], and the giant MCE is lost [36].

Using hydrogen as an interstitial element in the compounds $La(Fe, Si)_{13}H_x$, the first order phase transition is preserved, thus the giant MCE as well, and the transition temperature increases with x (i.e. $T_{Curie} = 342$ K for the compound $LaFe_{11.6}Si_{1.4}H_{2.3}$) [36]. However, these compounds may suffer from instability and may decompose when partially hydrogenated ($x < 1.5$). Adding Mn or Ce and fully hydrogenating ($x > 1.5$) allows obtaining stable compounds with tunable transition temperatures and giant MCE in the room temperature range. As an example, the compound $LaFe_{11.35}Mn_{0.39}Si_{1.26}H_{1.53}$

exhibits a maximum Δs_m of $-12\,J\,kg^{-1}\,K^{-1}$ at 295 K under a magnetic field change from 0 to 1.6 T [36].

As indicated by several authors, the low cost of the raw materials, the low hysteresis, large MCE, and scalability of production of these compounds make them attractive for the use in heat pump applications [18, 29, 36]. However, mechanical stability due to volume change across the transition and dehydrogenation are still issues that undermine the commercial applicability of these materials.

2.4.6. $(Mn, Fe)_2(P, Si)$ compounds

The binary compound Fe_2P exhibits a first-order FM to PM transition at 216 K. This critical temperature can be increased by substitution of P with As, Ge, Si, or B. The substitution of Fe with Mn leads to larger magnetic moments in the 3g crystallographic sites. Several of the resulting compounds have been studied extensively, among which the most representatives are $(Mn, Fe)_2(P, As)$, $(Mn, Fe)_2(P, Ge)$, and $(Mn, Fe)_2(P, Si)$. The crystal structure of the $(Mn, Fe)_2(P, Si)$ compound is illustrated in Figure 2.3.

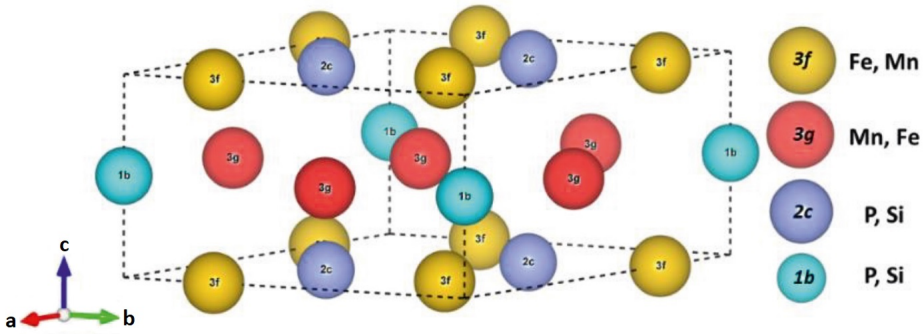

Figure 2.3.: Unit cell of the $(Mn, Fe)_2(P, Si)$ compound. Adapted from [47].

Despite the giant MCE and low thermal hysteresis (even < 1 K) found in the compound family $Mn_{2-y}Fe_y(P_xAs_{1-x})$, along with negligible volume change, and tunable T_{Curie} (from 200 to 350 K by changing the P/As ratio from 3/2 to 1/2 for $y = 1$) [18], the toxicity of As reduces its chances to be used in magnetocaloric systems. The search for elements to replace As led to the study of the $(Mn, Fe)_2(P, Ge)$ and $(Mn, Fe)_2(P, Si)$ compound families.

Trung et al. [48] investigated the MCE of the $(Mn, Fe)_2(P, Ge)$ compounds and observed that in the compounds $Mn_{1.1}Fe_{0.9}P_{1-x}Ge_x$ an increasing amount of Ge leads to an increase in T_{Curie} and a reduction of ΔT_{hys}. For $x = [0.19, 0.22, 0.25]$, they observed

$T_{\text{Curie}} = [260, 296, 330]$ K and $\Delta T_{\text{hys}} = [6, 4, 2]$ K. They also found that T_{Curie} and ΔT_{hys} can be reduced by increasing the amount of Mn. In $Mn_{2-y}Fe_yP_{0.75}Ge_{0.25}$, they found $\Delta T_{\text{hys}} = [5, 3, 0]$ K and $T_{\text{Curie}} = [322, 310, 302]$ K for $y = [0.84, 0.82, 0.80]$.

Dung et al. [37] reported a giant MCE in $(Mn, Fe)_2(P, Si)$ compounds, which is accompanied by small hysteresis, tunable T_{Curie}, and negligible volume change. The volume change at the phase transition is associated in these materials with changes of the lattice parameters a and c in opposite directions, that is, as c increases, a decreases. They found that T_{Curie} and ΔT_{hys} decrease with increasing Mn content.

For the compounds $Mn_xFe_{1.95-x}P_{0.5}Si_{0.5}$, $T_{\text{Curie}} = [304, 285, 269]$ K and $\Delta T_{\text{hys}} = [5, 2, 1]$ K for $x = [1.20, 1.25, 1.30]$, respectively. The Δs_{m} for these series of compounds in a magnetic field change from 0 to 5 T are $-[31, 27, 21]$ J kg^{-1} K^{-1}, respectively. Likewise, T_{Curie} increases and ΔT_{hys} decreases with increasing Si content. For the series of compounds $Mn_{1.25}Fe_{0.7}P_{1-y}Si_y$, $T_{\text{Curie}} = [246, 285, 323]$ K and $\Delta T_{\text{hys}} = [7, 2, 1]$ K for $y = [0.45, 0.50, 0.55]$, respectively. The Δs_{m} for these series of compounds in a magnetic field change from 0 to 5 T are $-[33, 27, 19]$ J kg^{-1} K^{-1}, respectively.

The MnFePSi material is a strong candidate for commercial magnetocaloric systems due to the abundance and low cost of its raw materials, the absence of toxic or environmentally harmful elements, the giant magnetic entropy change it exhibits under low magnetic fields, and its low thermal hysteresis. However, further improvements, particularly increasing the adiabatic temperature change at low fields and addressing mechanical stability issues, are essential to fully achieve the commercial viability of this material system.

2.5. THERMODYNAMIC CYCLES IN MAGNETIC REFRIGERATION

Adiabatic demagnetization is one way to exploit the MCE in practical applications. It is a non-cyclic process primarily used for achieving ultra-low temperatures. In adiabatic demagnetization, an MCM is first placed in thermal contact with a heat bath, where it is magnetized under isothermal conditions. The MCM is then removed from the bath and demagnetized adiabatically. As a result, its temperature drops, in some cases reaching below 1 K. While adiabatic demagnetization is effective for achieving ultra-low temperatures in non-cyclic applications, practical refrigeration or heat pumping at room temperature requires a fundamentally different approach, one that employs thermodynamic cycles to enable continuous operation. This section will briefly present some general aspects of thermodynamic cycles in magnetocaloric systems.

2.5.1. BRAYTON, ERICSSON, AND CARNOT CYCLES

In vapor compression refrigeration, thermodynamic cycles such as Brayton, Ericsson and Carnot consist of processes that occur between two isobaric lines in a *Ts* diagram. Analogously, in magnetic refrigeration, these cycles are composed of processes that take place between two isofield lines in a *Ts* diagram. Figure 2.4 illustrates the Carnot, Brayton, and Ericsson magnetic cycles in a *Ts* diagram [28].

To explain the basic Brayton cycle, let us consider a system consisting of a magnet, a small sample of an MCM, and the surrounding air at ambient temperature. Initially in thermal equilibrium with the surrounding air, the MCM is rapidly placed inside the magnetic field, resulting in (almost) adiabatic magnetization due to the limited time available for heat exchange. As a consequence of the MCE, the temperature of the sample increases. While remaining in the magnetic field, the sample releases heat to the external environment. After returning to its initial temperature, it is rapidly removed from the magnet and demagnetized (almost) adiabatically, causing its temperature to decrease further due to the reverse MCE. In this cooled state, the material provides refrigeration capacity, enabling it to absorb heat from the surrounding air while simultaneously returning to its initial temperature to complete the cycle.

Naturally, a thermodynamic cycle in which the heat source and heat sink are the same does not have practical applicability. Nevertheless, it is used here solely to facilitate understanding of the underlying concept. The temperature span of the cycle described above is limited by the magnitude of the adiabatic temperature change, which restricts its practical applicability. As illustrated in Figure 2.4, the temperature span of the Brayton cycle can be extended by incorporating regeneration. Regeneration is also an intrinsic feature of the Ericsson cycle, as shown in the same figure. This concept led to the development of the so-called active magnetic regenerative (AMR) cycle introduced by Steyert [49] and further developed by Barclay and Steyert [50], which is explained in section 2.6. The interested reader is referred to the works of Kitanovski et al. [6], Romero Gómez et al. [28], and Kitanovski and Egolf [35] for further details about these basic thermodynamic cycles, and other such as the cascade and the Stirling magnetic cycles.

2.6. ACTIVE MAGNETIC REGENERATIVE CYCLE

The AMR cycle emerged as a practical solution to increase the temperature span of magnetic refrigeration and heat pump systems [50]. As previously discussed, regeneration is essential to extend the limited temperature span of basic Brayton and Ericsson magnetic cycles. However, direct heat exchange between magnetized and demagnetized portions of MCM is impractical, necessitating the use of a

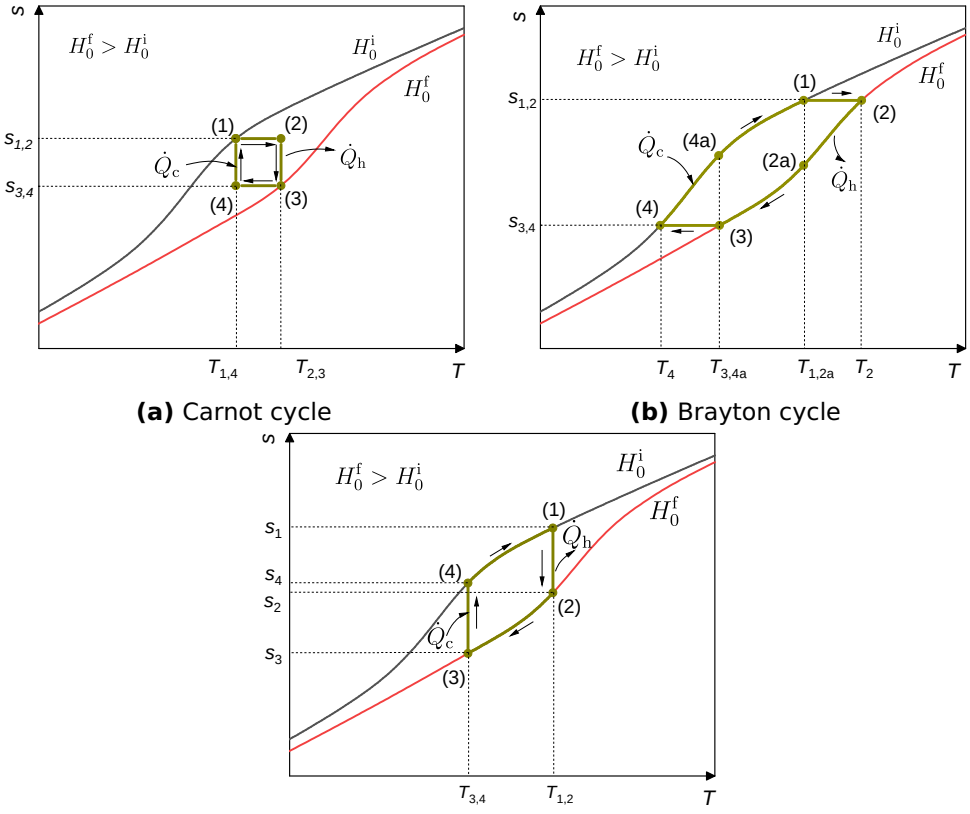

(a) Carnot cycle

(b) Brayton cycle

(c) Ericsson cycle

Figure 2.4.: Magnetic refrigeration cycles on *sT* diagrams: (a) Carnot, (b) Brayton with regeneration, (c) Ericsson with regeneration. Adapted from [28].

heat transfer fluid (HTF) for the regeneration. This fluid serves a dual purpose: it enables regenerative heat exchange within the cycle and facilitates the transfer of refrigeration or heating capacity from the MCM to external heat exchangers, where it can be harnessed for specific applications.

For any practical refrigeration or heat pump application, a significant amount of MCM is needed and must be shaped to allow efficient heat transfer. To achieve this, the MCM is typically structured as a porous matrix, allowing the working fluid to be pumped through it. During operation, a temperature gradient develops across the regenerator due to the alternating flow of hot and cold fluid from opposite ends. As a consequence of this gradient, the MCM at each position undergoes a distinct thermodynamic cycle, governed by its local thermal and

magnetic conditions. Depending on how the magnetic field variation and fluid flow are synchronized, the MCM in an AMR can undergo different thermodynamic cycles.

As described in the original AMR patent by Barclay and Steyert [50], it is possible to implement Brayton-, Ericsson-, Stirling-, or Carnot-like cycles within the regenerator. In a combined numerical and experimental study, Plaznik et al. [7] evaluated the coefficient of performance (*COP*), cooling power, and no-load temperature span for Brayton, Ericsson, and hybrid Brayton–Ericsson cycles applied to an AMR. Their results showed that, under the specific operating conditions examined, the Ericsson cycle achieved the highest *COP*, followed by the hybrid configuration. In contrast, the Brayton cycle provided the greatest cooling capacity, with the hybrid and Ericsson cycles performing slightly lower in this regard.

From the perspective of the HTF, the cycle proceeds as follows. After exiting the cold side of the regenerator at a temperature that, on average, is lower than that of the cold reservoir, the HTF enters the cold-side heat exchanger (CHEX), where it absorbes heat and its temperature rises, approaching that of the cold source. It then returns to the cold side of the regenerator and is pushed through the porous MCM, which is magnetized at that moment. The fluid flow promotes heat transfer, allowing the heat generated by the MCE to be transferred to the HTF, thereby increasing its temperature. The portion of the fluid that exits the regenerator during this cold-to-hot blow has, on average, a temperature higher than that of the heat sink.

Subsequently, the HTF flows into the hot-side heat exchanger (HHEX), where it releases heat to the sink, causing its temperature to decrease toward that of the heat sink. The fluid then returns to the hot side of the regenerator, and is pushed through the MCM in the opposite direction, at a moment when the material is demagnetized. Once again, the flow facilitates heat exchange, this time, the HTF releases heat to the MCM, reducing its own temperature. The portion of fluid exiting the regenerator during this hot-to-cold blow has, on average, a temperature lower than that of the cold reservoir. In this way, the cycle is completed.

A magnetocaloric refrigeration or heat pump device operating on the AMR cycle consists of five main components: (1) the AMR itself, (2) a magnetic circuit that generates a time-varying magnetic field to alternatively magnetize and demagnetize the MCM, (3) a hydraulic circuit that enables the bidirectional circulation of a HTF through the porous MCM bed during the heat exchange phases of the cycle, (4) the CHEX to transfer heat from the low-temperature heat source to the HTF, and (5) the HHEX to transfer heat from the HTF to the high-temperature heat sink. The circulation pump and the valve system required for the reciprocating flow in the regenerator are considered integral parts of the hydraulic circuit.

2.7. LAYERED AMR

To further optimize the performance of AMR-based devices, the selection of materials for the regenerator must also be considered. As mentioned earlier, each section of an AMR experiences a distinct thermodynamic cycle approximately centered around its local temperature. Because the MCE is strongest near a material's Curie point, AMR performance can be improved by using multiple MCMs with different transition temperatures. Each MCM should be selected so that its Curie temperature aligns approximately with the average temperature of its position in the regenerator.

This idea was introduced in the early stages of development of this technology. Brown [51] proposed a magnetic refrigerator consisting of several stages, each using MCMs with different Curie temperatures, so that the MCE would remain approximately constant across the device. Similarly, Barclay and Steyert [50] presented in their patent the concept of a regenerator made up of layers of MCMs with Curie temperatures spanning the operating range of the application. The goal was to ensure that each section of the regenerator operates near the optimal MCE region, thereby producing a relatively uniform effect along the AMR [50].

Building on this concept, many research groups have focused on developing MCMs with tunable Curie temperatures for use in layered AMRs designed for room-temperature applications. The layered-AMR approach is particularly important when working with first-order materials such as $La(Fe,Si)_{13}$ or MnFePSi given that their MCE occurs over a narrower temperature range compared to second-order materials. As illustrated in Figure 2.5, multiple layers of the first-order material $LaFe_{13-x-y}Co_xSi_y$ are required to maintain an adiabatic temperature change of approximately 2 K over a temperature span from 10 to 40 °C. In contrast, a second-order material such as Gd exhibit a $\Delta T_{ad} > 2$ K in this temperature range without the need for layering [52].

2.8. SUMMARY

In this chapter, we explored the fundamental concepts governing the MCE. Key thermodynamic relationships, such as the Maxwell equations, were introduced to quantify the behavior of MCMs. Figures of merit, including the adiabatic temperature change and the isothermal entropy change, were presented as essential parameters for evaluating material performance.

Among the available methods for estimating the magnitude of the MCE, we consider that using total entropy curves at constant magnetic field, derived from calorimetric measurements, is the most suitable from an engineering perspective, particularly for AMR modeling. From a

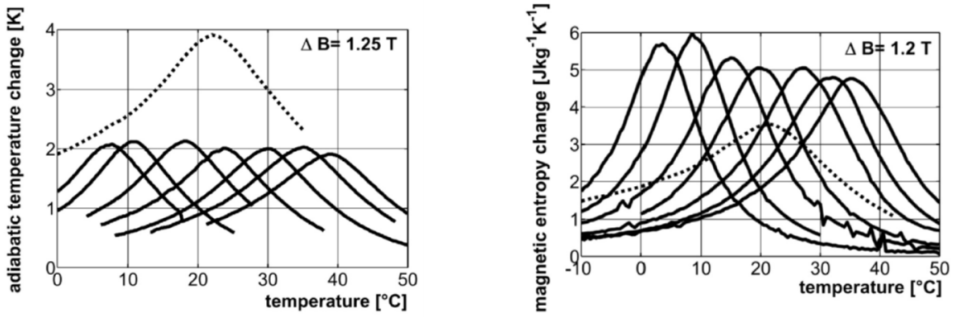

Figure 2.5.: Comparison of ΔT_{ad} and Δs_{m} of $LaFe_{13-x-y}Co_xSi_y$ (solid lines) and Gd (dotted lines). Adapted from [52].

material science perspective, however, magnetization measurements offer a more practical and accessible alternative for quantifying the Δs_{m}.

We also provided insight into selected MCMs with potential for room-temperature applications, discussing their respective advantages and limitations. We particularly highlighted the potential of the $(Mn, Fe)_2(P, Si)$ family of compounds for use in MCHP systems, owing to their giant MCE near room temperature, and the abundance of constituent elements. These materials also offer tunable transition temperatures through compositional adjustment, making them adaptable to specific application requirements.

The focus then shifted toward critical engineering concepts underlying the operation of MCHP systems. These included magnetic thermodynamic cycles, the AMR cycle, and the concept of layered AMRs. Together, these concepts provide the necessary theoretical foundation for analyzing, modeling, and designing MCHP systems. In the chapters that follow, we build upon this foundation to address key engineering challenges and system-level considerations necessary to transition MCHPs from conceptual designs to practical implementations.

3

LAYERING STRATEGIES FOR ACTIVE MAGNETOCALORIC REGENERATORS USING MnFePSi FOR HEAT PUMP APPLICATIONS

The development of affordable magnetocaloric materials (MCM) with a giant magnetocaloric effect (MCE) has brought magnetocaloric heat pumps a step closer to commercialization. The narrow temperature range in which these materials exhibit a large MCE demands the use of several materials with Curie temperatures covering the temperature span of the heat pump in a so-called layered active magnetocaloric regenerator (AMR). How to place these materials in the AMR in terms of distribution of Curie temperatures and thickness of each layer is still a topic of study. In this research we used a one-dimensional numerical model to unveil potential benefits of either using a distribution of Curie temperatures that follows a sigmoidal shape or using thicker layers at the cold and hot ends of the AMR along with a linear distribution of Curie temperatures. We found that these AMRs are less sensitive to changes in the hot and cold reservoir temperatures compared to an AMR that uses just a linear distribution of Curie temperatures with uniform layer length, but only the one with thicker ends produces similar heating capacities and second law efficiencies. The heating capacity of the simulated AMR with a sigmoidal distribution of Curie temperatures varies only 5.6% in a high utilization scenario, flow rate $37.5\,g\,s^{-1}$ *and a frequency of* $0.75\,Hz$ *, when the hot side temperature*

This chapter has been published in Applied Thermal Engineering **232**, 120962 (2023) [53].

changes from 308 K to 312 K and the temperature span is 18 K while the corresponding change is 8.7% for the AMR with thicker end layers, and 37.9% for the one with a linear distribution of Curie temperatures. For the considered geometry and operating conditions, the maximum heating capacities with temperature span 27 K in the high utilization scenario are 28.6 W, 23.0 W, and 28.5 W, whereas the corresponding second law efficiencies are 33.2%, 27.3%, and 32.7% for the AMRs with linear distribution of Curie temperatures, sigmoid distribution, and linear distribution with thicker ends respectively.

3.1. INTRODUCTION

The ongoing energy transition urges us to eliminate the use of natural gas and harmful refrigerants for heating and cooling applications. The heat pump market has reacted to this call in two directions: adapting the existing vapor compression technology for the use of natural or environmentally-friendly refrigerants [54] and turning the attention to alternative refrigeration technologies that are still under development [3]. Among the latter, the magnetocaloric heat pump (MCHP) technology has developed during the last 20 years to the point of having pre-commercial prototypes (see for example references [23, 55]) that can be potentially implemented in household refrigerators, air conditioners, and heat pumps and has gained recent attention due to more stringent legislation about the use of refrigerants [56].

MCHPs are based on the magnetocaloric effect (MCE), a thermal response that magnetocaloric materials (MCM) exhibit when subjected to a magnetic field change. The MCE can be quantified as an adiabatic temperature change or an isothermal entropy change resulting from the magnetization of the MCM in adiabatic or isothermal conditions respectively. MCHPs consist of three main elements: a magnetic field source, an active magnetocaloric regenerator (AMR), and a hydraulic circuit for the circulation of a heat transfer fluid (HTF). The AMR is the core element of a MCHP and is a porous structure of MCM where magnetic work is converted into heat that is transferred to the HTF. The interested reader can find very detailed information about the principle of operation, thermodynamic cycles, and devices in references [6, 28, 57].

MCHPs can in theory achieve higher efficiencies than traditional vapour compression heat pumps [11, 55], and due to the absence of a gas compressor they can also produce less noise, which is an important aspect that limits the widespread utilization of these devices. However, MCHPs are still less competitive than vapour compression heat pumps in terms of cost, which can be attributed to two main aspects. On the one hand side, permanent magnets are the preferred magnetic field source in small to medium capacity MCHPs [6], and these magnets offer a

limited magnetic field strength (usually less than 1.6 T is reported, see for example [23, 58–60], which limits the magnitude of the MCE) and are bulky and expensive. A second aspect that greatly influences the cost of MCHPs concerns the limited frequency and thus limited power density at which they can operate [61], which is primarily restricted by the switching of the valves required to produce an oscillating flow.

Nevertheless, the continuous development of this technology has focused in two main fronts: the development of AMRs and MCHP devices, and the improvement and discovery of MCMs. Engineers have implemented multiple conceptual designs in diverse prototypes all with advantages and disadvantages [57]. Some prototypes are designed as a proof of principle, some other for material testing [59], and a few are developed with an actual application in mind [15, 23, 55, 62]. The former are usually small devices with one or two AMRs, a linear relative movement between AMRs and magnet, and a piston displacer to pump the HTF. The latter are multi-bed devices with a rotating magnet that can achieve cooling capacities of the order of 100 to 1000 W. A few important lessons to consider in the design of a MCHP device are:

- The dead volume can be minimized by installing independent tubing for entering and leaving streams at each side of the AMRs [63].
- The magnetic field in the low field region must be ideally zero or as low as possible in order to maximize the MCE [29]. The duration of the low field part of the cycle must be comparable with the duration of the high field part to allow proper heat exchange between solid and fluid.
- In multi-bed MCHPs, differences in flow resistance between cold-to-hot and hot-to-cold blows in even a single bed cause a flow imbalance that negatively affects the performance of the whole system [20]. This can be controlled by adjusting the time that each bed is open to flow [64].
- In multi-bed devices, using an odd number of AMRs and a two pole magnet helps to reduce the peak torque necessary for the rotation of the magnet [65].
- AMR design must aim to maximize heat transfer between the MCM and HTF while minimizing pressure drop. Thus, an AMR needs a large heat transfer area per unit volume, a large heat transfer coefficient, and a small friction factor [50]. To achieve this, microstructures are potentially the best option [66, 67]. Demagnetizing losses also need to be minimized.

On the other hand, material scientists have worked on the search of ideal MCMs that:

- can be synthesized from abundant, non-toxic, and non-radioactive starting elements and compounds [68].
- exhibit a large MCE in low magnetic fields such as the ones produced by permanent magnets. A combination of large adiabatic temperature change and large isothermal entropy change is required to produce a good performance. Having just one of these parameters large and the other small seems to be ineffective [69, 70].
- exhibit none or low thermal and magnetic hysteresis. Some MCMs with low thermal hysteresis can still exhibit a reasonably good cyclic adiabatic temperature change [39, 71].
- are chemically and mechanically stable to withstand long term cyclic operating conditions. Mechanical stability is in connection with a low or negligible volume change across the phase transition.
- have good mechanical properties to facilitate shaping the MCM into a heat exchanger.
- allow tuning Curie temperature by adjusting the stoichiometry without significantly changing the magnetocaloric properties and the specific heat capacity [36].

Besides Gd, the benchmark MCM for room temperature magnetocaloric refrigeration, and its alloys with Y, Er, Tb, and Ho, all of which are second order MCMs, the $(Mn, Fe)_2(P, Si)$ and the $La(FeSi)_{13}$ families of MCMs have also been implemented in MCHP prototypes, for they have a good combination of properties and can be produced at low cost [72, 73]. These two promising MCMs are generally of the first order type (see [29, 36] for a clear explanation of differences between first and second order MCMs), which is typically accompanied by a large MCE in a small temperature range and some thermal and magnetic hysteresis. Given the smaller temperature range in which the MCE is expressed, it is necessary to stack several of these MCMs with different Curie temperatures to bridge the temperature span of the heat pump, the so-called layered AMR concept. In the following sections, an overview of experimental and numerical studies with layered AMRs is presented.

3.1.1. EXPERIMENTAL STUDIES OF LAYERED AMRS USING SECOND ORDER MCMS

First experimental works with layered AMRs focused on AMRs of 2 and 3 layers of uniform length of Gd and Gd alloys [74–76]. Gd and its alloys are second order MCMs, which exhibit the MCE in a wide

temperature range, and therefore the separation of Curie temperatures in a layered bed using this type of MCMs can be even as large as 40 K [77]. Table 3.1 presents a summary of the main characteristics of the layered AMRs used in these initial experimental works as well as some operating parameters and the zero-load temperature span. A few other layered AMRs in which Gd-like materials have been used are also included in Table 3.1.

The initial experiments with layered AMRs proved that it is possible to attain larger zero-load temperature spans by adding layers of Gd alloys to the cold side of a pure Gd layer, exploiting the fact that these alloys have Curie temperatures below that of Gd with similar magnetocaloric behavior. In AMRs of two layers of Gd-like materials, a larger separation of Curie temperatures is generally correlated with a larger zero-load temperature span [74, 76]. As in single layer Gd AMRs, it was also shown in these works that ΔT_{span} decreases also approximately linearly with increasing cooling capacity in layered AMRs using Gd-like MCMs. Layered beds can produce however a greater net cooling effect compared to single layer beds when the operating temperatures (cold and hot temperatures) enclose or are nearly above the Curie temperatures of the MCMs used in the bed, but this advantage disappears when the cooling load increases and the temperature span decreases so much that the colder layers operate far from their Curie temperature [78]. So, layered AMRs of Gd-like materials generally produce greater cooling capacities than single Gd AMRs at large temperature spans but poorer cooling capacities at small temperature spans.

Table 3.1.: Summary of Curie temperatures and experimental performance of some layered AMRs using second order MCMs.

Ref.	MCMs and their corresponding T_{Curie} in [°C] in parenthesis				T_{cold}	T_{hot}	ΔT_{span}	B_{max}	f_{AMR}	$\dot{m}$ or	HTF
	Mat.1	Mat.2	Mat.3	Mat.4	[°C]	[°C]	[°C]	[T]	[Hz]	V_{displ}	
[74]	$Gd_{0.74}Tb_{0.26}$ (4.8)	Gd (19.8)	—	—	3.8	23.8	20.0	2.00	0.80	$0.16\,g\,s^{-1}$	He (10 atm)
[75]	$Gd_{0.85}Er_{0.15}$ (-8.2)	$Gd_{0.74}Tb_{0.26}$ (3.8)	Gd (19.8)	—-	-21.7	28.3	50.0	2.00	0.80	—	He (9.5 atm)
[76]	$Gd_{0.85}Er_{0.15}$ (-8.2)	Gd (19.8)	—	—	-13.2	31.8	45.0	2.00	0.85	$0.33\,g\,s^{-1}$	He (9 atm)
[78]	$Gd_{0.975}Y_{0.025}$ (13.0)	Gd (17.0)	—	—	1.6	25.0	23.2	1.45	0.50	$13.90\,cm^3$	H_2O/EG[1]
[78]	$Gd_{0.95}Y_{0.05}$ (10.0)	Gd (17.0)	—	—	0.1	25.0	24.7	1.45	0.50	$13.90\,cm^3$	H_2O/EG[1]
[78]	$Gd_{0.925}Y_{0.075}$ (4.0)	Gd (17.0)	—	—	0.6	25.0	24.2	1.45	0.50	$13.90\,cm^3$	H_2O/EG[1]
[77]	$Gd_{0.33}H_{0.67}$ (-90.2)	$Gd_{0.32}Dy_{0.68}$ (-60.2)	$Gd_{0.30}Tb_{0.70}$ (-20.2)	Gd (19.8)	-132.8	11.8	150.0	5.00	0.17	$3\,g\,s^{-1}$	He (27 atm)

EG: Ethylene glycol
[1] 70/30 %V

Table 3.2.: Summary of Curie temperatures and performance achieved with layered AMRs using first order MCMs tested experimentally.

Ref.	Material family	Geom.	Curie temperature in [°C] (up) and length in [mm] (down) per layer										f_{AMR} [Hz]	$\dot{V}_{HEX,AMR}$ [Lpm]	T_{hot} [°C]	B_{max} [T]	$\dot{q}_c$ [W/kg]	ΔT_{span} [K]
			1	2	3	4	5	6	7	8	9	10						
[62]	$La(Fe,Si)_{13}H$	PBSP*	30.5	33.2	36.1	38.6	40.7	43.0	—	—	—	—	4.0	5.30	44	1.44	1375	12.0
			6.3**	6.3	6.3	6.3	6.3	6.3	—	—	—	—						
[52]	$La(Fe,Co,Si)_{13}$	PP	7.8	10.8	18.2	23.8	30.0	35.0	39.0	—	—	—	0.4	0.23	35	1.15	10	12.0
			11.4	11.4	11.4	11.4	11.4	11.4	11.4	—	—	—						
[52]	$La(Fe,Co,Si)_{13}$	PP	18.2	23.8	30.0	35.0	—	—	—	—	—	—	0.4	0.23	35	1.15	10	12.0
			11.4	22.8	22.8	22.8	—	—	—	—	—	—						
[52]	$La(Fe,Co,Si)_{13}$	PP	18.2	23.8	—	—	—	—	—	—	—	—	0.4	0.23	35	1.15	8	12.0
			34.2	45.6	—	—	—	—	—	—	—	—						
[79]	MnFePAs	PBCP	13.8	17.8	21.8	—	—	—	—	—	—	—	0.8	0.62	25	1.45	26	10.0
			14.0	14.0	14.0	—	—	—	—	—	—	—						
[79]	MnFePAs	PBCP	2.2	5.8	8.1	14.5	17.8	22.4	—	—	—	—	0.8	0.61	26	1.45	0	20.4
			10.0	10.0	10.0	10.0	10.0	10.0	—	—	—	—						
[79]	MnFePAs	PBCP	1.9	5.9	9.7	14.4	18.1	22.2	26.1	29.8	—	—	0.7	0.85	35	1.45	0	32.0
			15.0	15.0	15.0	15.0	15.0	15.0	15.0	15.0	—	—						
[80]	$La(Fe,Mn,Si)_{13}H_y$	PBCP	17.3	20.6	—	—	—	—	—	—	—	—	0.15	0.04^{++}	30	1.10	0	13.6
			20.0	20.0	—	—	—	—	—	—	—	—						
[80]	$La(Fe,Mn,Si)_{13}H_y$	PBCP	11.4	13.6	17.5	21.6	26.1	—	—	—	—	—	0.15	0.10^{++}	30	1.10	21	12.0
			8.0	8.0	8.0	8.0	8.0	—	—	—	—	—						
[80]	$La(Fe,Mn,Si)_{13}H_y$	PBCP	11.4	12.3	13.6	15.3	17.5	19.5	21.6	23.7	26.1	—	0.15	0.08^{++}	30	1.10	14	12.0
			4.4	4.4	4.4	4.4	4.4	4.4	4.4	4.4	4.4	—						
[81]	$La(Fe,Mn,Si)_{13}H_y$	PBSP[1]	0.0	2.7	5.3	7.5	9.5	10.7	13.9	15.6	17.0	19.0	1.2	4.55	22	1.44	139	10.0
			28.8	25.0	21.0	19.0	22.5	23.0	28.0	25.5	29.0	40.5						
[82]	MnFePSi	PBCP	19.2	21.5	—	—	—	—	—	—	—	—	1.0	0.33	28	1.47	43	6.0
			22.0	23.0	—	—	—	—	—	—	—	—						
[82]	MnFePSi	PBCP	17.6	21.5	—	—	—	—	—	—	—	—	1.0	0.33	28	1.47	40	5.0
			23.0	23.0	—	—	—	—	—	—	—	—						
[82]	MnFePSi	PBCP	9.9	21.5	—	—	—	—	—	—	—	—	1.0	0.33	37	1.47	39	3.6
			22.0	23.0	—	—	—	—	—	—	—	—						
[82]	MnFePSi	PBCP	8.3	21.5	—	—	—	—	—	—	—	—	1.0	0.33	37	1.47	40	3.6
			22.0	23.0	—	—	—	—	—	—	—	—						
[82]	MnFePSi	PBCP	9.9	19.2	—	—	—	—	—	—	—	—	1.0	0.33	27	1.47	42	3.6
			22.0	22.0	—	—	—	—	—	—	—	—						

Some foot notes regarding Table 3.2 are:
PBSP: Packed bed of spherical particles
PBCP: Packed bed of crushed particles
PP: Parallel plates
* The diameter of the spherical particles ranged from 177 to 246 μm.
** Calculated assuming a uniform layer length distribution.
[1] Mass in [g] per layer given instead of length in [mm].
[+] Only zero-load temperature span was reported.
[++] Calculated from reported utilization values and frequency.

3.1.2. EXPERIMENTAL STUDIES OF LAYERED AMRS USING FIRST ORDER MCMS

The discovery of affordable giant MCE materials was followed soon by their implementation in layered AMRs. Table 3.2 summarizes the main features of some layered AMRs using first order MCMs along with some information regarding the testing device and the resulting performance. As can be seen in Table 3.2, we focused our attention to layered AMRs based on the Fe_2P and $LaFe_{13}$ families. Compared to Gd, these two families of materials offer larger magnetic entropy change and similar cyclic adiabatic temperature change in a magnetic field change of 0 to 2 T [72]. They can also be produced at low cost, and their starting elements or compounds are widely available [5]. Most AMR prototypes in Table 3.2 are packed beds of either spherical or crushed particles because shaping these brittle materials into a more structured geometry has proved to be challenging.

Generally speaking, single layer Gd AMRs still perform better than most of the layered AMR prototypes presented in Table 3.2 with the exception of the AMR of Astronautics (reference [62]). The outstanding cooling capacity in this case results from the use of small particle diameters of the order of 200 μm which leads to large heat transfer coefficients (and also large pressure drops reducing thus the system *COP*), high cycle frequency of 4 Hz in combination with a large flow rate per AMR of 5.3 L min^{-1}, and naturally from the use of MCMs with a large and similar MCE under a magnetic field of 1.44 T arranged properly in the AMRs.

On the other hand, these experimental studies have also shown that the relation between ΔT_{span} and cooling capacity is not necessarily linear when using first order MCMs in the layered bed [62] as it was also pointed out by Smith et al. [29]. It has also been demonstrated that a large gap in the separation of Curie temperatures between two consecutive layers (e.g. when there is a gap in the full-width-half-maximum of the ΔT_{ad} of two consecutive MCMs in the bed [79]) could lead to having inactive layers above or below the position of the interface between the layers with the large gap [52, 82,

83]. If it is above or below depends on the operating temperatures. Larger zero load temperature spans are also attainable with layered AMRs whose MCMs have Curie temperatures covering a larger temperature range [79]. Some experimental studies suggest that there is a minimum Curie temperature separation between adjacent layers below which further improvements of performance are marginal. This means that there is a maximum number of layers to cover a certain temperature range after which the performance no longer improves [80]. This is likely related with the fact that the chances that a layer operates far from its Curie temperature increases upon decreasing its length.

3.1.3. LAYERING STRATEGIES USED IN EXPERIMENTAL STUDIES

Layering strategies depend on two main parameters: the separation of Curie temperature between adjacent layers, and the length of each layer. This second parameter is related to the amount of each material and its position along the AMR. Experimental studies with layered AMRs have typically considered a uniform layer length and a linear distribution of Curie temperatures (see Table 3.2). In practice some deviation from the intended Curie temperatures is typically present due to the difficulties in the fabrication of MCMs [81], and the final distribution is only approximately linear. On the other hand, a few layered AMRs have been fabricated following different layering strategies.

Masche et al. [81] tested a new MCHP prototype with thirteen AMRs of ten layers based on $La(Fe, Mn, Si)_{13}H_y$ MCM. The design of their AMRs considered a linear distribution of Curie temperatures. The novelty of their work lies on the filling strategy, for they calculated the length of each layer by considering a constant magnetic energy for each layer along the bed, which was relevant given the tapered shape of the AMRs (in the plane perpendicular to the magnetic field direction) and the variation of the magnetic field along the bed axis. They concluded from numerical simulations that in order to produce a greater cooling capacity this filling strategy is better than other, such as: keeping a constant magnetic flux, using a constant length per layer, or using a constant volume per layer.

Scientists from the Ames National Laboratory developed a magnetocaloric methane liquefier using two AMRs of 4 layers consisting of Gd and Gd alloys with Curie temperatures distributed almost linearly from $-90.2\,^{\circ}C$ to $19.8\,^{\circ}C$ and using helium as HTF (see reference [77]). They used layers of increasing mass from the cold side to the hot side. They claim this is necessary in order to compensate the additional load imposed on hotter layers as these layers have to pump the heat extracted from the cold source plus the magnetic power invested in the

colder layers [77].

3.1.4. NUMERICAL STUDIES WITH LAYERED AMRS

Numerical simulations facilitate the design and optimization of layered AMRs and have been used to understand the performance of these devices. Lei et al. [24] performed simulations of layered AMRs based on $La(Fe, Mn, Si)_{13}H_y$ and found that 2.24 layers are necessary for every 5 K of temperature span when the Curie temperatures of the materials are distributed linearly from cold to hot side and the maximum applied magnetic field is 1.2 T.

The same group also studied the influence of the number of layers on the performance of layered AMRs. They modelled the magnetocaloric properties of the MCMs using a modified Lorentzian equation [70]. They found that a greater specific cooling capacity is attainable with a smaller number of layers when the peaks of the magnetic entropy change and heat capacity curves are broader. They concluded that there is a maximum number of layers after which the performance of an AMR no longer improves. They also found that the deviations from the Curie temperatures dictated by a linear distribution have a detrimental impact on the performance of layered AMRs. They proposed mixing first and second order MCMs as a method for reducing the sensitivity to the deviations in Curie temperatures.

On the other hand, Li et al. [84] proposed the use of a composite MCM based on a mixture of different compositions of MnFePGe as a way of enlarging the temperature range over which the material exhibits a large magnetic entropy change. However, they did not demonstrate experimentally that such composite material performs as they predicted in an actual AMR. Zhang et al. [85] studied the impact of slightly enlarging 1 or 2 layers of a 16-layer AMR composed of materials of the $La(Fe, Mn, Si)_{13}H_x$ family, and they found that the simulations in which the coldest layer of the AMR was thicker resulted in an increase in the cooling capacity.

Yuan et al. [86] proposed to use an MCE-length diagram as a guide to optimize the design of layered AMRs. After implementing a genetic algorithm optimization process, they also found that using thicker end layers leads to greater specific cooling powers for temperature spans above the design temperature span. They also suggested that temperature distributions of the solid material along the bed must be included in the analysis of the layering strategy. Risser et al. [87] also used evolutionary algorithms for the optimization of the design of layered AMRs.

Monfared and Palm [88] simulated a 6-layer AMR using Gd-like materials. They considered initially a linear distribution of Curie temperatures and uniform layer length (base case). Then, they created

many different AMRs by matching Curie temperatures of new materials with the average temperature of the layers of the base case at many different moments of the cycle. After simulating the new AMRs obtained in this way, they concluded that matching the distribution of Curie temperatures with the solid temperature profile obtained at the end of the magnetization process would produce the highest *COP* whereas matching it with the profile obtained at a moment near the end of the cold-to-hot blow would produce the largest temperature span.

3.1.5. CHALLENGES OF LAYERED AMRS

The design and fabrication of layered AMRs face several general challenges that must be addressed to ensure reliable and efficient system performance:

- The magnetocaloric properties of the MCMs are difficult to reproduce when applying manufacturing methods needed for massive production. As a result, it is difficult to obtain the exact Curie temperatures required for a particular layered AMR [23].
- It is also difficult to have uniformity of magnetocaloric properties in a layered bed. Typically there are variations in the height and width of the peaks of the specific heat capacity, adiabatic temperature change, and magnetic entropy change from one material to another even if there are only slight changes in their compositions [82].
- Depending on the manufacturing method, each layer can have a different porosity and pore geometry [23]. This is especially difficult to control in packed beds, but it could be controlled using additive manufacturing techniques.

As the previous literature study suggests, the definition of the layering strategy of layered AMRs, i.e. the definition of the Curie temperature and thickness of each layer, is still a challenging topic of study. This is a critical task when using first order materials with narrow MCE peaks because each material must be placed in a position in the AMR bed whose temperature closely fluctuates around its Curie temperature so that the entire AMR can exhibit a good MCE [50]. To enable this, it is necessary to decrease the ratio of the thermal mass of fluid to that of the solid in the regenerator. This ratio, known as the utilization of the regenerator, will be introduced in detail in section 3.3. This is achievable by increasing the peak specific heat capacity of every MCM in the bed. However, a high specific heat capacity has a detrimental effect on the adiabatic temperature change of MCMs, so a compromise is needed. The utilization factor can also be limited by decreasing the mass flow rate or increasing the cycle frequency, but this will limit the cooling and heating capacity that the AMR can develop.

Nevertheless, as each layer has a finite length, only a portion of the MCM in each layer will actually fluctuate around the optimum temperatures. Because of this, it has been said that a layered AMR should ideally have an infinite number of layers so that it can have a continuous change in Curie temperature [29], but this is impractical using traditional manufacturing methods. Alternatively, researchers from the Fundamental Aspects of Materials and Energy (FAME) group at TU Delft have hypothesized that an AMR based on the $(Mn, Fe)_2(P, Si)$ family of compounds could have a continuous change in Curie temperature along its length by applying additive manufacturing to produce a regenerator matrix initially consisting of a few compositions and then allowing the diffusion of elements during the heat treatment process to obtain a continuous change in composition and thus also a continuous change in Curie temperatures.

Depending on the selected initial compositions, it could be possible to obtain a linear or a sigmoidal distribution of Curie temperatures, or any other arbitrary function in theory. So, a question that immediately comes out is: which distribution of Curie temperature would be more advantageous for the performance of an AMR for a particular MCHP application?.

3.1.6. GOALS OF THE PRESENT STUDY

The previous sub-sections make clear that different studies have concluded differently for what concerns the optimum layering strategy. In this thesis chapter we compare the performance of three AMRs with different Curie temperature distributions: one following a simple linear function, a second following a sigmoidal function, and a third also following a linear function but using thicker end layers at the same time. For this comparison, we use a one dimensional physical model of an AMR. Because the model equations are solved using numerical methods, a large but finite number of layers are considered to resemble the continuous change in Curie temperatures.

The operating temperatures of the AMRs are defined in the context of a heat pump application. However, the findings are equally applicable to refrigeration systems, as both are thermodynamically equivalent. This study considers a system similar to that described by Johra et al. [10], which employs a borehole ground heat exchanger as the heat source and an underfloor heating system as the heat sink. Accordingly, the operating temperatures of the heat source and heat sink are set to 281 K and 308 K respectively, resulting in a design temperature span of 27 K.

3.2. METHODS

3.2.1. MATHEMATICAL MODEL

The influence of different layering strategies on the performance of an AMR was studied with a one-dimensional numerical model of an AMR. The model is based on the implementation of Christiaanse and co-workers, whose details are reported in [89] and is publicly available [90]. For the sake of completeness, some necessary information about this model is reproduced here. This model departs from the following basic assumptions, common to many models as pointed out by Nielsen et al. [91]:

- The fluid remains always in the liquid phase.
- Heat transfer by radiation is negligible.
- The MCM is uniformly distributed in the volume occupied by the AMR.
- The velocity of the fluid is uniform in any cross section of the AMR, i.e. plug flow is assumed.
- The mass flow rate of the fluid entering the AMR is imposed via a mass flow rate vs time profile.
- The applied magnetic field is uniform along the fluid flow direction

The energy conservation equations for the fluid and solid domains are presented in Equation 3.1 and Equation 3.2 respectively. As can be read in Equation 3.1 from left to right, thermal energy storage, energy accompanying mass flow, heat conduction, viscous dissipation, heat leaks to ambient, and heat transfer with the solid have been considered in the fluid energy balance. For the solid energy balance of Equation 3.2, thermal energy storage, heat conduction, the MCE modelled as a heat source term and calculated with Equation 3.3, and the heat transfer with the fluid are the physical phenomena considered.

Some researchers include the momentum conservation equation in their AMR models, and they solve it uncoupled from the energy conservation equations by considering constant fluid properties independent of temperature and assuming a $\Delta P(t)$ function (see for example 1D models [16, 92] and 2D models [93, 94]). Then, they use the resulting velocity field in the energy conservation equations presented in Equation 3.1 and Equation 3.2. On the other hand, the vast majority of 1D AMR models omit the solution of the momentum equation for the sake of simplicity and derive a velocity field from a mass flow rate vs time profile used as a boundary condition [20, 95, 96]. These models still produce sufficiently accurate results [97]. Here we opt for the second approach.

$$\rho_f c_f A_{cs} \varepsilon \frac{\partial T_f}{\partial t} + \frac{\partial}{\partial x}(\dot{m} c_f T_f) - \frac{\partial}{\partial x}\left(k_{f,eff} A_{cs} \varepsilon \frac{\partial T_f}{\partial x}\right) = \left|\frac{\dot{m}}{\rho_f}\frac{\partial P}{\partial x}\right| + \dot{Q}_{amb} + A_{cs}\beta h (T_s - T_f) \tag{3.1}$$

$$\rho_s c_s A_{cs}(1-\varepsilon)\frac{\partial T_s}{\partial t} - \frac{\partial}{\partial x}\left(k_{s,eff} A_{cs}(1-\varepsilon)\frac{\partial T_s}{\partial x}\right) = \dot{Q}_{MCE} + A_{cs}\beta h (T_f - T_s) \tag{3.2}$$

$$\dot{Q}_{MCE} = -\rho_s A_{cs}(1-\varepsilon) T_s \left.\frac{\partial s}{\partial B}\right|_{T_s} \frac{dB}{dt} \tag{3.3}$$

In this study we consider that the AMRs are packed beds of spherical particles. Consequently, the following constitutive equations were implemented. The heat transfer coefficient was calculated from the Nusselt correlation shown in Equation 3.4, where the Reynolds number is based on pore velocity and particle diameter. This correlation was developed by Macias-Machin et al. [98] and adopted by Park et al. [99] for an AMR model. Even though this correlation was developed for fluidized beds, it provides smaller heat transfer coefficients in comparison with other correlations typically used in AMR modelling such as Wakao and Kaguei [100], which usually lead to over prediction of performance as pointed out by Frischmann et al. [101]. Macias-Machin et al. [98] gives heat transfer coefficient values that are comparable to the ones resulting from the correlation developed by Frischmann et al. [101], and it also produces a non-zero Nusselt number when the velocity of the fluid goes to zero, which is advantageous for flow profiles with stagnation periods in the AMR cycle. Temperature gradients inside the spherical particles have been considered by the use of a degradation factor, DF, as proposed by Engelbrecht et al. [102].

$$Nu = 1.27 + 2.66 Re^{0.56} Pr^{-0.41}\left(\frac{1-\varepsilon}{\varepsilon}\right)^{0.29} \tag{3.4}$$

$$h = \frac{Nu k_f}{D_{sp}} DF \tag{3.5}$$

The effect of thermal dispersion in the fluid phase in the direction parallel to the flow is considered by using an effective thermal conductivity, Equation 3.6, where $Pe = RePr$ with Reynolds number

calculated based on particle radius and superficial velocity. On the other hand, the thermal conductivity in the solid phase is corrected to account for the presence of the fluid in between the solid particles by the use of Equation 3.7 proposed by Hadley [103], where $a_0 = 10^{-1.084-6.778(\varepsilon-0.298)}$ and $f_0 = 0.8 + 0.1\varepsilon$

$$k_{\mathrm{f,eff}} = k_{\mathrm{f}}\left(1 + \frac{4}{3}Pe\right) \tag{3.6}$$

$$\begin{aligned} k_{\mathrm{s,\,eff}} = k_{\mathrm{f}}\Bigg(&\frac{(1+a_0)\left(\varepsilon f_0 + (1-\varepsilon f_0) + \frac{k_{\mathrm{s}}}{k_{\mathrm{f}}}\right)}{1-\varepsilon(1-f_0)+\varepsilon(1-f_0)\frac{k_{\mathrm{s}}}{k_{\mathrm{f}}}} \\ &+a_0\frac{2(1-\varepsilon)\frac{k_{\mathrm{s}}^2}{k_{\mathrm{f}}^2} + (1+2\varepsilon)\frac{k_{\mathrm{s}}}{k_{\mathrm{f}}}}{(2+\varepsilon)\frac{k_{\mathrm{s}}}{k_{\mathrm{f}}} + 1 - \varepsilon}\Bigg) \end{aligned} \tag{3.7}$$

Pressure drop per unit length is calculated with Equation 3.8, also known as Ergun's equation [104].

$$\frac{\partial P}{\partial x} = \frac{1.75 v_{\mathrm{sup}}^2 (1-\varepsilon)\rho_{\mathrm{f}}}{D_{\mathrm{sp}}\varepsilon^3} + \frac{150 v_{\mathrm{sup}}(1-\varepsilon)^2\mu_{\mathrm{f}}}{D_{\mathrm{sp}}^2\varepsilon^3} \tag{3.8}$$

The energy conservation equations were solved using a finite difference method. The discretization of these equations followed the Crank-Nicolson scheme for the diffusion terms in both equations, and also for the fluid temperature in the heat-leak term, and the solid temperature in the term corresponding to heat transfer by convection. The upwind scheme fully implicit in time was used for the enthalpy term of the fluid energy conservation equation and for the fluid temperature in the term corresponding to heat transfer by convection.

A full description of the discretization method can be found in Christiaanse [105]. The system of linear algebraic equations resulting from the discretization was solved using a three diagonal matrix algorithm. This model was implemented in Python. The validation of this model is presented in reference [106] for the case of two-layer MnFePSi AMRs. We also validated the model using the experimental data of a device with a single packed bed of Gd spheres reported by Trevizoli et al. [16] and we obtained good agreement.

3.2.2. PERFORMANCE METRICS

The heating capacity is one of the key performance parameters of a heat pump. It is calculated for the AMR case with Equation 3.9. Likewise, the cooling capacity can be calculated with Equation 3.10.

Another important performance parameter is the coefficient of performance (*COP*) of the heat pump, which is here calculated using Equation 3.11 where $\dot{W}_{\mathrm{m}}$ corresponds to the magnetic power, Equation 3.13. Finally, second law efficiency, defined by Equation 3.12, is used to compare the performance of the AMRs with the theoretical maximum.

$$\dot{Q}_{\mathrm{h}} = f_{\mathrm{AMR}} \int_0^{1/f_{\mathrm{AMR}}} \dot{m}(t) c_{\mathrm{f}} (T_{\mathrm{f}}(x = L, t) - T_{\mathrm{hot}})\, \mathrm{d}t \tag{3.9}$$

$$\dot{Q}_{\mathrm{c}} = f_{\mathrm{AMR}} \int_0^{1/f_{\mathrm{AMR}}} \dot{m}(t) c_{\mathrm{f}} (T_{\mathrm{cold}} - T_{\mathrm{f}}(x = 0, t))\, \mathrm{d}t \tag{3.10}$$

$$COP_{\mathrm{hp}} = \frac{\dot{Q}_{\mathrm{h}}}{\dot{W}_{\mathrm{pump}} + \dot{W}_{\mathrm{m}}} \tag{3.11}$$

$$\eta_{\mathrm{Carnot}} = \frac{COP_{\mathrm{hp}}}{COP_{\mathrm{Carnot}}} \tag{3.12}$$

$$\dot{W}_{\mathrm{m}} = \frac{1}{\tau} \int_0^L \int_0^\tau \rho_{\mathrm{s}} A_{\mathrm{cs}} (1 - \varepsilon) T_{\mathrm{s}} \frac{\mathrm{d}s}{\mathrm{d}t}\, \mathrm{d}t\, \mathrm{d}x \tag{3.13}$$

3.2.3. MODEL INPUTS

The fluid flow and magnetic field profiles used in the simulations are illustrated in Figure 3.1. These profiles resemble those of a rotating-magnet, multi-bed magnetocaloric heat-pump device as the one developed by Huang et al. [26]. Stagnation periods are possible in this particular device thanks to solenoid valves that allow the reciprocating flow in synchronization with the magnetic field. Vieira et al. [107] measured the flow profiles that are attained when using commercial solenoid valves and found that the resulting profiles are very close to a trapezoidal shape. They found only small discrepancies in the results obtained when using the measured profiles vs the trapezoidal profiles in a numerical model [107].

The overall regenerator geometry considered for the simulations presented in Figure 3.2 also matches with the one proposed by Huang et al. [26]. This overall shape is constrained by the shape and size of the air gap of the magnet, which for the case of the device considered here is a C-shaped magnet. Table 3.3 presents a summary of other key parameters that were used in the simulations. Mass flow rate of HTF corresponds to a single AMR.

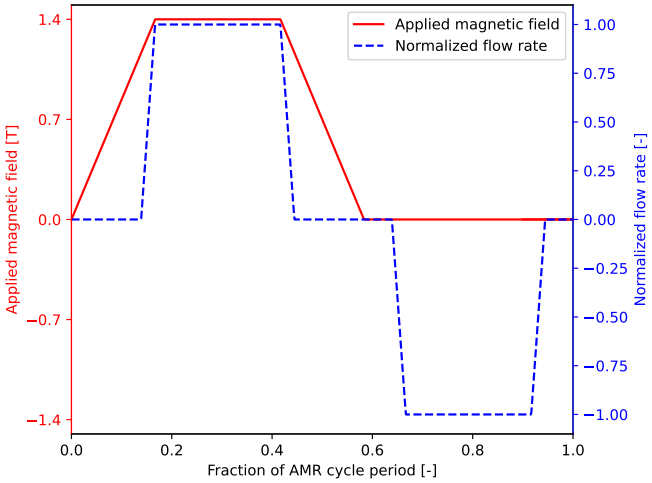

Figure 3.1.: Fluid flow and magnetic field profiles.

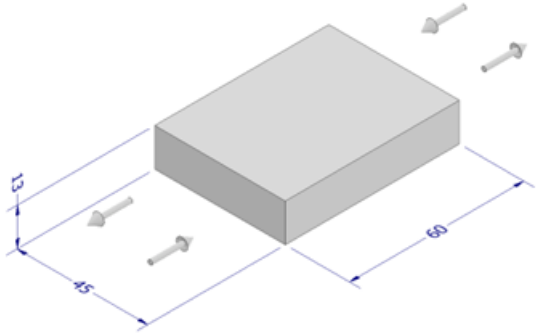

Figure 3.2.: Overall geometry and dimensions of the AMR (in mm).

3.2.4. MATERIAL PROPERTIES

Selected properties of the $Mn_{1.18}Fe_{0.73}P_{0.48}Si_{0.52}$ MCM are presented in Figure 3.3. This has been taken as the reference material for this study, and the corresponding dataset can be found in [90]. This material exhibits a small amount of thermal hysteresis of about 0.6 K, but in Figure 3.3 only heating curves are presented. Neglecting thermal hysteresis conducts to an overestimation of AMR performance because smaller MCE is attainable in an MCM with hysteresis. However, the goal of this study is to compare different layering strategies rather than predicting real performance of these AMRs thus including hysteresis will not change the conclusions.

Figure 3.3a shows the isofield magnetization curves for 0.9 T and 1.4 T

Table 3.3.: Parameters used in the simulations.

Parameter	Value	Units
AMR *W*x*H*x*L*	45x13x60	mm x mm x mm
Porosity (ε)	0.36	–
Particle diameter (D_{sp})	300	µm
Max. Magnetic field	1.4	T
Frequency AMR	[0.75, 4.50]	Hz
Max. mass flow rates	[25.0, 37.5]	$g\,s^{-1}$
T_{amb}	288	K
T_{hot}	[308, 310, 312]	K
$\Delta T_{span} = T_{hot} - T_{cold}$	[18, 21, 24, 27, 30, 33]	K

for this material and for Gd. The sharper transition of the MnFePSi material compared to Gd is evident in this figure. Figure 3.3b shows the specific heat capacity of the MnFePSi material and Gd as a function of temperature for 0 T, 0.9 T and 1.4 T. The first-order character of the MnFePSi material is also apparent from this figure. Figure 3.3c shows the magnetic entropy change, and Figure 3.3d shows the adiabatic temperature change of the MnFePSi material and Gd for magnetic field changes from 0 T to 0.9 T and from 0 T to 1.4 T. These properties have been calculated from total entropy data. The high specific heat capacity of the MnFePSi compound is responsible for the small adiabatic temperature change that this material exhibits.

The properties of the materials in the layered bed were obtained by artificially shifting the properties of the $Mn_{1.18}Fe_{0.73}P_{0.48}Si_{0.52}$ compound to the desired Curie temperatures. Curie temperature is taken in this study as the temperature of the peak of the specific heat of the MCM in zero field. It has been demonstrated that it is possible to continuously tune the Curie temperature of the MnFePSi compound over a wide temperature range by changing the Fe:Mn and the P:Si ratio without compromising the MCE or considerably modifying the thermal hysteresis, as can be seen in Figure 3.4 [108]. Therefore, even though artificially created properties are used in this study, it is feasible to produce materials with similar properties in the temperature range used here, from 281 K to 308 K, by using different compositions of the material selected system.

3.2.5. LAYERING STRATEGIES

An ideal AMR should have a continuous change in the transition temperature of the material along the bed so that the MCE is maximum at any position [50]. In order to resemble this ideal condition of continuous change in transition temperature, it was decided to

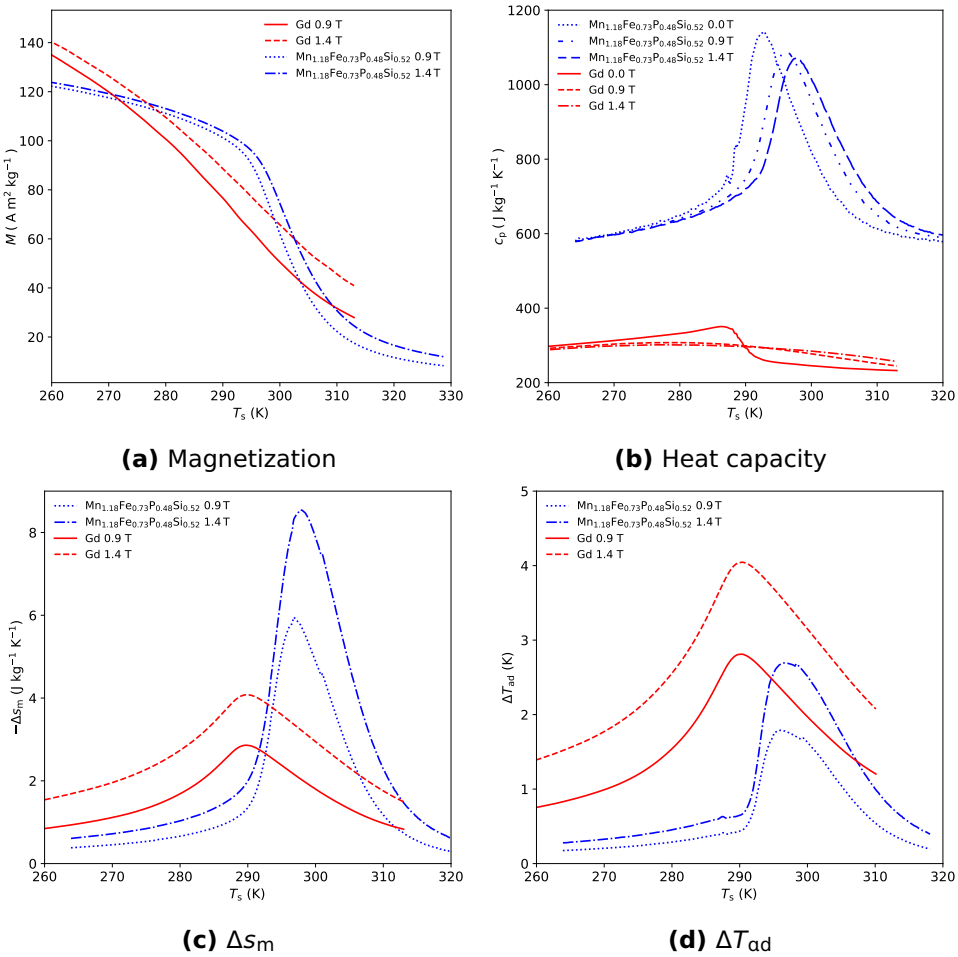

(a) Magnetization **(b)** Heat capacity

(c) Δs_m **(d)** ΔT_{ad}

Figure 3.3.: Magnetization (a), heat capacity (b), magnetic entropy change (c), and adiabatic temperature change (d) of the $Mn_{1.18}Fe_{0.73}P_{0.48}Si_{0.52}$ material as a function of temperature in comparison with the same properties of Gd.

compare AMRs of 30 layers. This number of layers is not so large to consider that this AMR has a continuous change in Curie temperature, but it is large enough taking into account the conclusions of numerical simulations with layered AMRs using $La(Fe,Mn,Si_{13})H_y$ materials which indicated that using more than 15 layers would generally not improve the performance of the AMR [70]. This was also confirmed by prior simulations (not presented here) for the material system MnFePSi that is considered in this study. The question is how to distribute the transition temperatures along the bed so that the temperature at every section of

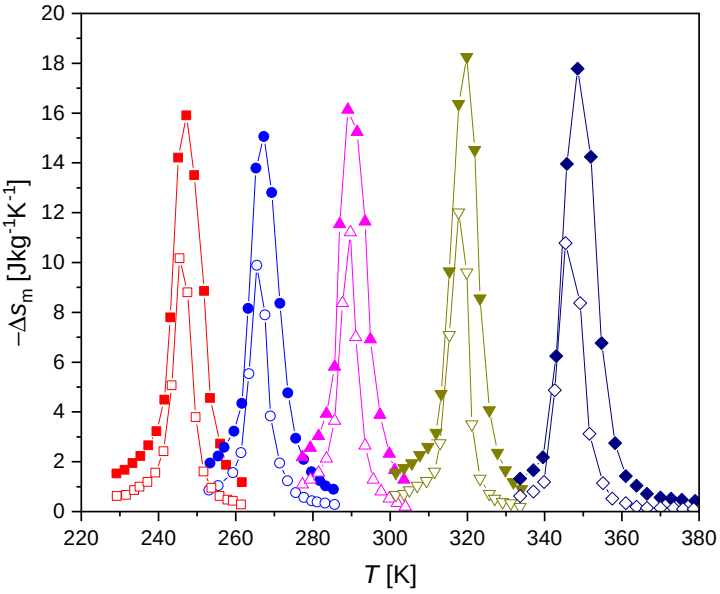

Figure 3.4.: Magnetic entropy change of $Mn_xFe_{1-x}P_{1-y}Si_y$ for a series of compositions. From left to right x = 1.32, 1.30, 1.28, 1.24, 0.66 and y = 0.48, 0.50, 0.52, 0.54, 0.34. Solid symbols correspond to a magnetic field change from 0 to 2 T and open symbols from 0 to 1 T . Adapted from [108].

the AMR actually fluctuates around its transition temperature.

Figure 3.5 presents a Curie temperature vs AMR length diagram for the three basic layering strategies that are considered in this study. In the three cases, 30 layers of MCM were considered with Curie temperatures ranging from 281 K to 308 K (the design temperature span) each with a length of 2 mm (L_{AMR} / 30). The base layering strategy, which is shown in black dashed line in Figure 3.5, is a linear distribution of Curie temperatures along the bed, i.e. an uniform separation of Curie temperatures and layers of equal length.

The second layering strategy, shown in red dotted line in Figure 3.5, corresponds to a distribution of Curie temperatures that follows a sigmoidal function, i.e. the separation of Curie temperature is smaller between the layers located near the ends of the AMR and bigger for the layers near the middle, with all layers of the same length. The Curie temperature of each layer as a function of the position of its middle point is obtained by using Equation 3.14. The motivation behind considering this shape comes from the fact that the temperature distributions of the solid material observed in numerical simulations of single layer AMRs are flat at the cold end of the AMR during the

cold-to-hot blow and flat at the hot end during the hot-to-cold blow (see [95] as an example), which is a consequence of the heat exchange between fluid and solid. Therefore, using a sigmoidal shape for the distribution of Curie temperatures could lead to have each MCM fluctuating around its Curie temperature and thus to maximize the MCE along the bed.

In the third layering strategy, shown in blue solid line in Figure 3.5, it was considered that five layers at each end have the same Curie temperature and the rest internal layers follow a linear distribution. This is the same as considering that there are 22 layers of MCM in the bed with uniform separation of Curie temperatures, with the length of the first and the last layers being 10 mm each (L_{AMR} / 6), and the length of the middle layers being 2 mm each (L_{AMR} / 30). An analysis about the influence of the length of these thicker layers is presented in subsection 3.3.4.

$$T_{Curie} = \frac{27}{1 + e^{-0.17(x-30)}} + 281 \tag{3.14}$$

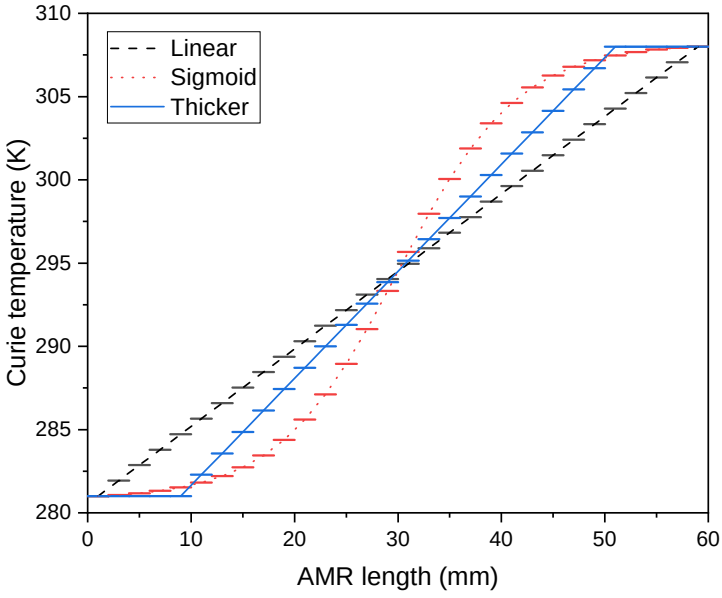

Figure 3.5.: Curie temperature separation between materials vs the position of each material along the bed for the layering strategies considered in this study: linear distribution of Curie temperatures (black dashed line), sigmoid distribution of Curie temperatures (red dotted line), and linear distribution with thicker ends (blue solid line).

3.3. RESULTS AND DISCUSSION

All heating capacities presented in section correspond to a single AMR. Two scenarios were considered in terms of combination of operating conditions. First, the results of a high utilization scenario, i.e. large mass flow rate ($37.5\,\mathrm{g\,s^{-1}}$) and low frequency (0.75 Hz), will be presented. Then, the results of a low utilization scenario, i.e. smaller mass flow rate ($25.0\,\mathrm{g\,s^{-1}}$) and higher frequency (4.5 Hz), will follow. These two combinations of flow rates and frequencies correspond to the following utilization values: $\varphi_{\mathrm{high}} = 0.53$ and $\varphi_{\mathrm{low}} = 0.06$, which were calculated using Equation 3.15.

$$\varphi = \frac{c_{\mathrm{f}} \int_{t_1}^{t_2} \dot{m}\,\mathrm{d}t}{A_{\mathrm{cs}} L_{\mathrm{AMR}} (1-\varepsilon) \rho_{\mathrm{s}} c_{\mathrm{s}}} \tag{3.15}$$

Where $c_{\mathrm{s}} = 800\,\mathrm{J\,kg^{-1}\,K^{-1}}$ was taken as reference heat capacity of the MCM and corresponds approximately to the half peak heat capacity, $\rho_{\mathrm{s}} = 6100\,\mathrm{kg\,m^{-3}}$, $c_{\mathrm{f}} = 4200\,\mathrm{J\,kg^{-1}\,K^{-1}}$ and t_1 and t_2 correspond to the beginning and end of the cold-to-hot blow process.

3.3.1. HIGH UTILIZATION SCENARIO

The temperature span vs heating capacity curves for the three layering strategies at three different hot side temperatures are presented in Figure 3.6a, Figure 3.6b, and Figure 3.6c. Figure 3.7 a), c), and e) show the same information presented in Figure 3.6 in a different way to facilitate the comparison of the performance between the different layering strategies.

As can be seen in Figure 3.6, the AMR with a sigmoidal distribution of Curie temperatures is less sensitive to the changes in the hot and cold temperatures compared to the other two. For example, for a temperature span of 18 K, the heating capacity of the AMR in Figure 3.6a changes from 29.0 W to 40.0 W when the hot side temperature changes from 312 K to 308 K, corresponding to a variation of 37.9 %, whereas this variation would be 5.6 % in Figure 3.6b and 8.7 % in Figure 3.6c.

An AMR that is less sensitive to changes in the hot and cold temperatures is desirable in MCHPs, which can be continuously subjected to changes in the temperatures of the heat source and heat sink during operation, even though the temperature span of the AMR can also be fixed by using a control system. Comparing the AMR with sigmoid distribution of Curie temperatures and the one with linear distribution of Curie temperatures but thicker end layers, the latter produces greater heating capacities for almost all combinations of T_{hot} and ΔT_{span} that were simulated, although it exhibits more variation in heating capacity with changes of the hot side temperature.

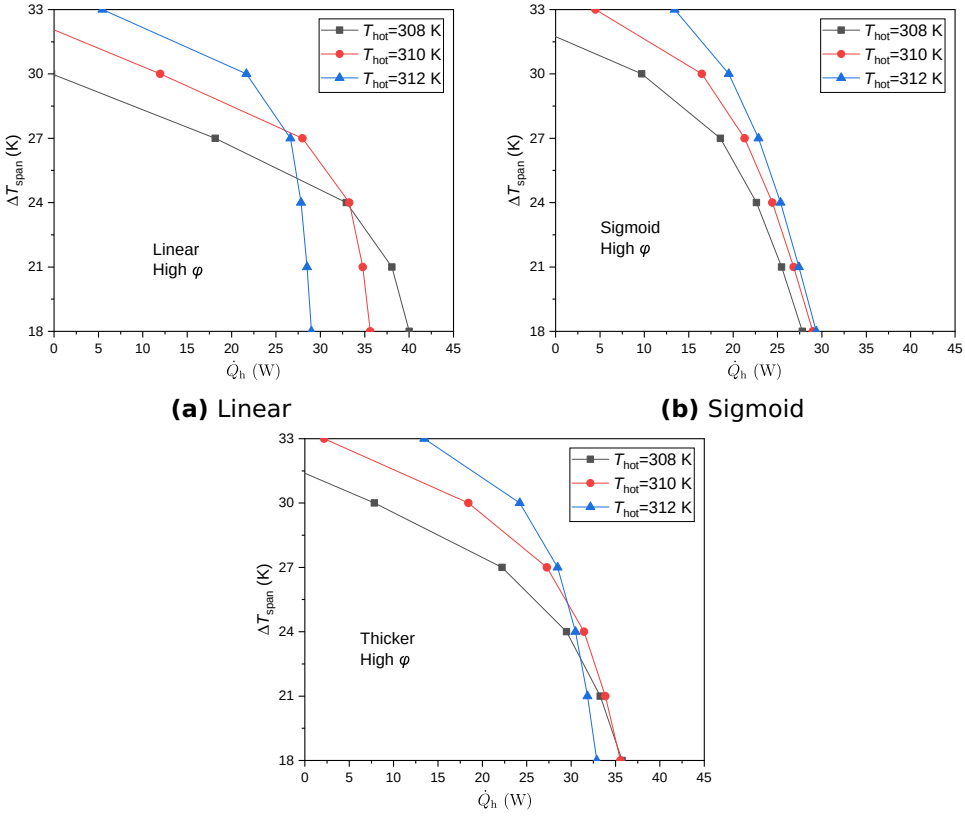

(a) Linear **(b)** Sigmoid

(c) Thicker

Figure 3.6.: Temperature span vs heating capacity of an AMR with a linear distribution of Curie temperatures (a), a sigmoid distribution of Curie temperatures (b), and a linear distribution with thicker end layers (c) for a case with large flow rate 37.5 g s^{-1} and low frequency 0.75 Hz, i.e. high utilization.Three hot side temperatures are considered $T_{\text{hot}} = [308, 310, 312]$ K.

In Figure 3.7 we compile the performance of the three AMRs in the high utilization scenario. Figure 3.7a, Figure 3.7c, and Figure 3.7e show heating capacities vs temperature span curves while Figure 3.7b, Figure 3.7d, and Figure 3.7f show the second law efficiency as a function of temperature span. Second law efficiency was calculated with Equation 3.12. The AMR with linear distribution of Curie temperatures performs better than the other two in terms of heating capacity and second law efficiency when the hot side temperature is below 310 K and the temperature span is smaller than 27 K. The AMR with linear distribution of Curie temperatures and thicker ends performs better

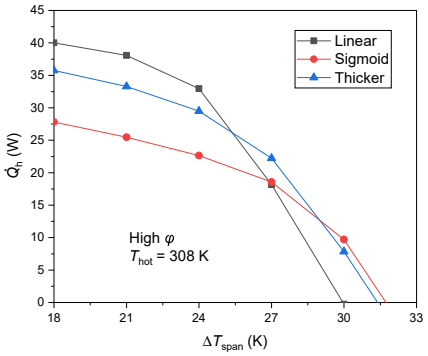

(a) $\dot{Q}_h$ at T_{hot} = 308 K

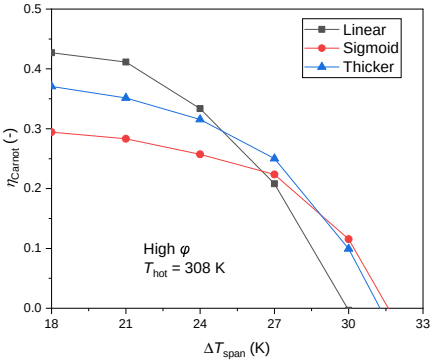

(b) η_{Carnot} at T_{hot} = 308 K

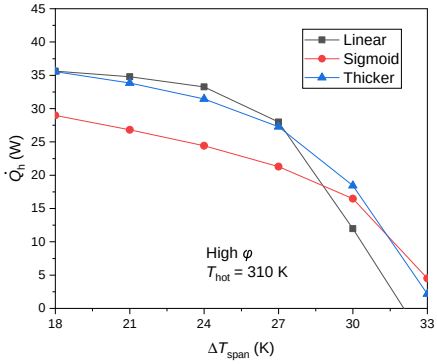

(c) $\dot{Q}_h$ at T_{hot} = 310 K

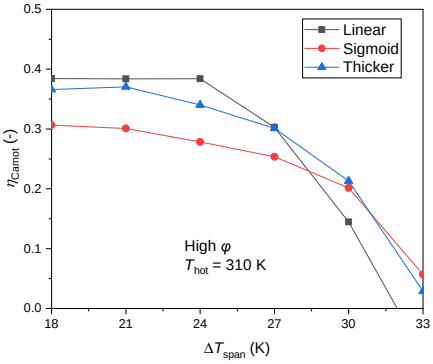

(d) η_{Carnot} at T_{hot} = 310 K

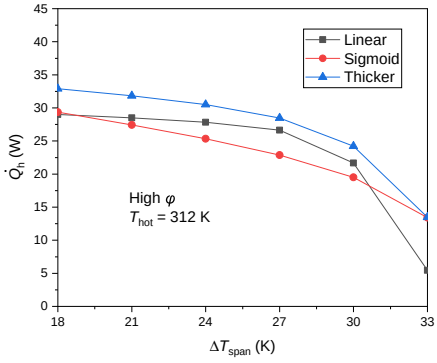

(e) $\dot{Q}_h$ at T_{hot} = 312 K

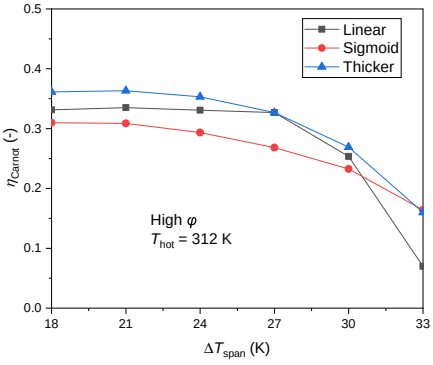

(f) η_{Carnot} at T_{hot} = 312 K

Figure 3.7.: Heating capacity and second law efficiency vs temperature span of AMRs working under high utilization conditions (max. mass flow rate 37.5 g s^{-1} and frequency 0.75 Hz for T_{hot} = 308 K (a, b), T_{hot} = 310 K (c, d) and T_{hot} = 312 K (e, f) and for the three layering strategies considered.

than the other two when the hot side temperature is 312 K. This suggests that the optimum hot side temperature is not the same for the three AMRs even though the Curie temperatures of the MCMs range between 281 K and 308 K in all three cases.

An additional observation in Figure 3.7 is that the AMR with a sigmoid distribution of Curie temperatures produces a greater heating capacity and higher second law efficiency than the other two for temperature spans above 30 K. However, for such large temperature spans the heating capacity reduces considerably, and thus it is not expected that an AMR operates under such conditions. It is also remarkable from Figure 3.7 that the AMRs with linear distribution of Curie temperatures and the one with thicker ends exhibit bigger changes in their second law efficiency at $\Delta T_{span} = 27$ K (from approx. 20 % and 25 % respectively to approx. 33 % in both cases) when T_{hot} changes from 308 K to 312 K compared with the AMR with a sigmoid distribution of Curie temperatures (from approx. 22 % to approx. 26 %). This is also an indication of the lower sensitivity to changes of operating temperatures that the sigmoid AMR has.

Furthermore, none of the three simulated AMRs produces second law efficiencies over 40 % for a $\Delta T_{span} = 25$ K while a vapour compression heat pump can achieve second law efficiencies of the order of 43 % for the same ΔT_{span} according to Kiss and Infante Ferreira [109]. Finally, by looking at overall trends in Figure 3.7a, Figure 3.7c, and Figure 3.7e, it is possible to say that greater heating capacities for small temperature spans are attainable when $T_{hot} = 308$ K, and larger zero-load temperature spans when $T_{hot} = 312$ K. This is because a better alignment of the range of Curie temperatures of the MCMs with the range of operating temperatures is only possible by decreasing T_{hot} for small temperature spans or increasing T_{hot} for large temperature spans.

In order to confirm that the optimum hot side temperature is not the same for the three AMRs, additional simulations were carried out to see the influence of the hot side temperature for a fixed temperature span of 27 K (the design ΔT_{span}). Figure 3.8 shows the results of these additional simulations for the high utilization scenario. The optimum hot side temperature is equal to 311 K for the AMR with a linear distribution of Curie temperatures, 313 K for the one with a distribution of Curie temperatures following a sigmoid function, and 312 K for the AMR with the linear distribution and thicker ends. This must be considered in the design process of a layered AMR. For example, if the design point of an AMR corresponds to $T_{hot} = 308$ K, $T_{cold} = 281$ K, and the above-mentioned flow rate and frequency and a linear distribution of Curie temperatures with thicker end layers is chosen, the Curie temperatures of the materials should range between approximately 277 K and 304 K (instead of 281 K and 308 K as it was simulated here) so

that the maximum performance is obtained when T_{hot} = 308 K.

Figure 3.8 shows that the AMR with thicker ends performs better in terms of heating capacities and second law efficiencies in comparison with the one using a linear distribution of Curie temperatures when the hot side temperature (and the cold side temperature since ΔT_{span} = 27 K is fixed in this figure) moves away from the optimum. In other words, as mentioned above, when using thicker ends the AMR becomes less sensitive to changes in the operating temperatures. It is relevant to remark that for ΔT_{span} larger than 27 K the hot side temperature that produces the maximum heating power is higher than the one shown in Figure 3.8 and vice versa, because only by increasing (or decreasing) T_{hot} the working temperature range of the AMR, i.e. [T_{cold}, T_{hot}], can be better aligned with the range of Curie temperatures of the materials to maintain all layers as active and the MCE as large as possible. This can also be seen in Figure 3.6 for the 3 layering strategies considered.

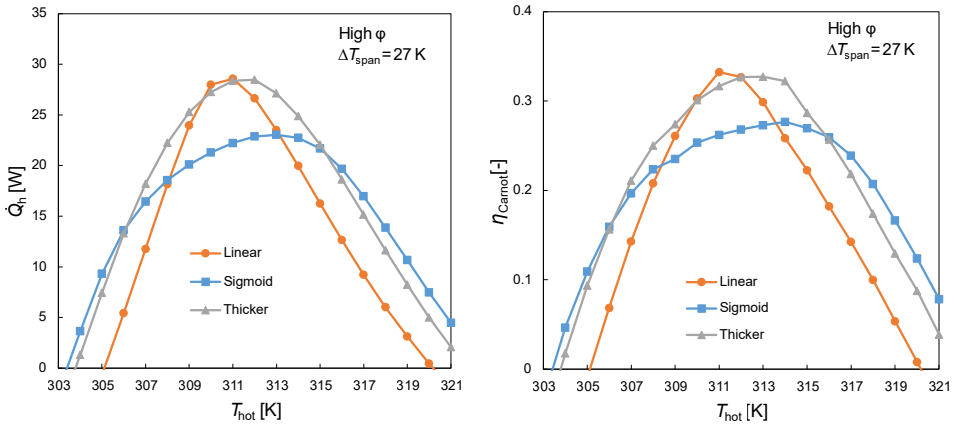

Figure 3.8.: Heating capacity and second law efficiency as a function of hot side temperature for a fixed temperature span of 27 K for the high utilization scenario.

Figure 3.9a, Figure 3.9c, and Figure 3.9e show the total entropy vs temperature curves at 0 T and 1.4 T for the first MCM adjacent to the cold side of the AMR, MCM number 16 near the middle of the AMR, and the MCM adjacent to the hot side. The curves corresponding to the other MCMs are not shown to avoid excessive overlapping. A different reference point has been chosen for the total entropy of each layer in order to see the peak MCE happening in the same total entropy range although in the own temperature range of each MCM. The horizontal lines in these three figures enclose the region of each material where the $\Delta T_{ad} \geq 2$ K, an explanation of which can be found in Appendix A.

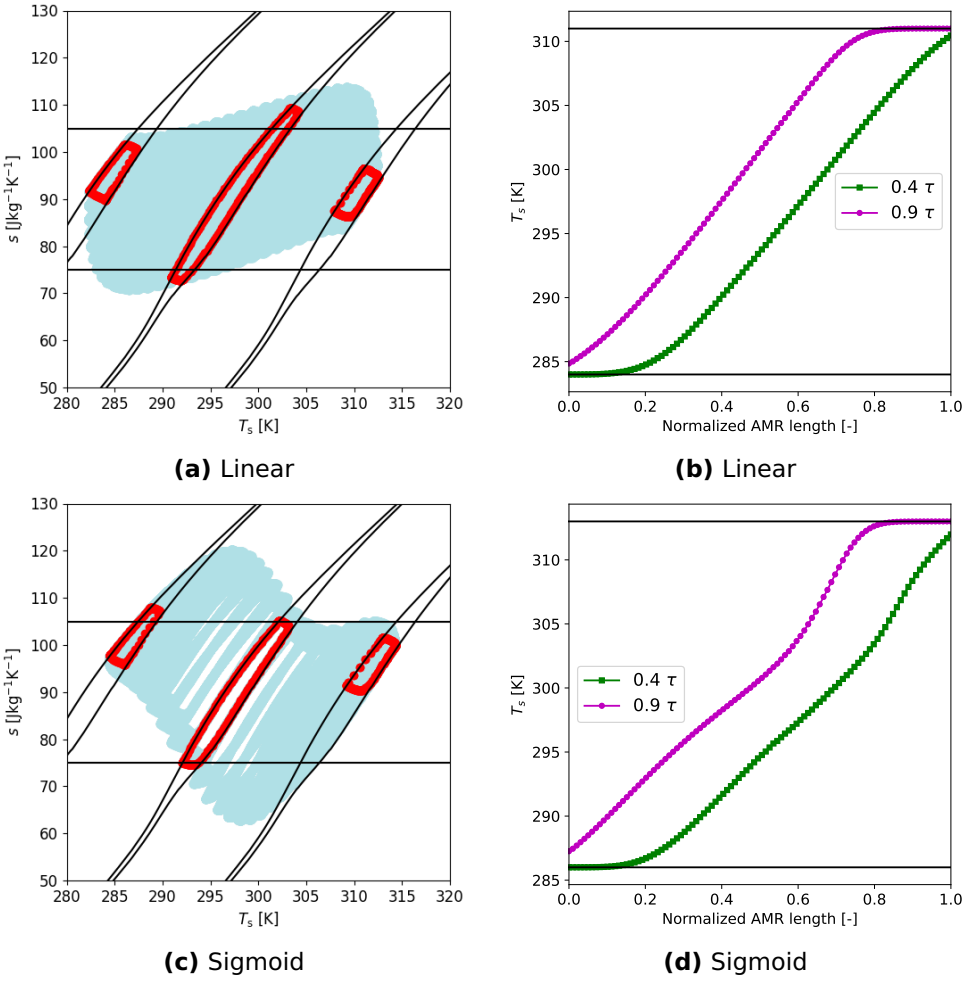

(a) Linear **(b)** Linear

(c) Sigmoid **(d)** Sigmoid

Figure 3.9.: (left) Thermodynamic cycles in a sT diagram and (right) temperature distributions of the solid material at $t = 0.4\tau$ (near the end of cold-to-hot blow: green squares) and $t = 0.9\tau$ (near the end of hot-to-cold blow: magenta circles). Region between horizontal lines in a), c) and e) correspond to an $\Delta T_{ad} \geq 2\,\mathrm{K}$ for each material. Horizontal lines in b), d) and f) represent T_{cold} and T_{hot} for each case.

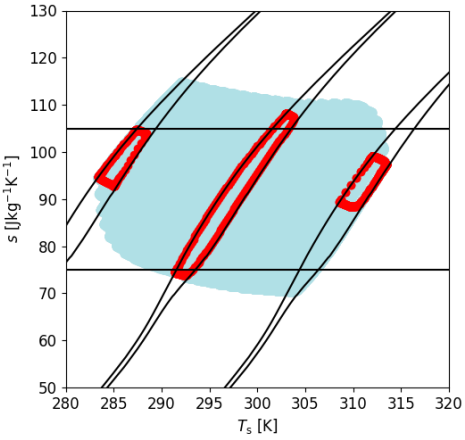

(e) Thicker ends

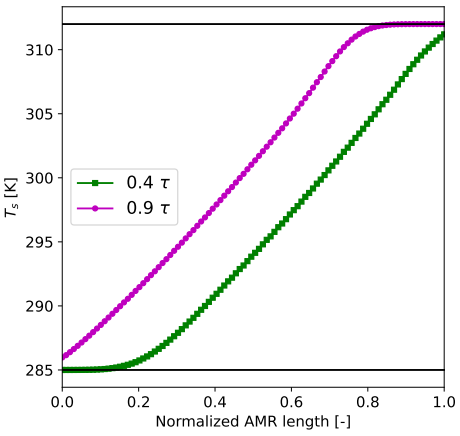

(f) Thicker ends

Figure 3.9.: (continued).

The thermodynamic cycles experienced by the first, the middle, and the last nodes in the discretized solid domain are depicted in red whereas the light blue region corresponds to the region where the thermodynamic cycles of the rest of the nodes in the discretized solid domain occur. The performance data used for constructing these diagrams correspond to those of the points of maximum heating capacity of Figure 3.8. This diagrams are useful to visualize how well the MCMs are aligned in their full thermodynamic cycle with the temperature range of maximum MCE. In Figure 3.9a and Figure 3.9e, corresponding to the AMRs with linear distribution of Curie temperatures and linear distribution with thicker ends respectively, most of the MCMs experience thermodynamic cycles that are well aligned with the region of maximum MCE of each MCM.

On the contrary, in Figure 3.9c, corresponding to the AMR with a sigmoid distribution of Curie temperatures, the materials close to the cold side experience thermodynamic cycles in which the magnetization process is out of the range of maximum MCE. For this reason, poorer cooling and heating capacities are attainable. On the other hand, Figure 3.9b, Figure 3.9d, and Figure 3.9f show the temperature distributions of the solid material near the end of the cold and hot blow processes respectively. These figures suggest that the layering strategy influences the shape of the temperature distribution profiles with the linear layering strategies also producing more linear temperature distributions in the middle part of the AMR when the operating temperature span is close to the design temperature span.

3.3.2. LOW UTILIZATION SCENARIO

In the low utilization scenario, see Figure 3.10, the three AMRs produce slightly poorer heating capacities for temperature spans equal or below 27 K and also larger zero-load temperature spans in comparison with the high utilization scenario, see Figure 3.6. It is also evident when comparing Figure 3.6 and Figure 3.10 that the three AMRs become more sensitive to changes in the hot side and cold side temperatures in the high utilization scenario. Regarding Figure 3.10, in a low utilization scenario, the three AMRs perform similarly although the one with the linear distribution of Curie temperatures is again slightly more sensitive to changes of the hot side and cold side temperatures.

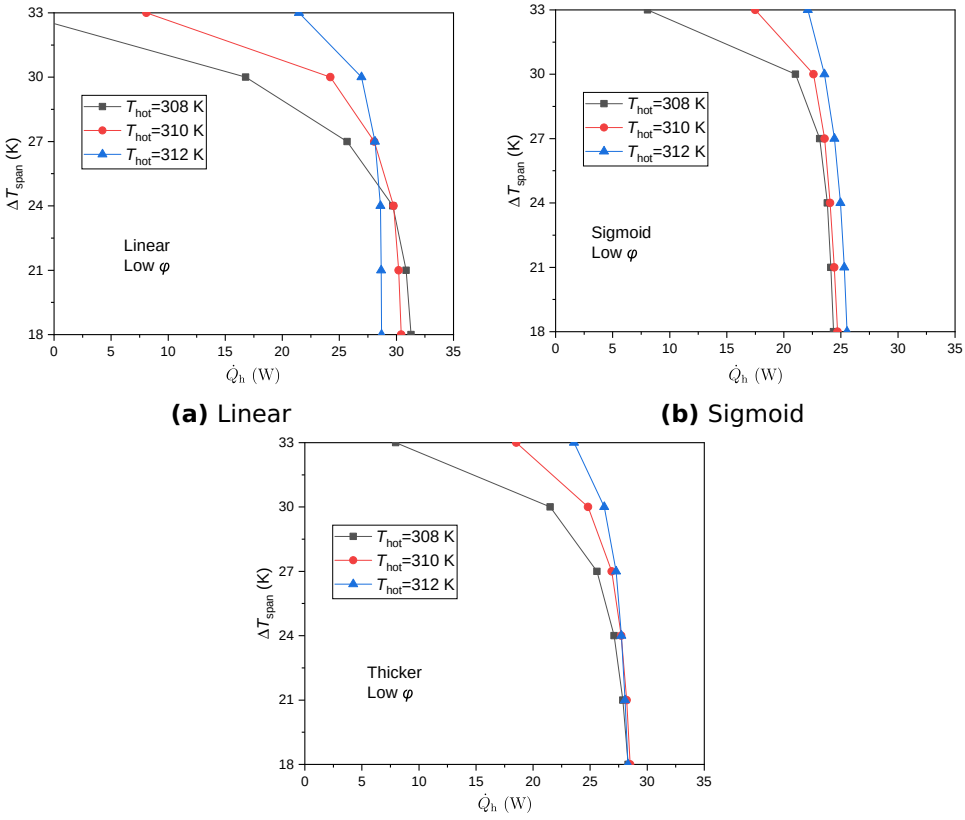

(a) Linear **(b)** Sigmoid

(c) Thicker

Figure 3.10.: Temperature span vs heating capacity of an AMR with a linear distribution of Curie temperatures (a), a sigmoid distribution of Curie temperatures (b), and a linear distribution with thicker end layers (c) for a case with small flow rate 25 g s^{-1} and high frequency 4.5 Hz, i.e. low utilization.

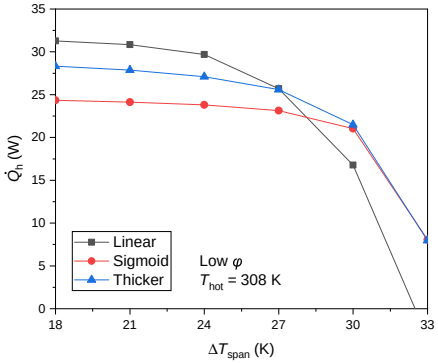

(a) $\dot{Q}_h$ at T_{hot} = 308 K

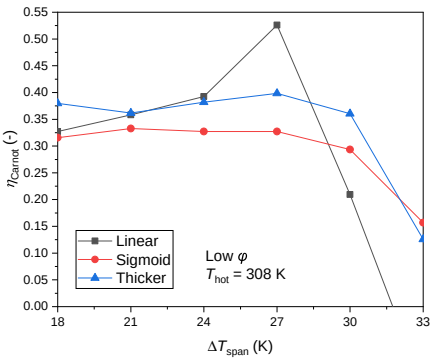

(b) η_{Carnot} at T_{hot} = 308 K

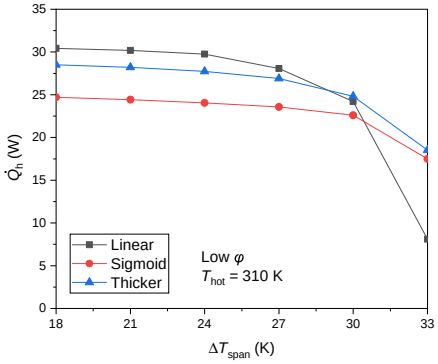

(c) $\dot{Q}_h$ at T_{hot} = 310 K

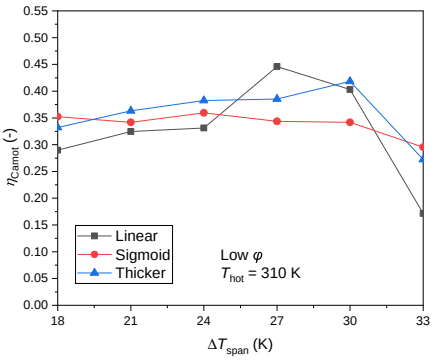

(d) η_{Carnot} at T_{hot} = 310 K

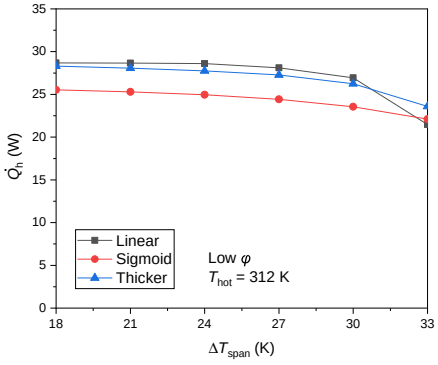

(e) $\dot{Q}_h$ at T_{hot} = 312 K

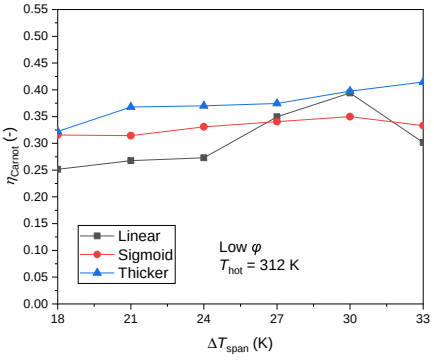

(f) η_{Carnot} at T_{hot} = 312 K

Figure 3.11.: Heating capacity and second law efficiency vs temperature span of AMRs working under low utilization conditions (max. mass flow rate 25 g s^{-1} and frequency 4.5 Hz) for T_{hot} = 308 K (a, b), T_{hot} = 310 K (c, d) and T_{hot} = 312 K (e, f) and for the three layering strategies considered.

Figure 3.11 shows the heating capacity and second law efficiency of the three different AMRs comparatively for the low utilization scenario. Figure 3.11a and Figure 3.11b correspond to a hot side temperature of 308 K, Figure 3.11c and Figure 3.11d to 310 K, and Figure 3.11e and Figure 3.11f to 312 K. For the low utilization scenario, the AMR with a linear distribution of Curie temperatures and thicker ends performs better in terms of second law efficiency for a wide variety of operating temperatures. However, the AMR with a linear distribution of Curie temperatures performs better in terms of heating capacity for temperature spans below 27 K for the three hot side temperatures considered.

Regarding the efficiencies shown in Figure 3.11, it can be seen that the peaks move to larger ΔT_{span} when T_{hot} increases. This can be due to a better alignment of the Curie temperature of the MCMs in the AMRs with the working temperatures. It is also noticeable in Figure 3.10 and Figure 3.11 that for temperature spans below 24 K these AMRs produce essentially the same heating capacity. A similar behaviour was observed by Jacobs et al. [62], who tested a magnetocaloric refrigerator prototype equipped with 12 multi-layer AMR beds of LaFeSiH compounds. Smith et al. [29] also showed a figure that suggests that layered AMRs typically exhibit an almost constant cooling capacity for small to medium temperature spans before dropping to zero after a critical point.

This occurs because the temperature of the portion of the AMR closest to the hot end, which is the section of the AMR responsible for producing the heating capacity, fluctuates around the same values for temperature spans that are smaller than the design temperature span when the hot side temperature is fixed. This condition is easier to achieve in low utilization conditions, but it is also observable in some cases under high utilization conditions. Figure 3.12a shows the solid temperature distribution at $t = 0.25\tau$ for the AMR with linear distribution of Curie temperatures when $T_{\text{hot}} = 310$ K and $\Delta T_{\text{span}} = [18, 21, 30, 33]$ K under low utilization conditions. Figure 3.12b shows the same for the high utilization conditions.

It can be seen that the temperature of the solid (and also the temperature of the fluid even though not depicted in these figures) for temperatures spans equal to 21 K and 18 K is nearly the same from roughly 50 % of the AMR length to the hot end in the low utilization condition. In the high utilization condition, a smaller portion of the AMR exhibits nearly the same temperatures for temperature spans equal to 18 K and 21 K. The heating capacities in the low utilization scenario are 30.4 W and 30.2 W for temperatures spans 18 K and 21 K respectively, whereas in the high utilization scenario the heating capacities are 35.6 W and 34.8 W for temperatures spans 18 K and 21 K respectively. Figure 3.13 also confirms that for the points with approximately equal

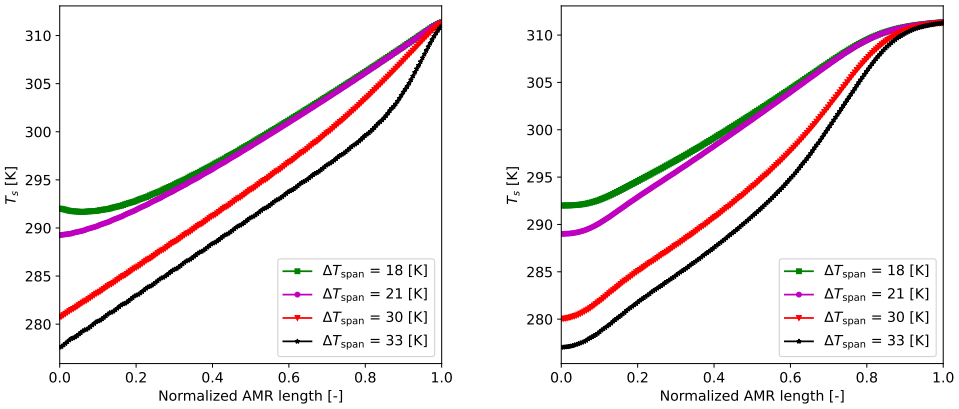

(a) Low utilization **(b)** High utilization

Figure 3.12.: Solid temperature distribution at 1/4 of the cycle period for the AMR with linear distribution of Curie temperatures in the low utilization scenario a) and high utilization scenario b), and T_{hot} = 310 K.

heating capacity and different temperature spans of Figure 3.10 the temperature of fluid and solid at the hot end of the AMR coincide.

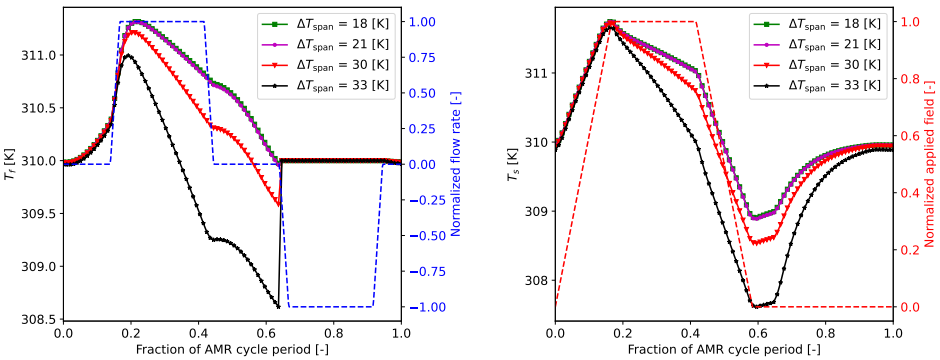

(a) Fluid temperature at $x = L$ **(b)** Solid temperature at $x = L$

Figure 3.13.: Temperature of fluid (a) and solid (b) at $x = L$ (hot side of the AMR) as a function of time for 4 different temperature spans. An AMR following a linear distribution of Curie temperatures in a low utilization scenario is considered, and T_{hot} = 310 K. Fluid flow and magnetic field profiles are also depicted using dashed lines to facilitate visualization of the different stages of the AMR cycle.

In Figure 3.12a, the temperature distribution of the solid

corresponding to a temperature span of 18 K has a minimum at a normalized AMR length of approximately 0.1. A similar behavior has been observed in experiments with two-layer AMRs conducted by Teyber et al. [78]. They attribute this behavior to heat transfer from the AMR to ambient through the casing because ambient temperature was smaller than T_{cold} in such experiments. Ambient temperature was fixed at 288 K in our simulations while T_{cold} is 292 K for the case under consideration. So, heat leaks to ambient could explain that the lowest temperature is not located at the cold end of the AMR when T_{cold} is above ambient temperature.

3.3.3. PERFORMANCE FOR OTHER RANGES OF OPERATING CONDITIONS

Given that the results presented above are only for two utilization values, a bigger range of operating conditions in terms of flow rate and AMR cycle frequency was explored to see if there is an operating point (or region) for which the AMR that follows a sigmoidal distribution of Curie temperatures achieves a better matching between temperature distribution and the region of maximum MCE of each material in order to produce greater heating capacities than the other two. Figure 3.14 shows the results of this group of simulations for which $T_{hot} = 310$ K, $\Delta T_{span} = 27$ K, the mass flow rate ranged between 16.66 and 83.33 g s^{-1} and the cycle frequency between 0.5 and 5 Hz.

As it can be seen in Figure 3.14, the AMR with the linear distribution of Curie temperatures produces the greatest maximum heating capacity of the three AMRs. These results follow the same trend as in Figure 3.7c and Figure 3.11c where the AMR with linear distribution of Curie temperatures outperforms the other two when $T_{hot} = 310$ K and $\Delta T_{span} = 27$ K. A real maximum heating capacity is not observable in the simulated range for any of the three AMRs, but larger flow rates and frequencies are difficult to achieve in practice because of the reciprocating nature of the flow and because of significant increases in pressure gradient. For the point of largest flow rate and frequency considered in this group of simulations the maximum calculated pressure gradient was approximately 3.2 bar. This pressure gradient could be reduced by optimizing the shape of fluid channels [46, 110].

On the other hand, second law efficiency is also depicted in Figure 3.14 for the three AMRs. For the particular combination of operating temperatures, the AMR with the linear distribution of Curie temperatures also produces higher second law efficiencies reaching a maximum of 69 % while the maximum is 49 % for the sigmoidal and 60 % for the one with thicker ends. This difference in performance is mainly due to greater heating capacities of the linear case given that the magnetic power input and pumping power are comparable for the

three cases. The pumping power of the three AMRs at the maximum efficiency point is approximately the same given that the maximum occurs at the same flow rate and frequency for the three cases.

3.3.4. INFLUENCE OF END LAYER THICKNESS

The results of an additional group of simulations carried out to see the influence of the thickness of the end layers on the performance of an AMR with linear distribution of Curie temperatures and thicker end layers are illustrated in Figure 3.15. These simulations were carried out for a $\Delta T_{span} = 27\,K$, with $T_{cold} = 285\,K$ and $T_{hot} = 312\,K$, which was the optimum working temperature range found in Figure 3.8. The flow rate was fixed equal to $37.5\,g\,s^{-1}$, and three frequencies were considered in order to produce three different utilizations, 0.75 Hz, 1.5 Hz, and 2.25 Hz. The same 22 MCMs introduced in subsection 3.2.5 for the third layering strategy (thicker end layers) are also used here, the Curie temperatures of which range between 281 K and 308 K. The total length of the AMR, L_{AMR}, was fixed equal to 60 mm for all cases as in the previous sections, and the length of the inner layers was defined as $L_{inner} = (L_{AMR} - 2L_{end})/20$.

It was found that the optimum end layer thickness for a fixed total AMR length depends on the utilization (or penetration of fluid in the AMR). The higher the utilization (and penetration of fluid) the greater the length of the end layer that maximizes the heating capacity. This can be seen in Figure 3.15, where for lower frequencies, i.e. longer cycle periods and thus longer blow time and larger penetration distances, the maximum heating capacity moves to greater end layer thicknesses. By fitting the data points to 4^{th} order polynomials, the maxima were found at end layer thicknesses equal to 5.63 mm, 7.11 mm, and 8.57 mm for frequencies 2.25 Hz, 1.50 Hz, and 0.75 Hz respectively.

3.4. CONCLUSIONS

A one-dimensional numerical model was used to study the performance of layered AMRs composed of materials of the MnFePSi family arranged in three different layering strategies: one following a linear distribution of Curie temperature, a second with a distribution of Curie temperatures that follows a sigmoid function, and a third one in which there is a linear distribution of Curie temperatures with thicker end layers. The following can be concluded from this study:

- It was found that a layered AMR with a linear distribution of Curie temperatures whose end layers are thicker than the middle ones can perform better in terms of heating capacity for a wide range of operating temperatures in a high utilization scenario when

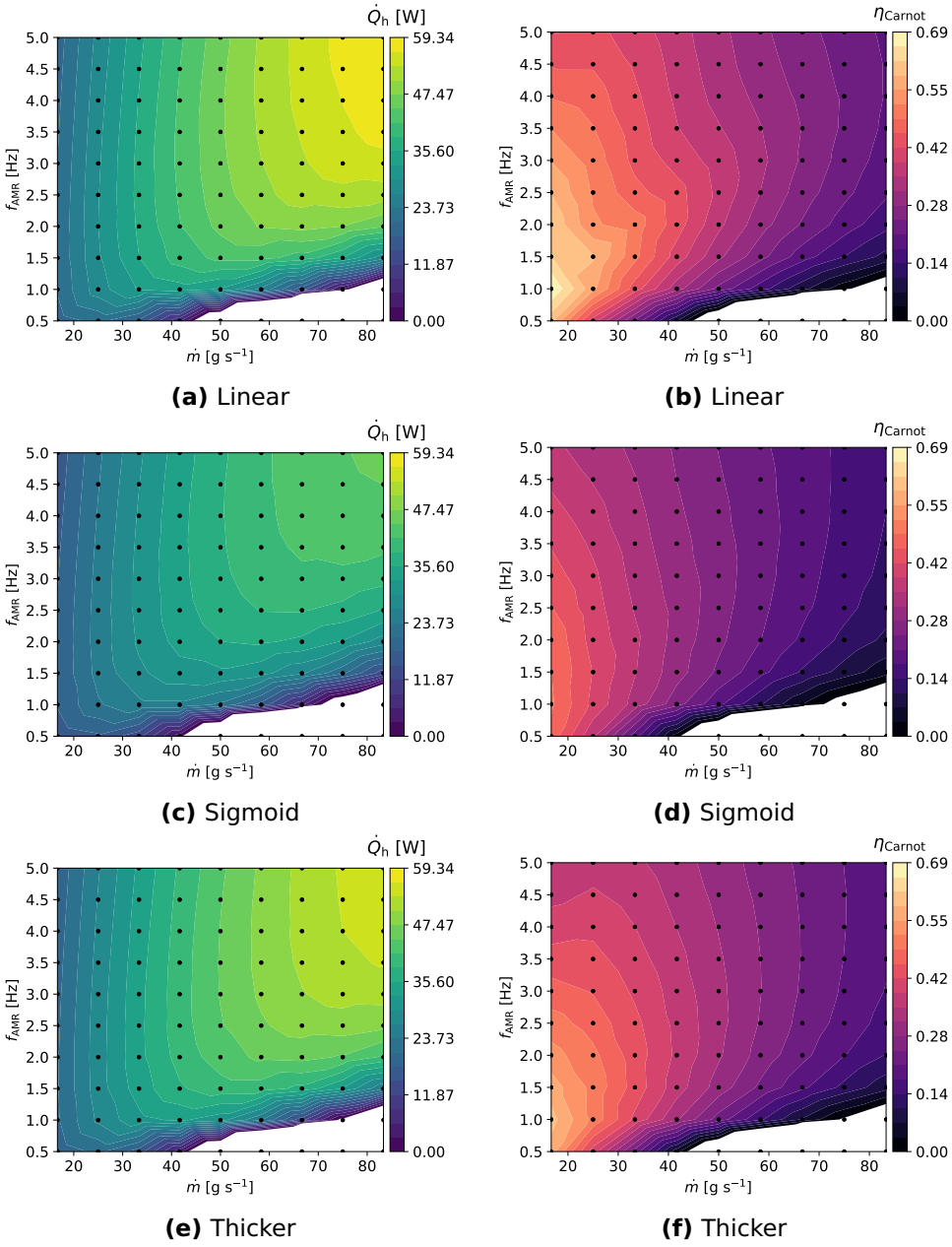

(a) Linear **(b)** Linear

(c) Sigmoid **(d)** Sigmoid

(e) Thicker **(f)** Thicker

Figure 3.14.: Heating capacities in [W] (left) and second law efficiencies (right) of the three selected layering strategies as a function of cycle frequency and flow rate for $T_{hot} = 310\,K$ and $\Delta T_{span} = 27\,K$.

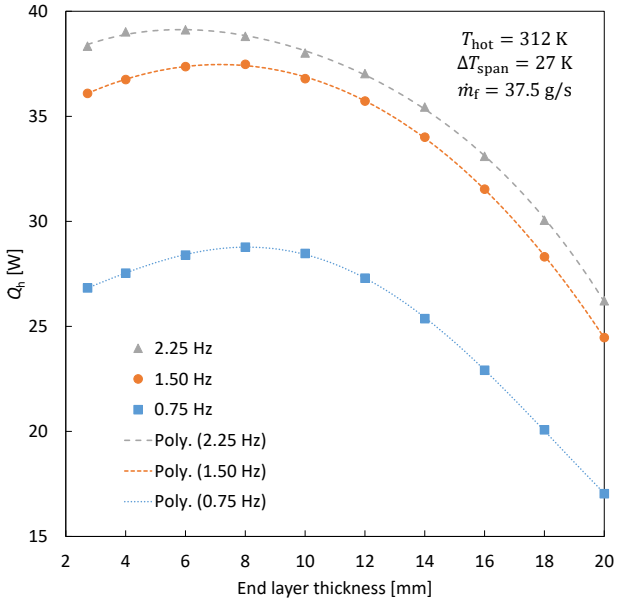

Figure 3.15.: Influence of the end layer thickness on the heating capacity of a 22-layer AMR for a fixed $\Delta T_{span} = 27$ K. Lines correspond to 4th order polynomial fits.

compared to an AMR with linear distribution of Curie temperatures and uniform layer length. This AMR is also less sensitive to changes in the hot and cold reservoir temperatures, which is advantageous given that these parameters usually fluctuate during the operation of a heat pump.

- It was also found that the optimum hot side temperature depends on the selected layering strategy (besides depending also on the operating conditions flow rate and frequency). Even though the Curie temperatures of the materials, which in this study are defined as the temperatures of the peaks of the heat capacity in zero field, range from 281 K to 308 K in all three cases, the optimum performance with temperature span 27 K, flow rate 37.5 g s^{-1}, and a frequency of 0.75 Hz is observed when the hot side temperature is 311 K, 313 K and 312 K for the AMRs with linear distribution of Curie temperatures, sigmoid distribution, and linear distribution with thicker ends respectively.
- The selected layering strategy has an influence on the shape of the temperature distributions. A linear distribution of Curie temperatures also produces a more linear solid temperature

distribution in the middle part of the AMR in comparison with the distribution of Curie temperatures that follows a sigmoid function. This applies when the operating temperature span is close to the design temperature span.

- The AMR with a linear distribution of Curie temperatures and uniform layer length outperforms the other two in terms of maximum heating capacity and second law efficiency when a wider range of flow rates and frequencies was explored for a fixed hot side temperature of 310 K and temperature span of 27 K. The heating capacity of this AMR reaches a maximum equal to approximately 59.3 W for a frequency of 5 Hz and a mass flow rate of 83.3 g s^{-1} while for the same operating conditions the AMR with a sigmoidal distribution of Curie temperatures reaches 45.1 W and the one with thicker end layers 55.5 W. The maximum second law efficiency is 69 % for the AMR with a linear distribution of Curie temperatures, and 49 % and 60 % for the AMRs with sigmoidal distribution and thicker end layers respectively. The maximum second law efficiency occurs when the mass flow rate is 16.6 g s^{-1} and frequency is 1 Hz in all three cases.

- In AMRs with thicker end layers, it was found that for a given set of operating conditions (flow rate, frequency, T_{hot}, and T_{cold}) there is an optimum length of the end layers that maximizes the heating capacity. This length tends to increase as the utilization increases.

4

SEASONAL COP OF A RESIDENTIAL MAGNETOCALORIC HEAT PUMP

The performance of a magnetocaloric heat pump (MCHP) consisting of active magnetocaloric regenerators (AMR) of 12 layers of MnFePSi magnetocaloric materials (MCM) with a linear distribution of Curie temperatures was investigated using a 1D numerical model. The model predicted the heating power and coefficient of performance (COP) of the AMR for a fixed temperature span of 27 K, between 281 K and 308 K, and variable flow rates and AMR cycle frequencies. A maximum applied magnetic field strength of 1.4 T was used. A well-insulated house with a maximum heating power demand of 3 kW (under quasi steady state conditions) was considered. Ambient temperature in the Netherlands was taken as a reference for the estimation of the seasonal heating power demand. Without optimizing the design of the AMR, the model predicts a maximum single-AMR heating power equal to 43.5 W when the AMR operates at 3 Hz and 3 L min^{-1}, and a maximum COP equal to 5.8 when it operates at 1.5 Hz and 1 L min^{-1}. Considering the maximum heating power of a single AMR, approximately 69 AMRs are needed to provide the design heating power demand of the house. It was found that it is possible to achieve an AMR seasonal COP of 5.6 by continuously adjusting the flow rate and frequency of operation of the MCHP along with the ON/OFF switching of some groups of AMRs in order to adjust the heating power of the MCHP to the heating power demand of the house.

This chapter has been published in International Journal of Refrigeration **164**, 38-48 (2024) [19].

4.1. INTRODUCTION

The International Energy Agency (IEA) estimated that by 2020 only about 10 % of the worldwide heating needs of buildings were supplied by heat pumps. The IEA also estimated that this figure has to increase to at least 20 % by 2030 in order to meet the climate goals [111]. Aligned with these ambitions, the European Union (EU) has targeted to deploy 30 million units of heat pumps between 2022 and 2030 [111] and at the same time has enforced more stringent legislation regarding the use of refrigerants with high global warming potential [56]. This is consistent with the ambitious emission reduction plans, but it also represents a challenge for manufacturers and end users. The EU is also stimulating the development of new heat pumping technologies (see for example [112]). Among the technologies that are currently under development, the magnetocaloric heat pump (MCHP) technology was classified by the US Department of Energy as one of the non-vapour compression "very promising" technologies with high energy savings potential that offers a non-energy related benefit such as noise reduction. However, it is still poorly rated regarding cost and complexity [3].

4.1.1. MAGNETOCALORIC HEAT PUMPS

MCHPs generally consist of three main elements: a porous structure of magnetocaloric material (MCM), a type of compound that exhibits a thermal response when subjected to a magnetic field change known as the magnetocaloric effect (MCE); a magnetic field source such as a permanent magnet to trigger the MCE; and a heat transfer fluid (HTF) that flows through the porous structure of MCM and through external heat exchangers transporting heat from the cold to the hot side of the heat pump in this process.

The porous structure of MCM is known as active magnetocaloric regenerator (AMR) and has the double function of regenerator and solid refrigerant. The HTF flows in a reciprocating manner in the AMR, and as a result a temperature gradient is established between the two ends of the AMR, from approximately the temperature of the cold reservoir to approximately the temperature of the hot reservoir. Consequently, the MCM in every section of the AMR undergoes a unique thermodynamic cycle in a different temperature range.

The MCE is expressed as an adiabatic temperature change or an isothermal entropy change when the material undergoes a magnetic field change. Since the MCE peaks within a narrow temperature range around the Curie temperature of the MCM in first-order materials such as LaFeSi and MnFePSi (the most promising material families for commercial MCHPs systems), it becomes necessary to use multiple of these materials in a layered bed configuration. This approach broadens

the operating temperature range of the AMR and requires that the Curie temperature of each material is closely aligned with the temperature range it experiences during cycling [53].

The magnetocaloric refrigeration cycle consists of four steps: magnetization, iso-field cooling (also known as cold-to-hot blow of HTF), demagnetization, and iso-field heating (also known as hot-to-cold blow of HTF). Depending on the synchronization between the magnetic field change and the flow of HTF, the magnetization and demagnetization processes can be adiabatic, isothermal, or somewhere in between, producing a Brayton-like cycle, an Ericsson-like cycle, or a cycle in between Brayton and Ericsson respectively [6, 7, 28]. The working principle of MCHPs and AMRs has been extensively reported, and the interested reader is referred to the work of Kitanovski et al. [6], Smith et al. [29], and Trevizoli et al. [57] for further and detailed explanation.

The magnetocaloric device described above can be used for cooling and heating applications. MCHPs and refrigerators operate under the same working principle and could be regarded as the same device just as vapor compression heat pumps and refrigerators. The use of one or the other term depends mainly on the purpose of use of the device. In general in both technologies, refrigerators and heat pumps use different refrigerants because the selection of the refrigerant(s) depends on the working temperature range of the device.

4.1.2. MCHPS FOR THE BUILT ENVIRONMENT

This study focuses on the application of the magnetocaloric technology for heating in the built environment. Johra et al. [9] proposed an MCHP system consisting of a ground-source heat exchanger (GSHEX) used as heat source, connected in a single hydraulic circuit, i.e. without intermediate heat exchangers and using a single recirculation pump, to the MCHP and to an underfloor heating (UFH) system used as heat sink. Using a GSHEX is advantageous for any type of heat pump given that the temperature of the ground is higher than ambient temperature in the coldest months of the heating season and fluctuates less throughout the year. On the other hand, an UFH system can operate at lower temperatures in comparison with radiators while providing comfort to the occupants of the house, which is also beneficial for any type of heat pump given that smaller temperature spans are linked to higher efficiencies. Another possible system configuration includes intermediate heat exchangers between the MCHP and the external heat exchangers, which has advantages and disadvantages. On the positive side, it may provide increased flexibility in the design of the GSHEX and UFH systems and higher controllability at part-load conditions in comparison with the single hydraulic loop case. For the system configuration without intermediate heat exchangers, the UFH

system and the GSHEX must be designed to manage larger flow rates and smaller fluid temperature drops compared to a normal design given that the temperature difference between outgoing and returning flows of an MCHP is usually of the order of magnitude of the adiabatic temperature change of the MCM (between 2 to 3 K). Separating the MCHP from the external heat exchangers also minimizes the risk of contamination of the HTF that flows through the AMRs. Furthermore, the HTF that flows through the MCHP needs some special additives to avoid corrosion of the MCM and freezing, so minimizing its volume is convenient. One disadvantage of the system configuration with intermediate heat exchangers is that the entropy production increases and thus the overall efficiency of the heat pump reduces.

4.1.3. CAPACITY CONTROL OF MCHPS

Part load control of heat pump systems is an issue of great importance. The main reason is that the heat pump has to be designed for peak load, but it operates most of the time at part-load conditions. MCHPs in particular have the advantage that the COP is larger at part-load conditions even when they operate at a fixed temperature span [53, 113, 114]. Therefore, a good control strategy is necessary to exploit this advantage in order to maximize their seasonal coefficient of performance (SCOP).

A few capacity control strategies have been proposed for MCHP systems, ranging from simple ON/OFF to feedback controllers. Johra et al. [9] proposed to control the capacity of an MCHP by operating at a constant cycle frequency of 1 Hz and a variable flow rate. They simulated a house of nine rooms, every one of which was equipped with an independent UFH circuit that was switched ON and OFF to maintain a desired temperature in the room. The total flow rate of the MCHP changed in discrete steps depending on the number of UFH circuits demanding warm water. When none of the UFH circuits was demanding warm water, the MCHP and the circulation pump were turned OFF. When considering a room temperature of 22 °C, an undisturbed ground temperature of 10 °C, and the Danish weather conditions for the months January to April 2013, they calculated an AMR SCOP of 3.93 and a corresponding system SCOP of 1.84. The difference between these two results originated from running a centrifugal pump far from its optimum operating region.

To reduce the difference between AMR and system SCOP, the same research group proposed later an ON / OFF control strategy whereby the MCHP was operated most of the time at the flow rate that produced the maximum COP (for the same cycle frequency of 1 Hz) and the thermal mass of the house was used to store the excess energy supplied by the heat pump. The average temperature inside the house (calculated as

the weighted average using the floor area of the rooms as weighting parameter) was allowed to fluctuate between an upper and a lower limit. When these limits were reached, the MCHP was switched OFF and ON respectively. When a particular room reached the upper temperature limit the corresponding UFH circuit was closed and the total flow rate of the MCHP decreased moving the heat pump from its optimum performance point. When considering an upper / lower limit temperature difference of 4 K and a house thermal inertia of 60 $W\,h\,K^{-1}\,m^{-2}$, they found that the system operated at least 70 % of the time at the optimum flow rate and the system SCOP increased to 3.48 [10]. The disadvantage of this strategy is that the temperature fluctuation could bring discomfort to occupants.

Qian et al. [114] proposed a feedback control system that used the AMR cycle frequency and utilization as control variables. Utilization is the ratio between the thermal mass of the fluid in a single blow and the thermal mass of the solid AMR. A proportional-integral-derivative (PID) controller determined the cycle frequency based on the assumption of a linear dependence of cooling power with AMR cycle frequency. Then, the HTF flow rate was calculated assuming a constant utilization value of 0.8 and using the frequency obtained from the PID controller. These two assumptions may not hold for all MCHP systems, but the overall control strategy offers great flexibility and allows the system to operate at a small fraction of the nominal cooling capacity with higher efficiency.

Later, Qian et al. [115] eliminated the second assumption, and, using numerical steady state simulations, they calculated the utilization value that maximizes COP for every frequency and temperature span considered in their parameter domain. Then, they used these optimum pre-calculated steady state operating points (frequency, utilization, temperature span) in the feedback loop to determine the optimum utilization value corresponding to every frequency obtained from the PID controller. An issue that we see in their approach and that was in fact causing problems in their control loop is that utilization is not a truly independent variable since it depends on flow rate as well as on frequency. So, using flow rate and frequency should be a better choice of control variables for this system.

Liang et al. [116] suggested to control the capacity of an MCHP (designed to be used as a booster heat pump in an ultra-low-temperature district heating system) by continuously modulating the cycle frequency and the mass flow rate. Using steady state numerical simulations, they mapped the performance of the MCHP in terms of COP and heating power for a fixed temperature span. The authors found that simultaneously tuning frequency and flow rate enables to reduce the heating power by 52.6 % while increasing the COP by 68 % compared to the full load condition. They also studied the effect of using the blow fraction and the offset fraction between

magnetic and fluid flow profiles as capacity control variables, but concluded that using cycle frequency and flow rate was more effective in terms of capacity reduction and efficiency increase.

Finally, Masche et al. [113] proved experimentally that it is possible to tune the capacity of an MCHP by simultaneous modulation of the cycle frequency and HTF flow rate for a constant temperature span.

4.1.4. GOAL AND ASSUMPTIONS OF THIS STUDY

The previous literature study demonstrated the technical feasibility of the application of a MCHP for the built environment. However, none of the previous studies considered MnFePSi as the base material for the MCHP. Furthermore, a research study combining the lessons mentioned above has not yet been presented to the community. Therefore, the main goal of this study is to estimate the SCOP of an MCHP based on MnFePSi that provides heat to a house using a similar system configuration as the one proposed by Johra et al. [9] and the part-load control strategy suggested by Qian et al. [115] and Liang et al. [116]. This study is based on the following assumptions:

- It is assumed that the MCHP operates at a fixed temperature span, which is important for the activation of all layers in a layered AMR. This is approximately feasible for the adopted system configuration since the ground temperature is unaffected by ambient temperature fluctuations at depths below 10 m. However, ground temperature decreases over the heating season due to depletion of the geothermal reservoir [117].

- AMR SCOP will be primarily reported rather than system SCOP given that only the AMR is modelled and therefore only intrinsic AMR power consumption is calculated. However, a system SCOP can be estimated by considering representative motor and drive train efficiencies as it will be shown.

- Since the attention is on the AMR performance, it is assumed that the external heat exchangers work as efficiently at part-load conditions as in full load operation. Further research is conducted at the moment to size these heat exchangers for a proper operation under off-design conditions.

- A well insulated house is assumed for the estimation of the heating power demand.

- Ambient temperature in the Netherlands in the heating season of years 2009/2010 is used as a reference for the estimation of the heating power demand [118].

4.2. METHODS

For the estimation of the SCOP of an MCHP, we first mapped the performance of an AMR in terms of COP and heating power as a function of HTF flow rate and AMR cycle frequency for a fixed temperature span using a 1D numerical model. We used a modified version of the model implemented by Christiaanse [90], which is documented in references [105, 106]. This model, as all one-dimensional models, departs from the following general assumptions [91]:

- In any cross sectional area of the AMR, the fluid velocity, the distribution of MCM, the magnetic field, and the fluid and solid temperatures are uniform.
- Only heat transfer by convection occurs between solid and fluid.
- The HTF remains in the liquid phase.

4.2.1. GOVERNING EQUATIONS

The governing equations of the model, Equation 4.1 and Equation 4.2, correspond to the energy balance of the fluid and solid domains of the AMR respectively. The fluid energy conservation equation considers the following physical phenomena from left to right: thermal energy storage, enthalpy transfer, axial diffusion, viscous dissipation, heat leaks from / to the environment, and heat transfer with the solid. On the other hand, as pointed out by Lei [30], in the absence of irreversibilities the first two terms (inside parenthesis) on the left hand side of the solid energy conservation equation, Equation 4.2, are equivalent to energy storage and magnetic work. The second term on the left hand side of Equation 4.2 corresponds to diffusion in the solid phase, and the term on the right hand side is again the heat exchange between fluid and solid that couples the two equations.

4.2.2. CONSTITUTIVE EQUATIONS

Constitutive equations were chosen assuming that the AMR consists of a packed bed of spherical particles. The Ergun equation was used for the calculation of viscous losses [104]. The heat transfer coefficient for the heat exchange between fluid and solid was calculated using a correlation derived by Macias-Machin et al. [98]. This heat transfer coefficient was multiplied by a degradation factor to account for temperature gradients inside the spherical particles, as proposed by Engelbrecht et al. [102]. The diffusion in the liquid phase was calculated using an effective thermal conductivity, $k_{f,eff}$ [119]. The diffusion in the solid phase was calculated considering an effective thermal

$$\rho_f c_f A_{cs} \varepsilon \frac{\partial T_f}{\partial t} + \dot{m} \frac{\partial}{\partial x}(c_f T_f) - \frac{\partial}{\partial x}\left(k_{f,\text{eff}} A_{cs} \varepsilon \frac{\partial T_f}{\partial x}\right) = \left|\frac{\dot{m}}{\rho_f}\frac{\partial P}{\partial x}\right| + \dot{Q}_{amb} + A_{cs}\beta h(T_s - T_f) \tag{4.1}$$

$$\rho_s A_{cs}(1-\varepsilon)\left(c_s \frac{\partial T_s}{\partial t} + T_s\left(\frac{\partial s}{\partial B}\right)_{T_s}\frac{\partial B}{\partial t}\right) - \frac{\partial}{\partial x}\left(k_{s,\text{eff}} A_{cs}(1-\varepsilon)\frac{\partial T_s}{\partial x}\right) = A_{cs}\beta h(T_f - T_s) \tag{4.2}$$

conductivity, $k_{s,\text{eff}}$, using an equation proposed by Hadley [103] to account for the presence of the fluid in the spaces between the solid particles.

4.2.3. MAGNETOCALORIC MATERIALS

The MnFePSi family of MCMs was considered for this study. As the MCE peaks in a somewhat narrow temperature range in these materials (because they are first order MCMs), it is necessary to implement a layered AMR configuration, whereby materials with slightly different compositions and Curie temperatures are stacked one after another in the flow direction. Ideally, there should be a continuous change in Curie temperature along the AMR covering the temperature range of the MCHP to maximize the MCE at every axial position, which is analogous to use an infinite number of layers. However, this is still difficult to achieve in practice, and numerical simulations have also indicated that only a small number of layers is enough to achieve a performance comparable to that of a quasi-continuous layered AMR [70].

In an unpublished study, we also performed numerical simulations to determine the number of layers necessary to maximize the heating power of a layered AMR based on MnFePSi. We departed from the properties of the $Mn_{1.18}Fe_{0.73}P_{0.48}Si_{0.52}$ compound (see reference [90]), the Curie temperature of which, given by the peak of the zero-field heat capacity, is approximately 293 K. Some relevant properties of this material are presented in Figure 4.1. Then, we obtained the properties of the other materials in the simulated layered AMRs by shifting the properties of this base material to different Curie temperatures, i.e. the size and shape of the peaks (heat capacity, ΔT_{ad}, and Δs_m) of each material in the simulated AMRs is the same but the

temperature at which these peaks occur is different. We also considered an uniform layer length and a linear distribution of Curie temperatures for these AMRs.

We concluded that under these considerations the heating power only increases marginally when the number of layers grows beyond 12. Therefore, we use an AMR of 12 layers in the present study. The peaks of the in-field heat capacity of these 12 MCMs span from 281 K to 308 K, the cold and hot reservoir temperatures of the heat pump respectively.

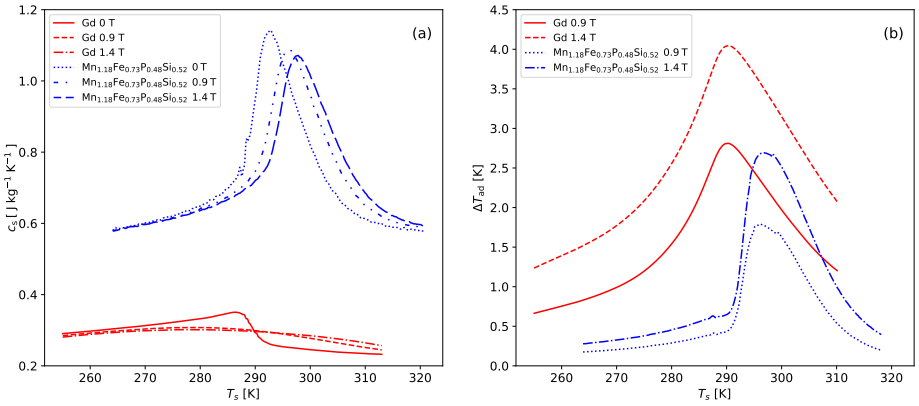

Figure 4.1.: Specific heat capacity (a) and adiabatic temperature change (b) of $Mn_{1.18}Fe_{0.73}P_{0.48}Si_{0.52}$ compared to those of Gd. Only heating curves are shown for the MnFePSi material.

4.2.4. SELECTED GEOMETRY

The main geometric parameters concerning the AMR used in the simulations are summarized in Table 4.1. The overall dimensions of this AMR coincide with the dimensions of the AMRs installed in the FAME cooler, the MCHP prototype developed by the Fundamental Aspects of Materials and Energy (FAME) group at TU Delft [26].

Table 4.1.: Geometric parameters used in the simulated AMR.

Parameter	Value	Units
AMR W x H x L	45 x 13 x 60	mm x mm x mm
Porosity (ε)	0.36	—
Particle diameter	300	μm

4.2.5. MAGNETIC FIELD AND FLUID FLOW PROFILES

The magnetic field and fluid flow profiles used in the simulations of this study are illustrated in Figure 4.2. The magnetic field and fluid flow profiles are specific for every type of MCHP device and depend on the type of magnet and hydraulic circuit considered in the design of the MCHP. The shape of these profiles and their mutual synchronization determine the type of thermodynamic cycle that the MCMs undergo in the device [7]. For the profiles presented in Figure 4.2, the attainable thermodynamic cycles are close to Brayton-like cycles.

These profiles are typical of devices using C-shaped, rotating magnets and rotating pumps such as the ones described in references [23, 26, 120]. A maximum applied magnetic field strength of 1.4 T was selected to guarantee an adiabatic temperature change of more than 2 K for the selected MCM. This is also approximately the magnetic field strength of several pre-commercial prototypes (see for example references [62] and [23]) and is closely related to the remanence of NdFeB, grade N50 magnets.

It is important to mention here that the blow fraction, defined as the ratio between the time the valves are open to flow in one direction and the cycle period, is the same for all simulations presented in this study. The blow fraction depends on the flow profile, but it is independent on the cycle frequency and maximum flow rate. The actual blow time does depend on cycle frequency. On the other hand, the volume displaced per blow process depends on the cycle frequency, maximum flow rate, and flow profile, and it corresponds to the area under the flow rate vs time profile. Some recent publications have considered the influence of flow profile on AMR performance as research topic [107, 121, 122].

4.2.6. PERFORMANCE METRICS

The performance of the MCHP was evaluated in terms of the AMR heating power, calculated using Equation 4.3, and AMR COP, calculated using Equation 4.4. The AMR cooling power was calculated using Equation 4.5.

$$\dot{Q}_{\mathrm{h}} = \frac{1}{\tau}\int_0^{\tau} \dot{m} c_{\mathrm{f}} (T_{f,x=L} - T_{\mathrm{h}})\,\mathrm{d}t \tag{4.3}$$

$$COP = \frac{\dot{Q}_{\mathrm{h}}}{\dot{Q}_{\mathrm{h}} + \dot{Q}_{\mathrm{amb}} - \dot{Q}_{\mathrm{c}}} \tag{4.4}$$

$$\dot{Q}_{\mathrm{c}} = \frac{1}{\tau}\int_0^{\tau} \dot{m} c_{\mathrm{f}} (T_{\mathrm{c}} - T_{f,x=0})\,\mathrm{d}t \tag{4.5}$$

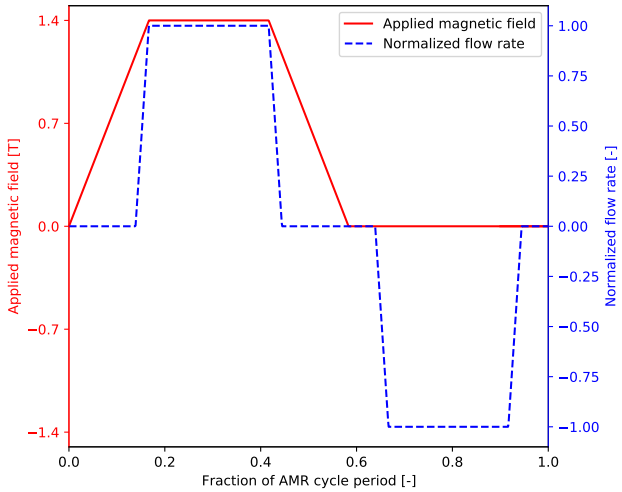

Figure 4.2.: Magnetic field and fluid flow profiles. These profiles resemble those of a C-shaped, rotating-magnet MCHP such as the one described in [26].

4.2.7. SOLUTION, IMPLEMENTATION, AND VALIDATION

The governing equations were integrated using the finite difference method. The enthalpy term (also called advection by some authors) was discretized following an implicit upwind scheme. The diffusion terms were discretized using central difference in space and Crank-Nicolson in time. The solution of the system of algebraic equations for every time step is performed using the tridiagonal matrix algorithm. The model was implemented in Python. We validated the model with experimental data of a single AMR magnetocaloric refrigeration device that uses Gd as MCM (see reference [16]) and obtained good agreement between experimental and numerical results (see Appendix B). The original developers also validated the model with experiments of AMRs using two layers of MnFePSi [82].

4.3. RESULTS AND DISCUSSION

4.3.1. HEATING POWER DEMAND

The calculation of the SCOP of a heat pump requires the definition of the part load heating demand. To do this, we follow a procedure similar to the one used in the European standard EN-14825:2022, “Air conditioners, liquid chilling packages and heat pumps, with electrically driven compressors, for space heating and cooling, commercial and process cooling - Testing and rating at part load conditions and

calculation of seasonal performance". We adopted the average design (outdoor) and indoor temperatures of the EN-14825:2022, −10 °C and 20 °C respectively [123]. At the design point, we assume that the heat pump unit has to deliver a heating power of 3 kW. The heating requirement of a Dutch terrace house built between 2015 and 2018 with improved insulation in windows and doors and improved infiltration sealing is 46.8 $kWhm^{-2}$ per year [124]. These houses are typically 117 m^2 [124]. The heating system operates under average conditions 2066 h according to the EN-14825:2022. This gives an average heating power requirement of 2.65 kW, which indicates that our assumption is conservative. On the other hand, the EN-14825:2022 also considers a linear relationship between part-load heating demand and outdoor temperature. Following this, we consider a linear relationship between heating power demand and outdoor temperature by using Equation 4.6.

$$\dot{Q}_{\mathrm{h}}(t) = UA(T_{\mathrm{room}} - T_{\mathrm{out}}(t)) \tag{4.6}$$

The value of UA is assumed constant and is calculated at the design point where the heating power demand is 3 kW and the outdoor-indoor temperature difference is 30 K, so UA is equal to 100 WK^{-1}. The UA value of the Dutch house taken as a reference above is 68.62 WK^{-1}, which results from the sum of the products of the U value (overall heat transfer coefficient) of the different building-envelope elements (such as external walls, roof, ground floor, windows, doors) times their corresponding areas [124]. The value that we obtained, 100 WK^{-1}, is therefore conservative as well. The difference can account for the extra load due to the ventilation/infiltration minus the internal heat gains. Ambient temperature in the Netherlands during the heating season of the years 2009/2010 was used as $T_{\mathrm{out}}(t)$ [118]. The heating season in the Netherlands is assumed here between the 16th of September to the 15th of May.

Figure 4.3a shows the hourly and daily average heating power demand calculated using this approach. Figure 4.3b shows, on the other hand, the distribution of heating power demand values. From Figure 4.3b, it is clear that the frequency of occurrence of the design heating power demand is very low and that the heating device has to operate most of the time at part-load conditions. For the calculation of the SCOP presented in subsection 4.3.5, we excluded the hours in which $T_{\mathrm{out}} > 18$ °C (104 hours for the heating season of the years 2009/2010), for which the heating power demand is below 200 W according to Equation 4.6. During the heating season under consideration, T_{out} was always larger than −10 °C, so the calculated heating power demand values are always below 3 kW.

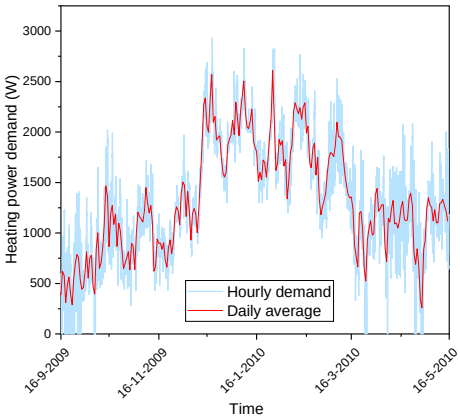

(a) Heating power demand profile

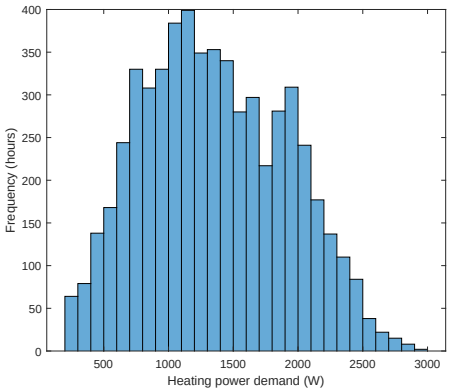

(b) Heating power demand distribution

Figure 4.3.: Heating power demand of a well insulated house characterized by $UA = 100\,\mathrm{W\,K^{-1}}$. Ambient temperature of the Netherlands in the heating season 2009/2010 is taken as a reference. Room temperature, T_{room}, is set to 20 °C.

4.3.2. AMR PERFORMANCE MAPS

The heating power and COP developed by a 12-layer MnFePSi AMR as a function of AMR cycle frequency and fluid flow rate are shown in Figure 4.4a and Figure 4.4b respectively. A fixed temperature span of 27 K with $T_c = 281\,\mathrm{K}$ and $T_h = 308\,\mathrm{K}$ was considered here. As shown in Figure 4.4a, the maximum heating power that a single AMR can develop in the explored parameter space occurs in the upper limits of the range, $3\,\mathrm{L\,min^{-1}}$ and 3 Hz, and is about 43.5 W. Assuming that this is the design operating point, as many as 69 AMRs would be needed to supply the design heating power demand of 3 kW.

Furthermore, taking into account that the mass of one AMR is approximately 137 g (considering a material density of $6100\,\mathrm{kg\,m^{-3}}$), the specific heating power of this AMR in the design point is approximately $318\,\mathrm{W\,kg^{-1}}$, which is in good agreement with the findings of Lei et al. [70]. The total mass of MCM needed is approximately 9.4 kg. On the other hand, the maximum COP of this AMR in the explored parameter space is approximately 5.8 and peaks at $1\,\mathrm{L\,min^{-1}}$, 1.5 Hz, where the heating power is only about 21 W. This trend is in agreement with the findings of other authors (see for example reference [116]). As suggested by Qian et al. [114], the fact that the AMR works more efficiently at part-load conditions can be exploited to increase the SCOP of an MCHP.

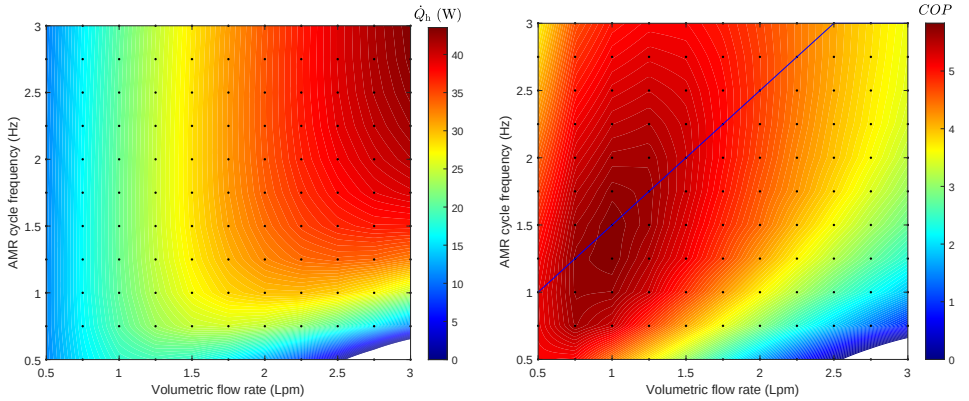

(a) Heating power [W] **(b)** COP

Figure 4.4.: Heating power (a) and COP (b) as a function of volumetric flow rate [Lpm] and AMR cycle frequency [Hz] of a single 12-layer MnFePSi AMR. $\Delta T_{span} = 27\,K$. Black dots correspond to the simulated points. The blue line joints the points where COP is maximum for every flow rate.

4.3.3. PART LOAD CONTROL STRATEGY

The performance maps shown in figures 4.4a and 4.4b are the base for the calculation of the SCOP for any part-load control strategy to be considered [115]. As Liang et al. [116] pointed out, the capacity of the AMR could be controlled by modulating only the flow rate and keeping frequency at maximum. Likewise, the heating power could also be controlled by fixing the flow rate at maximum and modulating frequency. However, none of these two paths leads to an optimum performance. Instead, a path that follows the operating points of maximum COP for every heating power could be chosen [115, 116].

The blue line in Figure 4.4b joints the points of maximum COP for every flow rate considered in the simulated parameter space. Figure 4.5 also shows the values of the maximum COP calculated for every flow rate considered in the parameter space along with the corresponding frequency and heating power. Following this path of frequencies, the heating power of a single AMR increases monotonically with flow rate from approximately 11.7 W at $0.5\,L\,min^{-1}$ to approximately 43.5 W at $3\,L\,min^{-1}$. COP first increases from 5.2 to 5.8 for flow rates between $0.5\,L\,min^{-1}$ and $1.0\,L\,min^{-1}$ and then decreases monotonically with flow rate to reach a minimum value of 3.6 at $3\,L\,min^{-1}$.

As mentioned above, for the selected geometry at least as many as 69 AMRs are necessary to satisfy the design heating power demand of 3 kW. If all 69 AMRs operate simultaneously, it is only possible to reduce the

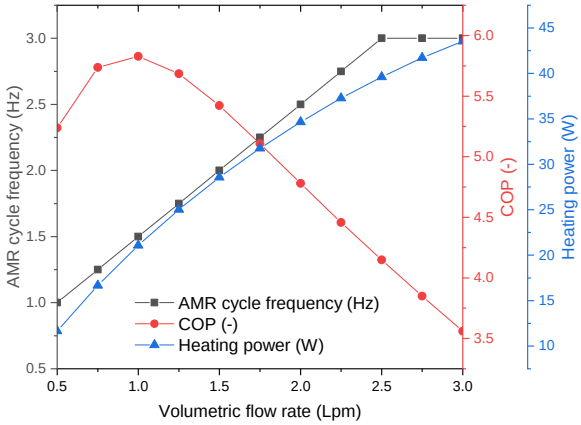

Figure 4.5.: Maximum COP calculated for every simulated flow rate and the corresponding frequency and heating power

heating power down to 805 W by reducing the flow rate and AMR cycle frequency to the minimum values presented in Figure 4.5. Flow rate and cycle frequency could be further reduced in theory to reach the minimum heating power demand of 200 W considered in this study, but in practice this is discouraged because reducing the speed of an electrical motor is in general inefficient.

Using a large number of AMRs offers an additional degree of freedom for the control of the capacity of the MCHP since the AMRs can be arranged in groups or modules each with an independent magnet and valve system that could be switched OFF as the heating power demand decreases. In this way the heating power of the MCHP could be further reduced below 805 W and down to 200 W.

4.3.4. MODULARIZATION STRATEGY

A large number of AMRs (such as 69) could be impractical to implement in a single-magnet configuration, and thus one of the options to obtain a simpler system could be to increase the mass of each AMR to reduce the total number. However, the optimization of the design of the AMRs was out of the scope of this study. The optimization of the dimensions of the AMR must be done in connection with the optimization of the design of the magnet assembly because the shape of the AMR is constrained by the dimensions of the air gap of the magnet. An example of such optimization process is presented in [55]. These researchers used an evolutionary algorithm for the simultaneous optimization of the design of the magnet and AMRs. In our case, we decided to use the dimensions of the AMRs installed in the FAME cooler [26].

Another option for the implementation of a MCHP that uses several kilograms of MCM is to split the system in independent modules each with its own magnet and valve system. We selected this approach. We propose to split the system in 2 modules of 27 AMRs each plus one module of 15 AMRs. A subsystem of 27 AMRs is easier to achieve from a practical perspective compared to a single-magnet system that drives 69 AMRs.

Several examples of multi-bed AMR devices can be found in literature, some of which are summarized in Table 4.2. Single modules could follow the design of any of these prototypes, but the configurations that use magnetic assemblies with either concentric Halbach cylinders or magnetic rotor and iron stator with the AMRs placed in an annular space between inner and outer elements of the magnet assembly are more suitable to accommodate a large number of AMRs. The prototype developed by Engelbrecht et al. [125] specially demonstrates that the implementation of a multi-bed system with 27 AMRs is technically feasible. Furthermore, it has also been shown that using an odd and large number of AMRs leads to a minimum torque [126], which justifies the use of 27 AMRs. It is also important to highlight that the mass of the AMRs that we are considering in this study, 137 g, is of the same order of magnitude of the AMRs installed in the prototypes presented in Table 4.2. Nevertheless, the design of a real MCHP requires in any case the simultaneous optimization of the design of the AMR and magnet assembly.

Table 4.2.: Some multi-bed MCHP systems developed in the last 15 years. The mass of the AMRs and the number of AMRs is presented

Ref.	N AMRs	AMR mass [g]	MCM	AMR Configuration	Magnet type
[26]	7	169	Gd spheres	Flat disc	Rotating C-shape
[120]	8	150	Gd spheres	Flat disc	Rotating C-shape
[21]	8	168	Gd particles	Cylinder	Rotating magnetic ring and iron core
[65]	11	154	Gd and GdY	Cylinder	Rotating magnetic ring and iron core
[62]	12	127	LaFeSiH particles	Unknown	Unknown
[23]	13	262	LaFeMnSiH particles	Flat disc	Rotating magnet
[127]	16	106	Gd spheres	Cylinder	Magnetic rotor and iron stator
[125]	24	117	Gd spheres	Rotating Cylinder	Concentric Halbach cylinders

In practice, this modularization strategy could be achieved by using

three independent subsystems, each with its own magnet assembly, motor, and valve and fluid distribution/collection structure. The independent magnet assemblies could also share the same shaft in order to enable the use of a single motor to drive the whole system. If this is the case, the activation and deactivation of a module could be done using a clutch between the rotating part of each magnet assembly and the common shaft.

4.3.5. SEASONAL COP

The SCOP was calculated based on the predefined operating points presented in Figure 4.5 and considering the profile of the heating power demand shown in Figure 4.3. The modularization strategy introduced in subsection 4.3.4 was implemented in order to have an additional degree of freedom for the part-load capacity control of the MCHP. The SCOP depends on this modularization strategy (number of modules and number of AMRs per module) because for any given heating power demand value the operating point of the AMRs, and thus their COP, depends on the number of operating AMRs.

To explain the calculation procedure, let us consider the MCHP system consisting of 3 modules, one of 15 AMRs (module A), and two of 27 AMRs each (modules B and C). With these modules it is possible to operate the MCHP with the following number of AMRs: 15, 27, 42, 54, or 69, corresponding to the operation of modules A, B (or C), A+B (or A+C), B+C, and A+B+C respectively. Then, for every heating power demand value, we first determine the minimum and maximum number of AMRs that must and could be in operation to supply the amount of heat under consideration. For example, a heating power demand of 550 W could be supplied using 15, 27, or 42 AMRs, in which cases every AMR would supply 36.7 W, 20.4 W, and 13.1 W respectively. The combination of modules corresponding to 54 AMRs cannot supply less than 629.9 W, so it cannot be considered for this heating power demand of 550 W. With these single-AMR heating capacities we obtain the cycle frequency, flow rate, and COP based on a piece-wise linear interpolation of the curves presented in Figure 4.5. Using this approach for the present example, the COP values would be 4.5, 5.8, and 5.4 respectively. Therefore, for a heating power demand of 550 W, it is more efficient to operate with 27 AMRs since a higher COP is attainable. The same process is repeated for every heating power demand value in the range from 200 W to 3000 W using steps of 10 W, which gives a total of 281 values. These correspond to the heating power demand values obtained from the approach used to calculate part-load heating power demand described in subsection 4.3.1.

Figure 4.6 shows the COP, AMR cycle frequency, and total volumetric flow rate obtained when following the calculation process described

above for all considered heating power demand values. The total volumetric flow rate was calculated by multiplying the flow rate of a single AMR times the number of active AMRs times the blow fraction considered in this study, which is approximately equal to 28 % (see Figure 4.2). The discontinuities appreciable in Figure 4.6 are due to the ON/OFF switching of AMR modules. It is relevant to mention that an automatic control of the MCHP will use flow rate as main control variable because it can be easily measured and because, as already mentioned, the capacity of an UFH system and a GSHEX can also be controlled by modulating the flow rate.

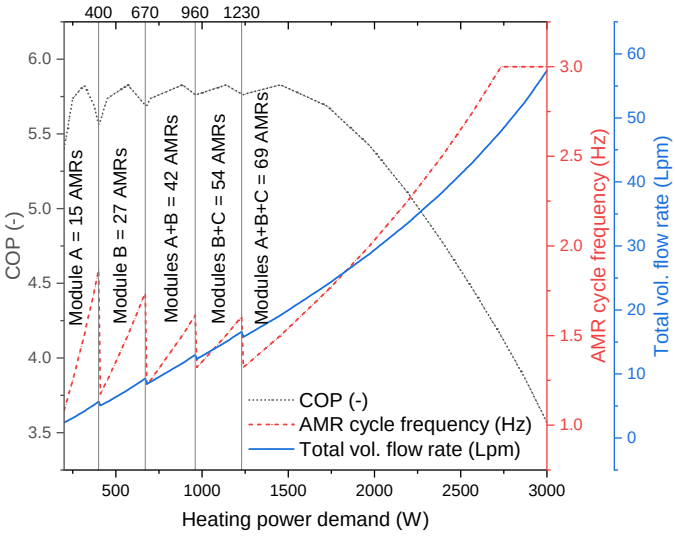

Figure 4.6.: COP, AMR cycle frequency and total volumetric flow rate as a function of total heating power demand for an MCHP with 3 modules, one module of 15 AMRs and two modules of 27 AMRs each.

The SCOP is calculated as the weighted average of the COP values using the number of hours that every heating power demand value (or outdoor temperature) occurs as the weighting factor.

The distribution of COPs is shown in Figure 4.7, and the calculated AMR SCOP is equal to 5.6 in this case. Figure 4.8 shows the distribution of hours that the modules or combination of modules of AMRs would be in operation. It is clear that most of the time all modules operate, 3115 h, corresponding to heating power demand values above 1230 W. On the contrary, the MCHP operates with just 15 AMRs only 151 h, corresponding to heating power demand values below 400 W. A system SCOP can be estimated by considering representative efficiencies of motors and drive trains as proposed by Masche et al. [113]. If medium-efficiency equipment is taken into consideration, an overall

equipment efficiency of 80 % could be assumed [113], and the estimated system SCOP would be 4.5.

4.3.6. INFLUENCE OF NUMBER OF MODULES AND AMRS PER MODULE

The SCOP obtained using several combinations of AMRs per module and number of modules are presented in Table 4.3. Here only odd numbers of AMRs per module are used, which limits the possible combinations. As can be seen in Table 4.3, the total number of AMRs was varied from 69 to 78. From this, it is possible to see a trend towards slightly higher SCOP values when larger numbers of AMRs are used. This comes from the fact that by using more AMRs the MCHP is a bit oversized, and thus in the high overall heating power demand range the AMRs do not have to operate near the point of maximum heating power, which coincides with the point of minimum COP. However, an increase of 13 % of the number of AMRs only produces and increase of 3.6 % of the SCOP. Thus, the enhancement is just marginal.

On the other hand, several numbers of modules were also tested for the same total number of AMRs. This allows to observe a trend towards higher SCOP values when more modules are used. For example, when using 70 AMRs divided in two modules, one of 15 and one of 55 AMRs, the SCOP is 5.5, but if the 70 AMRs are divided in 4 modules, one of 13 AMRs and three of 19 AMRs each, the SCOP is 5.6. This is due to the fact that in the low overall heating power demand range (below 1000 W) the heating power per AMR remains around the values for which the COP is maximum when the number of available AMRs increases progressively, e.g. from 13, to 32, to 38, and so on (see Table 4.3 row 6). On the contrary, when there is a large gap in the number of available AMRs, e.g. from 15 to 55, the heating power per AMR has to increase to the upper limit where the COP is lower.

From Table 4.3 it is also clear that the SCOP has a weak dependence on the number of modules and number of AMRs per module. This is related to the fact that the MCHP operates most of the time with all available AMRs as can be seen for example in Figure 4.8. So, the modularization is mainly important for enabling the operation of the MCHP at low heating capacities. This suggests that the number of modules could be chosen following practical design reasons rather than performance reasons.

4.4. CONCLUSIONS

This study presents the calculation of the AMR SCOP of an MCHP for the built environment based on the MnFePSi material. A 12-layer AMR configuration with a linear distribution of Curie temperatures and uniform layer lengths was considered. A packed bed of spheres of 300 µm in diameter, 36 % porosity, and overall dimensions

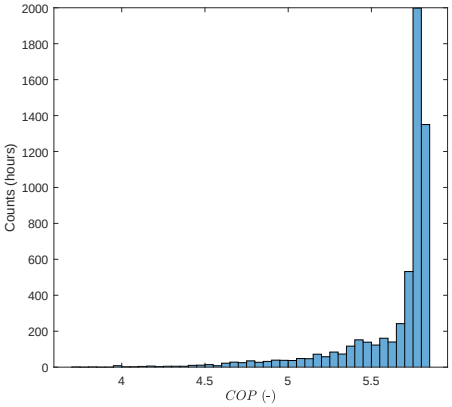

Figure 4.7.: Distribution of COPs for the heating season of the years 2009/2010 obtained when using modulation of flow rate and frequency as well as ON/OFF switching of modules of AMRs to control the capacity of the MCHP. The mean of this distribution is the seasonal COP, SCOP = 5.6

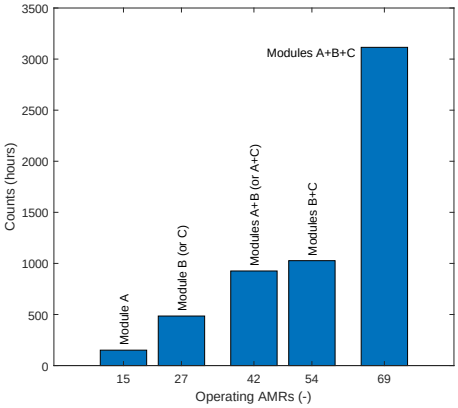

Figure 4.8.: Distribution of operating AMRs for the heating season of the years 2009/2010. The 5 possible combinations of the three selected modules (module A of 15 AMRs, module B and C of 27 AMRs) are shown in this figure.

$WxHxL$ = 45x13x60 mm^3 was assumed. A maximum applied magnetic field strength of 1.4 T was considered as well as trapezoidal magnetic and fluid flow profiles.

First, the performance of a single AMR was mapped using a 1D numerical model, i.e. the heating power and AMR COP was calculated for a fixed temperature span of 27 K and variable flow rate and AMR

Table 4.3.: SCOPs of different combinations of number of modules and AMRs per module.

Number of AMRs	Number of modules	AMRs per module	Operating AMRs by combination of modules	SCOP
70	2	[15, 55]	[15, 55, 70]	5.5
72	2	[17, 55]	[17, 55, 72]	5.6
69	3	[11, 29, 29]	[11, 29, 40, 58, 69]	5.6
69	3	[15, 27, 27]	[15, 27, 42, 54, 69]	5.6
71	3	[13, 29, 29]	[13, 29, 42, 58, 71]	5.7
70	4	[13, 19, 19, 19]	[13, 32, 38, 51, 57, 70]	5.6
72	4	[15, 19, 19, 19]	[15, 34, 38, 53, 57, 72]	5.7
75	5	[15, 15, 15, 15, 15]	[15, 30, 45, 60, 75]	5.7
77	7	[11, 11, 11, 11, 11, 11, 11]	[11, 22, 33, 44, 55, 66 77]	5.7
78	6	[13, 13, 13, 13, 13, 13]	[13, 26, 39, 52, 65, 78]	5.7

cycle frequency. Then, for every simulated flow rate value, the frequency that maximizes the COP and the corresponding heating power were found. In this way, it is possible to modulate the heating power of a single AMR from 11.66 W to 43.53 W following an optimum COP path by simultaneously changing the flow rate from 0.5 L min^{-1} to 3 L min^{-1} and the AMR cycle frequency from 1 Hz to 3 Hz. At least 69 AMRs are necessary to provide the design heating power demand of 3 kW considering the maximum heating power of a single AMR.

Ambient temperature data of the Netherlands in the heating season of the years 2009/2010 were used to obtain a time dependent distribution of heating power demand values assuming a linear relationship between the heating power demand and outdoor temperature and a constant overall heat transfer coefficient and heat transfer area of the house, $UA = 100\,\mathrm{W\,K^{-1}}$. The pre-calculated optimum operating points were taken as a basis for the calculation of the SCOP.

A modularization strategy was proposed to have an additional degree of freedom for controlling the capacity of the MCHP and enabling the reduction of the capacity of the MCHP to a minimum of 200 W. When considering the use of one module of 15 AMRs and two modules of 27 AMRs, the calculated AMR SCOP for the heating season of the years 2009/2010 is 5.6. If an efficiency of 80 % is considered for motors and drive systems, an estimated system SCOP of 4.5 is obtained.

The main conclusions that can be drawn from this study are:

- The heating power capacity of a MCHP can be controlled efficiently by simultaneous modulation of the flow rate and AMR cycle frequency.
- Dividing a large MCHP system into modules is not only a wise solution from a practical perspective but also it is convenient to enable the reduction of the capacity of the heat pump to very small values. The overall heating power of the MCHP can be reduced efficiently to less than 10 % of the design heating power by dividing the MCHP in modules, one of which should have a small number of AMRs to match the small heating power demand range.
- Flow rate is the preferred control variable in a MCHP system given that it is easy to measure for the implementation of a feedback control loop and given that the heating power of the MCHP and the UFH system and the heat transfer rate of the GSHEX can be modulated with this variable. AMR cycle frequency can be obtained from pre-calculated performance data so that the only control variable is the flow rate.
- Using an MCHP with a maximum heating power larger than the design heating power demand favours the SCOP given that the MCHP operates less hours at operating points where the COP is smaller.
- The SCOP has a weak dependence on the number of modules and number of AMRs per module. This has to do with the fact that the MCHP operates with all available AMRs from medium to high heating power demand values, and most of the time in the heating season the heating power demand is in this range.

Furthermore, it is likely that by optimizing their design a fewer number of AMRs are needed to provide the same overall heating power demand. However, the modularization strategy should still be implemented in order to have greater flexibility in the control of the capacity of the MCHP to cover the full range of heating power demand values and to maximize the SCOP. Finally, a proper selection of pumps and motors as well as an efficient control of these devices is important to obtain a high system SCOP. Future work will include the validation of the performance predicted by the model using layered MnFePSi AMRs in the FAME cooler. Furthermore, the off-design performance of external heat exchangers should also be a matter of investigation. It is important to determine what is the most suitable design of an UFH system and a GSHEX for a proper operation in combination with a MCHP in a single hydraulic circuit given the wide range of flow rates at which the MCHP operates.

5

PRESSURE DROP AND HEAT TRANSFER CHARACTERIZATION OF ACTIVE MAGNETOCALORIC REGENERATORS PRODUCED BY EXTRUSION-BASED ADDITIVE MANUFACTURING

5.1. INTRODUCTION

As introduced earlier in this thesis, most existing AMR models rely on closure relationships, also known as constitutive equations, to estimate pressure drop, heat transfer, effective thermal conductivity of the solid matrix, and fluid dispersion. Reliable predictions of AMR performance strongly depend on the accuracy of the heat transfer coefficient and pressure drop correlations. Overestimating the heat transfer coefficient can lead to an overestimation of the AMR cooling or heating capacity and the coefficient of performance (*COP*). Similarly, accurately estimating pressure drop is essential for a reliable *COP* evaluation, as a significant portion of the energy input in a magnetocaloric heat pump (MCHP) corresponds to pumping power.

Some of the geometries used in AMRs, particularly packed beds of particles and parallel plates, are also widely utilized in other industrial applications and have been extensively studied. Consequently, well-established closure relationships for these geometries are readily available in the literature. However, alternative geometries, especially those developed using additive manufacturing techniques, require

thorough investigation to characterize their flow and heat transfer performance. Developing accurate correlations for these geometries is critical to ensure reliable AMR performance predictions using existing numerical models.

Magneto B.V. developed an extrusion-based additive manufacturing technique for the production of MnFePSi active magnetocaloric regenerators (AMRs). The process involves mixing inactive magnetocaloric material (MCM) powders with an organic binder to form a paste suitable for extrusion through a nozzle. Layers of parallel fibers are then printed with controlled spacing between them, with each successive layer oriented at an alternating angle to create a porous block structure. The resulting green body is then subjected to a specialized heat treatment to remove the binder and sinter the remaining solids, thereby activating the material.

The resulting geometry resembles the cross-rod matrices studied by London et al. [128], who analyzed the pressure drop and heat transfer characteristics of such matrices with void fractions ranging from 50 % to 85% and rod diameters of approximately 8 mm. However, Magneto's design features significantly smaller fiber diameters and lower void fractions than those examined in [128]. In addition, unlike the earlier matrices, the rods in adjacent layers of Magneto's blocks slightly overlap and are fused together at their contact points. Moreover, the typical range of Reynolds numbers found in AMRs falls outside the range of Reynolds numbers tested in the earlier study.

Consequently, it is crucial to characterize the pressure drop and heat transfer behavior of Magneto's geometry to assess its suitability for magnetocaloric applications. Additionally, accurate correlations for predicting heat transfer and pressure drop are urgently needed to enable reliable AMR performance prediction through numerical simulations. This chapter summarizes the efforts undertaken to address these needs.

5.1.1. MANUFACTURING AMRS

Shaping MCMs into functional regenerators is a challenging task. Very small flow channel sizes are necessary to facilitate heat transfer and very small wall thicknesses are also necessary to allow removing the heat generated inside the material as fast as possible given the high frequencies that are required to increase the power density of magnetocaloric devices. To operate optimally, AMRs should have several characteristics:

- Large surface area per unit volume to facilitate heat transfer
- Small particle/wall size to avoid temperature gradients inside the solid
- Large heat transfer coefficient

- Small pressure drop to limit the amount of energy that is necessary for fluid flow
- Small void fraction to accommodate as much MCM as possible in the gap of a magnet

A large surface area per unit volume usually leads to high pressure drops given that there is a larger contact area between the fluid and the solid and therefore larger friction losses. Other factors, such as the straightness of flow channels, also affect pressure drop and heat transfer, as tortuosity in the fluid flow and turbulence can enhance heat transfer but simultaneously increase pressure drop. So, the geometry of the ideal regenerator must offer a surface area as large as it is necessary to maximize heat transfer while keeping the pressure drop as low as possible. In other words, the ratio between heat transfer to pressure drop must be maximized, which some authors have reduced to the maximization of the Nusselt number to friction factor ratio [110].

A widely used method for manufacturing AMRs is the packed bed of spherical or irregularly shaped particles. This geometry provides good heat transfer characteristics and a large heat transfer area, thus also significant friction losses, while being relatively easy to produce. Packed beds generally have a lower void fraction limit of 36 %. Another common approach for assembling AMRs is using parallel plates, which represents the other end of the spectrum of available designs [66]. While parallel plates have lower heat transfer performance compared to packed beds, they offer reduced friction losses. This is attributed to the smaller practically achievable contact areas and the tendency to promote laminar flow. Additionally, parallel plate AMRs can be manufactured in theory with very small void fraction and with very thin plates. However, in practice, very thin plates are difficult to handle, and they deform easily even under the magnetic forces they are subjected to in an AMR. Besides, although parallel plates seem to offer at first glance a good trade off between heat transfer rate and pressure drop, the non-uniformity of flow channels leading to flow channeling can hamper their performance in reality.

Other designs, such as the micro channel regenerators (circular, triangular, or squared), the arrays of pins (with squared or circular cross sections), and the cross-rod matrices, lie in the middle of the spectrum. These geometries could provide relatively large heat transfer coefficients and heat transfer areas while producing smaller friction losses compared to packed beds, but they are also more difficult thus more costly to produce. Very small porosities are also achievable with these methods. The trend in recent years has been to explore these alternatives to packed beds and parallel plates, which could potentially combine a good range of the ideal characteristics demanded by AMRs.

Packed beds and parallel plates have been extensively studied in the

past given that these geometries have been used in diverse heat and mass transfer equipment in the process industry for many decades. As a result, their heat transfer and pressure drop characteristics are very well understood. However, a thorough characterization of heat transfer and pressure drop is imperative for any newly proposed geometry to reveal its actual applicability in AMRs.

5.1.2. GEOMETRIES IMPLEMENTED IN AMRS USING FIRST AND SECOND ORDER MCMS

The manufacturability of an AMR with the aforementioned characteristics depends greatly on some of the properties of the MCM to be shaped. Gadolinium (Gd), a second-order MCM considered the benchmark material for room temperature applications, is a pure metal with good ductility that can be easily manufactured into diverse shapes. However, shaping first-order MCMs such as MnFePSi and Lanthanum-based MCMs is more difficult due to their brittleness and some other properties that lead to mechanical and/or chemical instability. For instance, one of the main issues of hydrogenated La-based materials is aging due to dehydrogenation. Although this phenomenon is reversible to some extent [62], it hinders the applicability of these materials. On top of the brittleness issue, La-based first order MCMs also suffer from volume changes upon crossing the transition temperature, which results in mechanical stability problems. The first order MnFePSi MCMs do not exhibit a significant volume change when they undergo a phase change due to the magneto-elastic nature of the transition. Instead, there is an elastic change of the lattice parameters c and a that can also lead to mechanical stability problems [38, 129].

Gadolinium AMRs have been manufactured in different shapes. Trevizoli et al. [46] compared the passive and active performance of Gd regenerators with various geometries: packed bed of spheres, pin arrays, and parallel plates, all of similar hydraulic diameter and mass. Pin arrays and parallel plates were manufactured using wire electrical discharge machining. The packed bed of spheres produced the largest cooling capacity and temperature span and the parallel plate the poorest whereas pin arrays offered almost the same cooling capacity as the packed bed and better *COP* due to the smaller pressure losses. Trevizoli et al. [130] also proposed the use of selective laser melting 3D printing technique to manufacture AMRs. Many researchers have used packed beds of Gd spheres in their MCHP prototypes [26, 131, 132] while others stick to the use of parallel plates [55, 133].

On the other hand, despite their brittleness and stability problems, which pose challenges in manufacturing, first-order MCMs have also been shaped into several AMR geometries. The easiest way to overcome

the brittleness problem is to assemble first order MCMs into packed beds of either spherical [23, 62, 134] or crushed particles [79, 82]. Besides this simple manufacturing approach, some other alternatives have been considered. Liang et al. [135] proposed the use of freeze casting to manufacture Lanthanum-based AMRs. Liang et al. [67] also studied the use of $La(Fe, Mn, Si)_{13}H_y$ shaped into a triangular-microchannel geometry for an AMR. Miao et al. [136] proposed to use electrodischarge drilling to manufacture circular microchannel AMRs using LaFeCoSi. N'dri et al. [137] used extrusion-based additive manufacturing to produce plates of $La(Fe, Si)_{13}H$. Navickaitė et al. [138] tested the performance of $La_{0.84}Ce_{0.16}Fe_{11.5}Mn_{1.5}Si_{1.3}H_x$ AMRs produced using a laser beam melting 3D printing technique. Some of their AMRs were printed using a nature-inspired geometry [139]. Imaizumi et al. [140] also studied the use of a laser melting 3D printing technique to shape $La(Fe, Si)_{13}$.

The diversity of geometries implemented in AMRs reflects the continuous efforts to optimize heat transfer, pressure drop, and overall system performance while addressing the unique manufacturing challenges posed by different magnetocaloric materials. While second-order MCMs like gadolinium offer flexibility in shaping due to their ductility, first-order MCMs require innovative fabrication techniques to overcome brittleness and stability issues. Additive manufacturing, freeze casting, electrodischarge machining, and other advanced processing methods have enabled the development of complex geometries that could enhance AMR efficiency to some extent. As research progresses, further advancements in material shaping and stabilization will be crucial for the widespread adoption of first-order MCMs in magnetocaloric applications.

5.1.3. PRESSURE DROP CHARACTERIZATION OF POROUS MEDIA

The characterization of pressure drop of fluid flow through porous media is a straightforward task from an experimental perspective given that the key variables, pressure drop, flow rate, and fluid temperature, can be measured directly. So, this characterization only requires a flow meter, a differential pressure sensor, and two temperature sensors to measure the temperature of the fluid flow entering and leaving the porous media. However, the derivation of general expressions to predict pressure drop as a function of flow rate, fluid properties, and geometric parameters is a more difficult task.

Extensive research on packed beds was conducted during the first half of the previous century to understand the mechanisms behind energy losses caused by fluid flow through porous media. Researchers concluded that the total energy losses result from the sum of viscous energy losses, which dominate at low flow rates or in laminar flow regimes, and kinetic energy losses, which dominate at high flow rates or

in turbulent flow regimes [104]. For certain geometries, such as parallel plates and microchannels, viscous energy losses dominate across the entire range of Reynolds numbers typically observed in AMR operation. In contrast, other geometries such as packed beds and packed screen beds tend to operate in the turbulent regime, resulting in higher kinetic energy losses [110].

Based on these principles, Ergun [104] proposed to correlate pressure drop and flow data of packed beds of particles with various shapes and sizes using the modified friction factor and Reynolds numbers developed by Blake [141], presented in Equation 5.2 and Equation 5.3 respectively. Ergun's correlation is presented in Equation 5.1. The first term of this correlation represents the viscous energy losses, and the second one the inertial energy losses.

$$ff_{\text{mod}} = \frac{150}{Re_{\text{mod}}} + 1.75 \text{ (Ergun)} \tag{5.1}$$

Blake's modified friction factor differs from the Darcy friction factor commonly used for internal flow, and the modified Reynolds number is also different from that used in internal flow scenarios. The primary distinction lies in the factors that include the void fraction of the bed, which enables the collapse of all experimental data onto a single line. A detailed analysis about the inclusion of void fraction in these terms can be found in reference [104]. The modified friction factor (Equation 5.2) and the modified Reynolds number (Equation 5.3) are based on an equivalent particle diameter and a superficial velocity.

$$ff_{\text{mod}} = \frac{\Delta P}{\Delta x} \frac{D_{\text{p}}}{\rho v_{\text{sup}}^2} \frac{\varepsilon^3}{(1-\varepsilon)} \tag{5.2}$$

$$Re_{\text{mod}} = \frac{\rho v_{\text{sup}} D_{\text{p}}}{\mu (1-\varepsilon)} \tag{5.3}$$

The equivalent particle diameter is defined as presented in Equation 5.4, where V_{s} is the total volume and A_{s} the total surface area of the solid particles. The superficial velocity, on the other hand, is calculated based on the volumetric flow rate and the total cross sectional area of the empty column [104]. Paraphrasing the definition from Mills' heat transfer book, it represents the velocity of the fluid just before it enters or immediately after it exits the packed section [142].

$$D_{\text{p}} = 6 \frac{V_{\text{s}}}{A_{\text{s}}} \tag{5.4}$$

5.1.4. HEAT TRANSFER CHARACTERIZATION METHODS

Diverse methods have been reported in literature to characterize heat transfer between porous materials and fluids. These methods always involve establishing a temperature difference between the solid element or sample and the fluid to trigger heat transfer. During these experiments, it is essential to measure the temperatures of the fluid and, often, the solid, as well as the fluid flow rate. The following paragraphs provide a brief review of various heat transfer characterization methods relevant for our study.

London et al. [128] investigated the heat transfer behavior of cross-rod matrices by analyzing the temperature history of a heated rod as it cooled by transferring heat to an air flow. The matrices tested consisted of 10 or 12 layers of approximately 9.5 mm rods, with one rod in the seventh layer made of copper and the rest made of plastic. The copper rod was preheated in an oven and inserted into the test rig through an opening in the main duct. The copper rod was treated as a lumped thermal capacitor with negligible internal heat transfer resistance, thereby enabling the use of the lumped capacitance model to derive the heat transfer coefficient from the temperature-versus-time data collected during the experiments. The main difficulty of this method is related to the transient nature of the experiments and the short time constants, which requires high data-sampling rates. Even with the modern instruments available today, this method remains difficult to implement when working with matrices that have small thermal capacitance.

Macias-Machin et al. [98] determined the heat transfer coefficient between a fluid and a platinum wire submerged in a fluidized bed of spherical particles by heating the wire with an electrical current. Because the wire had dimensions similar to the particles in the bed, the resulting heat transfer coefficient was considered representative of the heat transfer between the fluid and the spheres. The temperature of the wire was determined by measuring its resistance during the experiments and using the temperature-resistivity relationship of platinum. The heat transfer rate from the wire to water, $\dot{Q}$, was considered equal to the electrical power dissipated in the wire, VI. The heat transfer coefficient was then directly calculated using Equation 5.5:

$$\dot{Q} = \mathcal{V}I = hA_{\text{wire}}(T_{\text{wire}} - T_{\text{water}}) \tag{5.5}$$

where $\mathcal{V}$ is the voltage drop across the wire, I is the applied electrical current, h is the heat transfer coefficient, A_{wire} is the surface area of the wire, and T denotes temperature. A correlation was developed based on the calculated heat transfer coefficients.

Park et al. [143] investigated the heat transfer characteristics of fluid flow through rectangular-shaped samples of plain-weave screen laminates, also referred to as packed screen beds. The samples had

a cross-sectional area of 100×18 mm^2 and a maximum thickness of approximately 8 mm. A temperature difference between the screen laminates and water was established by using two electrical resistors, which heated the samples from two opposing surfaces. The heat transfer coefficient was determined using a heat transfer model that assumed plug flow, a constant heat transfer coefficient in the cross section, one-dimensional heat diffusion in the screen laminates in a direction perpendicular to the flow, and symmetrical heating from both resistors. The model differential equations were solved analytically to determine the temperature distribution within the screen laminates. By measuring the heat flow from the resistors and the surface temperature at the contact points between the resistors and the samples, the heat transfer coefficients were calculated for various experimental conditions, and a correlation was developed based on the calculated heat transfer data.

Frischmann et al. [101] conducted single blow experiments to determine the heat transfer coefficient in a packed bed of spheres. In these experiments, cold water was circulated through the packed bed column until a steady-state temperature was achieved. Subsequently, hot water was suddenly allowed to flow through the column, and the inlet and outlet water temperatures were recorded. For each set of experimental conditions, an average bed Nusselt number was derived by matching the measured outlet water temperature with values predicted by a one-dimensional numerical model that incorporated energy conservation equations for both fluid and solid phases. The Nusselt number was assumed constant within the model. Despite some inaccuracies in estimating heat leaks, which resulted in deviations between the measured and calculated outlet water temperatures, this method facilitated the development of a new correlation for the calculation of the heat transfer coefficient in packed beds of spherical particles.

Many researchers have used passive regenerator tests to evaluate the heat transfer performance of porous structures designed as AMRs. In these experiments, a temperature gradient is established along the porous material by creating a reciprocating flow, with cold fluid entering at one end and hot fluid entering at the other alternatively. The performance is typically assessed by calculating the thermal effectiveness of the regenerator. This method rarely leads to the development of a Nusselt number correlation, but it offers valuable insights for comparing different regenerator geometries or structures. For instance, Trevizoli et al. [46] compared the performance of various geometries, including parallel plates, squared-pin arrays, and packed bed of spheres, using passive regenerator tests. Despite the fact that all regenerators had the same void fraction, cross section, and surface area, they observed differences in effectiveness, with pin arrays and packed beds exhibiting the highest effectiveness at low and high utilization

factors respectively and parallel plates offering the poorest performance. The superior thermal performance of packed beds and pin-arrays was attributed to a better heat transfer coefficient and lower heat conduction in the flow direction. Likewise, Trevizoli et al. [130] compared the thermal performance of passive regenerators made of stainless steel using a selective laser melting 3D-printing technique. They tested regenerators with inline and staggered fiber arrangement and found that staggered configurations achieved better thermal effectiveness but also experienced larger pressure drops. Lastly, Navickaitė et al. [138] showcased the potential of laser beam-melted regenerators with nature-inspired flow geometries for use as AMRs. They compared printed regenerators using a Lanthanum-based MCM and also using $AlSi_7Mg_{0.6}$, and they found that the regenerators printed with $AlSi_7Mg_{0.6}$ had a smoother surface producing smaller pressure drops. Larger surface roughness of the MCM regenerators also resulted in slightly higher effectiveness due to increased tortuosity-induced heat transfer. Collectively, these studies underscore the versatility and limitations of passive regenerator tests in assessing the thermal performance of porous structures, particularly when the development of generalizable correlations, such as those for the Nusselt number, is not the primary goal.

Nevertheless, some researchers have ventured to derive Nusselt correlations based on passive regenerator tests. Lei et al. [144] compared the heat transfer performance of packed beds of epoxy-bonded LaFeMnSiH particles with that of packed beds made of stainless steel spheres using passive regenerator tests. Their findings indicated that smaller spherical particles achieved higher effectiveness. Additionally, the effectiveness of epoxy-bonded regenerators with irregularly-shaped particles was slightly larger than that of regenerators using spherical particles of similar size. Nusselt numbers were calculated using heat transfer coefficients derived from the overall number of transfer units, which were obtained by comparing the experimental and numerical values of effectiveness. The reported Nusselt numbers were found to be of the same order of magnitude as those predicted by well-established correlations. Similarly, Liang et al. [135] characterized various freeze-cast microchannel regenerators using passive regenerator tests and highlighted that regenerators with smaller pore width achieved higher heat transfer performance. They also employed a method similar to that used by Lei et al. [144] to derive heat transfer coefficients and Nusselt number correlations from these experiments.

Measuring both the solid material temperature and the fluid temperature is essential in three of the methods described in the previous paragraphs: the lumped capacitor experiment conducted by London et al. [128], the screen laminates heated with electrical resistors used by Park et al. [143], and the electrically heated wire

method employed by Macias-Machin et al. [98]. In contrast, the single blow experiments reported by Frischmann et al. [101] and the passive regenerator tests require only fluid temperature measurements. Except for experimental techniques where the samples are continuously heated using external resistors or electrical current, all other methods are transient in nature and thus require a large thermal mass of solid to facilitate accurate measurements.

5.1.5. SELECTED HEAT TRANSFER CHARACTERIZATION METHODS

As demonstrated in the previous section, characterizing the heat transfer performance of porous structures is inherently challenging because the heat transfer coefficient cannot be directly measured; instead, it must be inferred using a specific model tailored to the type of experiment. Consequently, determining the heat transfer coefficient between the porous 3D-printed blocks and water requires calculations based on temperature measurements and an appropriate heat transfer model. To achieve this, three different approaches were considered for estimating the heat transfer coefficient in these blocks.

The initial approach involved conducting single-blow experiments as described earlier and in Refs. [101, 145]. However, the transient nature of these experiments required highly accurate temperature measurements and a high sampling rate to detect differences between the incoming and outgoing fluid temperatures given the small thermal mass of the samples. Unfortunately, our experimental setup did not meet these requirements, making this method unusable. As an alternative, we attempted to determine the heat transfer coefficient through passive regenerator tests, following a calculation method similar to that proposed by Lei [30]. However, this second approach also failed to produce reliable heat transfer coefficients due to several reasons.

First, the reciprocating flow was generated using two diaphragm pumps and solenoid valves instead of a double-effect pump, leading to inaccurate flow rate measurements. Additionally, the geometry of the samples was poorly controlled during printing, and key geometric parameters, such as surface area and void fraction, were inadequately characterized. Further inaccuracies arose from the utilization values used in the calculations, which were affected by uncertainties in the heat capacity of the MCM and the fluid flow rate. Finally, even though thermocouples with fast time response were used, the temperature measurements included an important uncertainty given the transient nature of the experiments. Collectively, these errors resulted in unreliable estimations of heat transfer coefficients. The results and conclusions of the experiments conducted following these two methods are summarized in Ref. [146].

To avoid the challenges associated with transient experiments on

samples with small thermal mass, steady-state experiments were ultimately preferred. Inspired by the work of Macias-Machin et al. [98], the approach presented in this thesis chapter involves self heating single 3D-printed MCM blocks using electrical current while simultaneously cooling them with a unidirectional flow of water. This method was feasible because MnFePSi is an inter-metallic compound with relatively good electrical conductivity, making it possible to create a simple electrical circuit consisting of a DC power source and the 3D-printed block as a resistor. Given the low resistivity of the blocks, large electrical currents were required to generate sufficient heat to produce measurable temperature differences between the incoming and outgoing water streams.

Initially, we assumed that a simple heat transfer model would be sufficient for the derivation of heat transfer coefficients from these experiments. Specifically, we considered that determining only the average temperatures of solid and fluid would allow to calculate an average heat transfer coefficient using Equation 5.6, where the total heat transferred, $\dot{Q}$ could be obtained from Equation 5.7. Recognizing the inevitable existence of temperature gradients in both the block and the water stream during these experiments, we opted for small samples to minimize these effects while still relying on average temperatures.

$$\dot{Q} = \bar{h} A_s (\bar{T}_s - \bar{T}_f) \tag{5.6}$$

$$\dot{Q} = \dot{m} c_P (T_f^{out} - T_f^{in}) \tag{5.7}$$

The average fluid temperature was straightforward to determine as the mean of the incoming and outgoing fluid temperatures. However, determining the average solid temperature proved more challenging. We explored two approaches for this. First, following the method introduced by Macias-Machin et al. [98], we considered correlating the average temperature of the magnetocaloric block with its electrical resistance, similar to the working principle of resistive temperature detectors (RTDs). Our unsuccessful efforts to achieve this are summarized in Appendix D. As an alternative, we measured the temperatures of the four outer surfaces of the blocks during the experiments. This ultimately led to the conclusion that temperature gradients within the sample could not be ignored. Thus, a more complex heat transfer model was necessary to derive the heat transfer coefficients.

Fortunately, we identified similarities between our experiments and those conducted by Park et al. [143], whose mathematical approach provided the basis for developing a relatively simple heat transfer model that accounts for temperature gradients within the samples. The model is presented in subsection 5.1.6.

5.1.6. HEAT TRANSFER MODEL

The heat transfer experiments described earlier involve several physical phenomena including heat generation inside the 3D-printed MCM blocks due to its electrical resistance, heat generated in the contact surfaces between the blocks and the copper plates due to non-negligible electrical contact resistances, heat leaks to ambient through the casing, heat leaks through the copper plates, heat diffusion within the solid matrix, heat transfer by convection with the fluid, and complex velocity fields. Furthermore, the simultaneous presence of electricity and water in these experiments could potentially trigger electrochemical reactions. Despite the complexity of the real phenomena, the following assumptions were made to simplify the problem and facilitate the mathematical formulation:

- The temperature of the solid matrix only changes in the direction perpendicular to the copper plates, parallel to the direction of the current flow.
- The previous assumption requires that the sides of the block in contact with the plastic frame are also considered perfectly insulated. By assuming this, the problem becomes one-dimensional facilitating the solution and analysis. This is a reasonable assumption given the low thermal conductivity of the plastic material of the frame ($< 0.5\,\mathrm{W\,m^{-1}\,K^{-1}}$).
- There is uniform heat generation inside the block. The implicit assumptions are that the electrical resistance is also uniform as well as the distribution of current.
- The heat transfer coefficient is also uniform in the cross section of the block. This relies on the premise of a uniform fluid velocity distribution in the cross section, i.e., plug flow, and a uniform void fraction of the printed block.
- The surface area per unit volume of the block is assumed uniform for the entire matrix. The block may have slight variations in fiber diameters and fiber distances leading to also small variations in specific surface area. These variations are assumed negligible.
- The fluid temperature is assumed to be constant. This significantly simplifies the problem by decoupling the energy conservation equations for the fluid and the solid. This assumption is justified, as the fluid temperature increased by only a fraction of a degree during the experiments. Therefore, considering the fluid temperature as the average of the incoming and outgoing water temperatures is a reasonable and safe approach.
- Steady state condition is assumed.

- Any type of electrochemical reaction is ignored.

Based on the previous assumptions, a one-dimensional, steady-state heat equation with heat generation and convection can be formulated to model the heat transfer phenomena observed during the experiments, which is introduced in Equation 5.8.

$$\frac{\mathrm{d}^2T}{\mathrm{d}y^2} + \frac{\dot{g}}{k} = \frac{h\beta}{k}(T - T_\mathrm{f}) \tag{5.8}$$

This is a nonhomogeneous linear second order ordinary differential equation, where:

- $T(y)$: Temperature distribution along the domain [K]
- $\dot{g}$: Uniform heat generation rate per unit volume [$\mathrm{W\,m^{-3}}$]
- k: Effective thermal conductivity of the matrix [$\mathrm{W\,m^{-1}\,K^{-1}}$]
- h: Convective heat transfer coefficient [$\mathrm{W\,m^{-2}\,K^{-1}}$]
- β: surface area per unit volume of the matrix [$\mathrm{m^{-1}}$]
- T_f: Fluid temperature [K]

Since heat is generated not only within the 3D-printed blocks but also at the surfaces in contact with the copper plates—due to electrical contact resistances being of the same order of magnitude as the electrical resistance of the blocks—the heat fluxes at the block surfaces must also be accounted for in the heat transfer model. This is addressed through the use of Neumann boundary conditions, introduced below in Equation 5.9 and Equation 5.10.

Boundary Conditions:

$$-k\frac{dT}{dy}\Big|_{y=0} = \dot{q}_1 \tag{5.9}$$

$$-k\frac{dT}{dy}\Big|_{y=H} = \dot{q}_2 \tag{5.10}$$

Here, $\dot{q}_1$ and $\dot{q}_2$ represent the heat fluxes at the surfaces of the blocks in contact with the copper plates.

Solution Approach:

1. Homogeneous Solution: The homogeneous equation is:

$$\frac{\mathrm{d}^2T_\mathrm{hom}}{\mathrm{d}y^2} - \xi^2 T_\mathrm{hom} = 0 \tag{5.11}$$

where $\xi^2 = \frac{h\beta}{k}$.

The solution to this equation is:

$$T_{\text{hom}}(y) = C_1 e^{\xi y} + C_2 e^{-\xi y} \tag{5.12}$$

2. Particular Solution: A particular solution can be assumed as a constant:

$$T_{\text{par}}(y) = C_3 \tag{5.13}$$

Substituting this into the non-homogeneous equation (Equation 5.8) and solving for C_3, we get:

$$C_3 = T_f + \frac{\dot{g}}{h\beta} \tag{5.14}$$

3. General Solution: The general solution is the sum of the homogeneous (Equation 5.12) and particular (Equation 5.14) solutions:

$$T(y) = C_1 e^{\xi y} + C_2 e^{-\xi y} + T_f + \frac{\dot{g}}{h\beta} \tag{5.15}$$

4. Applying Boundary Conditions: By applying the boundary conditions given by Equation 5.9 and Equation 5.10, we can determine the constants C_1 and C_2 as:

$$C_1 = \frac{\dot{q}_1 e^{-\xi H} - \dot{q}_2}{k\xi(e^{\xi H} - e^{-\xi H})} \tag{5.16}$$

$$C_2 = \frac{\dot{q}_1 e^{\xi H} - \dot{q}_2}{k\xi(e^{\xi H} - e^{-\xi H})} \tag{5.17}$$

5.1.7. SENSITIVITY ANALYSIS OF THE HEAT TRANSFER MODEL

A sensitivity analysis could provide insights into which parameters have the most significant influence on the temperature distribution of the blocks described by Equation 5.15. Figure 5.1 presents the results of such a sensitivity analysis. Figure 5.1a illustrates the sensitivity to the heat transfer coefficient. When the heat transfer coefficient is low, significant temperature differences develop between solid and fluid. For very low values, such as $100\,\mathrm{W\,m^{-2}\,K^{-1}}$, the surface temperature can be nearly 40 K higher than the fluid temperature. Similarly, Figure 5.1b demonstrates the effect of the effective thermal conductivity of the matrix. When the conductivity is low, heat transfer from the surface to the interior of the block becomes difficult, causing the surface temperature to rise. Figure 5.1c further shows that increasing heat flux results in higher surface temperatures. Finally, Figure 5.1d illustrates the sensitivity to the specific surface area. Smaller specific surfaces areas

reduce the efficiency of heat transfer to water, leading to an increase in solid temperature as a compensatory effect.

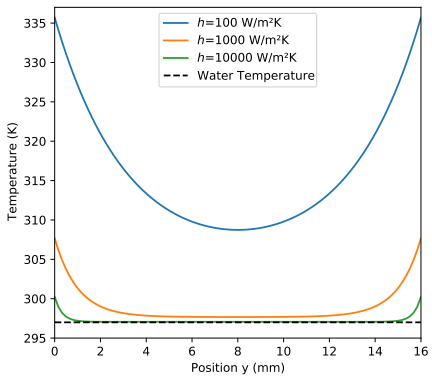

(a) Sensitivity to heat transfer coefficient

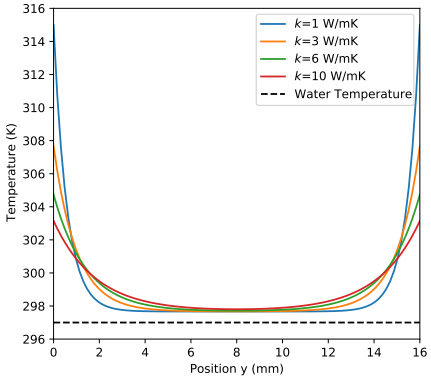

(b) Sensitivity to effective thermal conductivity

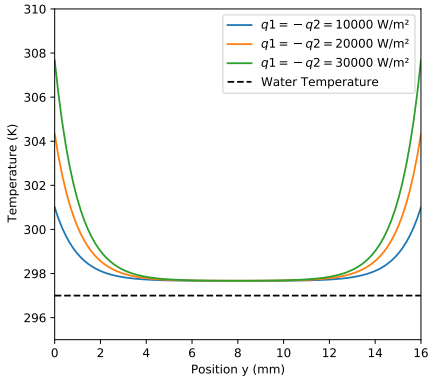

(c) Sensitivity to heat flux

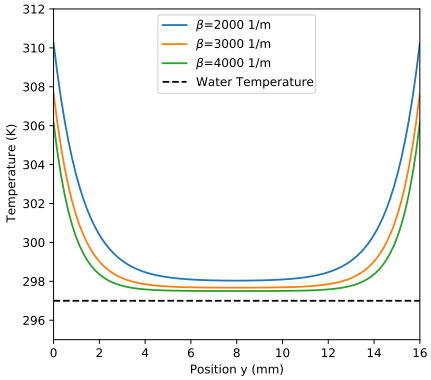

(d) Sensitivity to specific surface area

Figure 5.1.: Sensitivity analysis of the temperature distribution computed using the proposed heat transfer model with respect to: (a) heat transfer coefficient, (b) effective thermal conductivity of the matrix perpendicular to the flow direction, (c) heat flux at the surfaces of the block in contact with the copper plates, and (d) specific surface area. The base case parameters are: $T_f = 297$ K, $\dot{g} = 2.0e6$ Wm^{-3}, $h = 1000$ Wm^{-2}K^{-1}, $\beta = 3000$ m^{-1}, $k = 3$ Wm^{-1}K^{-1}, and $q1 = -q2 = 30000$ Wm^{-2}.

5.2. EXPERIMENTAL SETUP

A process flow diagram of the setup used to investigate the pressure drop and heat transfer characteristics of the 3D-printed MnFePSi blocks is presented in Figure 5.2. Demineralized water enriched with an anticorrosion additive served as fluid in these experiments. Since the addition of the anticorrosion agent has a negligible effect on the properties of water, the calculations in this chapter are based on the properties of pure water.

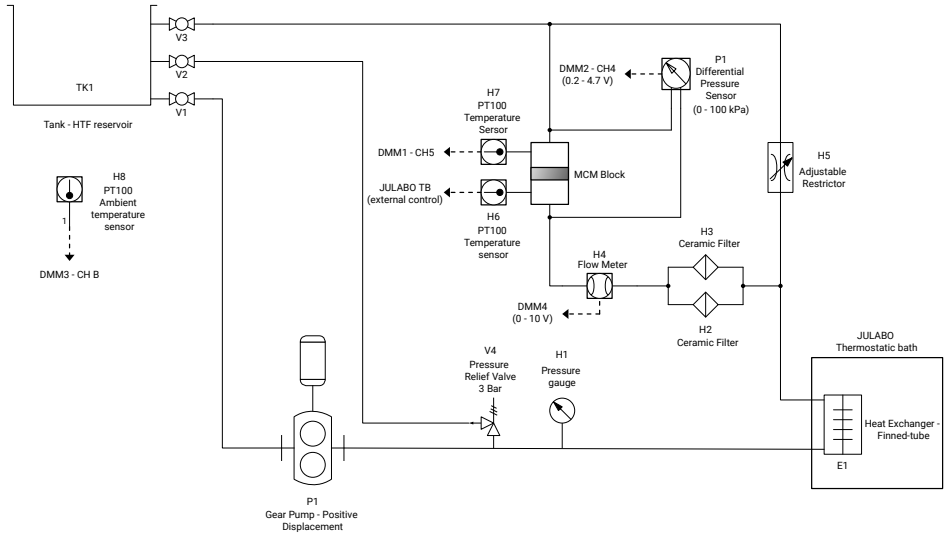

Figure 5.2.: Process flow diagram of the experimental setup used for the heat transfer and pressure drop characterization of the 3D printed MnFePSi blocks.

5.2.1. HYDRAULIC CIRCUIT

The main hydraulic circuit of the setup consists of several elements arranged in the following sequence: water tank, gear pump, finned-tube heat exchanger, filters, flow meter, and sample holder. These elements are interconnected using OD 10 mm transparent, plastic tubes. The first element in the circuit is the water tank. A 5 L jerry can was used as water tank. Three perforations allowed to install three ball valves to isolate the tank from the rest of the system when the sample holder is dismounted. The next element in the water flow direction is a gear pump (Marco UP10-P 24V) that has a maximum free flow rate capacity of 18 L min^{-1} and a maximum rated operating pressure of 7 bar. Next, water passes through a finned-tube heat exchanger

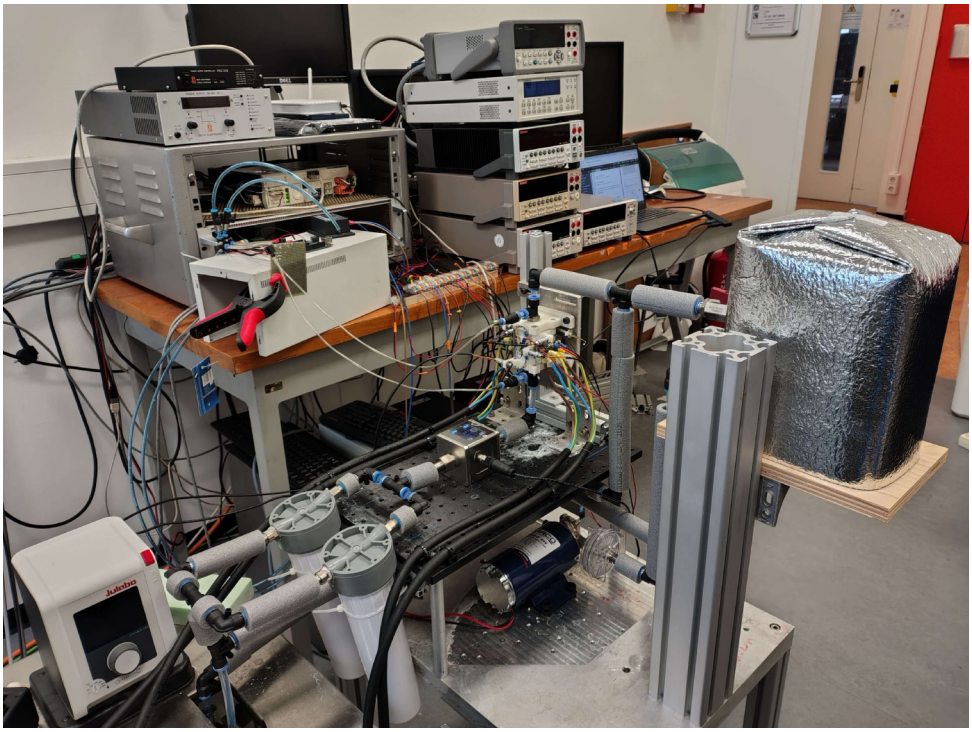

Figure 5.3.: Photography of the assembled experimental setup.

that is submerged in a thermostatic bath (Julabo Dyneo DD-1000F refrigerated circulator) filled with thermal oil. Then, water is filtered in two ceramic filters arranged in parallel (Doulton Ultracarb SI). Water goes then to an electromagnetic flow meter (Kobold MIM-1205HG4C3T0) that has a measuring range from 0.04 to 10 $\mathrm{L\,min^{-1}}$ and an accuracy of $\leq \pm(0.8\%$ of reading $+ 0.5\%$ of full scale). The sample holder is placed downstream the flow meter, and it is positioned vertically with the fluid flowing upwards to prevent air bubbles from getting trapped inside. After passing through the sample holder, water returns to the tank, and the circuit returns to the starting point. Further details about the hydraulic circuit are presented in Appendix C.

5.2.2. SAMPLE HOLDER

The sample holder is the main component of the system. This is a tailor-made, reusable assembly that allows placing the samples for the pressure drop and heat transfer experiments. The parts that make up this assembly were designed in Autodesk Inventor and manufactured by stereolithography 3D printing using a glass-filled rigid

resin. Figure 5.4 shows a computer-aided design (CAD) representation of the sample holder assembly whereas Figure 5.5 shows pictures of the sample holder with and without all temperature sensors and electrical elements connected.

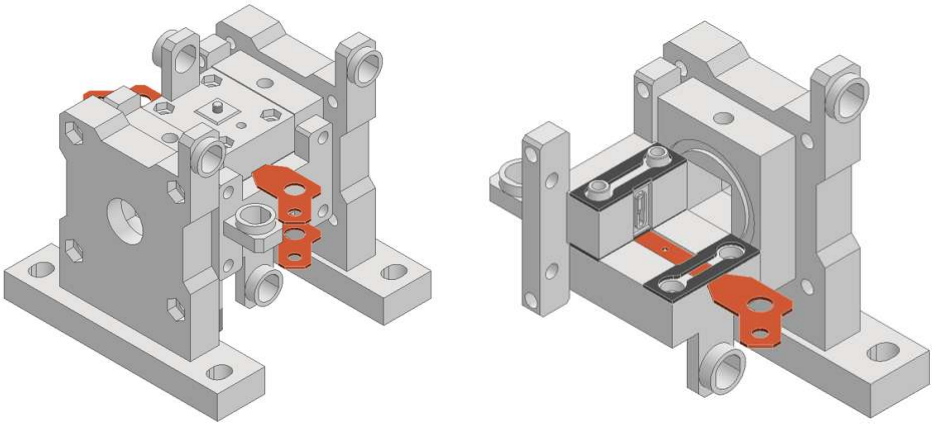

(a) Assembly view. **(b)** Section view.

Figure 5.4.: Design of the sample holder.

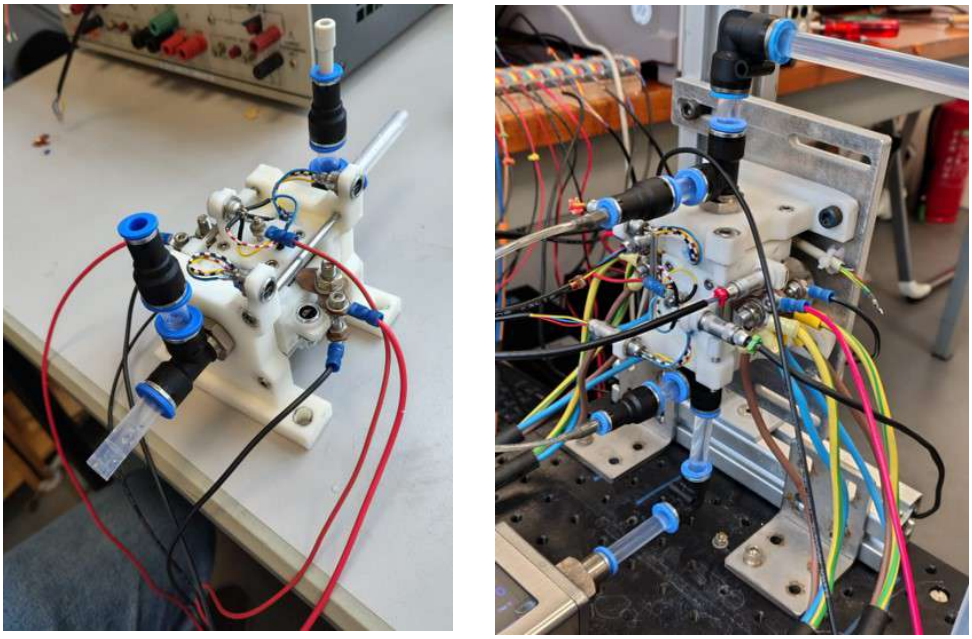

Figure 5.5.: Pictures of the sample holder.

Figure 5.6 shows a schematic representation of the sample holder highlighting the sensors and elements that are placed around the 3D printed MCM block. As depicted in Figure 5.6, the sample is positioned between two 1-mm-thick copper plates that are connected to a power supply (Delta Elektronika 30 V, 200 A). A large current is necessary for self-heating the sample, given that its electrical resistance is of the order of 1 mΩ.

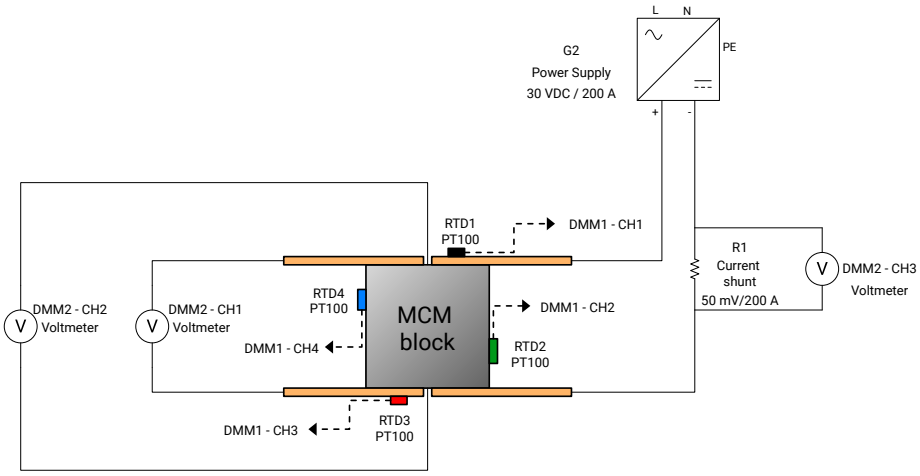

Figure 5.6.: Sensors and elements around the 3D printed MnFePSi block. The flow direction is oriented perpendicular to the plane of the page.

To minimize the contact resistance between the copper plates and the sample, the side surfaces of the samples were polished using super fine sand paper (FEPA P1200) on a rotating table. The copper plates were also polished carefully using the same sand paper. The resulting contact resistances were of similar magnitude as the resistances of the samples. The use of silver paint to enhance electrical contact between the sample and copper plates proved ineffective. Given that the surfaces of the samples contain holes, indium foil was proposed to fill the gaps between the copper plates and samples, thereby minimizing electrical and thermal contact resistances. However, at the time of writing this thesis chapter, its effectiveness has not yet been tested.

5.2.3. MEASUREMENT OF SAMPLE TEMPERATURE DURING HEAT TRANSFER EXPERIMENTS

Given the difficulties in using the blocks as resistive temperature sensors as described in Appendix D, we decided to measure their surface temperature using commercial RTDs. Figure 5.6 presents a schematic of a block and the four temperature detectors used: two sensors (RTD 4 and RTD 2 in the diagram) were placed in direct contact with the sides of the blocks, while the other two were positioned against the copper plates. All RTDs used were PT100 Class A sensors, which offer a tolerance of +/- 0.15 K. This redundancy was initially considered necessary to properly determine the average temperature of the blocks. However, the temperature readings of these four sensors revealed significant temperature gradients within the blocks, demonstrating that these gradients could not be ignored. As a result, a more sophisticated heat transfer model was developed, and the use of the average solid temperature was abandoned.

The voltage drop between copper plates was also measured to keep track of the contact resistance. The electrical current that was used in the experiments was also measured using a 50 mV/200 A current shunt. The accuracy of temperature sensors was verified using an ice point reference standard.

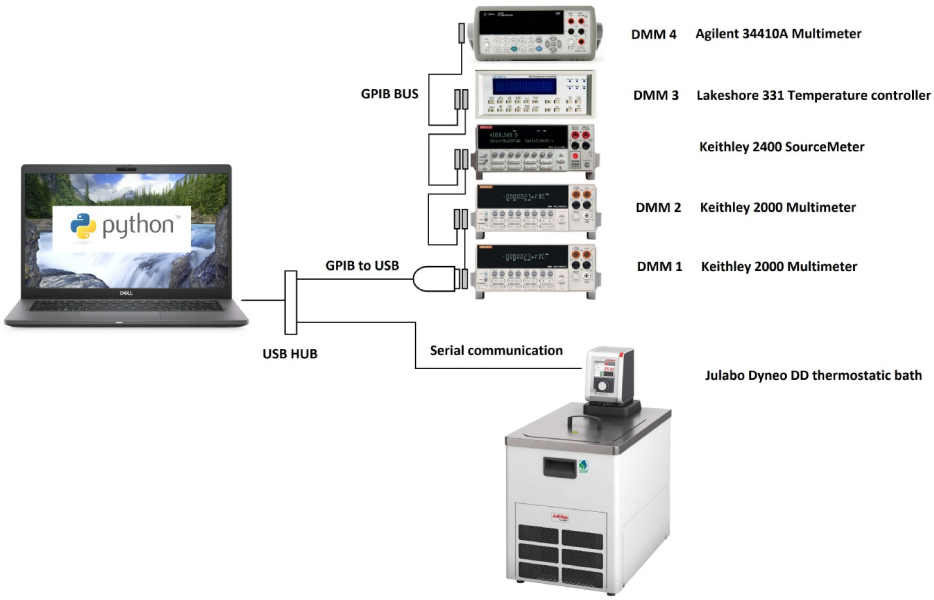

Figure 5.7.: Schematics of the architecture of the data logging system

5.2.4. CONTROL AND DATA LOGGING

A schematic of the architecture of the data logging system implemented for this experimental setup is presented in Figure 5.7. Python was used to establish the communication between the computer, the multimeters, and the refrigerated circulator. The software implementation can be found in [147]. Further details about the control and data logging system are presented in Appendix E.

5.3. GEOMETRIC CHARACTERIZATION OF THE SAMPLES

The company Magneto B.V. manufactured the six MCM blocks that were used for the pressure drop and heat transfer characterization study. These blocks were categorized into two groups, each corresponding to a different fiber diameter: 400 µm and 600 µm. The three blocks within each group varied in void fraction, controlled by adjusting the spacing between the fibers. Initially, we planned to test three additional blocks with 250 µm fibers to make our study more comprehensive, but they were not produced in time.

Table 5.1 summarizes the key printing parameters of the blocks. D_{nozzle}, S_{fiber}, and N_{layers} denote the diameter of the printing nozzle, the separation between fibers (or pitch), and the number of printed layers, respectively. Additionally, Z_{layer} refers to the vertical displacement of the nozzle between successive layers. Since Z_{layer} is smaller than D_{nozzle}, fibers overlap, an effect required to ensure good bonding between layers. In all blocks, consecutive layers are oriented at a 90° angle to one another, and fibers are parallel to the sides of the blocks.

Furthermore, $N_{\text{fibers,top}}$ and $N_{\text{fibers,bottom}}$ denote the number of fibers printed in directions parallel to the top and bottom layers, respectively. Both the total number of fibers and the number located within the Region Available for Flow (RAF) are reported. These values differ due to an issue with the slicing software used to generate the printing G-code. The last column in the table indicates the theoretical void fraction of a single layer calculated based on the fiber separation and nozzle diameter. This void fraction value was only used to fix the fiber separation and to identify the blocks.

Table 5.1.: Parameters used during the 3D printing process of the samples.

Block ID (Long)	Block ID (Short)	D_{nozzle} [μm]	S_{fiber} [μm]	N_{layers} [-]	$N_{fibers,top}$ Total / RAF	$N_{fibers,bottom}$ Total / RAF	Z_{layer} [mm]	ε_{th} [-]
90deg_400um_40p	DP_01	400	530	24	33 / 29	32 / 28	0.27	40
90deg_400um_45p	DP_02	400	570	24	31 / 27	30 / 26	0.27	45
90deg_400um_50p	DP_03	400	630	24	29 / 25	28 / 24	0.27	50
90deg_600um_40p	DP_04	600	780	18	23 / 18	22 / 19	0.36	40
90deg_600um_45p	DP_05	600	860	18	21 / 17	20 / 17	0.36	45
90deg_600um_50p	DP_06	600	940	18	19 / 15	18 / 15	0.36	50

Table 5.2.: Geometric parameters of the 3D printed samples after heat treatment and polishing. Reported values are given in the format $x(y)$, where x is the measured value and y represents the uncertainty in the last digit(s). For example, $0.123(4)$ means 0.123 ± 0.004.

Block ID	D_{fiber} [μm]	$S_{fiber,top}$ [μm]	$S_{fiber,bottom}$ [μm]	L_{ext} [mm]	W_{ext} [mm]	H_{ext} [mm]	W_{RAF} [mm]	H_{RAF} [mm]
DP_01	401(10)	490(3)	490(2)	6.20(5)	16.10(5)	16.10(5)	14.21(5)	14.21(5)
DP_02	385(20)	539(2)	533(2)	6.20(5)	16.10(5)	16.10(5)	14.01(5)	14.38(5)
DP_03	402(25)	593(3)	591(2)	6.20(5)	16.10(5)	16.10(5)	14.24(6)	14.78(5)
DP_04	510(14)	736(3)	735(3)	6.20(5)	16.10(5)	16.10(5)	13.99(5)	13.23(5)
DP_05	543(15)	815(3)	818(3)	6.20(5)	16.10(5)	16.10(5)	13.85(5)	13.90(5)
DP_06	554(18)	895(4)	886(4)	6.20(5)	16.10(5)	16.10(5)	13.43(6)	13.29(5)

Table 5.2 presents the key geometric parameters as measured (or calculated based on measured dimensions) after heat treatment and subsequent polishing, required for dimensional adjustment. The fiber diameters reported in Table 5.2 were obtained from scanning electron microscopy (SEM) images of the top and bottom layers of the printed blocks. Representative SEM images of selected samples are shown in Figure 5.8. All SEM images of the tested samples can be found in [148]. A Python script, available in [147], was developed to automate the measurement of fiber diameters from these images. Since a calibration ruler was not available, the SEM measurements were calibrated using a transmission electron microscopy grid with a mesh size of 200, a pitch of 125 µm, and a bar width of 35 µm. The uncertainty of the measured dimensions was estimated via error propagation, accounting for both a device uncertainty of 0.5% of the measured values and the standard deviation of repeated measurements taken at multiple locations within the samples.

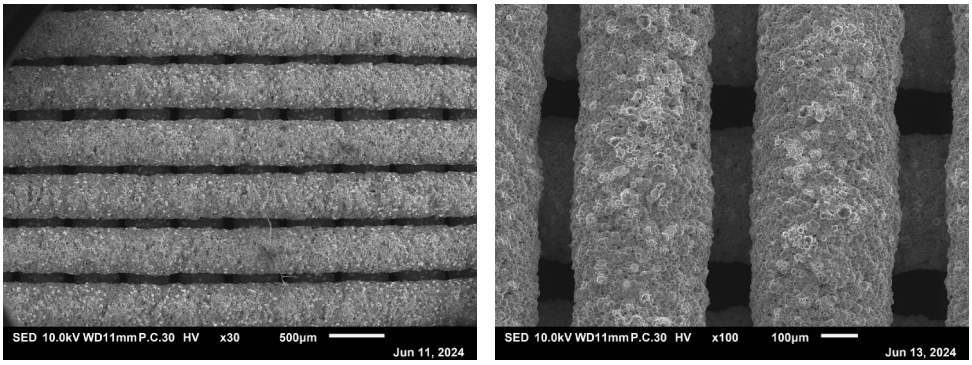

(a) 90deg_400um_40p_a **(b)** 90deg_400um_45p_a

Figure 5.8.: Scanning electron microscopy (SEM) images of selected samples.

By comparing the nozzle diameters in Table 5.1 with the final fiber diameters in Table 5.2, a trend of fiber shrinkage during heat treatment becomes apparent, with the exception of sample 90deg_400um_40p_a and 90deg_400um_50p_a. A worn-out nozzle (plastic nozzles were used for printing) could explain why these fiber diameters did not appear to shrink after heat treatment. Unfortunately, no SEM images of the samples were taken prior to heat treatment to confirm this. The shrinkage occurs because the binder used for printing is released during the initial stage of the heat treatment process. This also causes a reduction in the distance between fibers, as evident from the comparison of the two tables, and consequently, a decrease in the overall dimensions of the blocks.

In Table 5.2, W_{ext} and H_{ext} refer to the external dimensions of the blocks after polishing, whereas W_{RAF} and H_{RAF} represent the width and height of the RAF in the cross-section perpendicular to the flow direction. The latter dimensions are used for the calculation of the fluid velocity, crucial in the friction factor and Reynolds number calculations. The flow region dimensions differ from the overall block dimensions for two main reasons.

The first reason is the formation of solid walls along all four sides of the block, which reduce the area available for flow. These walls are at least as thick as one fiber diameter and form because the nozzle continues extruding material as it travels between the end point of one fiber and the starting point of the next, directly along the block's boundaries. The walls become even thicker due to material squishing at these boundaries, where fibers from successive layers are deposited on top of one another with a small overlap. This effect is illustrated in Figure 5.9a and is more pronounced in blocks where fibers are printed parallel to the sides (as in our samples), as each layer ideally begins with a fiber at one boundary and ends with another at the opposite one. As a result, more material accumulates and is squished at the boundary walls compared to blocks with fibers printed at an angle, where only fiber segments are deposited at the perimeter.

The second reason is the inconsistent separation between fibers that occurred in all blocks, with three fibers printed too closely together on one side, and, very often, one missing fiber on the opposite side. This is illustrated in Figure 5.9b and Figure 5.9c, both of which correspond to the block 90deg_400um_45p_a. This issue arises from the fact that the slicing software used to generate the printing G-code (UltiMaker Cura, a commercial tool typically used for Fused Deposition Modeling (FDM) 3D printing) prioritizes preserving the external dimensions of the blocks over maintaining a consistent infill pattern.

This behavior of the software only becomes problematic when the fibers are printed parallel to the sides of the block. In such cases, the length of both the missing fiber and the group of closely packed fibers matches the full length of the corresponding side of the block, thereby significantly modifying the flow region. In contrast, when fibers are printed at an angle with respect to the sides of the block, these defects are confined to the corners, where the affected fibers are much shorter and their impact becomes negligible.

W_{RAF} and H_{RAF} account for the reduction in the flow area caused by the solid boundary wall and the printing defects present in each specific block. Finally, in Table 5.2, $S_{fiber,top}$ and $S_{fiber,bottom}$ denote the fiber separation, or pitch, in the layers printed in the same directions as the top and bottom layers, respectively. These dimensions were calculated using Equation 5.18 and Equation 5.19. Pitch values obtained from SEM images were discarded due to their high variability, caused by

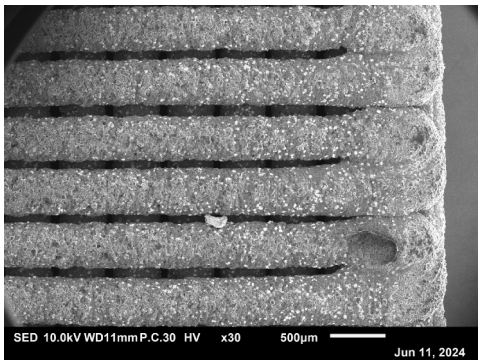

(a) Solid wall in one of the sides (right in image) of sample 90deg_400um_40p_a.

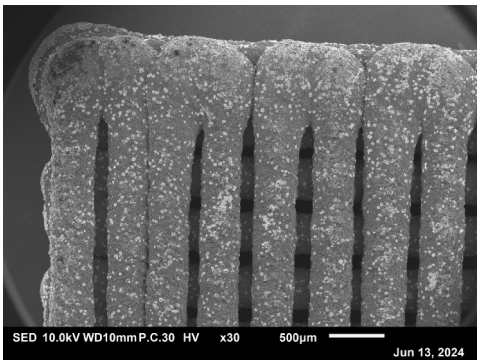

(b) Inconsistent fiber separation in one side (left in image) of sample 90deg_400um_45p_a.

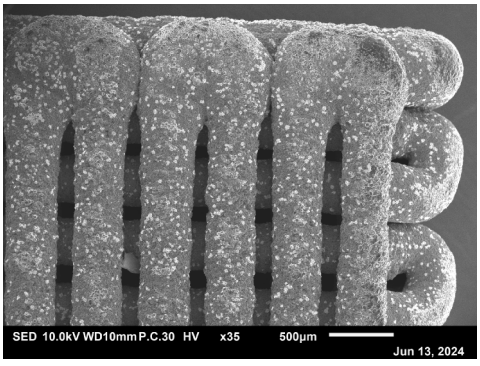

(c) Missing fiber in one side (right in image) of sample 90deg_400um_45p_a.

Figure 5.9.: SEM images of selected samples before polishing, showing the reduction of area available for flow. In a), the continuous extrusion of material between the end and start points of two consecutive fibers creates a wall that becomes thicker than the fiber diameter due to material squishing. In b), an issue in the G-code causes fibers to be printed too closely together on one side of sample 90deg_400um_45p_a. In c), a missing fiber is observed on the opposite side of the same sample, 90deg_400um_45p_a.

inconsistent inter-fiber spacing during the printing process.

$$S_{\text{fiber,top}} = \frac{W_{\text{RAF}}}{N_{\text{fibers,top,RAF}}} \tag{5.18}$$

$$S_{\text{fiber,bottom}} = \frac{H_{\text{RAF}}}{N_{\text{fibers,bottom,RAF}}} \tag{5.19}$$

5.3.1. SURFACE AREA AND VOID FRACTION OF THE SAMPLES

The specific surface area and void fraction of the blocks were calculated by modeling the fibers as rods with circular cross-sections. To perform these calculations, a characteristic unit cell was identified based on the repeating geometry within the region of the blocks available for flow. As illustrated in Figure 5.10, the geometry of this unit cell is fully defined by the average fiber diameter (D_{fiber}), the average pitch or separation between fibers (S_{fiber}), the number of printed layers (N_{layers}), and the total length of the block in the flow direction (L_{ext}).

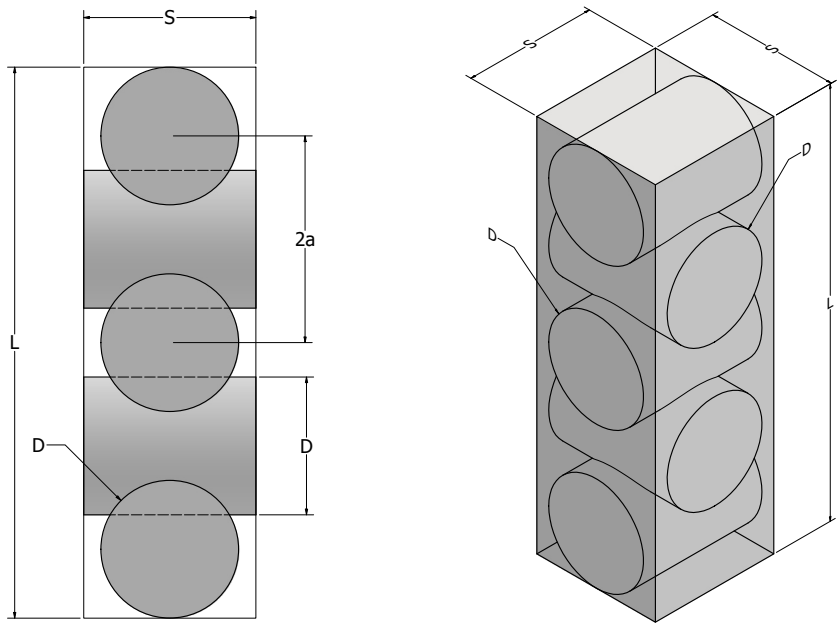

Figure 5.10.: CAD representation of a unit cell used for estimating the specific surface area and void fraction of the samples. The volume of the parallelepiped surrounding the fiber segments is used as overall volume of the unit cell in the calculations.

Each unit cell consists of N_{layers} rods of diameter D_{fiber} and length $S_{fiber,top,RAF}$ or $S_{fiber,bottom,RAF}$, depending on the orientation. The rods are stacked such that each rod is oriented at a 90-degree angle with respect to the one below, with a center-to-center distance $Z_{layer,post}$. Since $0 < Z_{layer,post} < D_{fiber}$, there is an overlap between consecutive rods. In the actual printed blocks, this overlap is necessary to achieve a better fusion between fibers of consecutive layers. The value of $Z_{layer,post}$ is determined using Equation 5.20.

$$Z_{layer,post} = \frac{L_{ext} - D_{fiber}}{N_{layers} - 1} \tag{5.20}$$

The surface area of the unit cell is given by the total area of the cylindrical surfaces of the rods, minus the area of the regions that lie within the volume of overlapping adjacent rods, as presented in Equation 5.21. The areas of the circular cross-sections of the rods are not included in this calculation because only the cylindrical surfaces are exposed to the fluid. The shape of the region on the cylindrical surface of one rod that lies within the volume of an adjacent rod is illustrated in the left drawing of Figure 5.11. The area of this region is a function of the rod diameter (D_{fiber}) and the center-to-center distance ($Z_{layer,post}$), and can be calculated using Equation 5.22. This equation was developed using a numerical approach, since, to the best of our knowledge, no analytical solution exists for this problem. The specific surface area of the unit cell, and by extension, of the region of the block available for flow, can then be calculated using Equation 5.23.

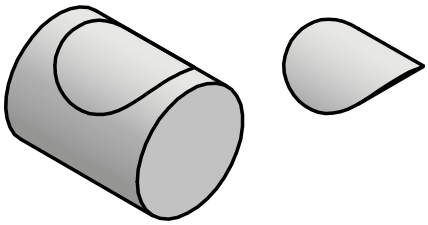

Figure 5.11.: CAD representation of the surface area and volume of the overlapping space between two adjacent rods. The left figure shows the area on the cylindrical surface of one rod that lies within the volume of the overlapping adjacent rod. The right figure shows the volume common to both overlapping rods.

$$A_{\text{sup,uc}} = \pi D_{\text{fiber}}(S_{\text{fiber,top}} + S_{\text{fiber,bottom}})\frac{N_{\text{Layers}}}{2} - 2(N_{\text{Layers}} - 1)A_{\text{ovr}} \tag{5.21}$$

$$A_{\text{ovr}} = 2D_{\text{fiber}}^2\left(1 - \left(\frac{Z_{\text{layer,post}}}{D_{\text{fiber}}}\right)^{\frac{8}{5}}\right) \tag{5.22}$$

$$\beta = \frac{A_{\text{sup,uc}}}{S_{\text{fiber,top}}S_{\text{fiber,bottom}}L_{\text{ext}}} \tag{5.23}$$

Similarly, the volume of solids within the unit cell is given by the total volume of the rods, minus the volume of the overlapping space, as presented in Equation 5.24. A CAD representation of the overlapping space between two adjacent rods is shown in the right drawing of Figure 5.11. The volume of this space is also a function of the rod diameter (D_{fiber}) and the center-to-center distance ($Z_{\text{layer,post}}$), and can be calculated using Equation 5.25. This equation was also developed using a numerical approach. The void fraction of the unit cell, and by extension, of the region of the block available for flow, can then be calculated using Equation 5.26.

$$V_{\text{s,uc}} = \frac{\pi D_{\text{fiber}}^2}{4}(S_{\text{fiber,top}} + S_{\text{fiber,bottom}})\frac{N_{\text{Layers}}}{2} - (N_{\text{Layers}} - 1)V_{\text{ovr}} \tag{5.24}$$

$$V_{\text{ovr}} = \frac{2}{3}D_{\text{fiber}}^3\left(1 - \left(\frac{Z_{\text{layer,post}}}{D_{\text{fiber}}}\right)^{\frac{8}{5}}\right)^2 \tag{5.25}$$

$$\varepsilon = 1 - \frac{V_{\text{s,uc}}}{S_{\text{fiber,top}}S_{\text{fiber,bottom}}L_{\text{ext}}} \tag{5.26}$$

On the other hand, the equivalent particle diameters can be calculated using Equation 5.27, which is an alternative way of writing Equation 5.4. Table 5.3 presents the calculated specific surface areas, void fractions, surface areas (calculated as $A_{\text{s}} = \beta V_{\text{RAF}}$), and equivalent particle diameters of the blocks under analysis.

$$D_{\text{p}} = 6\frac{1-\varepsilon}{\beta} \tag{5.27}$$

Table 5.3.: Specific surface area (β), void fraction (ε), surface area (A_s), and equivalent particle diameter (D_p) of the 3D-printed blocks.

Block ID	β [cm^2/cm^3]	ε [%]	A_s [cm^2]	D_p [μm]
90deg_400um_40p	47(2)	18(3)	59(3)	1035(58)
90deg_400um_45p	50(3)	28(5)	62(4)	868(75)
90deg_400um_50p	47(3)	30(5)	61(4)	906(88)
90deg_600um_40p	37(1)	30(3)	43(1)	1120(50)
90deg_600um_45p	34(1)	31(3)	41(1)	1212(54)
90deg_600um_50p	33(1)	34(3)	37(1)	1207(58)

5.3.2. VOID FRACTION FROM ARCHIMEDES MEASUREMENTS

The void fractions of the blocks obtained via the Archimedes method are reported in Table 5.4. A comparison between these values and those calculated using the geometric model, presented in Table 5.3, reveals significantly lower calculated void fractions. Before providing an explanation for these differences, it is important to note that the calculated void fractions refer only to the regions of the blocks available for flow, whereas the measured void fractions correspond to the entire blocks. Furthermore, since the perimeter of each block contains walls with negligible void space, the void fraction of an entire block is actually smaller than that of its flow region. Therefore, the actual difference between the measured and calculated void fractions for the flow region is even greater than the difference indicated by the values in Table 5.3 and Table 5.4.

One key difference between the geometric model and the actual fibers is that the model assumes perfectly smooth surfaces, whereas the real fibers exhibit surface roughness, including pores and cavities. These surface features can be filled with liquid during the Archimedes measurements, effectively increasing the measured void fractions. The rough nature of the fiber surfaces in one of the samples used in this study is evident in Figure 5.8. Additionally, the cross-sectional shape of the fibers may deviate from an ideal circle and resemble an ellipse due to deformation during printing and heat treatment. This deformation can alter the packing structure and the way empty spaces within the blocks are filled. Furthermore, the geometric model relies on average fiber dimensions, while in reality, there exists a distribution of fiber diameters and separations. Accounting for local variations in these parameters could lead to a more accurate estimation of the void fraction.

We attribute the observed discrepancy between the calculated and measured void fractions primarily to the presence of surface roughness, pores, and cavities on the printed fibers. While deviations in fiber shape

due to deformation during printing could influence packing density, such deformations would likely lead to denser packing and consequently smaller measured void fractions, contrary to the larger values obtained via the Archimedes method. Similarly, although incorporating local variations in fiber diameter and separation could improve the accuracy of the geometric model, these adjustments are expected to result in only minor corrections to the calculated void fraction. In contrast, the surface features of the fibers directly increase the volume accessible to the liquid during Archimedes measurements, offering a more plausible explanation for the significant differences observed.

It is also important to note that these surface irregularities, while impactful for volume-based measurements, are less relevant from a hydrodynamic perspective, particularly in relation to pressure drop analysis, where the geometric surface plays a more critical role [104]. The geometric model appropriately captures this geometric surface, making it more suitable for flow-related calculations despite its deviation from the Archimedes-based measurements.

Table 5.4.: Void fractions from Archimedes measurements. The uncertainties in solid volume, solid density, and void fraction were calculated using the error propagation method. The standard uncertainty in mass measurements is ± 0.15 mg. Ethanol was used as fluid. The effect of micro air bubbles was not accounted for in the estimation of uncertainty.

Block ID	m_{air} [g]	m_{eth} [g]	V_s [cm^3]	ρ_s $\left[\frac{g}{cm^3}\right]$	ε_{Arch} [-]
DP_01	6.2162(2)	5.2764(2)	1.197(2)	5.193(8)	0.255(7)
DP_02	5.7889(2)	4.9843(2)	1.025(2)	5.649(9)	0.362(6)
DP_03	5.5416(2)	4.7909(2)	0.956(2)	5.796(9)	0.405(6)
DP_04	5.9733(2)	5.1197(2)	1.087(2)	5.494(9)	0.324(6)
DP_05	5.8371(2)	5.0084(2)	1.055(2)	5.530(9)	0.343(6)
DP_06	5.5311(2)	4.7469(2)	0.999(2)	5.538(9)	0.379(6)

5.3.3. CHARACTERIZATION OF SAMPLES VIA X-RAY TOMOGRAPHY

X-ray computed tomography (XCT) was also considered for the geometric characterization of the samples. This advanced imaging technique provides a detailed view of the internal structure of the blocks. It can reveal internal defects such as micro cracks and pores within the fibers [134] while also offering the possibility to obtain valuable geometric information, including fiber diameter distribution, flow-channel size distribution, average void fraction, and surface area. As previously discussed, these parameters are essential

for a comprehensive characterization of the geometry of the blocks. However, due to its limited accessibility and high cost, XCT is not a practical solution for routine characterization of every 3D-printed block. Instead, it could serve as a validation tool for the geometric model presented in this chapter, enabling the model to be reliably applied for the characterization of future blocks.

Researchers from the German Federal Institute for Material Research and Testing (Bundesanstalt für Materialforschung und -prüfung BAM) analyzed the samples using this technique. Figure 5.12 shows a 3D rendering of sample 90deg_400um_40p_a, obtained using a voxel size of 20 µm. As expected, image analysis revealed internal defects such as pores and cracks, some of which propagate through several layers of fibers. In addition, BAM researchers developed image-processing methods to estimate the volume of solids from XCT data, allowing the calculation of void fraction within a defined region of interest (ROI) for each block. The ROI was selected to approximately match the RAF. Table 5.5 presents a comparison of the void fractions obtained from the XCT analysis, the geometric model described in subsection 5.3.1, and the Archimedes method.

As can be seen in Table 5.5, void fractions obtained from XCT are in very good agreement with those calculated using the geometric model developed in this thesis. This confirms that the model properly represents the geometry of the block and can be reliably used to compute critical parameters such as specific surface area and void fraction. The discrepancy between these values and those obtained via the Archimedes method suggests that the resolution of the XCT scans allowed to primarily capture the geometric surface of the fibers, without resolving the finer surface features such as pores and cavities that can be filled with liquid during the Archimedes measurements. The fact that this discrepancy is more pronounced in the samples with 400 µm fibers, those with larger surface areas, further supports this interpretation.

5.4. RESULTS AND DISCUSSION

5.4.1. PRESSURE DROP MEASUREMENTS

Pressure drop data was collected at three different water temperatures for each sample: approximately 7 °C, 25 °C, and 50 °C. A differential pressure sensor (NXP MPXV5100DP with a maximum error of +/- 2.5 %) connected between the inlet and outlet ports of the sample holder assembly was used to measure the pressure drop. The transfer function of the sensor was calibrated using a water column. The resulting relative error is approximately 0.68% at differential pressures around 50 kPa, increasing to 2.8 % at pressures below 1 kPa. These errors are so small that the corresponding error bars in the pressure drop vs flow rate plots are hardly noticeable. The hydrostatic pressure resulting from

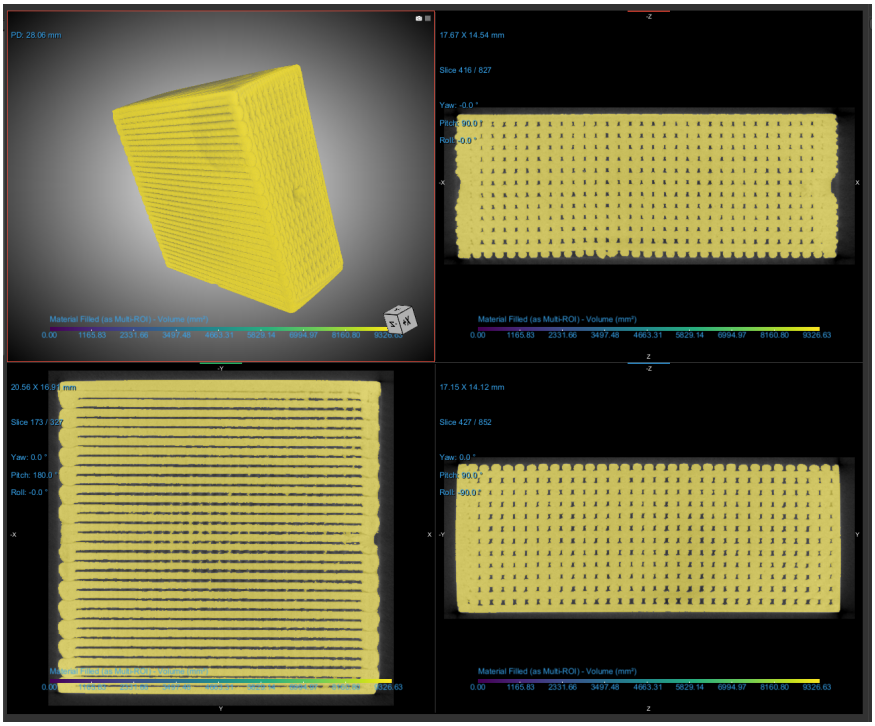

Figure 5.12.: Several views of the XCT reconstruction of sample 90deg_400um_40p_a. This image was provided by Savvina Papaioannou, PhD student at BAM, and it is presented here with her permission.

Table 5.5.: Comparison of void fractions obtained from XCT analysis, the geometric model developed in this thesis, and the Archimedes method. The scan resolution was 20 µm for sample 90deg_400um_40p_a and 12 µm for all other samples. XCT results are reproduced with permission of the authors. Error bars are not available for XCT void fractions.

Block ID	ε_{XCT} [-]	ε_{model} [-]	ε_{Arch} [-]
90deg_400um_40p_a	0.206(X)	0.18(3)	0.255(7)
90deg_400um_45p_a	0.275(X)	0.28(5)	0.362(6)
90deg_400um_50p_a	0.298(X)	0.30(5)	0.405(6)
90deg_600um_40p_a	0.297(X)	0.30(3)	0.324(6)
90deg_600um_45p_a	0.308(X)	0.31(3)	0.343(6)
90deg_600um_50p_a	0.339(X)	0.34(3)	0.379(6)

the vertical alignment of the sample holder was subtracted from the differential pressure measurements. The flow rate was measured using an electromagnetic flow meter (details given in subsection 5.2.1).

The temperature of water was regulated by circulating it through a finned-tube heat exchanger submerged in a thermostatic bath. Once the water temperature reached a steady-state value, the volumetric flow rate was systematically reduced from a maximum to a minimum value in small steps of equal duration. The combined effects of temperature-induced changes in water viscosity and variations in fluid velocity allowed for the exploration of Reynolds numbers spanning three orders of magnitude. The maximum volumetric flow rate was limited by the maximum allowable pressure of the system, 3 bar, which was reached primarily due to the pressure drop across the ceramic filters.

Figure 5.13 presents the measured pressure drop as a function of volumetric flow rate for the samples with 600 µm fibers, while Figure 5.14 shows the corresponding curves for the samples with 400 µm fibers. As shown in Figure 5.13 and Figure 5.14, pressure losses increase as the temperature decreases due to the higher viscosity of the fluid. Additionally, a decrease in the inter-fiber distance, i.e. the void fraction of the samples, results in smaller flow channels and larger surface areas, leading to higher velocities and increased friction losses. Similarly, blocks with smaller fiber diameters exhibit larger surface areas and consequently greater friction losses. This trend is evident when comparing Figure 5.13d and Figure 5.14d. For instance, at a flow rate of 2 L min^{-1}, the sample 90deg_600um_40p_a exhibited a pressure drop of 6 kPa, whereas the sample 90deg_400um_40p_a experienced a significantly higher pressure drop of 17 kPa.

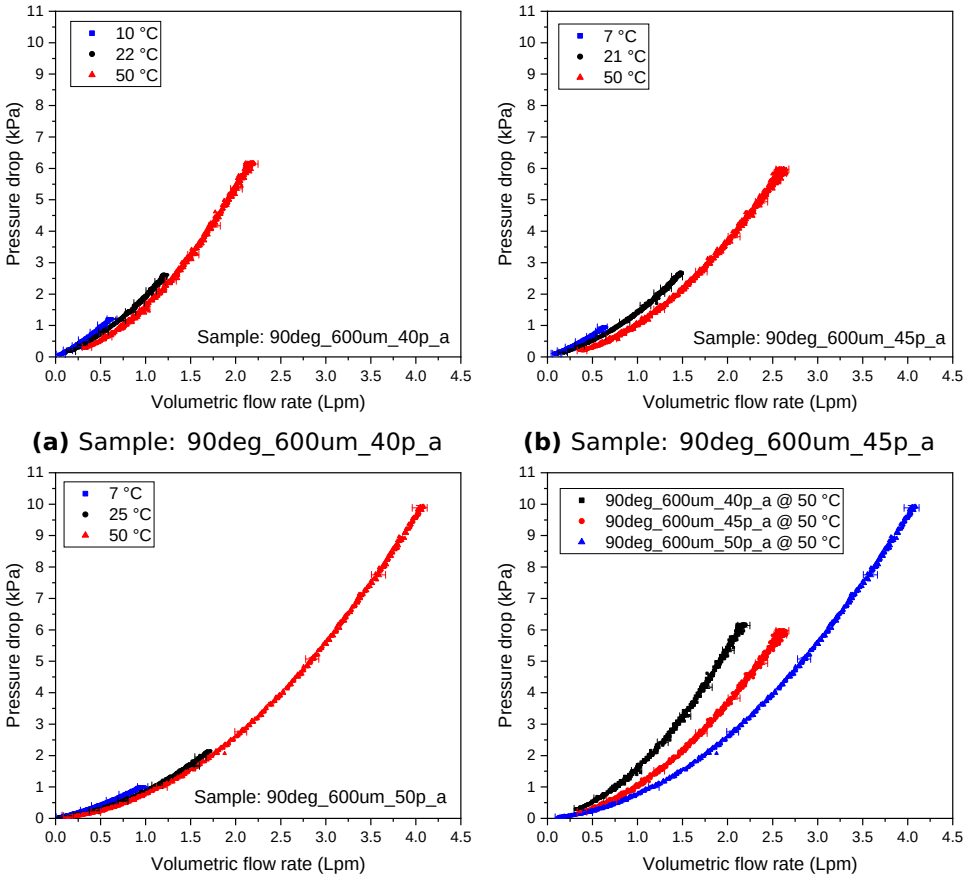

(a) Sample: 90deg_600um_40p_a

(b) Sample: 90deg_600um_45p_a

(c) Sample: 90deg_600um_50p_a

(d) 600 µm 50 °C

Figure 5.13.: Measured pressure drop as a function of volumetric flow rate for the samples 90deg_600um_40p_a (a), 90deg_600um_45p_a (b), 90deg_600um_50p_a (c), and a comparison of the pressure drop for these three samples with fluid temperature of 50 °C (d).

5.4.2. CORRELATION OF PRESSURE DROP AND FLOW RATE DATA

The 3D-printed blocks of MCM were treated as packed beds of particles to derive a general expression correlating the friction factor to the Reynolds number, a method previously adopted by others [149, 150]. This approach involves using the same definitions of friction factor and Reynolds number applicable to packed beds of particles, as introduced in subsection 5.1.3, and determining equivalent particle diameters based on the void fraction and specific surface area of the blocks using Equation 5.27.

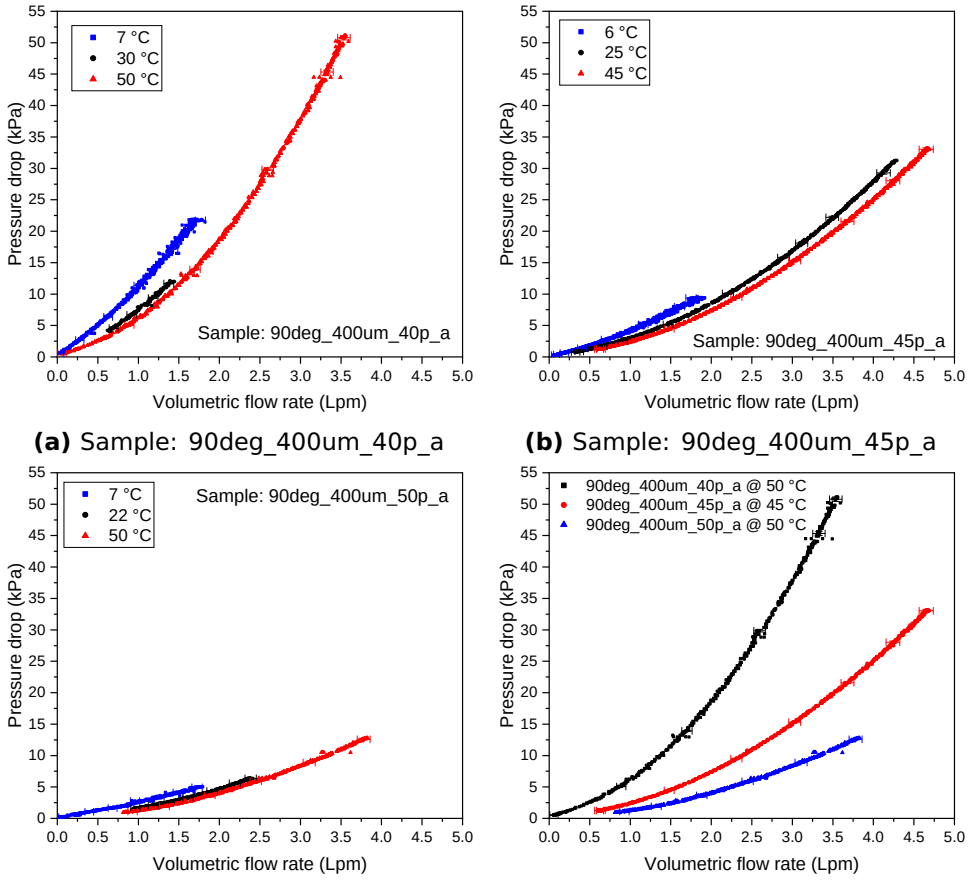

(a) Sample: 90deg_400um_40p_a **(b)** Sample: 90deg_400um_45p_a

(c) Sample: 90deg_400um_50p_a **(d)** 400 µm 50 °C

Figure 5.14.: Measured pressure drop as a function of volumetric flow rate for the samples 90deg_400um_40p_a (a), 90deg_400um_45p_a (b), 90deg_400um_50p_a (c), and a comparison of the pressure drop for these three samples with fluid temperature of approximately 50 °C (d).

Figure 5.15 presents the experimental data processed using this approach. As shown, the data for blocks with different fiber diameters and fiber separation distances collapse around a trend line. This grouping effect only occurred after applying the modified non-dimensional numbers, whereas previous attempts using alternative definitions of friction factor and Reynolds number failed to unify the curves. The spread in the data is attributed mainly to the uncertainties in the fiber diameters that propagate to the void fractions and equivalent particle diameters derived with the geometric model, as well to the

uncertainty in the flow rate measurements, which dominates at low flow rates. Errors bars in Figure 5.15 were calculated using the error propagation method and include the uncertainty in all measured variables such as flow rate, pressure drop, fiber diameter, water temperature, and block dimensions.

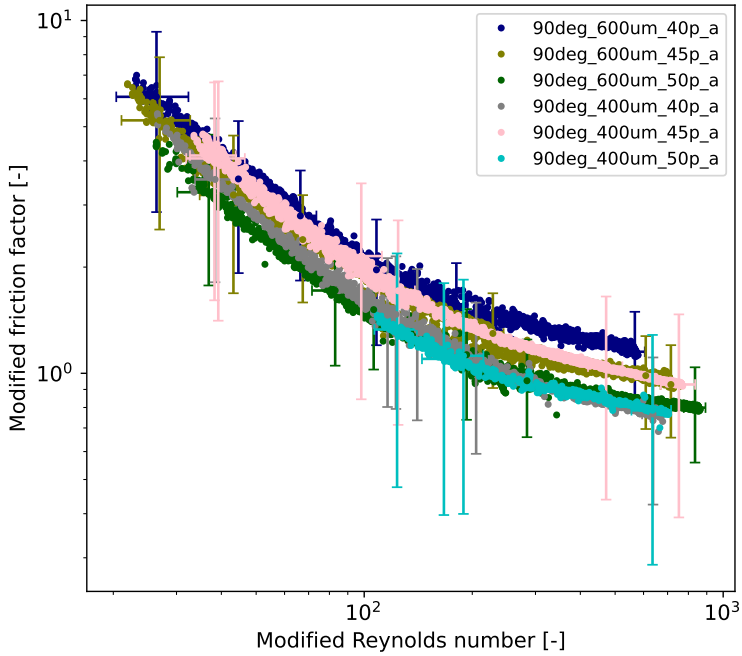

Figure 5.15.: Modified friction factor vs modified Reynolds number for all measured samples. Error bars represent the uncertainties in both friction factor and Reynolds number, calculated using the error propagation method. At high Reynolds numbers, the uncertainty in fiber diameter is the dominant contributor to the friction factor uncertainty, while at low Reynolds numbers the uncertainty in fluid velocity plays a more significant role.

Once the experimental data collapsed onto a well-defined trend line, deriving a suitable correlation became relatively straightforward. Given that our approach builds on Ergun's work and uses the same non-dimensional groups as his correlation (Equation 5.1), we chose to fit our data to an expression of similar form. Specifically, we used the model $ff_{\text{mod}} = a/Re_{\text{mod}} + b$, and developed a fitting method that explicitly incorporates uncertainty in both Reynolds number and friction factor.

To account for the measurement uncertainties, synthetic data points

were generated around each original (ff, Re) pair by randomly sampling from a normal distribution, using the known experimental uncertainties as standard deviations. To ensure fair statistical weight across the Reynolds number domain, a bin-aware sampling strategy was employed: more synthetic points were generated in underrepresented regions, resulting in an even distribution of synthetic data across bins. The prediction bounds were then determined by identifying the narrowest envelope, of the same functional form as the fitted model, that enclosed at least 68.3% of the synthetic points in each bin. This per-bin requirement ensures that the prediction interval captures local variability in the data, particularly the greater scatter observed at low Reynolds numbers.

The final fitted correlation, including the estimated bounds, is:

$$ff_{\text{mod}} = \frac{110 \pm 55}{Re_{\text{mod}}} + (0.7 \pm 0.5) \tag{5.28}$$

This expression is valid for the range $20 < Re_{\text{mod}} < 1000$. The prediction envelope reflects the combined effect of model and data uncertainty and corresponds to approximately a ±1 standard deviation interval. In practice, the fraction of synthetic points falling within the envelope ranged from about 68% in the low-Reynolds-number bins to over 90% in the higher bins. Figure 5.16 shows a selection of the synthetic data points, the original data with error bars, the fitted model, and the prediction interval.

5.4.3. COMPARISON WITH OTHER AMR GEOMETRIES

A fair comparative study of different AMR geometries must ensure that the regenerators have similar void fraction and total volume to achieve a comparable MCM mass. If active experiments are involved in the comparison, it is also important that they share similar shapes and overall dimensions to obtain comparable shape demagnetization factors. In addition, the total surface area of the AMRs must also be comparable to ensure that differences in convective heat transfer arise from variations in the heat transfer coefficient rather than differences in available heat transfer area. Only under these conditions can performance differences be primarily attributed to variations in the thermal-hydraulic characteristics of the geometries and potential differences in internal demagnetizing factors.

Some researchers have adhered to these principles when comparing the performance of AMRs with different geometries, either experimentally or numerically. For instance, Trevizoli et al. [46] experimentally compared the performance of three Gadolinium AMRs: a packed bed of spheres, a pin array, and a parallel plate. They carefully selected the dimensions and key geometric parameters of the AMRs to

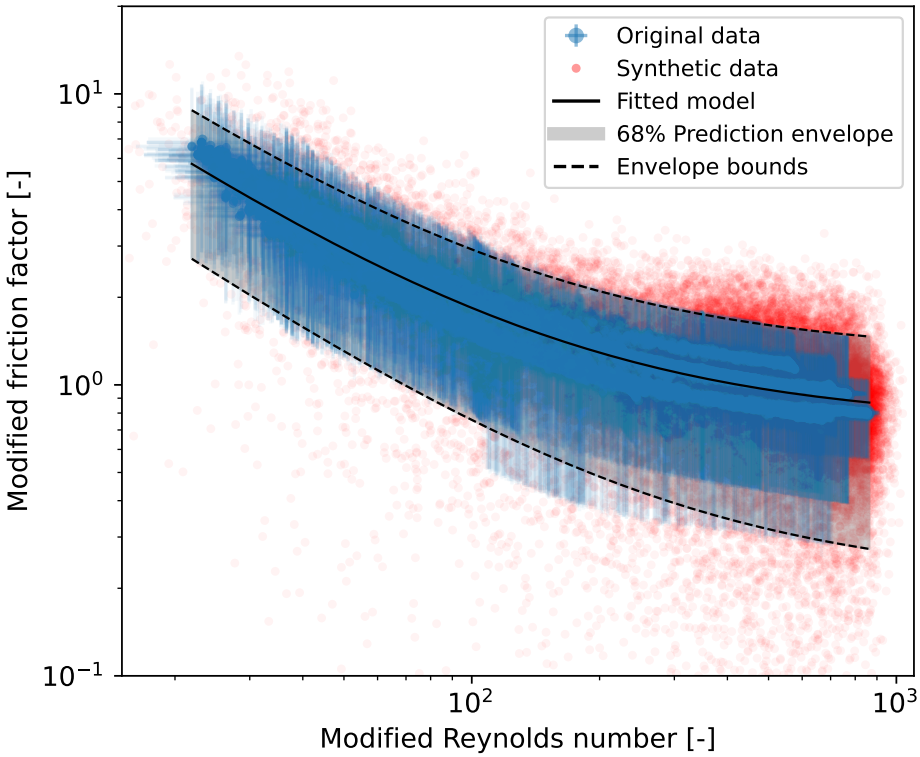

Figure 5.16.: Visualization of the correlation between friction factor and Reynolds number. The original experimental data are shown with error bars in blue, while the red points represent a 10% sample of the synthetic dataset generated via random perturbation based on measurement uncertainties. The fitted model, $ff_{\text{mod}} = 110/Re_{\text{mod}} + 0.7$, is shown as a solid black line. The shaded region represents the prediction envelope, constructed to enclose at least 68.3% of synthetic points in each Reynolds number bin. The dashed lines mark the upper and lower boundaries of this envelope, reflecting the propagated uncertainty in the correlation due to measurement uncertainties.

achieve comparable surface areas, void fractions, and total volumes. Lei et al. [110] conducted a numerical comparison of the performance of packed-bed, parallel-plate, packed-screen-bed, and micro-channel AMRs, using the same hydraulic diameter, void fraction, and total volume across all geometries. Since surface area is a function of void fraction and hydraulic diameter, it was automatically consistent.

Conversely, Yuan et al. [151] experimentally compared a packed-bed AMR with several parallel-plate AMRs, all with similar total volume and void fraction. However, the parallel-plate AMRs had a smaller heat transfer area than the packed-bed AMR, making the comparison less fair for the parallel-plate geometry.

Figure 5.17 presents a comparison of the correlations of the modified friction factor as a function of the modified Reynolds number for four regenerator geometries: packed beds, parallel plates, squared micro channels, and the 3D-printed geometry. The correlation for the parallel plates is presented in Equation 5.29 and that for squared micro channels is presented in Equation 5.30. These are equivalent to the equations $ff_D = 96/Re$ and $ff_D = 64/Re$ that are commonly used for parallel plates and micro channels respectively [110], where ff_D is the Darcy friction factor and Re is the Reynolds number, both calculated using the average channel velocity and the hydraulic diameter. The derivation of Equation 5.29 is presented in Appendix F, and a similar approach was used in the derivation of Equation 5.30.

$$ff_{mod} = \frac{108}{Re_{mod}} \text{ (Parallel plates)} \tag{5.29}$$

$$ff_{mod} = \frac{72}{Re_{mod}} \text{ (Squared micro channels)} \tag{5.30}$$

It is evident from Figure 5.17 that the pressure drop of the 3D-printed blocks falls between that of packed beds and parallel plates, getting much closer to that of the parallel plates at low Reynolds numbers. This is further illustrated in Figure 5.18, which presents a direct comparison of the measured pressure drop of the sample 90deg_400um_50p_a with that calculated for an equivalent packed bed of spheres and for an equivalent stack of parallel plates. Following the principles described above, the packed bed and the parallel-plate stack are modeled with the same void fraction, the same total volume, and the same surface area of the 3D-printed block under comparison. In this case, the particle diameter of an equivalent packed bed is 906 µm. Similarly, the plate thickness and spacing of an equivalent parallel-plate stack are 302 µm and 128 µm respectively.

Although the equivalent parallel-plate regenerator would exhibit a much smaller pressure drop compared to the block used in this example, the thickness of the plates and the spacing needed to achieve the same surface area and void fraction are difficult to achieve in practice. Plate thickness should be above 350 µm to avoid excessive deformation during the AMR cycle. Maintaining uniformity of channel spacing is also challenging with such small gaps between the plates. Non-uniform gaps lead to uneven flow distribution, which is undesirable for an appropriate AMR operation.

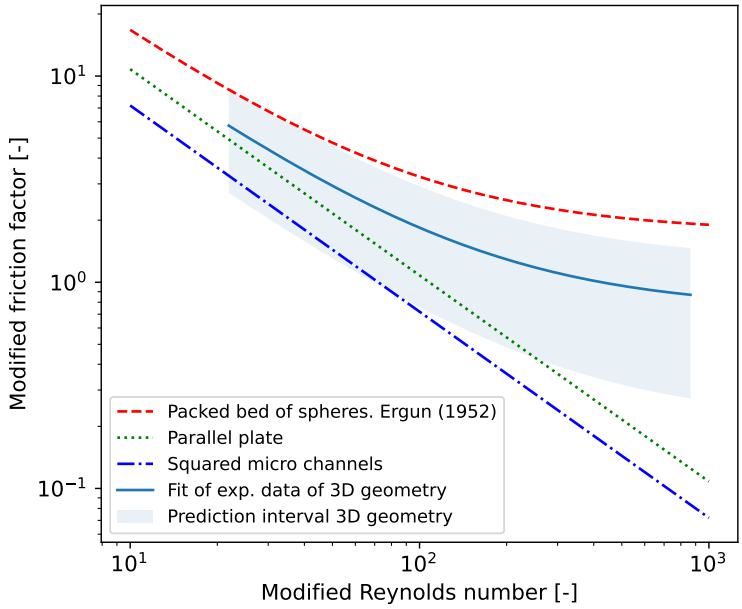

Figure 5.17.: Comparison of the correlations of the modified friction factor vs modified Reynolds number for four regenerator geometries: packed beds, parallel plates, micro channels, and the 3D printed geometry

5.4.4. HEAT TRANSFER EXPERIMENTS

As introduced in subsection 5.1.5, the heat transfer coefficients of the 3D-printed blocks of MCM were determined through steady-state experiments, in which a temperature difference between the blocks and water was established using an electrical current. Despite having made significant refinements to the setup, measurement method, and heat transfer model, the iterative development process, along with simultaneous testing, data collection, and analysis, required more time than was available to complete this thesis chapter. Therefore, we report here the most representative part of the data collected so far, acknowledging that our analysis indicates the need for further adjustments to improve the accuracy of the estimated heat transfer coefficients a the reproducibility of experiments. A list of the required improvements is provided at the end of this chapter. Nevertheless, we remain confident that this method is suitable for determining the heat transfer coefficients of the 3D-printed blocks.

Heat transfer experiments were conducted with water running at approximately room temperature to minimize heat exchange between

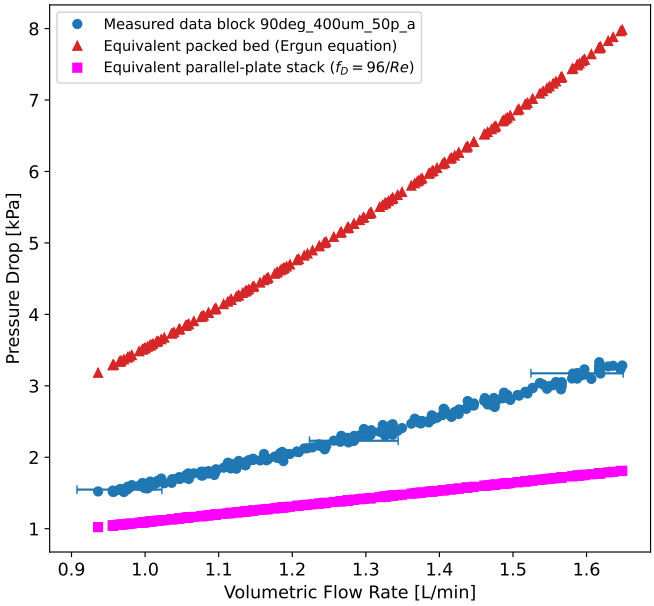

Figure 5.18.: Comparison of the pressure drop of the sample 90deg_400um_50p_a with that of an equivalent packed bed of spheres and an equivalent stack of parallel plates. The regenerators are considered equivalent when they have the same total volume, same void fraction, and same surface area, thus same equivalent particle diameter. The error bars of measured pressure drops are smaller than the marker size.

water and ambient through the casing of the sample holder. The experiments followed these steps: the thermostatic bath was set to operate in external temperature control mode, with its set-point adjusted as close as possible to room temperature; water was circulated at the highest possible flow rate; after temperatures stabilized, the high-current power supply was turned on; the flow rate was then gradually decreased, allowing stabilization between each reduction step, until a very low flow rate was reached.

This process can be observed in the data presented in Figure 5.19, which corresponds to the sample 90deg_600um_40p_a, where a current of 50 A was used. On the other hand, a similar process was followed in the measurements conducted with the sample 90deg_600um_50p_a, presented in Figure 5.20, but this time using three different currents: 50 A, 100 A, and 150 A. In this case, the flow rate was decreased only after reaching the highest current. These variations in measurement procedures reflect our exploration of the different options offered by

the setup and the uncertainty we faced regarding the most appropriate procedure to follow in these experiments.

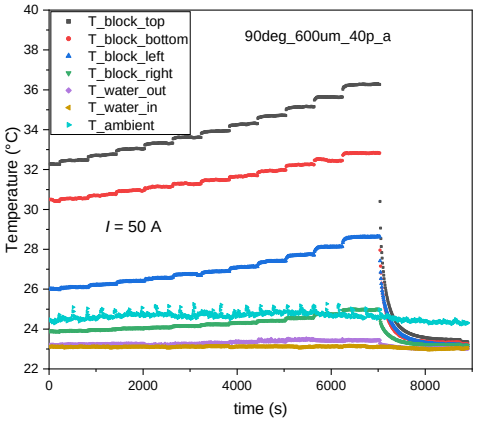

(a) Temperature measurements

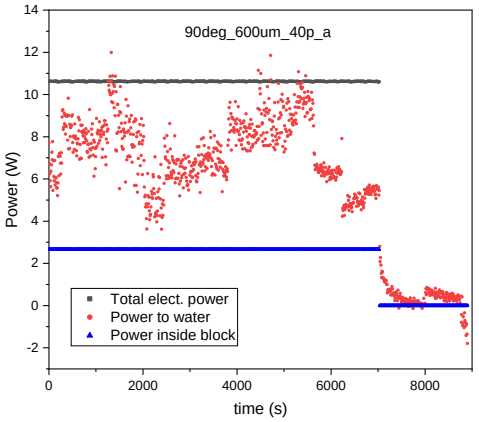

(b) Electrical power

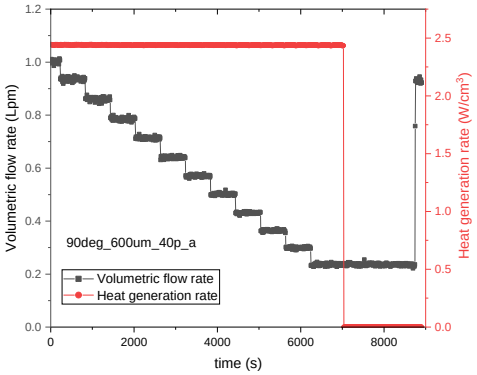

(c) Flow and heat generation rate

Figure 5.19.: Measured variables during the heat transfer experiment of the sample 90deg_600um_40p_a. Temperatures versus time are shown in (a), the total electrical power, the heat absorbed by the water, and the power generated inside the block are shown in (b), and the volumetric flow rate and the calculated rate of heat generation per unit volume shown in (c).

A few additional aspects to highlight regarding the experiments presented in Figure 5.19 and Figure 5.20 are:

- It is evident from Figure 5.20a that the stabilization time after each flow rate reduction was insufficient. As a result, only a limited number of data points from the final part of the stabilization periods were used to compute heat transfer coefficients. In contrast, the

temperature stabilization was more effectively controlled in the experiment of the sample 90deg_600um_40p_a, as illustrated in Figure 5.19a, allowing for the inclusion of more data points in the calculation.

- In Figure 5.20a, the temperature of the right surface of the block was higher than that of the top surface after $t = 7000\,\mathrm{s}$. This occurred because the internal electrical resistance of the block was slightly greater than the total contact resistance in this case.

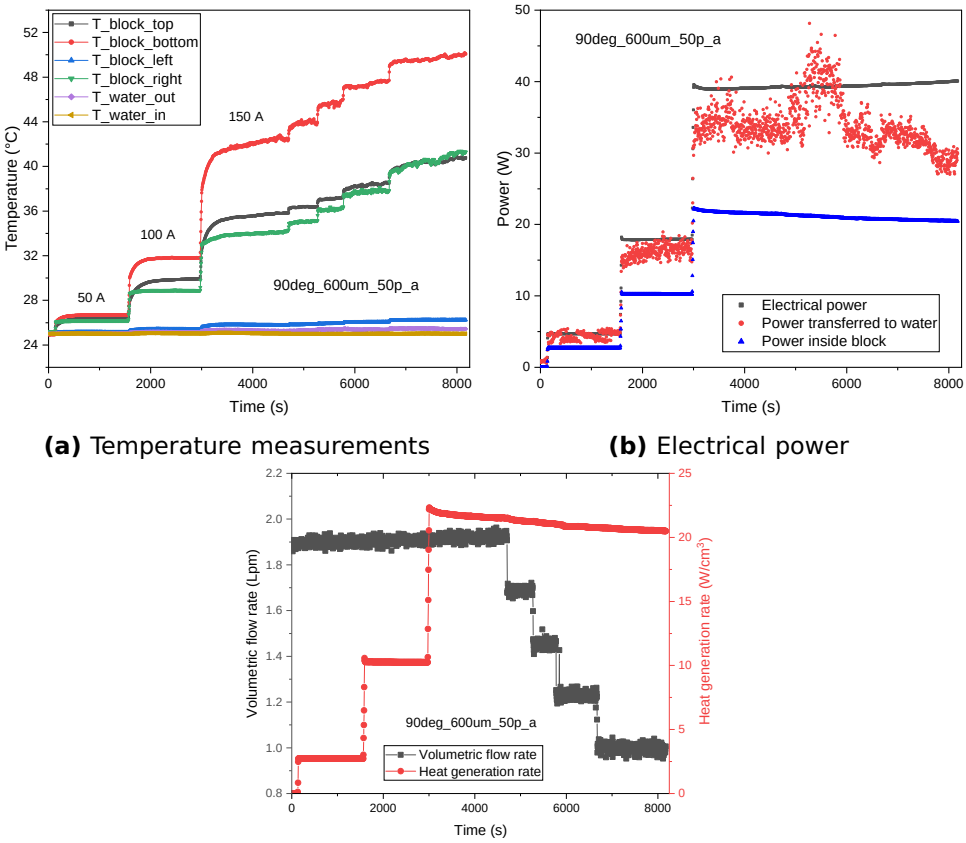

(a) Temperature measurements

(b) Electrical power

(c) Flow and heat generation rate

Figure 5.20.: Measured variables during the heat transfer experiment of the sample 90deg_600um_50p_a. Temperatures versus time are shown in (a), the total electrical power used and the power generated inside the block are shown in (b), and the volumetric flow rate and the calculated rate of heat generation per unit volume shown in (c)

Consequently, more heat was generated within the block than at its surfaces, an effect that became noticeable only when the flow rate decreased significantly. However, since the proposed heat transfer model is one-dimensional, it does not incorporate these side temperatures.

- The temperature of the right surface of sample 90deg_600um_40p_a and that of the left surface of sample 90deg_600um_50p_a are close to the temperature of water because those sides of the blocks were missing one fiber during printing. This defect is illustrated in Figure 5.21. The corresponding temperature sensors measured an average of the water and solid temperatures, as half of their surface were in contact with water and half with the solid.

- A significant amount of heat may have been lost to the environment from the copper plates due to the high temperatures they reached toward the end of both experiments (see $T_{\text{block,top}}$ and $T_{\text{block,bottom}}$). Data analysis further suggests that such large temperature differences between the block surface and water should be avoided to increase accuracy of the calculated heat transfer coefficients.

- Contact resistance was lower in the experiment of sample 90deg_600um_50p_a. Because of this, it was possible to reach 150 A.

- The heat absorbed by water in each experiment is shown in Figure 5.19b and Figure 5.20b. This was calculated using Equation 5.7. In Figure 5.20b, an artifact appears around $t = 6000$ s, where the heat absorbed by water exceeds the total electrical power input. This discrepancy is attributed to errors in the water temperature measurements.

One important aspect that was difficult to control, and significantly influenced experimental results, was the variability in contact resistance between the blocks and the copper plates across different experiments. High contact resistance led to increased surface heating and a higher likelihood of hot spots, which could cause the formation of micro bubbles of water vapor. Micro bubbles in the copper-sample interface may lead to increased contact resistance. Additionally, some micro bubbles might travel with the water flow and adhere to the downstream water temperature sensor, affecting measurement accuracy. In the worse case scenario, a combination of high resistance and high currents could result in voltages between the copper plates sufficient to trigger electrolysis of water.

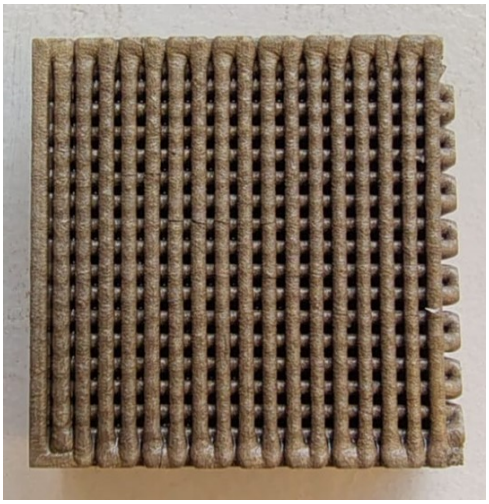

Figure 5.21.: Photograph of of sample 90deg_600um_50p_a. A missing fiber on the right surface allows water to influence the temperature measurement on that side.

Furthermore, large contact resistances increased the uncertainty in estimating the surface temperature of the blocks, which was not directly measured but rather assumed to be equal to the temperature of the copper plates. The use of indium foil promises to be an effective way to minimize the contact resistance. However, its effectiveness could not be tested before the completion of this thesis chapter.

5.4.5. HEAT TRANSFER COEFFICIENTS

The heat transfer coefficient is presented in Figure 5.22a as a function of volumetric flow rate for the two samples with 600 µm fibers, whose temperature measurements were introduced in subsection 5.4.4. Similarly, Figure 5.22b presents the corresponding Nusselt numbers as a function of Reynolds numbers. In this case, the Nusselt number is defined according to Equation 5.31, while the Reynolds number is calculated using the superficial velocity and the equivalent particle diameter, D_p.

$$Nu = \frac{hD_p}{k} \tag{5.31}$$

The heat transfer model introduced in subsection 5.1.6 was used to calculate the heat transfer coefficients. The calculation involved a double iterative process in which the heat fluxes used as boundary conditions were iteratively adjusted along with the value of the heat

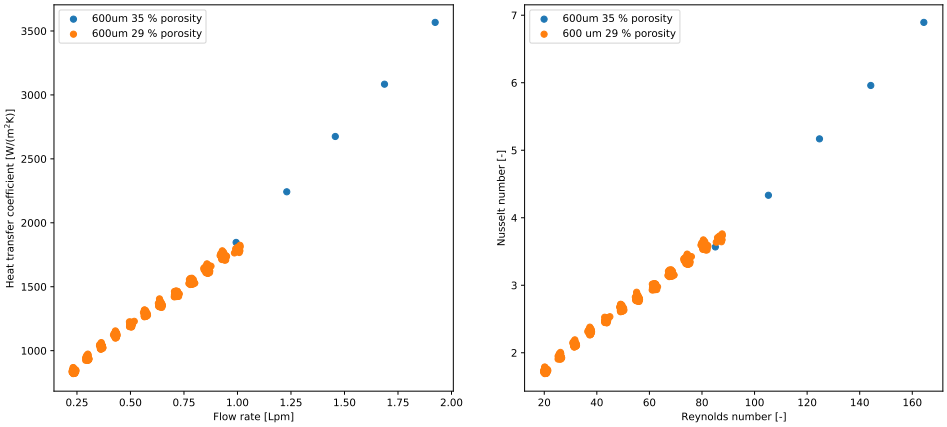

(a) Heat transfer coefficient **(b)** Nusselt vs Reynolds

Figure 5.22.: (a) Heat transfer coefficient versus volumetric flow rate and (b) Nusselt numbers versus Reynolds numbers calculated for the samples with 600 µm fibers

transfer coefficient to match the temperatures of the top and bottom sensors. This iterative approach was necessary because the fraction of the heat generated at the top and bottom surfaces was unknown. However, the combined heat generated at both surfaces together could be estimated from the experimental data using Equation 5.32. As previously mentioned, $\dot{Q}_{\text{water}}$, the heat transferred to the water, showed a large spread in the data, resulting from the propagation of uncertainties in the measured quantities used for its calculation. Therefore, the corresponding data was linearly interpolated to help reduce fluctuations in the calculated heat transfer coefficients.

$$\dot{Q}_{\text{surfaces}} = \dot{Q}_{\text{water}} - \dot{Q}_{\text{inside}} \tag{5.32}$$

A correlation between the Nusselt number and the Reynolds number could not be derived because of the lack of sufficient data. Since the measuring method was still being refined, the collected data across different samples was not very consistent. Further improvements are necessary to improve the quality of data as well.

5.4.6. Uncertainties in the estimation of heat transfer coefficients

The estimation of heat transfer coefficients in this study is subject to several sources of uncertainty. This section focuses on two key contributors: (1) the effective thermal conductivity of the 3D-printed

block in the direction perpendicular to the water flow and parallel to the electrical current, and (2) the estimation of heat flux through the surfaces of the block in contact with the copper plates. Both factors significantly influence the accuracy of the calculated heat transfer coefficients and must be carefully considered in the interpretation of the experimental results.

The effective thermal conductivity of the block in the direction perpendicular to the water flow and parallel to the electrical current flow has a big impact in the calculated values of the heat transfer coefficient. The sensitivity to this parameter can be seen in Figure 5.1b. As stated by Chang [152], thermal resistance analysis can be used to determine the minimum and maximum effective thermal conductivity of a porous solid filled with a fluid. The minimum value is obtained when the fluid and solid volumes are arranged in series (Equation 5.33), while the maximum value is obtained when they are arranged in parallel (Equation 5.34). The actual effective thermal conductivity of the porous material filled with a fluid lies in between these limits. For the case of the 3D-printed blocks of MCM, the average between these boundaries is a reasonable assumption (see the caption of Figure 5.23).

$$k_{\text{eff}}^{\text{min}} = \left[\frac{\varepsilon}{k_{\text{f}}} + \frac{1-\varepsilon}{k_{\text{s}}} \right]^{-1} \tag{5.33}$$

$$k_{\text{eff}}^{\text{max}} = \varepsilon k_{\text{f}} + (1-\varepsilon) k_{\text{s}} \tag{5.34}$$

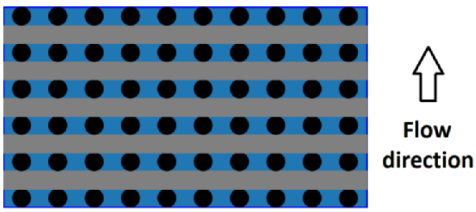

Figure 5.23.: Simplified representation of the top view of a 3D printed block for a thermal resistance analysis. Heat flow is assumed to be perpendicular to the plane of the page. Blue represents water. In 50 % of the printed layers, the solid fibers (black circles) and water are arranged in a parallel configuration. In the remaining 50 %, the fibers (gray rectangles) and water are arranged in series.

A second source of uncertainty has to do with the estimation of the heat flux on both surfaces of the block in contact with the copper plates. Because the contact resistance is different in both cases, the heat generated in those surfaces is also different. This can be seen in the fact that the temperatures of both copper plates are not the same.

Furthermore, as the temperature of the block increases upon reduction of flow rate during the experiments, it is expected that the amount of heat that leaks to the surrounding environment also increases. This was not measured. The total electrical power was measured, the heat generated inside the block was also measured, and the heat transferred to water could be in principle calculated.

However, given the small temperature change that water experiences, which practically lies within the range of accuracy of the temperature sensors, and considering the intrinsic error of the flow rate measurement, the calculated heat absorbed by water includes a significant error. Therefore, the calculated heat transferred to water was linearly interpolated in order to obtain the heat flux from the surfaces. The heat lost to the environment increased with increasing temperature of the copper plates. As a result the heat transferred to water decreased. This can be seen approximately in the decreasing trend of the heat absorbed by water presented in Figure 5.19b and Figure 5.20b. Additionally, the temperature of the copper plates can be so high that heat transfer by radiation becomes important, but this effect was not included in the heat transfer model and analysis.

5.5. CONCLUSIONS

A correlation was developed for the prediction of the pressure drop in blocks of MCM manufactured using an extrusion-based additive manufacturing technique. The correlation uses the definitions of equivalent particle diameter, modified Reynolds number, and modified friction factor used in packed beds of particles. The experimental data suggest that the 3D printed geometry offers an advantage in terms of pressure drop when compared to packed beds of particles. This is due to the fact that the studied geometry has straight flow channels causing less tortuosity in the fluid flow, which is specially relevant at high flow rates.

A method for determining the heat transfer coefficient in the 3D printed blocks of MCM was proposed. The method consists of creating a temperature difference between the sample and water under steady-state conditions by self-heating the samples using large electrical currents. The method has been significantly refined and remains promising for the intended purpose as long as some important aspects are further controlled. The most important aspect to control is the contact resistance between the blocks and the copper plates used for transferring electricity to the blocks. Indium foil is expected to help solving this issue. A correlation between the Nusselt number and the Reynolds number could not be derived because the experimental method was still being refined and because the data across different samples was not collected consistently.

Better-quality blocks are needed to develop correlations with reduced prediction intervals and increased reliability. The blocks received for this research exhibited several defects, including missing fibers along the edges, inconsistent spacing between fibers, contacting fibers, variations in fiber diameter, and surface roughness. These issues make it difficult to properly characterize the geometry of the blocks and to construct a reliable flow and heat transfer analysis.

The preferred method for a simple, accessible, and relatively accurate geometric characterization of the blocks consists of capturing microscope images of the block surfaces, from which parameters such as average fiber diameter, fiber separation, and fiber overlap can be extracted using image-processing software. These dimensions can be used in a geometric model to calculated surface area and solid volume of the blocks. XCT is a valuable tool for validating this approach, but due to its high cost and limited accessibility, it is unlikely to become the standard characterization method.

A geometric model of the 3D-printed blocks was proposed. It considers modeling the fibers as smooth circular rods that overlap with those of adjacent layers. The surface area and solid volume of a characteristic unit cell were calculated using four geometric parameters: the average fiber diameter, the center-to-center spacing between fibers within a layer, the vertical spacing between layers, and the overall height of the block from the bottom to the top layer. These parameters were extracted from SEM images for each of the samples studied.

The void fraction of each block was calculated based on the surface area and solid volume of its characteristic unit cell and compared with values obtained from XCT analysis. The comparison revealed a good agreement between both methods, increasing confidence in the validity of the proposed geometric model. This analysis should be repeated with additional samples to increase the reliability of the model.

5.6. RECOMMENDATIONS AND FUTURE WORK

Several actions should be taken to improve the accuracy of the pressure drop and heat transfer analysis of the 3D-printed MCM blocks. The most relevant ones are listed below:

- The size of the temperature sensors placed on the sides of the block should be reduced as much as possible so that the temperature in a particular position can be determined rather than an average temperature over a range of positions.
- The thermal conductivity of the dry and wet printed block must be determined to improve the accuracy of the calculated heat transfer coefficients. This must be done in the directions perpendicular to the water flow.

- A two dimensional heat transfer model with Dirichlet boundary conditions on the lateral sides of the blocks and Neumann boundary conditions on the surfaces in contact with the copper plates could help to improve accuracy of calculated heat transfer coefficients. Heat transfer by conduction through the lateral sides could be considered in such a model.
- An additional level of complexity could be introduced by incorporating a velocity profile obtained from computational fluid dynamics simulations and coupling the fluid and solid energy conservation equations.
- Analyze blocks with staggered arrangement. Blocks analyzed so far have an in-line arrangement of the fibers. This alternative geometry is also printable using the extrusion-based method employed for printing the samples that we studied, and it has been demonstrated that staggered arrangement leads to better heat transfer coefficients although also producing higher pressure drops [130].
- The temperature difference between water stream and copper plates must be limited to 5 K to minimize heat leaks. This would also facilitate calculating an average temperature of the block with higher confidence.
- Heat leaks from the copper plates to ambient must be minimized in order to minimize uncertainties in the calculations.
- Electrical contact resistances should be measured to better estimate the heat fluxes at the surfaces of the blocks.
- Electrical and thermal contact resistances between the copper plates and the blocks should be minimized by using Indium foil. This will minimize the uncertainty in the measurement of the surface temperature of the block, which could then be assumed equal to the temperature of the copper plates with more confidence.
- The initial electrical current should be as large as necessary to produce a maximum temperature difference of 5 K between the copper plates and water. This can vary from one experiment to another due to differences in contact resistance. Larger temperature differences will cause larger uncertainties in the calculations due to larger heat leaks. This would also help to minimize the uncertainty associated with the temperature of the surfaces of the blocks in contact with the copper plates.
- Filter cartridges must be replaced more often to enable reaching high flow rates.

A

REGION IN ST DIAGRAM EXHIBITING AN ADIABATIC TEMPERATURE CHANGE GREATER THAN 2 K

In this section some details about the construction of the *sT* diagrams of Figure 3.9 is presented. Figure A.1a shows the adiabatic temperature change of the base material $Mn_{1.18}Fe_{0.73}P_{0.48}Si_{0.52}$ as a function of temperature for a magnetic field change from 0 T to 1.4 T. Figure A.1b shows the specific entropy of the same material as a function of temperature for two magnetic fields, 0 T and 1.4 T. The vertical lines in Figure A.1a enclose the temperature range where the adiabatic temperature change is larger than 2 K. This temperature range is also drawn as vertical lines in Figure A.1b. The entropy values of the points where these vertical lines intersect the zero field entropy curve correspond approximately to 75 and 105 $J\,kg^{-1}\,K^{-1}$. The same applies for the other materials in the bed but in their own temperature range.

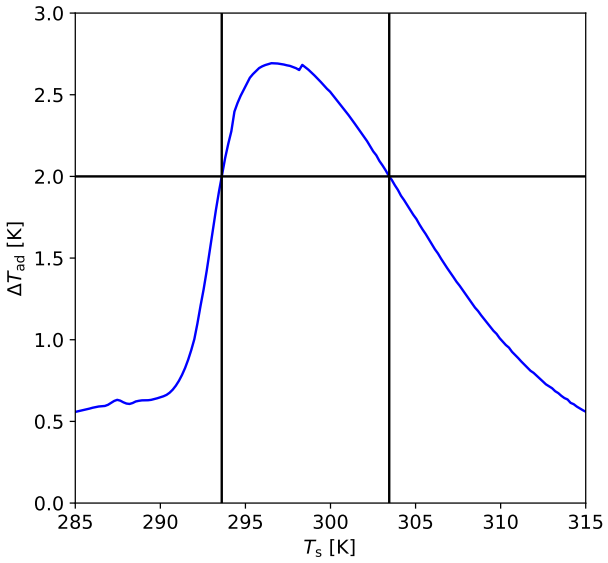

(a) Adiabatic temperature change

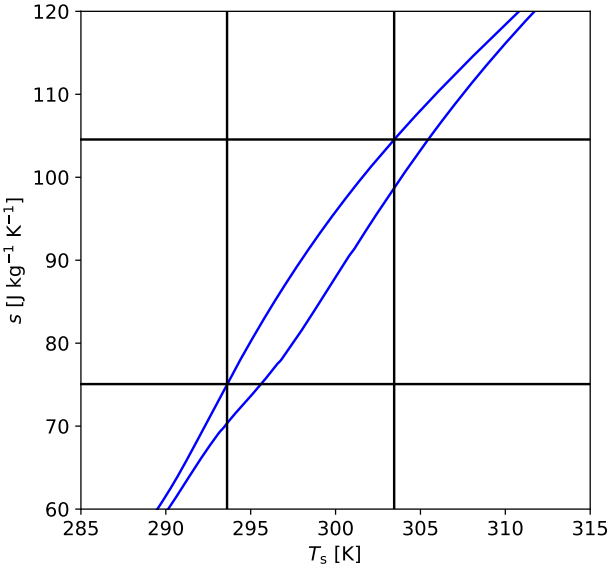

(b) Total entropy

Figure A.1.: a) Adiabatic temperature change vs temperature, and b) specific entropy vs temperature for the material $Mn_{1.18}Fe_{0.73}P_{0.48}Si_{0.52}$. Vertical lines on figure a) enclose the temperature range where the adiabatic temperature change is larger than 2 K.

B

MODEL VALIDATION

The model was validated using experimental data of a Gd-based, single-AMR device [16]. A comparison between the experimental and numerical data is presented in Figure B.1.

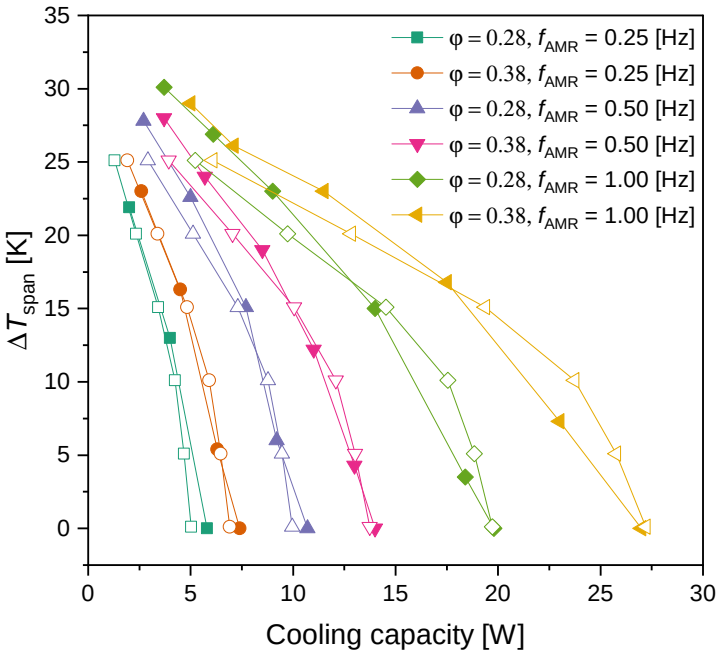

Figure B.1.: Comparison of experimental and numerical results of simulations performed for the validation of the model. Performance data of a Gd-based, single-AMR device was used [16]. Open symbols correspond to numerical results while solid symbols correspond to experimental data.

C

DETAILS ABOUT THE HYDRAULIC CIRCUIT OF THE EXPERIMENTAL SETUP

Additional details of the hydraulic circuit of the experimental setup are presented in this appendix. These could be relevant for reproduction of the experimental setup.

Two secondary pipe lines are visible in Figure 5.2. The first one of these starts from a pressure relief valve and discharges the fluid directly to the tank. This valve is installed to limit the maximum pressure that the pump can build up in the system, and it is necessary given that a positive displacement pump is used. The pressure setting of this valve is 3 bar. A pressure gauge (WIKA 0 - 5 bar) is also installed near this point to keep track of the maximum pressure developed in the system as the flow rate is increased. The other secondary line of the hydraulic circuit is a bypass of the branch containing the filters, flow meter, and sample holder. This secondary line includes a needle valve that acts as a flow control element. This line has a two-fold purpose. First, it allows considerably increasing the flow rate of water flowing through the finned-tube heat exchanger to reduce the time needed to change the temperature of the water between experiments. The needle valve is completely open for this. Second, it enables reaching very low flow rates in the parallel branch containing the sample holder. The flow rate is normally controlled by changing the rotational speed of the direct current (DC) motor of the pump using pulse width modulation (PWM), but the pulse width can only be reduced to a minimum value below which the pump simply stops pumping water. So, to reach smaller flow rates, the needle valve is open manually while keeping the PWM value constant.

The use of a filtration stage was important in order to maintain all the small flow channels of the 3D printed blocks open and free from contaminants so that the pressure drop measurements were reliable. The source of contaminants could be traces of the glue that was used for sealing some openings of the sample holder, residues of the polymer resin

that is used for the 3D printing of the sample holder, algae growing in the water (even though the likelihood of this happening was minimized by darkening the transparent pipes and water tank with insulating material), dust from the samples, and / or corrosion residues from other metallic components of the system such as the finned-tube heat exchanger.

After mounting a new sample and before starting any experiment, air needs to be removed from the system. This is done by running water through the system for several minutes until air bubbles are no longer visible in the fluid flow. After installing new filter cartridges, this procedure must be carried out for a longer period of time since, in particular, the filters trap a considerably large amount of air that is released as micro bubbles in the water flow.

Some important remarks about design choices made during the development of the setup are:

- The water tank was located in the uppermost level of the system. Placing the tank in this position helps to avoid getting air trapped in pipes or other components of the system and to provide a positive head at the suction of the pump.
- A gear pump was preferred over a centrifugal pump because it can achieve higher pressures at high flow rates and is easier to control. It was also preferred over a diaphragm pump because it can produce a quasi-continuous flow and is less sensitive to pressure changes.
- The thermostatic bath was operated in external-control mode using the temperature of the water that enters the sample holder as the feedback control signal. In this way, the temperature of the water that enters the block is better controlled, and it is easier to maintain it approximately constant during the experiments.
- The flow meter was configured to output a 0-10 V signal that is proportional to the flow rate.
- Ceramic filters were chosen because they tolerate higher water temperatures (compared to cellulose-based filters) and can retain particles as small as 5 µm. A disadvantage of this type of filters is that they introduce a large pressure drop in the system limiting the range of flow rates that can be tested with the setup, but arranging two filters in parallel allowed to expand this range.
- The sample holder was placed in a vertical position. This was necessary to avoid air being trapped in the upper part of the casing. If air is trapped the water flow cannot be distributed over the entire cross section of the block. Air could be trapped inside the sample holder due to the fact that the entering and leaving tubes have an internal diameter of 8 mm and the sample holder a squared cross-section of 15 x 15 mm^2, and the pipes are centered with respect to the sample holder cross-section. The hydrostatic pressure was subtracted from the differential pressure measurements.

D

EXPERIMENTS FOR CHARACTERIZATION OF RESISTANCE OF THE BLOCKS AS A FUNCTION OF TEMPERATURE

As briefly mentioned in subsection 5.1.5, we explored the possibility of determining the average sample temperature during the heat transfer experiments by correlating its change in electrical resistance with temperature. Initially, this approach seemed feasible, as the same working principle is used in reliable and accurate resistance temperature detectors (RTDs). However, in practice, the MnFePSi MCM is far more complex than the pure platinum typically used in RTDs.

One major challenge is that the MCM undergoes a phase transition near the temperature range in which we aimed to characterize its resistance-temperature relationship. It has been demonstrated that the resistivity of this material exhibits a peak near the transition temperature [38], meaning that, unlike the materials used in commercial RTDs, its resistivity does not increase approximately linearly with temperature. Additionally, Guillou et al. [38] showed that this material can suffer mechanical degradation upon thermal cycling, resulting in a consistent increase in electrical resistivity over multiple cycles.

Furthermore, a practical difficulty with this approach is that the electrical resistance of the blocks was about 1 mΩ at room temperature, whereas RTDs are typically designed to have resistances of either 100 Ω or 1000 Ω at 0 °C. Moreover, preliminary measurements showed that the change in electrical resistance of the blocks with temperature was minimal.

Nevertheless, despite these fundamental challenges that could hinder the suitability of the blocks as resistive temperature sensors, we made

significant efforts to characterize the change in their resistance with temperature, which are worth reporting here.

Initially, we attempted to measure the resistance of these blocks by submerging them in a custom-built thermostatic bath filled with an special water-based alkaline solution. A Lakeshore 340 temperature controller, with a Nickel-Chromium wire resistor submerged in the solution, was used to set the temperature of water to different values. However, the voltages required by the resistor were high enough to trigger an electrochemical reaction in the solution. The solution had a ph of approximately 11 and was especially chosen to prevent corrosion of the sample. While demineralized water would have prevented the electrochemical reaction, it would have led to sample corrosion. Due to these challenges, this method was ultimately disregarded.

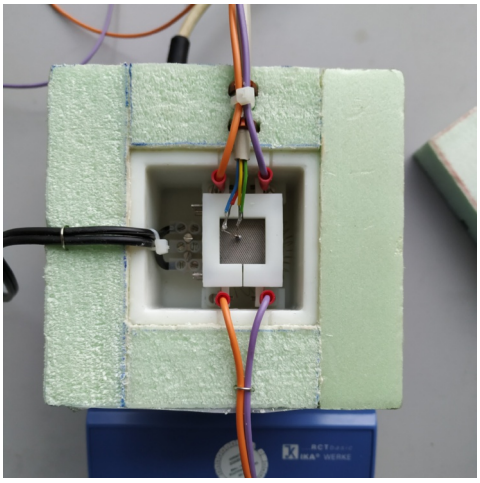

(a) Assembled setup with a sample

(b) Nickel-Chromium wire resistor

Figure D.1.: Custom-built thermostatic bath designed and assembled for characterization of resistance-temperature relationship of 3D-printed MCM blocks. An image with a sample mounted is shown in (a), and the detail of the Nickel-Chromium wire resistor used for heating the water is shown in (b).

As an alternative, we opted to perform the characterization using the setup developed for the heat transfer experiments. Special probes with sharp ends were designed to pass through, without touching, the copper plates for measuring the voltage drop across the sample in a four-wire resistance measurement method. The blocks were expected to adopt the temperature of the circulating water, and RTDs were used to measure the water temperature before and after the blocks as well as the surface temperature of the blocks.

First, a Delta Elektronika E 030-3 power supply provided a current of 1 A, and the voltage drop across the blocks was measured using a Keithley 2000 digital multimeter. Later, we implemented the so-called delta method for measuring small resistances using a Keithley 2400 SourceMeter and a Keithley 2182 NanoVoltmeter. With this method, constant thermoelectric voltages are canceled out by alternating between positive and negative currents.

However, even with this later approach, it was not possible to obtain repeatable resistance measurements during thermal cycling. Figure D.2 shows the measured resistance of two different blocks during thermal cycling experiments. From this figure, it is evident that the blocks could not be used as temperature sensors. The sudden increase in electrical resistance upon crossing a certain temperature could be attributed to microcracks forming when crossing the transition temperature for the first time, a phenomenon previously reported in the literature [129]. However, this could not be confirmed, as we did not determine the transition temperature of these samples using magnetization or heat capacity measurements.

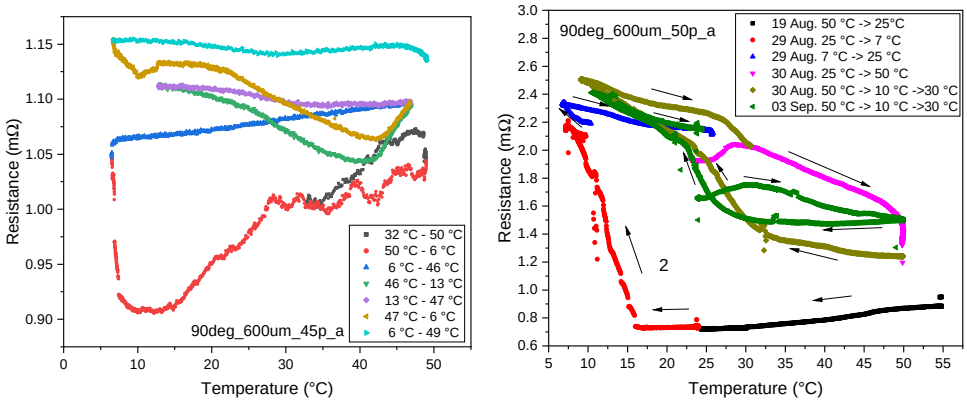

(a) sample 90deg_600um_45p_a **(b)** sample 90deg_600um_50p_a

Figure D.2.: Characterization of the resistance-temperature relationship of two samples: (a) sample 90deg_600um_45p_a, and (b) sample 90deg_600um_50p_a. These results demonstrate that the blocks cannot be used as temperature sensors.

E

DETAILS OF THE CONTROL AND DATA LOGGING SYSTEM OF THE EXPERIMENTAL SETUP

As shown in Figure 5.7, digital multimeters (DMM) were used to read the signals of the multiple sensors installed in the setup. DMM1, a Keithley 2000 equipped with a Model 2000-SCAN Scanner Card, was configured in 4-wire resistance mode to read the resistances of 5 resistive temperature detectors (RTDs), RTD1 to RTD5 (see Figure 5.6 and Figure 5.2). DMM2, a second Keithley 2000 also equipped with a Model 2000-SCAN Scanner Card, was configured in DC voltage mode to read the differential pressure sensor as well as the voltage drop over the current shunt and the voltage drop across the copper plates. DMM3 is a Lakeshore 331 Temperature Controller that is only used in this setup as a multimeter to read the resistance of the RTD sensor that measures ambient temperature. DDM4 is an Agilent 34410A multimeter used to read the output of the flow meter. The output signal of the flow meter was initially connected to the multi-channel scanning card of the DMM2, but it was found that this signal disturbed other voltage measurements performed on the same card. Thus, a dedicated multimeter was necessary for the flow meter to avoid this.

All multimeters are interconnected using the general purpose interface bus (GPIB). A GPIB-to-USB adapter was used to connect the bus to a laptop. The Julabo Dyneo DD-1000F refrigerated circulator was also connected to the computer using serial communication. This last communication is solely intended to monitor and log the temperature of the water entering the sample holder. This temperature sensor is used by the refrigerated circulator as feedback signal in the temperature control loop. The goal of this control loop is to ensure a constant temperature at the inlet of the sample holder.

Python was used to establish the communication between the

computer, the multimeters, and the refrigerated circulator. The PyVISA library was used to manage the devices connected to the GPIB bus, and the serial library manages the serial communication with the circulator.

F

RELATIONSHIP BETWEEN DARCY AND MODIFIED FRICTION FACTORS FOR THE PARALLEL PLATE REGENERATORS

The pressure drop in parallel plate regenerators is commonly analyzed using characteristic non-dimensional numbers applicable to internal flow: the Darcy friction factor and the Reynolds number, both based on an average channel velocity and a hydraulic diameter. These non-dimensional numbers differ from those used to analyze friction losses in packed beds. This appendix presents a derivation that establishes the relationship between these two groups of non-dimensional numbers for parallel plate regenerators, enabling direct comparisons with packed beds, and the novel 3D-printed blocks.

RELATIONSHIP BETWEEN REYNOLDS NUMBERS FOR INTERNAL FLOW AND FLOW IN PACKED BEDS

The definition of Reynolds number used in internal flow analysis, applied to the case of parallel plate regenerators is:

$$Re_{\text{int}} = \frac{\rho v_{\text{chan}} D_{\text{hyd}}}{\mu} \tag{F.1}$$

The parallel plate regenerator consists of N parallel channels, and the geometry is usually fully characterized from a hydraulics perspective, with the plate spacing, s_{p}, and the plate thickness, t_{p}. Using these parameters, the void fraction is defined as:

$$\varepsilon = \frac{s_p}{s_p + t_p} \tag{F.2}$$

The hydraulic diameter is calculated using the relation $4A_{cs}/P_{cs}$, where A_{cs} is the flow cross sectional area and P_{cs} the wetted perimeter. For a parallel plate regenerator with plate height much larger than plate thickness, this can be approximated by:

$$D_{hyd} = 2s_p \tag{F.3}$$

The relation between the channel velocity and the superficial velocity is:

$$v_{chan} = \frac{v_{sup}}{\varepsilon} = v_{sup}\frac{s_p + t_p}{s_p} \tag{F.4}$$

By replacing Equation F.2, Equation F.3, and Equation F.4 in Equation F.1, the internal Reynolds number in terms of superficial velocity for a parallel plate regenerator can be found:

$$Re_{int} = \frac{2\rho v_{sup}(s_p + t_p)}{\mu} \tag{F.5}$$

On the other hand, the definition of the modified Reynolds number for packed beds is:

$$Re_{mod} = \frac{\rho v_{sup} D_p}{\mu(1-\varepsilon)} \tag{F.6}$$

The equivalent particle diameter, D_p, is calculated using the relation $6V_s/A_s$, where V_s and A_s are the volume and the surface area of the solid particles respectively. This reduces to the following expression for a parallel plate regenerator:

$$D_p = 3t_p \tag{F.7}$$

Replacing Equation F.2 and Equation F.7 into Equation F.6, gives the expression of the modified Reynolds number applicable for the parallel plate geometry:

$$Re_{mod} = \frac{3\rho v_{sup}(s_p + t_p)}{\mu} \tag{F.8}$$

Combining the results of Equation F.8 and Equation F.5, the relation between the modified and internal Reynolds numbers can be found as:

$$Re_{mod} = \frac{3}{2}Re_{int} \tag{F.9}$$

RELATIONSHIP BETWEEN FRICTION FACTORS FOR INTERNAL FLOW AND FLOW IN PACKED BEDS

The definition of the modified friction factor for flow in packed beds is based on an equivalent particle diameter and superficial velocity:

$$ff_{\text{mod}} = \frac{\Delta P D_{\text{p}}}{L \rho v_{\text{sup}}^2} \frac{\varepsilon^3}{1-\varepsilon} \tag{F.10}$$

Using the definitions of equivalent particle diameter and void fraction of the parallel plate geometry given in Equation F.7 and Equation F.2 respectively, the modified friction factor becomes:

$$ff_{\text{mod}} = \frac{3\Delta P}{L \rho v_{\text{sup}}^2} \frac{s_{\text{p}}^3}{(s_{\text{p}} + t_{\text{p}})^2} \tag{F.11}$$

On the other hand, the Darcy friction factor applied to parallel plate regenerators is given by:

$$ff_{\text{D}} = \frac{\Delta P \cdot D_{\text{hyd}}}{L \cdot \frac{1}{2} \rho v_{\text{chan}}^2} \tag{F.12}$$

Using the definitions of the hydraulic diameter and the equivalence between channel and superficial velocities as presented in Equation F.3 and Equation F.4 respectively, Equation F.12 becomes:

$$ff_{\text{D}} = \frac{4\Delta P}{L \rho v_{\text{sup}}^2} \frac{s_{\text{p}}^3}{(s_{\text{p}} + t_{\text{p}})^2} \tag{F.13}$$

Combining Equation F.11 and Equation F.13, the relationship between the Darcy friction factor used in internal flow and the modified friction factor used in flow through packed beds simplifies to:

$$ff_{\text{mod}} = \frac{3}{4} ff_{\text{D}} \tag{F.14}$$

MODIFIED FRICTION FACTOR AS FUNCTION OF MODIFIED REYNOLDS NUMBER FOR PARALLEL PLATES

For fully developed laminar flow between parallel plates, the following expression is widely used to correlate the Darcy friction factor to the Reynolds number:

$$ff_D = \frac{96}{Re_{\text{int}}} \tag{F.15}$$

This equation can be rewritten in terms of a modified friction factor and a modified Reynolds number by applying the relationships that link them to their corresponding internal-flow analogues, as given in Equation F.14 and Equation F.9:

$$ff_{\text{mod}} = \frac{3}{4}\frac{96}{Re_{\text{int}}} = \frac{108}{Re_{\text{mod}}} \tag{F.16}$$

REFERENCES

[1] IPCC. *Climate Change 2021: The Physical Science Basis. Contribution of Working Group I to the Sixth Assessment Report of the Intergovernmental Panel on Climate Change*. Tech. rep. Intergovernmental Panel on Climate Change, 2021, p. 2391. doi: 10 . 1017 / 9781009157896. url: https://www.ipcc.ch/report/ar6/wg1/.

[2] Rijksoverheid. “Klimaatakkoord”. *Klimaatakkoord* (2019), p. 250.

[3] W. Goetzler, R. Zogg, J. Young, and C. Johnson. *Energy savings potential and RD&D opportunities for non-vapor-compression HVAC technologies*. Tech. rep. U.S. Department of Energy, 2014. doi: https://doi.org/10.2172/1220817.

[4] A. Kitanovski. “Energy Applications of Magnetocaloric Materials”. *Adv. Energy Mater.* 10 (2020), p. 1903741.

[5] E. Brück, O. Tegus, D. T. Thanh, and K. H. Buschow. “Magnetocaloric refrigeration near room temperature (invited)”. *J. Magn. Magn. Mater.* 310 (2007), pp. 2793–2799.

[6] A. Kitanovski, J. Tušek, U. Tomc, U. Plaznik, M. Ožbolt, and A. Poredoš. *Magnetocaloric energy conversion - From theory to applications*. 2015, p. 456. isbn: 9783319087405.

[7] U. Plaznik, J. Tušek, A. Kitanovski, and A. Poredoš. “Numerical and experimental analyses of different magnetic thermodynamic cycles with an active magnetic regenerator”. *Appl. Therm. Eng.* 59 (2013), pp. 52–59.

[8] International Energy Agency. *Installation of about 600 million heat pumps covering 20% of buildings heating needs required by 2030 – Analysis - IEA*. 2022. url: https://www.iea.org/reports/installation-of-about-600-million-heat-pumps-covering-20-of-buildings-heating-needs-required-by-2030 (visited on 05/07/2025).

[9] H. Johra, K. Filonenko, P. Heiselberg, C. Veje, T. Lei, S. Dall’Olio, K. Engelbrecht, and C. Bahl. “Integration of a magnetocaloric heat pump in a low-energy residential building”. *Build. Simul.* 11 (2018), pp. 753–763.

[10] H. Johra, K. Filonenko, P. Heiselberg, C. Veje, S. Dall'Olio, K. Engelbrecht, and C. Bahl. "Integration of a magnetocaloric heat pump in an energy flexible residential building". *Renew. Energy* 136 (2019), pp. 115–126.

[11] K. A. Gschneidner and V. K. Pecharsky. "Thirty years of near room temperature magnetic cooling: Where we are today and future prospects". *Int. J. Refrig.* 31 (2008), pp. 945–961.

[12] J. A. Lozano, K. Engelbrecht, C. R. Bahl, K. K. Nielsen, D. Eriksen, U. L. Olsen, J. R. Barbosa, A. Smith, A. T. Prata, and N. Pryds. "Performance analysis of a rotary active magnetic refrigerator". *Appl. Energy* 111 (2013), pp. 669–680.

[13] D. Eriksen, K. Engelbrecht, C. R. Haffenden Bahl, and R. Bjørk. "Exploring the efficiency potential for an active magnetic regenerator". *Sci. Technol. Built Environ.* 22 (2016), pp. 527–533.

[14] M. S. Capovilla, J. A. Lozano, P. V. Trevizoli, and J. R. Barbosa. "Performance evaluation of a magnetic refrigeration system". *Sci. Technol. Built Environ.* 22 (2016), pp. 534–543.

[15] A. T. D. Nakashima, F. P. Fortkamp, N. M. D. Sá, V. M. A. Santos, G. Hoffmann, G. F. Peixer, S. L. Dutra, M. C. Ribeiro, J. A. Lozano, and J. R. Barbosa Jr. "A magnetic wine cooler prototype". *Int. J. Refrig.* 122 (2021), pp. 110–121.

[16] P. V. Trevizoli, A. T. Nakashima, G. F. Peixer, and J. R. Barbosa. "Performance evaluation of an active magnetic regenerator for cooling applications - part I: Experimental analysis and thermodynamic performance". *Int. J. Refrig.* 72 (2016), pp. 192–205.

[17] N. M. De Sá, A. T. Nakashima, J. A. Lozano, and J. R. Barbosa. "Thermodynamic comparison of magnetocaloric and vapor compression wine coolers". *Int. J. Refrig.* 156 (2023), pp. 29–39.

[18] E. Brück. "Developments in magnetocaloric refrigeration". *J. Phys. D: Appl. Phys.* 38 (2005), R381–R391.

[19] D. Pineda Quijano, B. Fonseca Lima, C. Infante Ferreira, and E. Brück. "Seasonal COP of a residential magnetocaloric heat pump based on MnFePSi". *Int. J. Refrig.* 164 (2024), pp. 38–48.

[20] D. Eriksen, K. Engelbrecht, C. R. Bahl, R. Bjørk, and K. K. Nielsen. "Effects of flow balancing on active magnetic regenerator performance". *Appl. Therm. Eng.* 103 (2016), pp. 1–8.

[21] P. Hai, J. Shen, Z. Li, K. Li, and W. Dai. "Development and experimental analysis of a multi-bed active magnetic regenerator". *Int. J. Refrig.* 162 (2024), pp. 169–178.

[22] J. Slaughter, L. Griffith, A. Czernuszewicz, and V. Pecharsky. “Scalable and compact magnetocaloric heat pump technology”. *Appl. Energy* 377 (2025), p. 124696.

[23] S. Dall’Olio, M. Masche, J. Liang, A. R. Insinga, D. Eriksen, R. Bjørk, K. K. Nielsen, A. Barcza, H. A. Vieyra, N. V. Beek, H. N. Bez, K. Engelbrecht, and C. R. Bahl. “Novel design of a high efficiency multi-bed active magnetic regenerator heat pump”. *Int. J. Refrig.* 132 (2021), pp. 243–254.

[24] T. Lei, K. K. Nielsen, K. Engelbrecht, C. R. Bahl, H. Neves Bez, and C. T. Veje. “Sensitivity study of multi-layer active magnetic regenerators using first order magnetocaloric material La(Fe,Mn,Si) 13 H y”. *J. Appl. Phys.* 118 (2015), p. 014903.

[25] U. Tomc, S. Nosan, K. Klinar, and A. Kitanovski. “Towards powerful magnetocaloric devices with static electro-permanent magnets”. *J. Adv. Res.* 45 (2023), pp. 157–181.

[26] B. Huang, J. W. Lai, D. C. Zeng, Z. G. Zheng, B. Harrison, A. Oort, N. H. van Dijk, and E. Brück. “Development of an experimental rotary magnetic refrigerator prototype”. *Int. J. Refrig.* 104 (2019), pp. 42–50.

[27] P. Weiss and A. Piccard. “Le phènomène magnètocalorique”. *J. Phys. Theor. Appl.* 7 (1917), pp. 103–109.

[28] J. Romero Gómez, R. Ferreiro Garcia, A. De Miguel Catoira, and M. Romero Gómez. “Magnetocaloric effect: A review of the thermodynamic cycles in magnetic refrigeration”. *Renew. Sustain. Energy Rev.* 17 (2013), pp. 74–82.

[29] A. Smith, C. R. Bahl, R. Bjork, K. Engelbrecht, K. K. Nielsen, and N. Pryds. “Materials challenges for high performance magnetocaloric refrigeration devices”. *Adv. Energy Mater.* 2 (2012), pp. 1288–1318.

[30] T. Lei. “Modeling of active magnetic regenerators and experimental investigation of passive regenerators with oscillating flow”. PhD Thesis. Technical University of Denmark, 2016, p. 270. url: https://orbit.dtu.dk/en/publications/modeling-of-active-magnetic-regenerators-and-experimental-investi.

[31] V. K. Pecharsky and K. A. Gschneidner. “Magnetocaloric effect from indirect measurements: Magnetization and heat capacity”. *J. Appl. Phys.* 86 (1999), pp. 565–575.

[32] T. V. Christiaanse, O. Campbell, P. V. Trevizoli, S. Misra, D. Van Asten, L. Zhang, P. Govindappa, I. Niknia, R. Teyber, and A. Rowe. “A concise approach for building the S-T diagram for Mn-Fe-P-Si hysteretic magnetocaloric material”. *J. Phys. D: Appl. Phys.* 50 (2017), p. 365001.

[33] Yibole. “Nature of the first-order magnetic phase transition in giant-magnetocaloric materials”. PhD Thesis. Delft University of Technology, 2016, p. 111. isbn: 978-94-6186-625-7. url: https://repository.tudelft.nl/record/uuid:29152e5c-f6ba-44ad-8bd2-f9784c6a2f0d.

[34] Hanggai. “Phase transitions and magnetic properties of transition metal based magnetocaloric materials”. PhD Thesis. Delft University of Technology, 2025. doi: 10.4233/uuid:07e1fac3-ae48-4677-8557-693bbb6bbe64.

[35] A. Kitanovski and P. W. Egolf. “Thermodynamics of magnetic refrigeration”. *Int. J. Refrig.* 29 (2006), pp. 3–21.

[36] J. Lyubina. “Magnetocaloric materials for energy efficient cooling”. *J. Phys. D: Appl. Phys.* 50 (2017), p. 053002.

[37] N. H. Dung, L. Zhang, Z. Q. Ou, and E. Brück. “Magnetoelastic coupling and magnetocaloric effect in hexagonal Mn-Fe-P-Si compounds”. *Scr. Mater.* 67 (2012), pp. 975–978.

[38] F. Guillou, H. Yibole, N. H. Van Dijk, L. Zhang, V. Hardy, and E. Brück. “About the mechanical stability of MnFe(P,Si,B) giant magnetocaloric materials”. *J. Alloys Compd.* 617 (2014), pp. 569–574.

[39] F. Guillou, G. Porcari, H. Yibole, N. Van Dijk, and E. Brück. “Taming the first-order transition in giant magnetocaloric materials”. *Adv. Mater.* 26 (2014), pp. 2671–2675.

[40] K. A. Gschneidner and V. K. Pecharsky. “Magnetocaloric Materials”. *Annu. Rev. Mater. Sci.* 30 (2000), pp. 387–429.

[41] A. Gschneidner, V. K. Pecharsky, and A. O. Tsokol. “Recent developments in magnetocaloric materials”. *Reports Prog. Phys.* 68 (2005), pp. 1479–1539.

[42] V. Franco, J. S. Blázquez, B. Ingale, and A. Conde. “The magnetocaloric effect and magnetic refrigeration near room temperature: Materials and models”. *Annu. Rev. Mater. Res.* 42 (2012), pp. 305–342.

[43] M. S. Kamran, H. O. Ahmad, and H. S. Wang. “Review on the developments of active magnetic regenerator refrigerators – Evaluated by performance”. *Renew. Sustain. Energy Rev.* 133 (2020), p. 110247.

[44] A. Greco, C. Aprea, A. Maiorino, and C. Masselli. “A review of the state of the art of solid-state caloric cooling processes at room-temperature before 2019”. *Int. J. Refrig.* 106 (2019), pp. 66–88.

[45] V. K. Pecharsky and K. A. Gschneidner. “Giant magnetocaloric effect in Gd5 (Si2 Ge2)”. *Phys. Rev. Lett.* 78 (1997), pp. 4494–4497.

[46] P. V. Trevizoli, A. T. Nakashima, G. F. Peixer, and J. R. Barbosa. “Performance assessment of different porous matrix geometries for active magnetic regenerators”. *Appl. Energy* 187 (2017), pp. 847–861.

[47] A. Kiecana. “Magnetic phase transitions and magnetic structures in Mn-based compounds”. PhD Thesis. Delft University of Technology, 2023, p. 161. doi: 10.4233/7851D718-D584-45FF-BC68-AB77188E286E.

[48] N. T. Trung, Z. Q. Ou, T. J. Gortenmulder, O. Tegus, K. H. Buschow, and E. Brück. “Tunable thermal hysteresis in MnFe(P,Ge) compounds”. *Appl. Phys. Lett.* 94 (2009), pp. 2009–2011.

[49] W. A. Steyert. “Stirling-cycle rotating magnetic refrigerators and heat engines for use near room temperature”. *J. Appl. Phys.* 49 (1978), pp. 1216–1226.

[50] J. A. Barclay and W. A. Steyert. *US Patent No. 4,332,135. Active magnetic regenerator*. Jan. 1982.

[51] G. V. Brown. “Magnetic heat pumping near room temperature”. *J. Appl. Phys.* 47 (1976), pp. 3673–3680.

[52] J. Tušek, A. Kitanovski, U. Tomc, C. Favero, and A. Poredoš. “Experimental comparison of multi-layered La-Fe-Co-Si and single-layered Gd active magnetic regenerators for use in a room temperature magnetic refrigerator”. *Int. J. Refrig.* 37 (2014), pp. 117–126.

[53] D. Pineda Quijano, C. Infante Ferreira, and E. Brück. “Layering strategies for active magnetocaloric regenerators using MnFePSi for heat pump applications”. *Appl. Therm. Eng.* 232 (2023), p. 120962.

[54] H. Lv, H. Ma, N. Mao, and T. He. “Boiling heat transfer mechanism of environmental-friendly refrigerants: A review”. *Int. J. Refrig.* 133 (2022), pp. 214–225.

[55] S. Lionte, M. Risser, and C. Muller. “A 15kW magnetocaloric proof-of-concept unit: Initial development and first experimental results”. *Int. J. Refrig.* 122 (2021), pp. 256–265.

[56] Environmental Investigation Agency. *EU F-gas regulation handbook: keeping ahead of the curve as Europe phases down HFCs*. Tech. rep. Environmental Investigation Agency, 2015. url: https://eia-international.org/wp-content/uploads/EIA-F-Gas-Regulation-Handbook.pdf.

[57] P. V. Trevizoli, T. V. Christiaanse, P. Govindappa, I. Niknia, R. Teyber, J. R. Barbosa, and A. Rowe. “Magnetic heat pumps: An overview of design principles and challenges”. *Sci. Technol. Built Environ.* 22 (2016), pp. 507–519.

[58] D. S. Arnold, A. Tura, A. Ruebsaat-Trott, and A. Rowe. “Design improvements of a permanent magnet active magnetic refrigerator”. *Int. J. Refrig.* 37 (2014), pp. 99–105.

[59] L. Griffith, A. Czernuszewicz, J. Slaughter, and V. Pecharsky. “CaloriSMART: Small-scale test-stand for rapid evaluation of active magnetic regenerator performance”. *Energy Convers. Manag.* 199 (2019), p. 111948.

[60] P. V. Trevizoli, A. T. Nakashima, and J. R. Barbosa. “Performance evaluation of an active magnetic regenerator for cooling applications – part II: Mathematical modeling and thermal losses”. *Int. J. Refrig.* 72 (2016), pp. 206–217.

[61] R. Bjørk, A. Smith, C. R. Bahl, and N. Pryds. “Determining the minimum mass and cost of a magnetic refrigerator”. *Int. J. Refrig.* 34 (2011), pp. 1805–1816.

[62] S. Jacobs, J. Auringer, A. Boeder, J. Chell, L. Komorowski, J. Leonard, S. Russek, and C. Zimm. “The performance of a large-scale rotary magnetic refrigerator”. *Int. J. Refrig.* 37 (2013), pp. 84–91.

[63] C. Zimm, A. Boeder, B. Mueller, K. Rule, and S. L. Russek. “The evolution of magnetocaloric heat-pump devices”. *MRS Bull.* 43 (2018), pp. 274–279.

[64] M. Masche, J. Liang, K. Engelbrecht, and C. Bahl. “Performance assessment of a rotary active magnetic regenerator prototype using gadolinium”. *Appl. Therm. Eng.* 204 (2022), p. 117947.

[65] D. Eriksen, K. Engelbrecht, C. R. Bahl, R. Bjørk, K. K. Nielsen, A. R. Insinga, and N. Pryds. “Design and experimental tests of a rotary active magnetic regenerator prototype”. *Int. J. Refrig.* 58 (2015), pp. 14–21.

[66] A. Waske, M. E. Gruner, T. Gottschall, and O. Gutfleisch. “Magnetocaloric materials for refrigeration near room temperature”. *MRS Bull.* 43 (2018), pp. 269–273.

[67] J. Liang, K. Engelbrecht, K. K. Nielsen, K. Loewe, H. Vieyra, A. Barcza, and C. R. Bahl. “Performance assessment of a triangular microchannel active magnetic regenerator”. *Appl. Therm. Eng.* 186 (2021), p. 116519.

[68] I. Batashev. “Rational approaches to the design of magnetocaloric materials”. PhD thesis. Delft University of Technology, 2022, p. 289. doi: https://doi.org/10.4233/uuid:0f2ee7c8-70d2-43b2-93e7-26a328ded3a9.

[69] W. Brey, G. Nellis, and S. Klein. “Thermodynamic modeling of magnetic hysteresis in AMRR cycles”. *Int. J. Refrig.* 47 (2014), pp. 85–97.

[70] T. Lei, K. Engelbrecht, K. K. Nielsen, H. Neves Bez, and C. R. Bahl. “Study of multi-layer active magnetic regenerators using magnetocaloric materials with first and second order phase transition”. *J. Phys. D: Appl. Phys.* 49 (2016), p. 345001.

[71] F. Guillou, H. Yibole, G. Porcari, L. Zhang, N. H. Van Dijk, and E. Brück. “Magnetocaloric effect, cyclability and coefficient of refrigerant performance in the MnFe(P, Si, B) system”. *J. Appl. Phys* 116 (2014), p. 63903.

[72] T. Gottschall, K. P. Skokov, M. Fries, A. Taubel, I. Radulov, F. Scheibel, D. Benke, S. Riegg, and O. Gutfleisch. “Making a Cool Choice: The Materials Library of Magnetic Refrigeration”. *Adv. Energy Mater.* 9 (2019), p. 1901322.

[73] R. Gauß, G. Homm, and O. Gutfleisch. “The Resource Basis of Magnetic Refrigeration”. *J. Ind. Ecol.* 21 (2017), pp. 1291–1300.

[74] M. A. Richard, A. M. Rowe, and R. Chahine. “Magnetic refrigeration: Single and multimaterial active magnetic regenerator experiments”. *J. Appl. Phys.* 95 (2004), pp. 2146–2150.

[75] A. Rowe and A. Tura. “Experimental investigation of a three-material layered active magnetic regenerator”. *Int. J. Refrig.* 29 (2006), pp. 1286–1293.

[76] D. S. Arnold, A. Tura, and A. Rowe. “Experimental analysis of a two-material active magnetic regenerator”. *Int. J. Refrig.* 34 (2011), pp. 178–191.

[77] C. Archipley, J. Barclay, K. Meinhardt, G. Whyatt, E. Thomsen, J. Holladay, J. Cui, I. Anderson, and S. Wolf. “Methane liquefaction with an active magnetic regenerative refrigerator”. *Cryogenics (Guildf).* 128 (2022), p. 103588.

[78] R. Teyber, P. V. Trevizoli, T. V. Christiaanse, P. Govindappa, I. Niknia, and A. Rowe. “Performance evaluation of two-layer active magnetic regenerators with second-order magnetocaloric materials”. *Appl. Therm. Eng.* 106 (2016), pp. 405–414.

[79] P. Govindappa, P. V. Trevizoli, O. Campbell, I. Niknia, T. V. Christiaanse, R. Teyber, S. Misra, M. A. Schwind, D. Van Asten, L. Zhang, and A. Rowe. “Experimental investigation of MnFeP1-xAsx multilayer active magnetic regenerators”. *J. Phys. D: Appl. Phys.* 50 (2017), p. 315001.

[80] K. Navickaitė, H. N. Bez, T. Lei, A. Barcza, H. Vieyra, C. R. Bahl, and K. Engelbrecht. “Experimental and numerical comparison of multi-layered La(Fe,Si,Mn)13Hy active magnetic regenerators”. *Int. J. Refrig.* 86 (2018), pp. 322–330.

[81] M. Masche, J. Liang, S. Dall'Olio, K. Engelbrecht, and C. R. Bahl. "Performance analysis of a high-efficiency multi-bed active magnetic regenerator device". *Appl. Therm. Eng.* 199 (2021), p. 117569.

[82] T. V. Christiaanse, P. V. Trevizoli, S. Misra, C. Carroll, D. Van Asten, L. Zhang, R. Teyber, P. Govindappa, I. Niknia, and A. Rowe. "Experimental study of 2-layer regenerators using Mn-Fe-Si-P materials". *J. Phys. D: Appl. Phys.* 51 (2018), p. 105002.

[83] P. Govindappa, P. V. Trevizoli, I. Niknia, T. V. Christiaanse, R. Teyber, and A. Rowe. "Experimental characterization of multilayer active magnetic regenerators using first order materials: Multiple points of equilibrium". *J. Appl. Phys.* 124 (2018), p. 134901.

[84] Y. Li, G. Lin, and J. Chen. "Numerical investigation and performance evaluation of the MnFe-based composite magnetocaloric material with large magnetic entropy change over a wide temperature range". *Int. J. Refrig.* 121 (2021), pp. 61–71.

[85] M. Zhang, O. Abdelaziz, A. M. Momen, and A. Abu-Heiba. "A numerical analysis of a magnetocaloric refrigerator with a 16-layer regenerator". *Sci. Rep.* 7 (2017), pp. 1–12.

[86] L. Yuan, S. Qian, and J. Yu. "Numerical study on the multi-layered magnetocaloric regenerators". *Appl. Therm. Eng.* 204 (2022), p. 118001.

[87] M. Risser, P. Collet, J.-B. Chaudron, S. Lionte, and C. Muller. "Optimization of a layered regenerator inside a magnetocaloric cooling system using an evolutionary algorithm". *Thermag VIII*. September. 2018, pp. 120–125. doi: 10.18462/iir.thermag.2018.0019.

[88] B. Monfared and B. Palm. "Optimization of layered regenerator of a magnetic refrigeration device". *Int. J. Refrig.* 57 (2015), pp. 103–111.

[89] T. V. Christiaanse, P. V. Trevizoli, and A. Rowe. "Modelling two layer Mn–Fe–Si–P materials in an active magnetic regenerator". *Int. J. Refrig.* 106 (2019), pp. 225–235.

[90] T. V. Christiaanse. *An opensource active magnet regenerator model written in python*. 2019. url: https://github.com/TheoChristiaanse/AMRmodel (visited on 10/14/2020).

[91] K. K. Nielsen, J. Tusek, K. Engelbrecht, S. Schopfer, A. Kitanovski, C. R. Bahl, A. Smith, N. Pryds, and A. Poredos. "Review on numerical modeling of active magnetic regenerators for room temperature applications". *Int. J. Refrig.* 34 (2011), pp. 603–616.

[92] I. Niknia, O. Campbell, T. V. Christiaanse, P. Govindappa, R. Teyber, P. V. Trevizoli, and A. Rowe. “Impacts of configuration losses on active magnetic regenerator device performance”. *Appl. Therm. Eng.* 106 (2016), pp. 601–612.

[93] T. F. Petersen, N. Pryds, A. Smith, J. Hattel, H. Schmidt, and H. J. Høgaard Knudsen. “Two-dimensional mathematical model of a reciprocating room-temperature Active Magnetic Regenerator”. *Int. J. Refrig.* 31 (2008), pp. 432–443.

[94] C. Aprea, A. Greco, A. Maiorino, and C. Masselli. “A comparison between rare earth and transition metals working as magnetic materials in an AMR refrigerator in the room temperature range”. *Appl. Therm. Eng.* 91 (2015), pp. 767–777.

[95] J. Tušek, A. Kitanovski, I. Prebil, and A. Poredoš. “Dynamic operation of an active magnetic regenerator (AMR): Numerical optimization of a packed-bed AMR”. *Int. J. Refrig.* 34 (2011), pp. 1507–1517.

[96] C. Aprea, A. Greco, and A. Maiorino. “Modelling an active magnetic refrigeration system: A comparison with different models of incompressible flow through a packed bed”. *Appl. Therm. Eng.* 36 (2012), pp. 296–306.

[97] D. J. Silva, J. Ventura, and J. P. Araújo. “Caloric devices: A review on numerical modeling and optimization strategies”. *Int. J. Energy Res.* 45 (2021), pp. 18498–18539.

[98] A. Macias-Machin, L. Oufer, and N. Wannenmacher. “Heat transfer between an immersed wire and a liquid fluidized bed”. *Powder Technol.* 66 (1991), pp. 281–284.

[99] I. Park, Y. Kim, and S. Jeong. “Development of the tandem reciprocating magnetic regenerative refrigerator and numerical simulation for the dead volume effect”. *Int. J. Refrig.* 36 (2013), pp. 1741–1749.

[100] N. Wakao and S. Kaguei. *Heat and mass transfer in packed beds*. Gordon and Breach Science Publishers, 1982, p. 364. isbn: 0-677-05860-8.

[101] M. Frischmann, K. Engelbrecht, G. Nellis, and S. Klein. “Heat Transfer Coefficient in a Packed Sphere Regenerator for use in Active Magnetic Regenerative Refrigeration”. *Int. Refrig. Air Cond. Conf.* 2008, pp. 1–8. doi: http://docs.lib.purdue.edu/iracc/935.

[102] K. L. Engelbrecht, G. F. Nellis, and S. A. Klein. “The effect of internal temperature gradients on regenerator matrix performance”. *J. Heat Transfer* 128 (2006), pp. 1060–1069.

[103] G. R. Hadley. “Thermal conductivity of packed metal powders”. *Int. J. Heat Mass Transf.* 29 (1986), pp. 909–920.

[104] S. Ergun. “Fluid flow through packed columns”. *Chem. Eng. Prog.* 48 (1952), pp. 89–94.

[105] T. V. Christiaanse. “Characterization, experimentation and modeling of Mn-Fe-Si-P magnetocaloric materials”. PhD Thesis. University of Victoria, 2018. isbn: 9781119130536.

[106] T. V. Christiaanse, P. V. Trevizoli, and A. Rowe. “Modelling two layer Mn–Fe–Si–P materials in an active magnetic regenerator”. *Int. J. Refrig.* 106 (2019), pp. 225–235.

[107] B. P. Vieira, H. N. Bez, D. dos Santos, J. A. Lozano, and J. R. Barbosa. “Interrelationship between flow profiles and the magnetic waveform and their influence on the performance of first-order active magnetic regenerators”. *Appl. Therm. Eng.* 219 (2023), p. 119581.

[108] N. H. Dung, Z. Q. Ou, L. Caron, L. Zhang, D. T. Thanh, G. A. De Wijs, R. A. De Groot, K. H. J. Buschow, and E. Brück. “Mixed magnetism for refrigeration and energy conversion”. *Adv. Energy Mater.* 1 (2011), pp. 1215–1219.

[109] A. A. Kiss and C. A. Infante Ferreira. *Heat Pumps in Chemical Process Industry*. 2016. isbn: 9781498718950. doi: 10.1201/9781315371030.

[110] T. Lei, K. Engelbrecht, K. K. Nielsen, and C. T. Veje. “Study of geometries of active magnetic regenerators for room temperature magnetocaloric refrigeration”. *Appl. Therm. Eng.* 111 (2017), pp. 1232–1243.

[111] L. Cozzi, Y. Monschauer, D. Wetzel, and S. Bouckaert. *The Future of Heat Pumps*. Tech. rep. Paris: International Energy Agency, 2022. url: https://www.iea.org/energy-system/buildings/heat-pumps.

[112] EU. *Clean and efficient cooling - Call for proposals*. 2023. url: https : / / eic . ec . europa . eu / eic - funding - opportunities / calls - proposals/clean-and-efficient-cooling%7B%5C_%7Den.

[113] M. Masche, J. Liang, K. Engelbrecht, and C. Bahl. “Efficient modulation of the magnetocaloric refrigerator capacity”. *Int. J. Refrig.* 145 (2023), pp. 59–67.

[114] S. Qian, L. Yuan, J. Yu, and G. Yan. “Variable load control strategy for room-temperature magnetocaloric cooling applications”. *Energy* 153 (2018), pp. 763–775.

[115] S. Qian, L. Yuan, and J. Yu. “An online optimum control method for magnetic cooling systems under variable load operation”. *Int. J. Refrig.* 97 (2019), pp. 97–107.

[116] J. Liang, M. Masche, K. Engelbrecht, T. Zhu, and C. Bahl. “The potential application of a magnetocaloric heat pump in ultra-low temperature district heating systems”. *ECOS 2022 - 35th Int. Conf. Effic. Cost, Optim. Simul. Environ. impact energy Syst.* Copenhagen, 2022, pp. 1–12.

[117] A. S. Shirazi and M. Bernier. “Thermal capacity effects in borehole ground heat exchangers”. *Energy Build.* 67 (2013), pp. 352–364.

[118] KNMI. *Hourly data of the weather in the Netherlands*. 2010. url: https://www.knmi.nl/nederland-nu/klimatologie/uurgegevens.

[119] D. L. Koch and J. F. Brady. “Dispersion in fixed beds”. *J. Fluid Mech.* 154 (1985), pp. 399–427.

[120] C. Aprea, A. Greco, A. Maiorino, R. Mastrullo, and A. Tura. “Initial experimental results from a rotary permanent magnet magnetic refrigerator”. *Int. J. Refrig.* 43 (2014), pp. 111–122.

[121] F. P. Fortkamp, D. Eriksen, K. Engelbrecht, C. R. Bahl, J. A. Lozano, and J. R. Barbosa. “Experimental investigation of different fluid flow profiles in a rotary multi-bed active magnetic regenerator device”. *Int. J. Refrig.* 91 (2018), pp. 46–54.

[122] Z. Li, K. Li, X. Guo, X. Gao, W. Dai, M. Gong, and J. Shen. “Influence of timing between magnetic field and fluid flow in a rotary magnetic refrigerator”. *Appl. Therm. Eng.* 187 (2021), p. 116477.

[123] European Committee for Standardization. *Air conditioners, liquid chilling packages and heat pumps, with electrically driven compressors, for space heating and cooling, commercial and process cooling - Testing and rating at part load conditions and calculation of seasonal performance (EN 14825:2*. 2022.

[124] RVO. *Voorbeeldwoningen 2022 bestaande bouw*. Tech. rep. Rijksdienst voor Ondernemend Nederland, 2022.

[125] K. Engelbrecht, D. Eriksen, C. R. Bahl, R. Bjørk, J. Geyti, J. A. Lozano, K. K. Nielsen, F. Saxild, A. Smith, and N. Pryds. “Experimental results for a novel rotary active magnetic regenerator”. *Int. J. Refrig.* 35 (2012), pp. 1498–1505.

[126] M. Wiesheu, M. Merkel, T. Sittig, D. Benke, M. Fries, S. Schöps, O. Weeger, and I. C. Garcia. “How to build the optimal magnet assembly for magnetocaloric cooling: Structural optimization with isogeometric analysis”. *Int. J. Refrig.* 152 (2023), pp. 62–73.

[127] J. A. Lozano, M. S. Capovilla, P. V. Trevizoli, K. Engelbrecht, C. R. Bahl, and J. R. Barbosa. “Development of a novel rotary magnetic refrigerator”. *Int. J. Refrig.* 68 (2016), pp. 187–197.

[128] A. L. London, J. W. Mitchell, and W. A. Sutherland. “Heat-Transfer and Flow-Friction Characteristics of Crossed-Rod Matrices”. *J. Heat Transfer* 82 (1960), pp. 199–213.

[129] M. Fries, L. Pfeuffer, E. Bruder, T. Gottschall, S. Ener, L. V. Diop, T. Gröb, K. P. Skokov, and O. Gutfleisch. “Microstructural and magnetic properties of Mn-Fe-P-Si (Fe2 P-type) magnetocaloric compounds”. *Acta Mater.* 132 (2017), pp. 222–229.

[130] P. V. Trevizoli, R. Teyber, P. S. da Silveira, F. Scharf, S. M. Schillo, I. Niknia, P. Govindappa, T. V. Christiaanse, and A. Rowe. “Thermal-hydraulic evaluation of 3D printed microstructures”. *Appl. Therm. Eng.* 160 (2019), p. 113990.

[131] C. Aprea, G. Cardillo, A. Greco, A. Maiorino, and C. Masselli. “A rotary permanent magnet magnetic refrigerator based on AMR cycle”. *Appl. Therm. Eng.* 101 (2016), pp. 699–703.

[132] J. A. Lozano, M. S. Capovilla, P. V. Trevizoli, K. Engelbrecht, C. R. H. Bahl, and J. R. Barbosa Jr. “Development of a novel rotary magnetic refrigerator”. *Int. J. Refrig.* 68 (2016), pp. 187–197.

[133] C. Vasile and C. Muller. “Innovative design of a magnetocaloric system”. *Int. J. Refrig.* 29 (2006), pp. 1318–1326.

[134] A. Funk, M. Zeilinger, A. Miehe, D. Sopu, J. Eckert, F. Dötz, and A. Waske. “MnFePSi-based magnetocaloric packed bed regenerators: Structural details probed by X-ray tomography”. *Chem. Eng. Sci.* 175 (2018), pp. 84–90.

[135] J. Liang, C. D. Christiansen, K. Engelbrecht, K. K. Nielsen, R. Bjørk, and C. R. Bahl. “Characterization of Freeze-Cast Micro-Channel Monoliths as Active and Passive Regenerators”. *Front. Energy Res.* 8 (2020), p. 54.

[136] L. Miao, K. Wang, X. Lu, Y. Zhang, and J. Liu. “Microchannel magnetic regenerators with optimized porosity by electrodischarge drilling: Microstructure and refrigeration performance”. *Materialia* 33 (2024), p. 102034.

[137] K. D. N’dri, N. Charpentier, L. Hirsinger, A. Gilbin, and T. Barriere. “Highly loaded magnetocaloric composites by La(Fe,Si)13H powder dedicated to extrusion-based additive manufacturing applications”. *Powder Technol.* 425 (2023), p. 118616.

[138] K. Navickaitė, J. Liang, C. Bahl, S. Wieland, T. Buchenau, and K. Engelbrecht. “Experimental characterization of active magnetic regenerators constructed using laser beam melting technique”. *Appl. Therm. Eng.* 174 (2020), p. 115297.

[139] K. Navickaite, C. Bahl, and K. Engelbrecht. “Nature-inspired flow patterns for active magnetic regenerators assessed using a 1D AMR model”. *Front. Energy Res.* 7 (2019), p. 68.

[140] K. Imaizumi, A. Fujita, A. Suzuki, M. Kobashi, and M. Kato. “Additive manufacturing for 3D microchannel structure using La(FexSi1-x)13 magnetic refrigerant via laser powder bed fusion”. *Addit. Manuf.* 83 (2024), p. 104076.

[141] F. Blake. “The resistance of packing to fluid flow”. *Trans. Am. Inst. Chem. Eng.* 14 (1922), pp. 415–421.

[142] A. F. Mills. *Heat transfer*. Pearson Education, 1999, p. 878. isbn: 0-13-947624-5.

[143] J. W. Park, D. Ruch, and R. A. Wirtz. “Thermal /fluid characteristics of isotropic plain-weave screen laminates as heat exchange surfaces”. *40th AIAA Aerosp. Sci. Meet. Exhib.* (2002).

[144] T. Lei, K. Navickaitė, K. Engelbrecht, A. Barcza, H. Vieyra, K. K. Nielsen, and C. R. Bahl. “Passive characterization and active testing of epoxy bonded regenerators for room temperature magnetic refrigeration”. *Appl. Therm. Eng.* 128 (2018), pp. 10–19.

[145] N. Wakao, S. Kaguei, and T. Funazkri. “Effect of fluid dispersion coefficients on particle-to-fluid heat transfer coefficients in packed beds: Correlation of nusselt numbers”. *Chem. Eng. Sci.* 34 (1979), pp. 325–336.

[146] J. Kirana. *Testing the Heat Transfer and Pressure Drop of Magnetocaloric Regenerators with an Experimental Setup*. Master Thesis. 2023.

[147] D. Pineda Quijano and M. Goemans. *KAdatalogger*. Delft, 2024. url: https://github.com/diego-pineda/Keithley%7B%5C_%7DArduino%7B%5C_%7Ddata%7B%5C_%7Dlogger%7B%5C_%7Dand%7B%5C_%7Dcontroller.

[148] D. Pineda Quijano, M. Goemans, E. Pieter, S. Papaioanou, A. Waske, C. Infante Ferreira, and E. Brück. “A friction factor correlation for flow through blocks of MnFePSi magnetocaloric material produced by extrusion-based additive manufacturing”. *(in preparation)* (2025).

[149] J. C. Armour and J. N. Cannon. “Fluid flow through woven screens”. *AIChE J.* 14 (1968), pp. 415–420.

[150] P. V. Trevizoli. “Development of thermal regenerators for magnetic cooling applications”. PhD Thesis. Federal University of Santa Catarina, 2015. doi: 10.13140/RG.2.2.18965.52965. url: http://www.polo.ufsc.br/portal/en/publicacoes.

[151] L. Yuan, Y. Liu, J. Yu, and S. Qian. “Experimental study on cooling performance of active magnetic regenerators with different structures”. *Int. J. Refrig.* 153 (2023), pp. 184–193.

[152] W. S. Chang. “Porosity and Effective Thermal Conductivity of Wire Screens”. *J. Heat Transfer* 112 (1990), pp. 5–9.

SUMMARY

In the context of the energy transition heat pumps are expected to play a key role in the decarbonization of the built environment by reducing the reliance on fossil fuels for heating residential and commercial buildings. However, alternative heat pump technologies are urgently needed due to the environmental and safety concerns associated with conventional vapor-compression systems, particularly the high global warming potential, toxicity, and/or flammability of some of their working fluids. In response, the scientific community has been actively developing next-generation heat pump technologies, among which magnetocaloric systems stand out as one of the most advanced and promising alternatives with the potential to compete cost-effectively with vapor compression systems. This thesis explores various engineering and system-level aspects of magnetocaloric heat pump (MCHP) systems for application in the built environment.

As the central element of an MCHP, the active magnetocaloric regenerator (AMR) must be carefully designed to ensure high system performance. One important aspect to control in the design of AMRs using first order magnetocaloric materials in layered configurations is the distribution of Curie temperatures. While an ideal AMR would exhibit a continuous change of Curie temperature along its length, ensuring that the magnetocaloric effect (MCE) is maximized at each position, realizing such a gradient is difficult in practice. However, this may become feasible through the use of advanced additive manufacturing techniques in combination with a very well controlled heat treatment process. The concept involves printing the AMR with a limited number of carefully selected MnFePSi compositions, followed by the induction of a quasi-continuous Curie temperature gradient via diffusion of elements within the matrix during the sintering stage.

The resulting spatial gradient in Curie temperature can, in principle, follow different functional forms depending on the initial composition choices. To investigate how these distributions influence AMR performance in residential MCHPs, a numerical study was conducted using a one-dimensional AMR model, as detailed in **chapter 3**. Three functional distributions were considered: (1) a linear gradient, (2) a sigmoidal curve, and (3) a linear profile with extended first and last layers. The results showed that employing thicker end layers in conjunction with a linear distribution of Curie temperatures of the materials in the central layers reduces the sensibility of the AMR to

changes in the operating temperatures. This is particularly beneficial for residential MCHPs, where fluctuating ambient temperatures and diverse user behavior introduce unavoidable variability in system operation throughout the heating season.

One of the key performance indicators for residential heat pumps is the seasonal coefficient of performance (SCOP). In the case of a water-to-water system (hypothetically) operating between reservoirs at constant temperature, the SCOP can be estimated by incorporating the seasonal variation in heating demand, primarily influenced by outdoor temperature fluctuations. The SCOP of an MCHP was estimated based on these considerations, and the results are presented in **chapter 4**. The analysis was based on the performance map of a 12-layer AMR composed of MnFePSi materials with linearly distributed Curie temperatures spanning from 8 °C to 35 °C. Capacity control was achieved through continuous modulation of both the fluid flow rate and AMR cycle frequency. An additional degree of control was introduced by dividing the system into modules with multiple AMRs that can be selectively activated or deactivated depending on the heating demand of the house. These combined strategies enabled the system to reach an estimated SCOP of 4.5 under realistic seasonal operating conditions.

As demonstrated in both **chapter 3** and **chapter 4**, the performance of MCHPs can be predicted using numerical AMR models. These models usually depend on constitutive equations to account for friction losses and heat transfer between the solid MCM and the heat transfer fluid. While such correlations are well-established for geometries typically used in the process industry such as packed beds, microchannels, and parallel plates, they are not yet available for new geometries made possible by extrusion-based additive manufacturing. To address this gap, an experimental setup was developed to measure the pressure drop across MnFePSi blocks manufactured using this technique. A geometric model of the printed blocks was proposed, and the accuracy of the void fraction predicted by this model was validated using X-ray tomography.

The pressure drop data were analyzed using the approach typically employed for packed beds, involving modified definitions of friction factor and Reynolds number based on equivalent particle diameters, superficial velocities, and void fractions. This method resulted in the tight clustering of multiple experimental curves around a consolidated friction factor-Reynolds number profile, from which a geometry-specific friction factor correlation was derived. The resulting curve resembles that of packed beds, with inertial losses dominating at Reynolds numbers above 100 and viscous losses prevailing at lower values. Compared to packed beds, parallel plates, and squared microchannels, the 3D-printed geometry shows a friction factor that falls between that of packed beds and parallel plates. These findings are detailed in

chapter 5.

Experiments to characterize the heat transfer behavior of the printed structures were also conducted using the same setup. A heat transfer model was proposed to extract heat transfer coefficients from the measured temperature data. However, the experiments lacked reproducibility, indicating a need for further improvements in both the setup and data acquisition method. The apparatus, methodology, modeling approach, and representative data are also presented in **chapter 5**.

This thesis has explored multiple aspects of advanced AMRs tailored for residential heat pump applications. Key investigations include the impact of different strategies for distributing the Curie temperatures in layered AMRs, the seasonal coefficient of performance of a residential MCHP incorporating MnFePSi-based regenerators, and the flow and heat transfer characteristics of a novel AMR geometry resulting from an extrusion-based additive manufacturing process, a method that supports the scalable production of MnFePSi AMRs. The progress achieved in the development of advanced AMRs through this work brings magnetocaloric technology one-step closer to commercial viability.

SAMENVATTING

In het kader van de energietransitie zullen warmtepompen naar verwachting een cruciale rol spelen bij de decarbonisatie van de gebouwde omgeving, doordat zij de afhankelijkheid van fossiele brandstoffen voor de verwarming van woonhuizen en bedrijfsgebouwen verminderen. Er is echter dringend behoefte aan alternatieve warmtepomptechnologieën vanwege de milieu- en veiligheidsproblemen die gepaard gaan met conventionele dampcompressiesystemen, met name de bijdrage aan de opwarming van de aarde, de giftigheid en/of ontvlambaarheid van sommige koudemiddelen. Als reactie hierop ontwikkelt de wetenschappelijke gemeenschap actief warmtepompen van de volgende generatie, waarbij magnetocalorische systemen zich onderscheiden als een van de meest geavanceerde en veelbelovende alternatieven met het potentieel om economisch te concurreren met dampcompressiesystemen. Dit proefschrift onderzoekt diverse technische en systeemgerichte aspecten van magnetocalorische warmtepompsystemen (MCHP) voor toepassing in de gebouwde omgeving.

Als centraal element van een MCHP moet de actieve magnetocalorische regenerator (AMR) zorgvuldig worden ontworpen om een hoge prestatie van het systeem te waarborgen. Een belangrijk ontwerpaspect bij het gebruik van magnetocalorische materialen met een eerste-orde-faseovergang in gelaagde configuraties is de verdeling van de Curietemperaturen. Terwijl een ideale AMR een continue verandering van de Curietemperatuur over haar lengte zou vertonen, zodat het magnetocalorische effect (MCE) op elke positie maximaal is, blijkt het in de praktijk moeilijk om een dergelijk verloop te realiseren. Dit kan echter haalbaar worden door het gebruik van geavanceerde additieve fabricagetechnieken in combinatie met een zeer goed gecontroleerd warmtebehandelingsproces. Het concept omvat het printen van de AMR met een beperkt aantal zorgvuldig gekozen MnFePSi-samenstellingen, gevolgd door de inductie van een quasi-continue Curietemperatuursgradiënt via diffusie van elementen binnen de matrix tijdens de sinterfase.

De resulterende ruimtelijke gradiënt in Curietemperatuur kan, afhankelijk van de initiële materiaalkeuze, verschillende functievormen aannemen. Om te onderzoeken hoe deze verdelingen de prestaties van de AMR in MCHP’s in woonhuizen beïnvloeden, werd een numerieke studie uitgevoerd met behulp van een eendimensionaal AMR-model,

zoals beschreven in **hoofdstuk 3**. Drie functies voor de verdeling werden beschouwd: (1) een lineaire gradiënt, (2) een sigmoïdale kromme en (3) een lineair profiel met verdikte eerste en laatste lagen. De resultaten toonden aan dat het gebruik van dikkere eindlagen in combinatie met een lineaire verdeling van Curietemperaturen in de centrale lagen de gevoeligheid van de AMR voor veranderingen in de bedrijfstemperaturen vermindert. Dit is bijzonder gunstig voor MCHP's in woonhuizen, waar variërende buitentemperaturen en divers gebruikersgedrag leiden tot onvermijdelijke variaties in de systeemwerking gedurende het stookseizoen.

Een van de belangrijkste prestatie-indicatoren voor residentiële warmtepompen is de seizoensgebonden prestatiecoëfficiënt (SCOP). In het geval van een water-water-systeem dat (hypothetisch) opereert tussen reservoirs met constante temperatuur, kan de SCOP worden geschat door de seizoensvariatie in verwarmingsvraag in rekening te brengen, die voornamelijk wordt beïnvloed door schommelingen in de buitentemperatuur. De SCOP van een MCHP werd op basis van deze overwegingen geschat en de resultaten worden gepresenteerd in **hoofdstuk 4**. De analyse was gebaseerd op de prestatiekaart van een 12-laagse AMR, samengesteld uit MnFePSi-materialen met lineair verdeelde Curietemperaturen van 8 °C tot 35 °C. Capaciteitsregeling werd bereikt door continue modulatie van zowel het debiet van de vloeistof als de frequentie van de AMR cyclus. Een extra regelingsmogelijkheid werd geïntroduceerd door het systeem op te delen in modules met meerdere AMR's die selectief konden worden geactiveerd of gedeactiveerd afhankelijk van de verwarmingsvraag van de woning. Deze gecombineerde strategieën stelden het systeem in staat een geschatte SCOP van 4,5 te bereiken onder realistische seizoensgebonden bedrijfsomstandigheden.

Zoals aangetoond in zowel **hoofdstuk 3** als **hoofdstuk 4**, kan de prestatie van MCHP's worden voorspeld met numerieke AMR-modellen. Deze modellen zijn doorgaans gebaseerd op constitutieve vergelijkingen die rekening houden met wrijvingsverliezen en warmteoverdracht tussen het vaste magnetocalorische materiaal en het warmteoverdrachtsmedium. Hoewel dergelijke correlaties goed zijn vastgesteld voor geometrieën die typisch in de procesindustrie worden gebruikt, zoals gepakte bedden, microkanalen en parallelle platen, zijn ze nog niet beschikbaar voor nieuwe geometrieën die mogelijk worden gemaakt door extrusiegebaseerde additieve fabricage. Om deze leemte te vullen werd een experimentele opstelling ontwikkeld om het drukverlies over MnFePSi-blokken, vervaardigd met deze techniek, te meten. Een geometrisch model van de geprinte blokken werd voorgesteld en de nauwkeurigheid van de voorspelde holtefractie in dit model werd gevalideerd met behulp van röntgentomografie.

De drukverliesgegevens werden geanalyseerd met de benadering die

typisch wordt toegepast op gepakte bedden, waarbij aangepaste definities van wrijvingsfactor en Reynoldsgetal werden gebruikt, gebaseerd op equivalente deeltjesdiameters, oppervlaksnelheden en holtefracties. Deze methode resulteerde in een nauwe clustering van meerdere experimentele curves rond een geconsolideerd profiel van wrijvingsfactor versus Reynoldsgetal, waaruit een geometriespecifieke correlatie voor de wrijvingsfactor werd afgeleid. De resulterende curve vertoont gelijkenis met die van gepakte bedden, waarbij inertiële verliezen overheersen bij Reynoldsgetallen boven 100 en viskeuze verliezen dominant zijn bij lagere waarden. In vergelijking met gepakte bedden, parallelle platen en vierkante microkanalen vertoont de 3D-geprinte geometrie een wrijvingsfactor die ligt tussen die van gepakte bedden en parallelle platen. Deze bevindingen worden uitgebreid besproken in **hoofdstuk 5**.

Experimentele studies naar het warmteoverdrachtsgedrag van de geprinte structuren werden eveneens uitgevoerd met dezelfde opstelling. Een warmteoverdrachtsmodel werd opgesteld om warmteoverdrachtscoëfficiënten te extraheren uit de gemeten temperatuurgegevens. De experimenten bleken echter onvoldoende reproduceerbaar, wat wijst op de noodzaak van verdere verbeteringen aan zowel de opstelling als de methode voor gegevensverzameling. De meetopstelling, methodologie, modelaanpak en representatieve resultaten worden eveneens gepresenteerd in **hoofdstuk 5**.

Dit proefschrift heeft meerdere aspecten onderzocht van geavanceerde AMR’s die zijn ontworpen voor warmtepomptoepassingen in woonhuizen. Belangrijke onderzoeken omvatten de invloed van verschillende strategieën voor de verdeling van Curietemperaturen in gelaagde AMR’s, de seizoensgebonden prestatiecoëfficiënt van een MCHP met MnFePSi-gebaseerde regeneratoren in woonhuizen en de stromings- en warmteoverdrachtseigenschappen van een nieuwe AMR-geometrie die voortkomt uit een extrusiegebaseerd additief fabricageproces — een methode die de schaalbare productie van MnFePSi-AMR’s ondersteunt. De in dit werk behaalde vooruitgang in de ontwikkeling van geavanceerde AMR’s brengt de magnetocalorische technologie een stap dichter bij commerciële haalbaarheid.

ACKNOWLEDGEMENTS

A little more than five years ago, I began the journey that is now coming to an end. Without a doubt, this has been the most challenging, yet also the most exciting and fulfilling period of my life. I could never have reached this point without the support and contributions of many people, whom I would like to acknowledge here.

First, I would like to express my deepest appreciation to **Prof. Dr. Ekkes Brück** and **Dr. ir. Carlos Infante Ferreira**, my promotors. I am profoundly grateful for the opportunity to embark on this life-changing experience under your supervision. Your guidance, understanding, and support throughout these years, as well as the countless meetings and discussions, have been invaluable. It has truly been an honor and a privilege to work with you both. Prof. Carlos, I consider you my mentor. During my master's in Sustainable Process and Energy Technologies at TU Delft, I attended all the courses you taught, and you also supervised both my internship and master's thesis projects. I learned immensely from you. I am especially grateful for your continued supervision of my PhD even after your retirement. Your insightful feedback and keen eye consistently helped me improve my results and, above all, my manuscripts. I will always remember your kindness and genuine interest in my well-being — you are a warm and generous person. Prof. Ekkes, your optimism always helped me overcome frustration during difficult moments. I am deeply thankful for your support to me and my family upon our arrival in the Netherlands, especially during the challenging months of COVID restrictions. I greatly appreciated your open-door policy, both for professional and personal matters. Thank you for pushing me when necessary and for your comforting words when things did not go as expected.

Dr. ir. Niels van Dijk, your comments and constructive criticism during the MCE meetings and FAME group discussions greatly contributed to my growth and to the quality of my work. I learned a great deal from you and feel privileged to have received input from such a knowledgeable person. **Ilse van der Kraaij** and **Nicole Banga**, thank you for your support with all the administrative matters that arose along the way. Without your help, everything would have been far more complicated. Ilse, I especially appreciate your willingness to speak Dutch with me. **Dr. Jouke Heringa**, I am sincerely grateful for your assistance with ICT-related matters — from choosing a laptop to resolving issues with TU Delft's supercomputer facilities. I also valued your presence at all my FAME group presentations, and I am thankful for your help in translating the summary of my thesis into Dutch.

I would like to express my gratitude to the people at the RID whose

contributions facilitated my work on the development of the experimental setup during the final part of my PhD trajectory. **Michel Thijs**, without your help, I could not have even started. Thank you for granting me access to the mechanical workshop, for helping me gather devices scattered around the building, for the crash course in soldering, for discussing my approach and sharing your expert opinion, and for providing so many essential components. My deepest gratitude also goes to **Sebastian Couweleers**. Thank you for your support with ordering components, for helping me locate equipment, and for always lending a hand with the drill in your workshop whenever I needed it. **Michel Steenvoorden**, thank you for your assistance with LabVIEW. **Kees de Vroege**, thank you for granting me unconditional access to the electronics laboratory. **Astrid van der Meer**, thank you for training me in the use of the SEM and for facilitating my access to that facility. **Martijn de Boer**, thank you for the tour around the experimental hall and for your help during one of my attempts to solder thermocouples onto the surface of 3D-printed MCM blocks. I also enjoyed our occasional conversations. **Anton Lefering**, thank you for showing me around the RID laboratories and for your support at various stages of my PhD. Special thanks go to the **DEMO team** for their continuous support and willingness to help, especially to **Hugo van der Kort**, **Maarten Lunenburg**, **Andries Oort**, and **Martin van Exter**. Finally, I am also grateful to **Dr. Jeroen Plomp**, **Robert Dankelman**, **Frans Ooms**, and **Johan de Haas** for their valuable contributions.

To my fellow PhD students of the FAME group: **Dr. Hanggai**, thank you for sharing your personal experiences of life in the Netherlands. We went through similar processes — buying a house, dealing with taxes and subsidies, working for Magneto, learning Dutch — and hearing about your experiences made me feel more at ease with each step. I also cherish our trip to Bielefeld and the moments we shared in Baotou. **Dr. Anika Kiekana**, I appreciated the collaboration we built while serving as teaching assistants for the Molecular Thermodynamics master course. **Dr. Qi Shen** and **Dr. Fengqi Zhang**, I truly admire your focus and dedication to academia. **Dr. Hamutu Ojiyed**, thank you for your constant willingness to help. **Dr. Ivan Batashev**, thank you for the fruitful discussions, especially during our time at Magneto. I greatly admire your intelligence and skills as a data scientist, as well as your broad knowledge and flexibility when performing experiments. **Dr. Xinmin You**, I admire your ability to pursue studies across different fields of knowledge, particularly medicine and materials science. Thank you for the pleasant conversations we shared from time to time. **Dr. Ziying Wu**, I truly enjoyed our lunchtime conversations and our chats during the social events at the RID. **Suye**, thank you for your valuable support before and during my trip to Baotou. I also enjoyed sharing the office with you during the final months of my PhD. Finally, I would like to extend my gratitude to **Øyvind Rørbakken**, **Zamran Khan**, and other PhD students from different groups with whom I shared stories and experiences — **Abdulkadir Biffo**, **Lassi Tiihonen**, **Marc van den Berg**, and **Yueer Li**.

Dr. Bowei Huang, you were the first person to welcome me in the FAME

group. Apart from my promotors, you were also the only person at TU Delft with whom I could discuss AMR modeling and magnetocaloric heat pumps. I truly appreciate the countless hours we spent discussing simulation results, ideas for the experimental setup, and prospects of the technology. I greatly admire your engineering skills and the extensive knowledge you possess about magnetocaloric systems. In addition, I would like to thank you and the co-founders of Magneto B.V., **Dr. Michael Maschek** and **Ivo Dusek**, for giving me the opportunity to work with you after completing my PhD.

Dr. Evgenii Velichko, I admire your ability to accomplish every goal you set for yourself. Thank you for welcoming me into the office we shared for some time and for the pleasant conversations we had. **Dr. Pedro Braga Groszewicz**, I very much enjoyed our conversations at the RID. **Prof. Dr. ir. Thijs Vlugt**, I am grateful for the opportunity to be part of the Engineering Thermodynamics group at ME for several years and for the insightful feedback provided by you and your group members. **Dr. Gilles de Wijs**, thank you for facilitating and maintaining my access to the supercomputer at Radboud Universiteit. **Savvina Papaioanou** and **Dr. Anja Waske** from the Bundesanstalt für Materialforschung und -prüfung (BAM), I am very grateful for the XCT analysis of the 3D printed MCM blocks that I used in the last part of my research.

I would like to express my gratitude to the students I had the pleasure of supervising. **Srikrishna Sivaramakrishnan**, your literature study was essential during the first stage of my PhD. **Beatriz Fonseca Lima**, thank you for your contribution to the seasonal COP study. **Jeremy Kirana**, your work on pressure drop and heat transfer in 3D-printed MCM blocks provided valuable input for my subsequent study on the same topic. **Eduard Pieter**, thank you for your willingness to go the extra mile to produce additional results. I am also grateful for your support at Magneto in fabricating the MCM blocks that I used in my research. **Michiel Goemans**, part of the data you collected was used in this thesis. Thank you for that and for your contribution to the development of the Python scripts used to control the experimental setup and process the data. I greatly enjoyed working with all of you and sharing thoughts, discussions, and a bit of our lives along the way.

I would like to acknowledge several people from Colombia who have played an important role in my professional development. **Prof. Dr. Ing. Carlos Borras Pinilla** from the Universidad Industrial de Santander, your academic trajectory has always been an inspiration to me. Thank you for encouraging me to continue my education abroad. **Ing. Álvaro Ruiz Rodríguez**, I deeply admire your perseverance and positive attitude despite setbacks. Thank you for shaping me into a better engineer and for allowing me to develop so many skills within your company. I am also grateful for your friendship and for keeping in touch after so many years. **Ing. Sergio Cavanzo**, I truly enjoyed working alongside you. Thank you for listening to my ideas during the years I worked at OTACC S.A. I have a deep appreciation for your company and great respect for you as a person and as a leader.

To my friends in Delft. **Febe**, **Vitali**, **Leila**, **Jose**, **Alexandra**, **Arturo**, **Conchi**, and **Rene**: you became our family in the Netherlands. We love celebrating with you the important moments of our lives. Gathering together

is always a pleasure, and seeing our children play reminds me of my own childhood with my siblings and cousins. Thank you for your friendship, your support, and for making our time in the Netherlands truly special. We hope to share many more years of friendship and joyful moments with all of you.

To my high school and university friends: **Yefferson Franco**, I admire your assertiveness, negotiation skills, and leadership. Thank you for visiting us in the Netherlands with your wife — we sincerely enjoyed having you and hope to host you again soon. **Iván Orduz** and **Jhony Martelo**, thank you for your friendship and for checking in from time to time to ask how I am doing. **Andrea Espinosa**, **Pablo Angulo**, and **Steven Pineda**, thank you for your lasting friendship.

A mis padres. Es difícil encontrar las palabras adecuadas para reconocer y agradecer el apoyo, la confianza, el ejemplo y las enseñanzas recibidas durante nuestra niñez y adolescencia. Gracias por brindarnos un ambiente adecuado para crecer y por formarnos como buenas personas a mis hermanos y a mi. Gracias por preocuparse siempre por nuestra educación. Mami, gracias por tu esfuerzo y dedicación a la familia. Solo ahora que soy padre puedo darme cuenta de lo difícil que debió haber sido nuestra crianza. Gracias por mostrarnos y enseñarnos que nunca es tarde para aprender algo nuevo y que todo lo que se aprenda en la vida es valioso y en algún momento nos será útil. Gracias por enseñarme a creer en mi. Papi, gracias por tu ejemplo y por tu sacrificio para proveer todo lo que necesitábamos. Gracias por enseñarnos los valores de la honestidad, la perseverancia y la paciencia. A mis hermanos. Gracias a ustedes aprendí la importancia del trabajo en equipo, de compartir, de colaborar y de ayudar desinteresadamente. Maria Paula y Carlos, gracias por visitarnos en los Paises Bajos. Agradezco también a mi suegra, Elva Rivera, por habernos apoyado durante los primeros meses de vida de nuestros hijos, Daniel en Colombia y Amelia en los Paises Bajos. Gracias por todo el amor que les brindas. Maria Fernanda Moros, gracias por tu ayuda convirtiendo algunos documentos de MS Word a LaTeX. A toda la familia Rivera, gracias por estar siempre pendientes de nosotros.

To my children **Daniel** and **Amelia**. I love you deeply, and I want only the best for you. You bring joy and meaning to our lives. I will always do my best to give you a happy childhood and to provide you with the tools you need for a fulfilling life. Finally, the most special place in this list belongs to my wife, **Adriana Guzmán**. I pursued this PhD because of you and for you and our children. Thank you for your understanding, your unconditional support, and your trust in me. You are my friend and confidant. I admire your strength, and I love you. I hope we can reach the end of our lives together, holding hands and enjoying the simple things in life.

LIST OF PUBLICATIONS

3. D. Pineda Quijano, M. Goemans, E. Pieter, S. Papaioanou, A. Waske, C. Infante Ferreira, and E. Brück. “A friction factor correlation for flow through blocks of MnFePSi magnetocaloric material produced by extrusion-based additive manufacturing”. *(in preparation)* (2025)

2. D. Pineda Quijano, B. Fonseca Lima, C. Infante Ferreira, and E. Brück. “Seasonal COP of a residential magnetocaloric heat pump based on MnFePSi”. *Int. J. Refrig.* 164 (Aug. 2024), pp. 38–48. doi: 10.1016/J.IJREFRIG.2024.04.014

1. D. Pineda Quijano, C. Infante Ferreira, and E. Brück. “Layering strategies for active magnetocaloric regenerators using MnFePSi for heat pump applications”. *Appl. Therm. Eng.* 232 (Sept. 2023), p. 120962. doi: 10.1016/J.APPLTHERMALENG.2023.120962

INTERNATIONAL ACTIVITIES

4. Friction factor correlation for flow through 3D-printed blocks of MnFePSi magnetocaloric material, Delft Days on Magnetocalorics (DDMC), 2025, Delft, The Netherlands (*oral presentation*).

3. Seasonal COP of a magnetocaloric heat pump for the built environment based on MnFePSi, Thermag X, 2024, Baotou, China (*oral presentation*).

2. Performance of MnFePSi-based AMRs with high and low heat capacity. A numerical study, Sino-German Workshop on Magnetocaloric Materials, 2024, Bielefeld, Germany (*oral presentation*).

1. Influence of gaps between layers of magnetocaloric materials in an active magnetocaloric regenerator, Dresden Days on Magnetocalorics (DDMC), 2023, Dresden, Germany (*oral presentation*).

CURRICULUM VITæ

Diego Fernando Pineda Quijano

09-11-1984	Born in Bucaramanga, Colombia
2002–2009	Bachelor in Mechanical Engineering Universidad Industrial de Santander, Colombia **Thesis:** *Design and construction of an autonomous mobile robot*
2014–2016	Master of Science in Mechanical Engineering Delft University of Technology, Delft, The Netherlands **Thesis:** *Heat recovery in the drying process of milk powder by using a liquid sorption system* Cum Laude
2020–2025	PhD. candidate in Applied Sciences Delft University of Technology, Delft, The Netherlands **Thesis:** *Advanced magnetocaloric regenerators for heat pump applications*

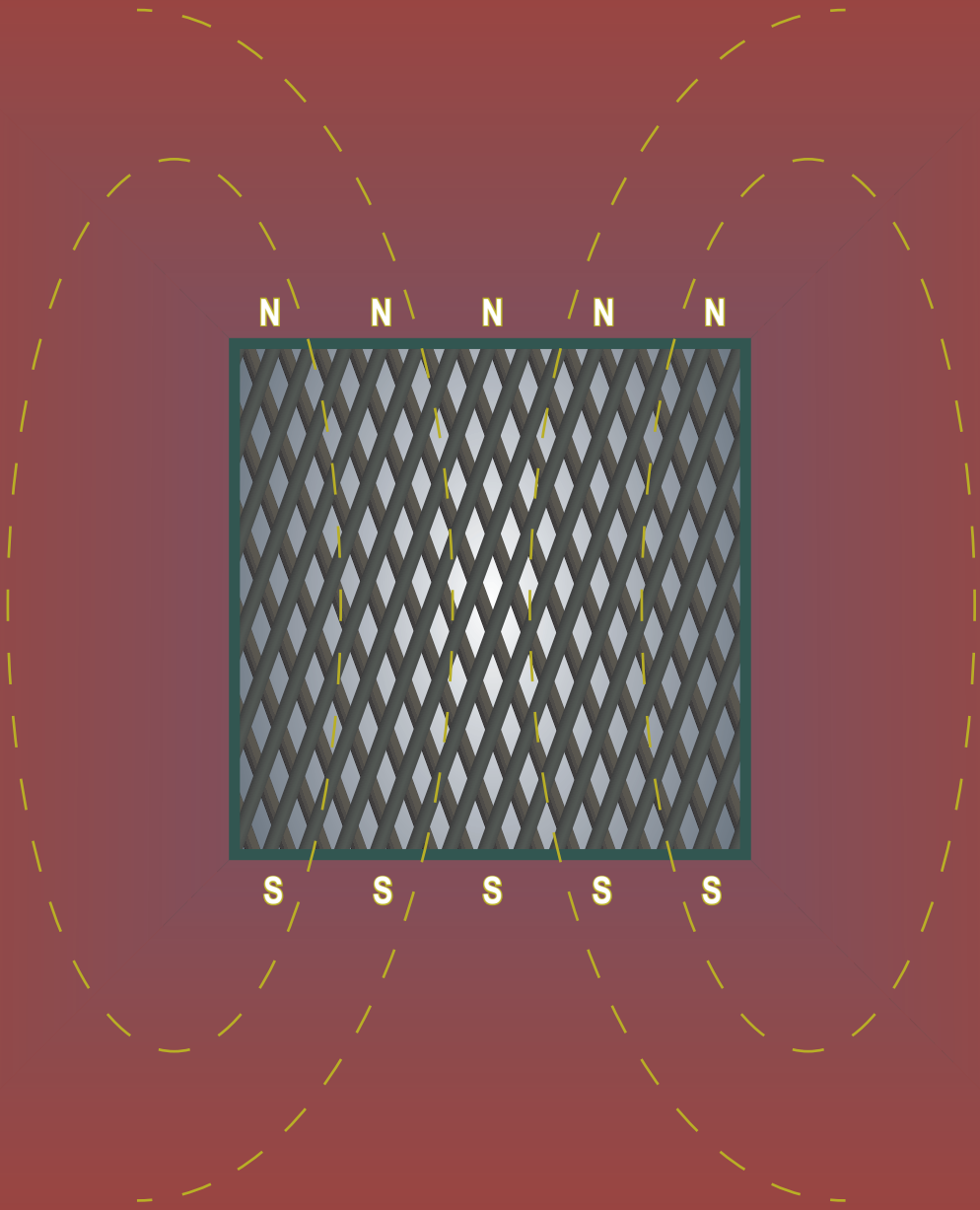

TU Delft